Multiscale morphological and biomechanical study of dentin : towards a better understanding of structure-properties relationship

Asef Hemmati

Thèse de doctorat

NNT : 2021UPAST123

université PARIS-SACLAY

Étude morphologique et biomécanique multi-échelle de la dentine : vers une meilleure compréhension des relations microstructures-propriétés

Multiscale morphological and biomechanical study of dentin : towards a better understanding of structure-properties relationship

Thèse de doctorat de l'Université Paris-Saclay

École doctorale n° 579, Sciences mécaniques et énérgétiques, matériaux et géosciences (SMEMaG)
Spécialité de doctorat : Science des matériaux
Unité de recherche : Université Paris-Saclay, CentraleSupélec, CNRS, Laboratoire de Mécanique des Sols, Structures et Matériaux, 91190, Gif-sur-Yvette, France
Référent : CentraleSupélec

Thèse présentée et soutenue à Gif-sur-Yvette, le 10.12.2021, par

Asef HEMMATI

Composition du jury

Pierre MILLET Professeur des Universités, Praticien Hospitalier, Université de Reims Champagne-Ardennes, Directeur de l'UFR Odontologie de Reims	Président
Yannick TILLIER Professeur à l'Ecole Nationale Supérieure des Mines de Paris (Mines ParisTech), chercheur au Centre de Mise en Forme des Matériaux (CEMEF)	Rapporteur & Examinateur
Jean-Marc ALLAIN Professeur des Universités, École Polytechnique, M3DISIM team	Rapporteur & Examinateur
Elisabeth DURSUN Professeur des Universités - Praticien Hospitalière, Unité de recherches biomatériaux innovants et interfaces (URB2i)	Examinatrice
Chloé ARSON Associate Professor Georgia Tech, School of Civil and Environmental Engineering	Examinatrice

Direction de la thèse

Nicolas SCHMITT Professeur des Universités, LMT, UPEC	Directeur
Elsa VENNAT Maître de Conférences, CentraleSupélec, Laboratoire MSSMat	Codirectrice

Aknowledgement

I would like to thank my supervisors, Elsa VENNAT and Nicolas SCHMITT, for their commitment, patience, knowledge, and kindness. Working with them was undoubtedly a great chance for me.
I also would like to thank the following group of wonderful people, without the help of whom, a thesis with a significant experimental side would not be possible: Nicolas ROUBIER, Thomas REISS, Eva HERIPRE, Paul HAGHI ASHTIANI, Pierre ARNAUD, François BRISSET, and Frédéric DOUIT.
I was lucky to work with Denis AUBRY and my supervisors on a paper, which helped me to better understand the numerical aspect of my thesis. Jan NEGGERS helped me especially with the part of the thesis about Digital Image Correlation. I thank them sincerely.
One interesting part of being a PhD student is to be a member of a group of students who not only have scientific conversations but also understand the challenges of a scientific project and encourage each other to continue. I thank Yannick YASOTHAN, Meisam MAJNOONI, Kyo SHINDO, Hossein KAMALINIA, Margot LECLERCQ, Louis CORNET, Laure LARIPPE, and Milad MOAZZAM for being good companions.
Finally, I would like to thank my family. I thank my sister, Sahar, who visited me every week and made sure that my life was more than only work. She planned activities like gatherings with friends, watching movies, shopping, and eating in restaurants. These kept me sane in the demanding period of doing a PhD. I thank my parents, who talked to me almost every day and encouraged me to continue working or to take a rest when the pressure was too much. Their kindness helped me mentally. I thank my brother, Saber, who made a sculpture of a blue whale for me. It brightened my mood and kept me going.

Table of contents

Abbreviations

AFM	Atomic force microscope (or microscopy)
BSE	Backscattered electron
CLSM	Confocal laser scanning microscopy
CSM	Continuous stiffness measurement
CSH	Calcium silicate hydrate
CT	Computed tomography
DEJ	Dentinoenamel junction
DIC	Digital image correlation
DSI	Depth sensing indentation
DXF	Drawing exchange format
EDS	Energy dispersive spectroscopy
FEG-SEM	Field emission gun SEM
FEM	Finite element method
FIB	Focused ion beam
GL	Grey level
HAADF	High angle annular dark field
HAP	Hydroxyapatite
HMP	Highly mineralized phase
IBID	Ion beam induced deposition
ITD	Intertubular dentin
ML	Mineral lamella
LB	Lateral branch
LBC	Lateral branch collar
LBL	Lateral branch lumen
LVDT	Linear variable differential transformer
MIP	Mercury intrusion porosimetry
PTD	Peritubular dentin
RAE	Representative area element
RUC	Repeated unit cell
RUS	Resonant ultrasound spectroscopy
RVE	Representative volume element
SCF	Stress concentration factor
SEM	Scanning electron microscope (or microscopy)
SGIT	Statistical grid indentation technique
STEM	Scanning transmission electron microscopy
TEM	Transmission electron microscope (or microscopy)
TL	Tubule lumen
TWS	Trainable Weka Segmentation
UM	Unloading method
UTS	Ultimate tensile strength
VN	Virtual Nanoindentation
ZOI	Zone of interest

Introduction

My thesis focuses on the tooth's main dental hard tissue, the dentin (Figure 0-1) and its morphological and mechanical properties.
Teeth play an important role in food mastication and speech production. Dentin is the heaviest and the most voluminous part of tooth, located beneath the enamel in crown dentin and covered by the cementum in root dentin. It surrounds the soft and sensitive pulp. Its roles are thought to be protecting the pulp [1], mechanically supporting the enamel and transferring the mastication loads to the jaws [2].

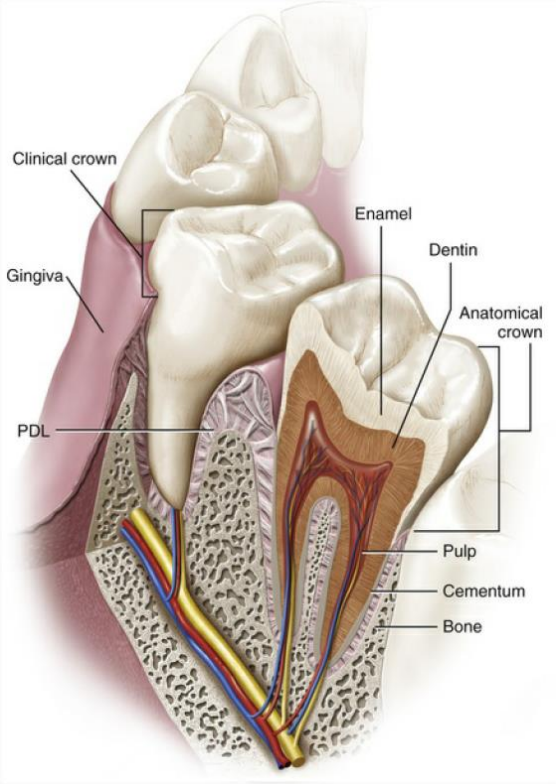

Figure 0-1. A cross-sectional view of tooth and its parts. [3]

However, dentin also has the role of being the anchorage tissue of most minimally invasive dental restorations. Dental restorations and especially the frequently used resin composite type, have a short lifetime -8 years according to Nieuwenhuysen et al. (2003)[4]-, which imposes enormous costs on patients and the state (dental health costs were 5.2% of the whole health expenses in France in 2020 [5]). The fact that dentists spend more than half of their time replacing previous restorations [6] also shows that tooth restoration's quality needs to improve.
One requirement for improving the dental restorations is to understand better and characterize the underlying dentinal tissue (its morphological and mechanical properties).

Microstructure of dentin

As visualized in Figure 0-2.b, the main features of the dentin microstructure are the tubules: hollow cylinders -made of peritubular dentin (PTD)- with 1.5 to 3 µm diameter that are

embedded in a matrix of intertubular dentin (ITD) and pass through the dentin from the enamel to the pulp. The porous phase inside the PTD is called tubule lumen (TL).

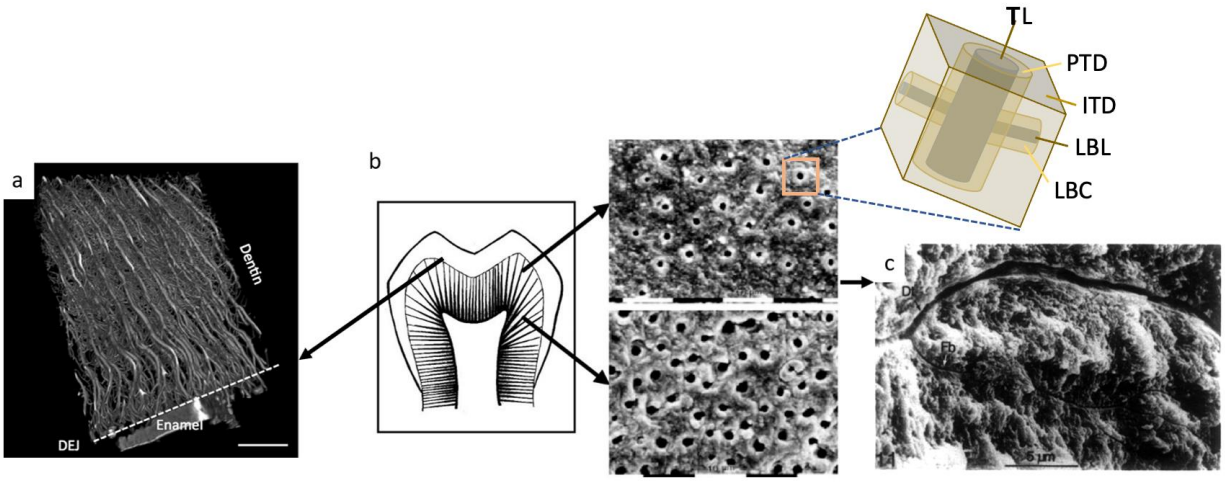

Figure 0-2. a) The complicated network of tubules and lateral branches below the enamel [7] *b) Tubular microstructure of dentin, revealing the variation in the diameter and density of tubules* [8]*, c) Detail of a fine branch connected to a tubule* [9]

The tubules are connected through lateral branches (LBs) that are similar to tubules but have smaller dimensions (Figure 0-2.c). Unlike tubules, the density of lateral branches increases by approaching the dentinoenamel junction, and they form a complicated network just beneath the enamel [7].

State of the art on dentin mechanical properties: where the disagreement begins…

There is much disagreement about dentin's mechanical properties. For example, elastic moduli are measured by mechanical tests in a range of roughly 10 to 30 GPa. This discrepancy has different reasons discussed in a review by Kinney et al. (2003) [10]. But one reason, especially interesting for this thesis, is the local variation in dentin's mechanical and morphological properties (from enamel to pulp). The variations in these properties make the measured mechanical characteristics depend on the sample size and its location inside the dentin. However, it is often not taken into account in the experimental protocols leading to such a scatter in the measured mechanical characteristics. Therefore, doing more experiments will not give better insight into the problem unless the following question is explored:

What is the relation between the mechanical properties of dentin and its microstructure, which locally varies?

Our approach

To answer this question, this thesis's approach is to develop a numerical model of dentin at the microscale. This numerical model must meet two requirements.

1. A geometry that represents the tubular microstructure of dentin.

The approximate periodicity in dentin's microstructure allows defining a periodical model of dentin, the repeating of which makes the microstructure. This "repeated unit cell" is defined in Chapter 3. For this task, a sample of dentin was imaged using scanning electron microscopy (SEM). To analyze the resulting images, an image analysis protocol has been developed.

2. Mechanical properties of the constituents (PTD and ITD).

In Chapter 2, nanoindentation tests are planned to characterize the constituents of dentin (PTD and ITD). To accomplish this, the suggested rules of the "statistical grid indentation technique" and a tool developed in this thesis ("Virtual Nanoindentation") were used to plan the nanoindentation tests.
Once these requirements were fulfilled, the numerical model was developed for simulation in Chapter 3. The modeling of RUCs was performed at three locations on dentin to take the local variation of the properties into account (Chapter 3). These not only give the local elastic stiffness matrices, but also reveal the distribution of stress and the stress concentration locations. Studying these results allows finding the locations where cracks may initiate.
Finally, in Chapter 4 an unconventional micro-tensile test of dentin is described. This test, which is performed in the smallest scale to the author's knowledge, allows an estimation of dentin's tensile strength. Performing other tests at such a small case would allow studying dentin's tensile behavior as a function of location. The micro-tensile test was simulated in 2D. The simulation results helped us to interpret and understand the test in particular by identifying stress concentration locations.
A schematic view of the chapters is shown in Figure 0-3.

Figure 0-3. The schema of the thesis, a) morphological characterization based on image analysis, b) The mechanical models that will be presented in chapters 3 and 0, c) Experimental methods used in this thesis (nanoindentation in chapter 2 and a micro-tensile test in chapter 0)

1 Morphology of the dentin microstructure

Dentinal tissue has a complex microstructure varying through the depth of the tissue. This variation confers gradients to the properties of dentin that are not fully characterized yet.
This chapter helps to understand dentin's complex multiscale structure better and characterize its specific components, namely the tubules and lateral branches (LBs). Dentin morphology is characterized by treating and analyzing Scanning Electron Microscopy (SEM) images. This analysis has permitted us to collect and complete both information and data to study further the relationship between the dentin's microstructure and mechanical properties.
By analyzing the set of acquired images, dentin morphology was characterized: cross-sectional area fraction and diameter (size) of the constituents and the tubular density have been assessed. The schematic organization of this chapter is shown in Figure 1-1.

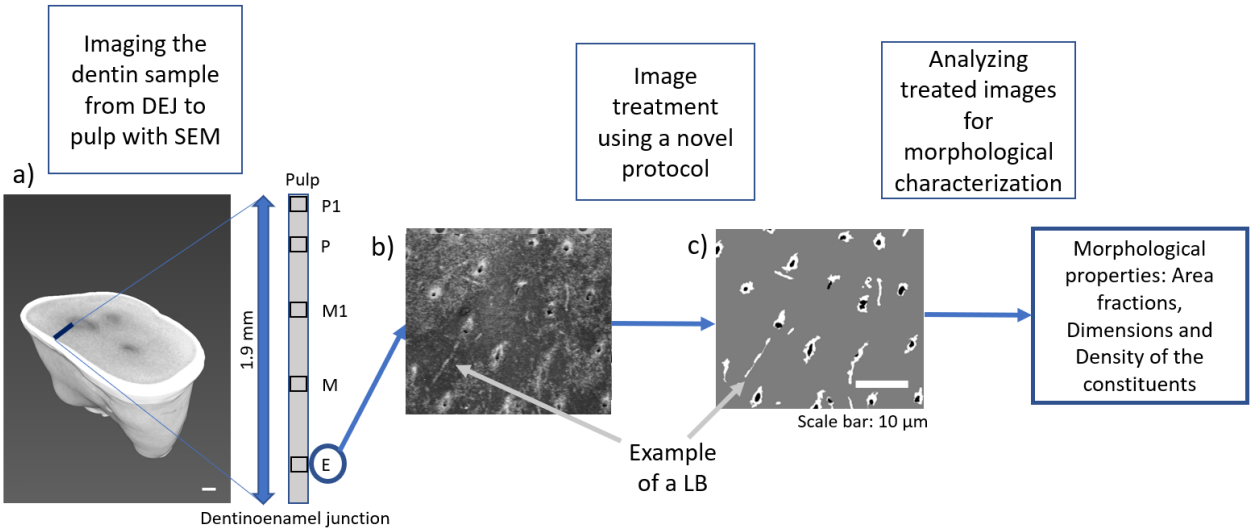

Figure 1-1. Image acquisition and analysis protocol followed in this chapter: a) a sample of dentin imaged from the DEJ to the pulp (with 5 zones of interest: "E", "M", "M1", "P", "P1"), b) the SEM image of dentin at "E", c) the image at "E" after treatment.

1.1 Literature review

1.1.1 Multiscale structure of the dentin of permanent teeth

Dentin has a multiscale structure with specific features at the micro- and nanoscale. At the microscale, the main features are the tubules made up of tubule lumens surrounded by a dense collar called peritubular dentin (PTD), which are embedded in an intertubular matrix (ITD) (Figure 1-2).

In coronal dentin, the tubules pass through all the dentin from the dentinoenamel junction (DEJ) to the pulp and are rising perpendicular to the DEJ (Figure 1-3) (or from the cementum-dentin junction in root dentin). The tubules have lateral branches (LBs). These branches constitute a secondary network of dentin pores.

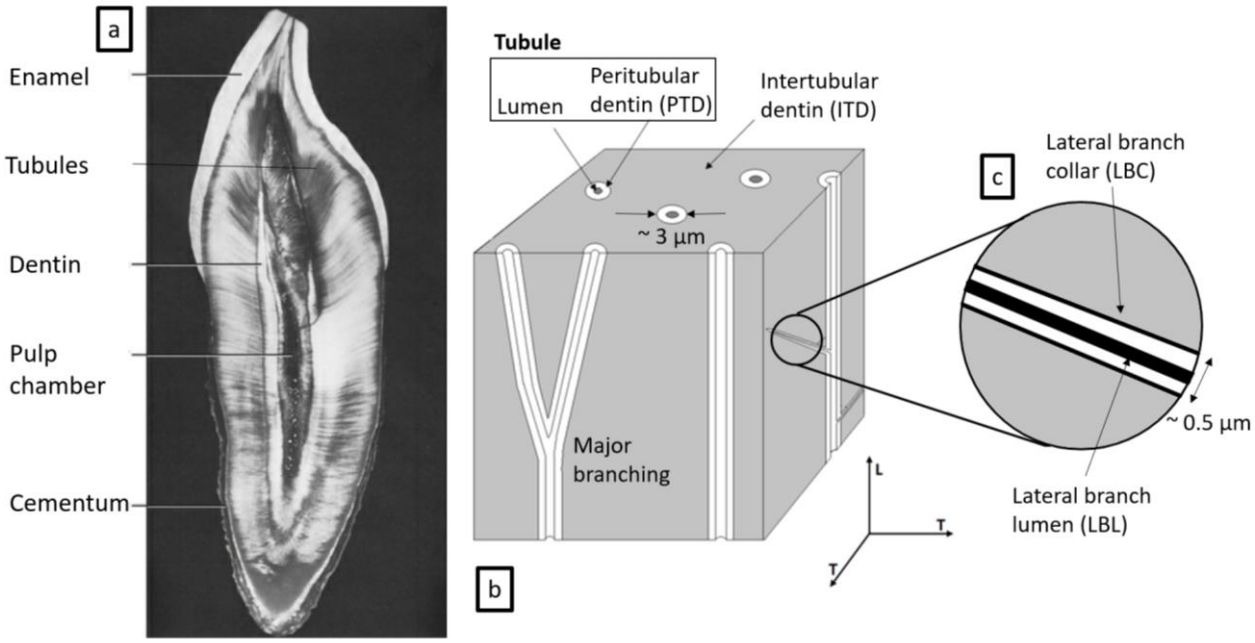

Figure 1-2.a) Microscopic image of the tooth's cross-section, adapted from Ten Cate [11]*. Notice the higher curvature of the tubules in coronal dentin, b) A schematic view of the dentin microstructure and its main constituents: the tubules (consisting of peritubular cuffs and tubule lumens), the intertubular matrix, and c) Lateral branches of the tubules (consisting of lateral branch collars (LBCs) and lateral branch lumens (LBLs))*

Mjör and Nordahl (1996)[9] studied and categorized the tubules' branching in detail. They grouped the branches into three categories:

1. Major branches: these branches fork at an acute angle from the tubules, have a diameter of 0.5 to 1 µm and are found in the peripheral zone of dentin. A recent study by Vennat et al. (2017) [7] investigated the zone near the DEJ in 3D using CLSM (Figure 1-3) and showed that these branches have complicated shapes.

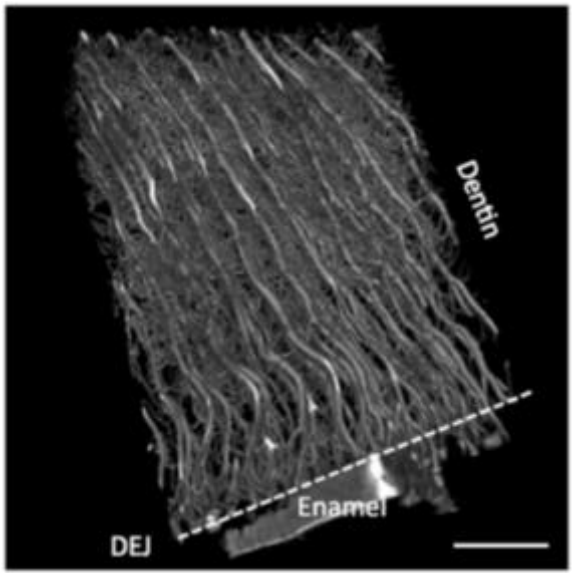

Figure 1-3. The complicated network of LBs beneath the DEJ as revealed by CLSM [7] *(Scale bar: 30 µm)*

2. Fine branches, more frequently seen in the radicular dentin with a diameter of 0.3 to 0.7 µm, form a complementary network with tubules. These branches are more numerous where there are fewer tubules and vice versa.

3. Microbranches are the smallest type of branches (0.025 to 0.2 µm diameter), and extend at a right angle from the tubules, and are observed throughout dentin.

At the nanoscale, the intertubular dentin (ITD) and peritubular dentin (PTD) reveal their chemical composition: ITD is composed of layers of organic material (mostly collagen fibrils of type 1 with a diameter of 50 to 100 nm [10]) mineralized by hydroxyapatite nanocrystals (with a mean thickness of 5 nm). The mineral nanocrystals can be inside or outside the collagen fibrils (called intra- or extrafibrillar minerals), as illustrated in Figure 1-4. To understand the relation between the micro- and nanostructure, it should be mentioned that collagen fibrils of the ITD are mostly lying in planes perpendicular to the tubule axis [12].

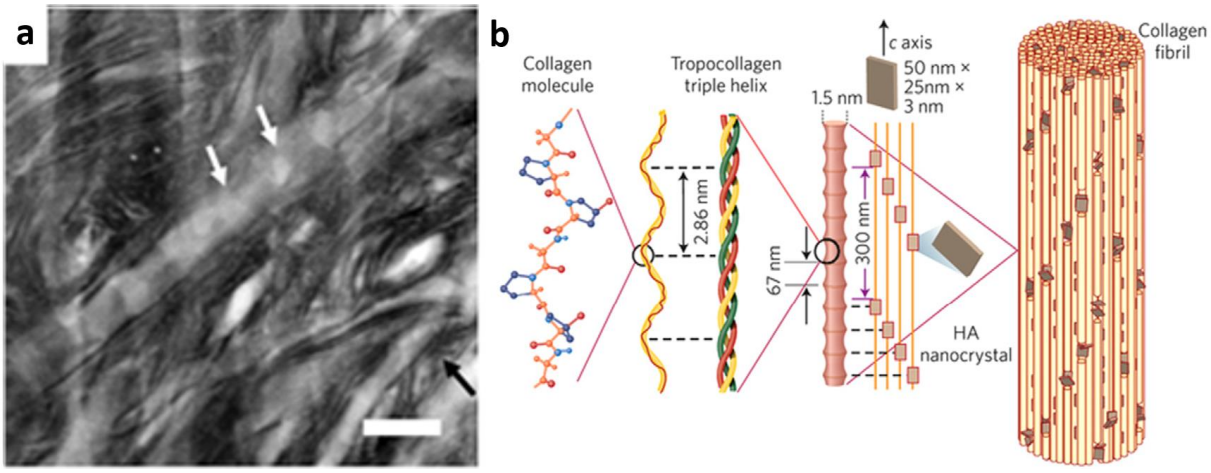

Figure 1-4.a) The intertubular dentin (ITD) of a deciduous tooth. The white arrows point to the 67 nm periodic pattern of intrafibrillar minerals, and the black arrow points to a group of extrafibrillar minerals that are dark in this bright-field STEM image, (Source: author) (Scale bar: 50 nm), b) Mineralized collagen fibril [13]

PTD is more than 90% mineralized, and therefore considerably more than the ITD (mineral mass content of 70%) [14].

The production of dentin from the mentioned organic and mineral components is called "Dentinogenesis". Studying dentinogenesis allows for understanding the variations in the morphological properties of the microstructure of dentin.

1.1.2 Dentinogenesis: How are tubules and their surrounding matrix formed?

Dentin is produced by cells called odontoblasts [15]. Moving from the DEJ toward the pulp (therefore downward in Figure 1-5), they first produce the organic phase of dentin (predentin, mostly made of collagen fibrils type 1) in layers. There remains an empty path behind each of them -like the inner space of a tube-, which will become the tubule lumen. As the odontoblasts move from the bigger DEJ towards the smaller zone where the interface between dentin and pulp will form, they get closer together.

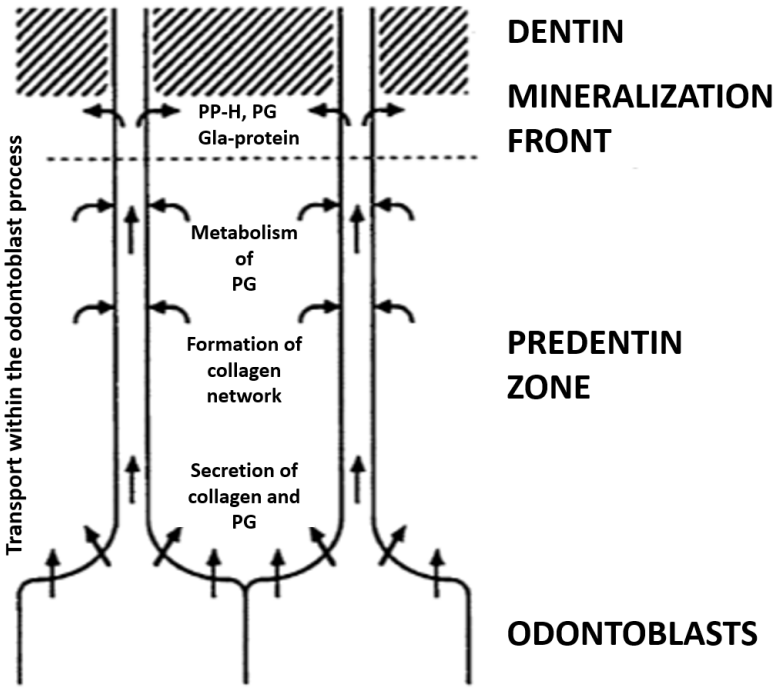

Figure 1-5. Schema of dentinogenesis [15]

Next, this interwoven network mineralizes and forms the intertubular dentin (ITD). This mineralization can be globular (spherical zones of mineralized tissue called calcospherites grow and coalesce) or linear (the border of the mineralized zone advances) [11]. Sometimes, for reasons including vitamin D deficiency, the calcospherites do not grow big enough to fuse and form a continuous mineralized tissue. In this case, interglobular dentin is formed (Figure 1-6).

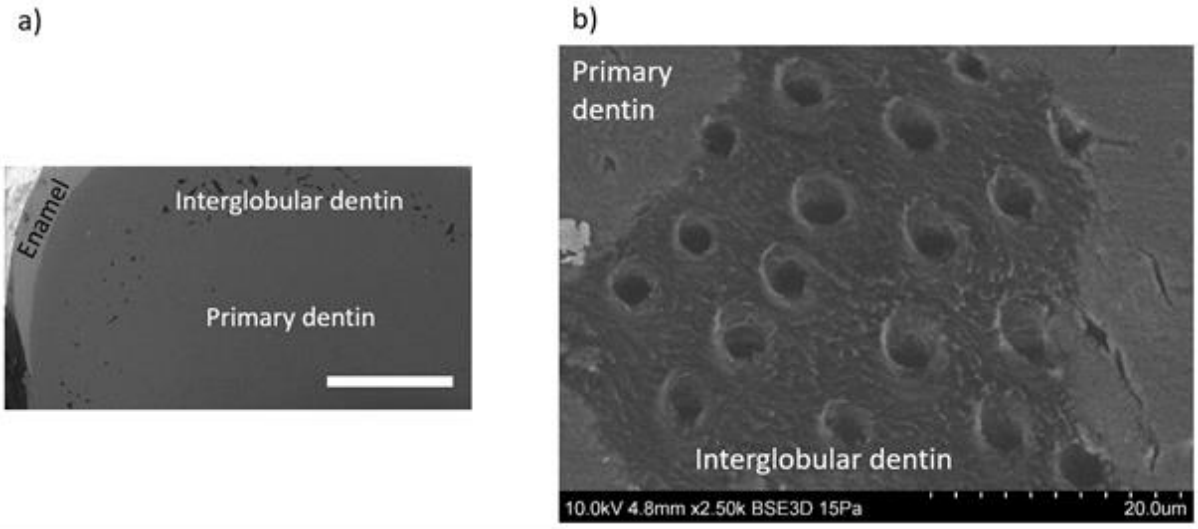

Figure 1-6.a) The small dark points represent interglobular dentin (Scale bar: 1 mm), b) Detail of a zone of interglobular dentin. Notice the lack of peritubular cuffs (Scale bar: 20 µm) (Source: author)

Finally, in the presence of the odontoblastic processes, a cuff of highly mineralized tissue (PTD) is produced around each tubule lumen. With age, the process of mineral secretion continues. An idea that will be put forward in this thesis is that the continuous production of peritubular dentin might repair the microcracks that may appear inside the tubules and lateral branches due to excessive local stresses known to be present there [7]. The secretion

of PTD material continues with age until the whole tubule lumen is filled with minerals, making the dentin sclerotic and transparent [11]. Another study suggests that sclerosis (at least partially) happens due to partial dissolution of the ITD minerals and their reprecipitation inside the tubules [16].

Besides the disadvantage of reducing the toughness of dentin [17], filling the tubule lumens has the benefit of protecting the pulp against external materials that might enter the tubules due to caries. It also might cure the hypersensitivity of teeth [18].

Immediately after the beginning of dentinogenesis, ameloblasts begin to produce enamel: the most highly mineralized tissue in the body. Similar to the way each odontoblast produces a tubule, each ameloblast produces a prism of highly mineralized material. These prisms are organized in a hexagonal pattern beside each other.

Fosse et al. (1992) [19] tried to identify an organization pattern for dentinal tubules. They observed that certain tubules are organized in rows (Figure 1-7.b). Kinney et al. (2001) [20] used "point pattern analysis" methods (points being the centers of gravity of the tubule lumens). They concluded that tubules are not randomly positioned within the ITD and that "points disordered about periodic lattice sites" visualized in Figure 1-7.d describes the tubule organization the best among the patterns they tested. They did not test the hexagonal pattern.

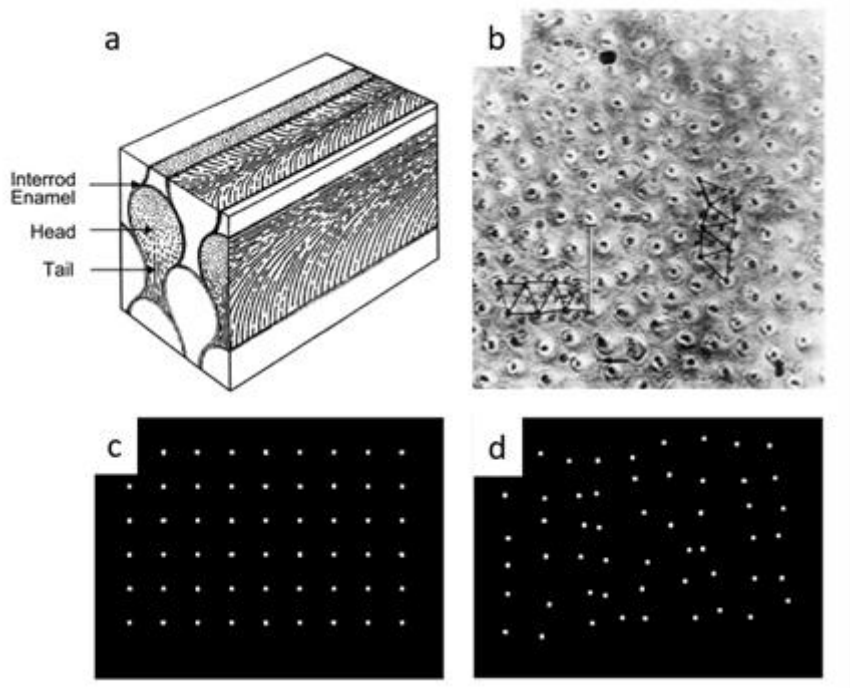

Figure 1-7.a) Enamel prisms, b) The identifiable rows of tubules from Fosse et al. (1992) [19]*, c) Square lattice, and d) Random displacement about square lattice from Kinney et al. (2001)* [20]

A simplified local model of the dentin microstructure based on the "square lattice" pattern is introduced in Chapter 3. This model allows analyzing the results and identifying the morphological properties.

Even though the main bulk of dentin is produced over a few years [11], dentinogenesis is a lifelong process with different stages that lead to different types of dentinal

tissue (visualized in Figure 1-8) with different morphologies. The significance of the types of dentinal tissue for its micromorphology makes them worthy of being mentioned here.

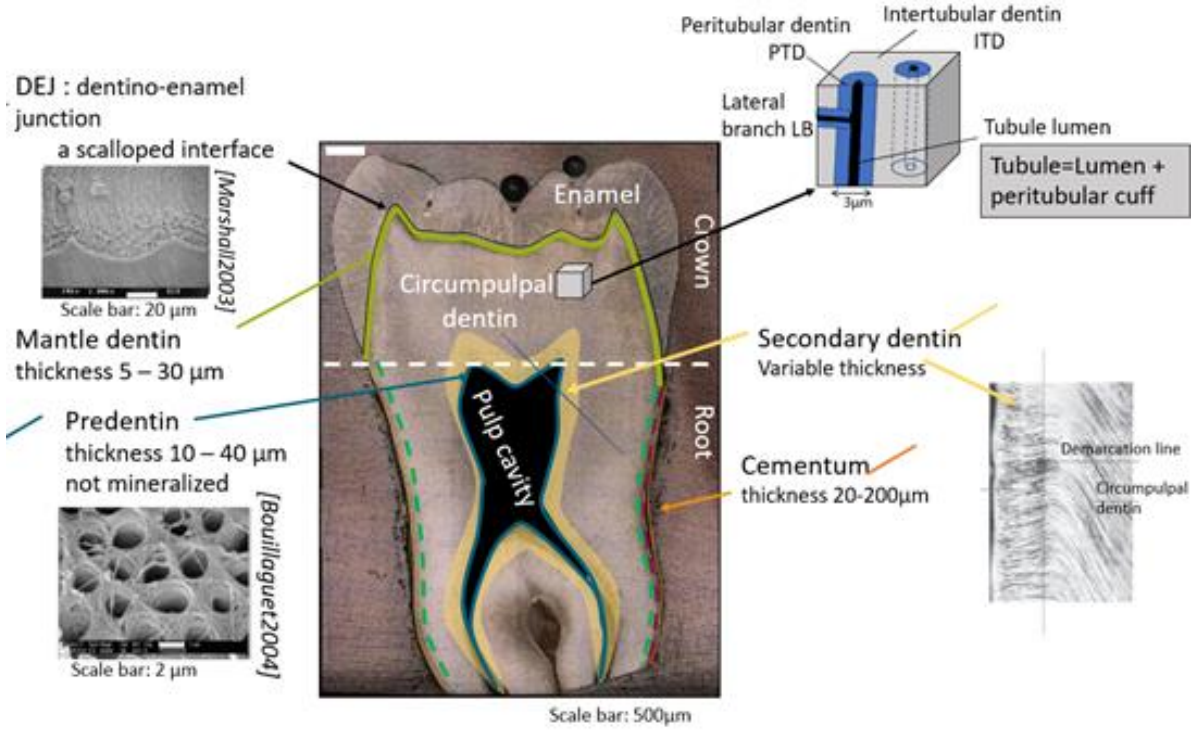

Figure 1-8. Schema of Dentin and its various types of dentinal tissue, Enamel and Cementum (Courtesy of Dr. Elsa Vennat)

1.1.3 Dentinal tissue

Here we review some types of dentinal tissue that exist in coronal dentin in order of formation [21].

Dentinoenamel junction

Dentinoenamel junction (DEJ) is traditionally thought to be the scalloped interface between dentin and enamel (Figure 1-8). A newer view is that this interface includes an inner aprismatic part of the enamel and an outer part of mantle dentin and is 7-15 µm thick [21].

Mantle dentin

Mantle dentin is the outermost layer of primary dentin beneath the enamel in coronal dentin [11]. Von Korff fibers (bundles of collagen fibril type 3 with a minor amount of type 1 collagen fibrils) are rising at DEJ and are a specificity of mantle dentin in addition to major branches with delta junctions [21].

As summarized in Table 1-1, there is disagreement about the thickness of mantle dentin between Goldberg et al. (2002) [22] and other authors.

Table 1-1. Thickness of mantle dentin, according to various studies

	Mantle dentin thickness (µm)
Linde & Goldberg (1994) [15]	5-30
Wang & Weiner (1997) [23]	20
Goldberg et al. (2002) [22]	100-150
Ten Cate (2017) [11]	15-20

Mantle dentin is part of a soft zone beneath the DEJ. This relatively soft and less mineralized zone (around 200 μm thick [23]) is thought to be a resilience zone, where higher strains can be supported, which allows the tooth to bear large occlusal loads without fracture [21]. Another hypothesis is that it minimizes the effect of thermal stress or protects the dentin against impact forces [23].

Primary dentin

Primary (circumpulpal) dentin is the main portion of dentin [21]. Primary dentin is named so because it is produced before secondary dentin and should not be confused with the dentin in deciduous teeth (which are also called primary teeth). Compared with the outer layer (mantle dentin), the tubules in the inner layer of primary dentin have less branching.

Secondary dentin

Secondary dentin is the newest tissue apposed, gradually filling the pulp cavity. Compared with primary dentin, secondary dentin has a lower rate of production that continues through life and causes the pulp to recede and to become progressively narrower. As shown in Figure 1-9, the tubules of secondary dentin have a slightly different curvature [21]. The tubules are fewer than the tubules of primary dentin and are less well-aligned [11].

Figure 1-9. The histological image of primary and secondary dentin stained by haematoxylin and eosin. Eosin makes protein pink. [11]

1.1.4 Characterization of the microstructure of dentin

The different morphological properties of the dentin microstructure have been defined in previous studies. These properties are reviewed in the literature and are summarized below.

Local area fraction of the microscale constituents of dentin from enamel to pulp

Few studies have quantified area fractions of the constituents comprehensively from the DEJ to the pulp (to include various kinds of dentinal tissue).
Wang (2014) [24] measured the area fraction of the constituents on samples that extended from crown to root dentin (Figure 1-10).

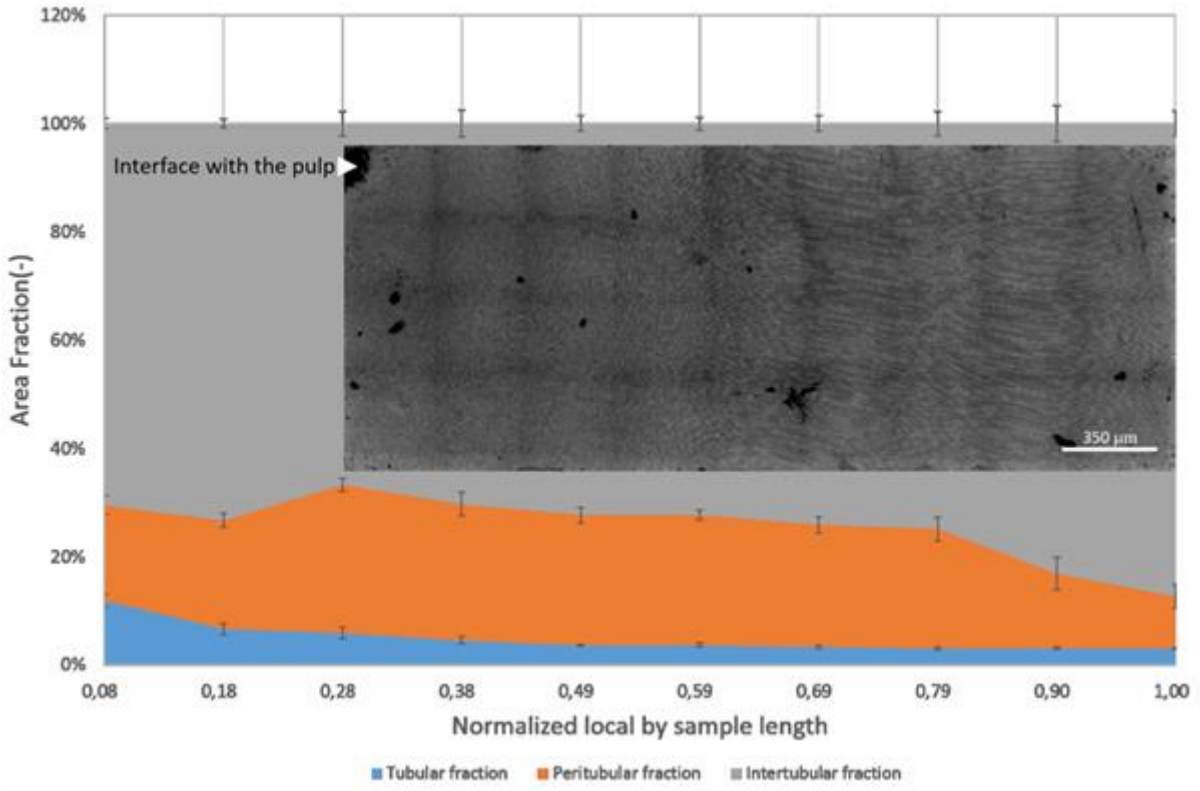

Figure 1-10. A dentin sample extending from root to crown dentin [24] *(the area fraction plot is a typical one and does not belong to the sample imaged above)*

Inner and outer diameter of the tubules

In normal dentin, the diameters of the pores are the diameters of the tubule lumens and LBLs (given in Table 1-2).

The Mercury Intrusion Porosimetry (MIP), which was used by Vennat et al. (2009) [25] gave an overall diameter of 0.6 µm for the pores of normal dentin, which is the average inner diameter of both the tubules and LBs. The diameter of only the LBLs could not be estimated by this method.

Vennat et al. (2017) [7] studied the superficial dentin by CLSM to measure the inner diameter of the pores. This method works in 3D and is, therefore, more precise than measurement on 2D images. They measured an average diameter of 1.82 µm for the tubule lumens.

Table 1-2. The inner diameter of tubules

	Diameter of tubule lumen in µm (superficial dentin)	Diameter of tubule lumen in µm (middle dentin)	Diameter of tubule lumen in µm (deep dentin)
Vennat et al. (2009) [25]	0.6		
Vennat et al. (2017) [7]	1.82	-	-

The outer diameter of tubules has been measured by several researchers using analysis of 2D microscopic images (Table 1-3). All studies, except Fosse et al. (1992) [19], report a smaller diameter near the DEJ.

Table 1-3. The outer diameter of tubules (PTD collar outer diameter)

	Tubule diameter in superficial dentin in µm	Tubule diameter in middle dentin in µm	Tubule diameter in deep dentin in µm
Garberoglio & Brännström (1976) [26]	0.9	1.5	2.9
Fosse et al. (1992) [19]	3.39	3.2	3.1
Lopes et al. (2009) [27]	2.42	2.94	2.99
Lenzi et al. (2013) [28]	2.4	3.7	4.28

Studying the outer and inner diameters of the tubules results in the thickness of the PTD. Nevertheless, Zanette et al. (2015) [29] used the method «Ptychographic X-ray nanotomography» to directly measure the thickness of the peritubular cuffs.
They observed high local variations in the thickness of the cuffs (from 0.2 to 2 µm in zones with dimensions of only a few micrometers). Another observation of this study was a mineralized sheath around LBs that has the same mass density as the material of peritubular cuffs.
Another source stated that the sheath around the LBs is the same material as PTD [11]. Apart from those two studies, little data is found about LBs and their possible collars that we will call "lateral branch collars" (LBCs) in this manuscript and that are quantified in the next sections.

Tubular density (per unit area or per unit length)

Tubular density per unit area is defined as the number of tubules per unit area (usually per mm²) when the cross-section of the sample is perpendicular to the tubules. Values measured for the tubular density of dentin in the literature are listed in Table 1-4.

Table 1-4.Tubular density (per mm²) in the literature

	Tubular density of superficial dentin (SD)	Tubular density in the middle (SD)	Tubular density of deep dentin (SD)	Convergence of dentinal tubules
Ketterl (1961) [30]	9000-24000	60000	70000	~4.2
Tronstad (1973) [31]	7000		60000	8.6
Garberoglio & Brännström (1976) [26]	20000	29500	45000	2.3
Pashley (1989) [32]	20000		50000	2.5
Fosse et al. (1992) [19]	16927	39694	51368	3
Mjör & Nordahl (1996) [9]	10000	28900	48400	4.8
Lopes et al. (2009) [27]	15385 (5309)	21006 (7473)	30595 (12247)	2
Earl et al. (2010) [33]		33000		
Lenzi et al. (2013) [28]	28541 (3870)	39947 (2658)	69427 (10397)	2.4

The tubular density per unit length describes the density of tubules in a different way. To determine this parameter, Mjör & Nordahl (1996) [9] proposed a method in which samples are cut parallel with the tubules, and the tubules are counted on a 100 µm line perpendicular to their long axis (schematically shown in Figure 1-11). To compare this 1D

tubular density with the 2D densities, it should be divided by the length of the measurement line and squared:

$$\left(\frac{n_{1D}}{l}\right)^2 = \rho_{2D} \tag{1.1}$$

with n_{1D} the number of tubules over the length l in mm, and ρ_{2D} the tubular density per unit area (tubules/mm²).

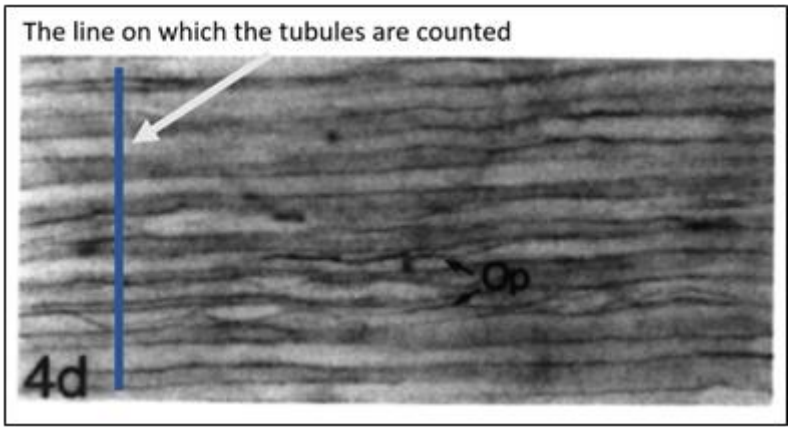

Figure 1-11. The demineralized stained specimen used for measuring the tubular density by Mjör & Nordahl (1996) [9]

The advantage of measuring the tubular density per length over measuring it the usual way is that the number of tubules per length is less affected by the angle between the tubules and the cross-section. It is enough that the cross-section is relatively parallel with the tubules.
However, this method has its drawbacks too. First, the constituents of the demineralized dentin (tubule lumens and demineralized ITD) are not easily recognizable (Figure 1-11). Besides, if the demineralized dentin is relatively transparent, one might count the tubules beneath the first row of tubules and overestimate the tubular density.

Convergence of tubules

The ratio of the tubular density at deep dentin to the density at superficial dentin (called the convergence of dentinal tubules and shown in Table 1-4) has been reported to have values varying from 3 to 5 [34]. But values as small as 2 ([11] and [27]) and as big as 8.6 ([31]) have also been observed.

Diameter of the lateral branches

LBs are much less studied than tubules, and that is partly because of their smaller size. Vennat et al. (2009) [25] measured the average outer diameter of the LBs to be 0.45 µm.

Vennat et al. (2017) [7] gave an average diameter of 0.68 µm for the LBLs in the superficial dentin. They estimated the share of LBLs in the total porosity of superficial dentin to be 30%.

Table 1-5. Inner and outer diameter of the LBs

	superficial dentin	middle dentin	deep dentin
Diameter of LBCs in µm (Vennat et al. (2009) [25])	0.45		
Diameter of LBLs in µm (Vennat et al. (2017) [7])	0.68	-	-

1.2 Materials and methods

In this work, 2D SEM images were used for studying the morphological features of the dentin's microstructure. In this section, the materials and methods are detailed.

1.2.1 Sample preparation

A third molar of a young adult patient was used in this study to develop the protocol for the morphological analysis. The tooth was embedded in epoxy resin and cut (ISOMET Low-Speed Saw, Buehler) to reveal a coronal surface in the cervical region (Figure 1-12), where the dentin showed an interface with both the enamel and the pulp cavity.

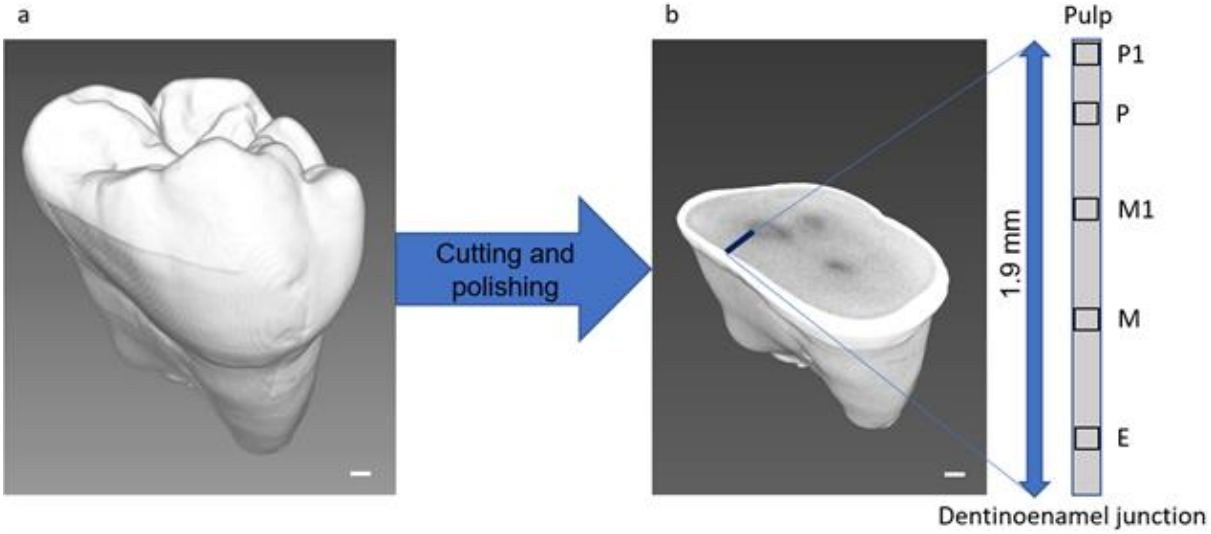

Figure 1-12. The third molar of a young adult patient: a) initial 3D shape visualized by Avizo software, b) The tooth cut and polished. The imaged band by SEM is marked on the image right. (Scale bar: 1 µm)

The surface was first polished with polishing disks of decreasing grit size (LaboPol-5, Struers) before it was polished using a polishing cloth and a 3 µm and then 1 µm diamond suspension (TegraPol-15, Struers). After each polishing step, the sample was cleaned in an ultrasonic bath.

The sample was then dehydrated in alcohol bathes with an increasing percentage of alcohol according to the protocol described by Vennat (2009) [25]: there, the sample was bathed with 25%, 50%, 75%, and 95% ethanol with ultrasonication between bathes. The dehydration was finished with two absolute alcohol bathes of 20 minutes each (during 12 hours).

1.2.2 Dentin imaging in order to characterize its microstructure

This microscopic morphological study aims to quantify the microscopic features of dentin (in size, area fraction, and number per area) and to consider the local variations in their properties.

Therefore, images of dentin are required which:

- have enough resolution for the microstructure features to be resolved,
- have enough contrast between the constituents for them to be distinguished,
- cover a row of micrographs from the DEJ to the pulp, to image the different types of (healthy) dentin (Figure 1-12).

Most of the digital images of the microstructure of constituents of dentin were taken with the scanning electron microscope (SEM) Helios Nanolab 660 under vacuum. The SEM was operated at an accelerating voltage of 2 kV and a working distance adjusted to 4 mm. The digital images have a resolution of 2048x1768 pixels, and their pixel depth is 256 grey levels. Each pixel is acquired in 0.02 µs, which means a 75 s frametime for each image. The size of the pixels is approximately 59 nm.

Backscattered electrons (BSE) imaging was used as this mode allows distinguishing between materials with relative changes of local mineral concentrations (Roschger et al. (1995) [35]). Thus, ITD having lower mineral content due to the presence of the organic material is darker than PTD and LBC and therefore more distinguishable (Figure 1-13). This difference in brightness makes the constituents easier to quantify. Quantification of the constituents is especially interesting for LBs, features that have yet to be fully quantified. Only the global porosity was estimated [7].

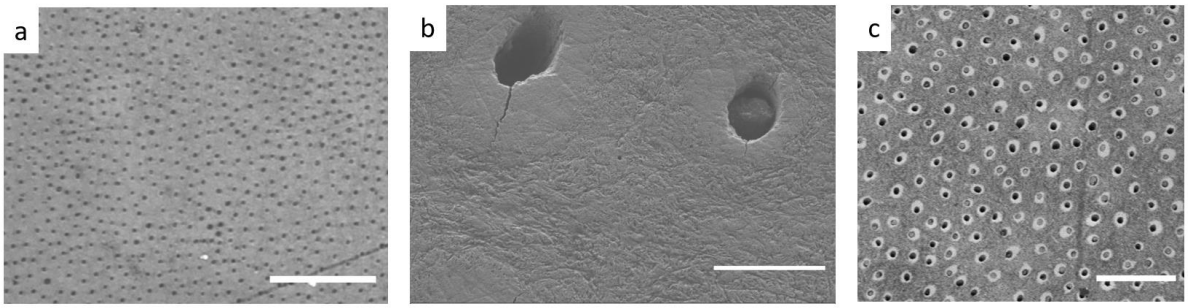

Figure 1-13. Dentin imaged with various methods: a) Light Microscopy (scale bar: 50 µm), b) SEM, secondary electron detector (Scale bar: 3 µm) and c) BSE mode SEM (Scale bar: 15 µm) (Source: author)

Twenty-one images were taken across the dentin from the dentinoenamel junction (DEJ) to the pulp on the row with a length of L=1.9 mm (shown in Figure 1-12). To allow a better comparison between different studies, the distance L_i of SEM image with the number "*i*" from the DEJ was *normalized* by the length L: L_i/L being 0 at the DEJ and L_i/L being 1 at the junction of pulp and dentin.
Some interesting areas on the same polished surface were also imaged at higher magnifications using a FEG-SEM (Zeiss Supra 55 VP) in BSE mode.

1.2.3 Protocol for image treatment

Based on the acquired images, a protocol is proposed for image treatment and analysis.
Automatically quantifying the morphological features of an image needs image segmentation. This process consists of partitioning the image pixels into multiple homogeneous regions or segments based on a criterion such as pattern (detection of similarities, edge detection, etc.), color or pixel intensity (minimum and maximum thresholds of pixel intensity) (Distante & Distante (2020), [36]).
In our SEM images, each group was assigned to one of the constituents, namely: tubule lumen, intertubular dentin (ITD), and bright and highly mineralized phase (HMP), which includes peritubular dentin (PTD) and lateral branch collars (LBC).

Segmentation of images with artifacts (like the image of dentin shown in Figure 1-14) is challenging. For this reason, the segmentation processing was done using a software

called Trainable Weka Segmentation (TWS) developed by I. Arganda-Carreras et al. (2017) [37]. This software performs pixel classification based on machine learning and recognizes the differences between the characteristics (for example texture) of pixel samples from different constituents. Then, the software classifies the whole image into labels, each representing one constituent. TWS is available in a plugin of the software “ImageJ” [38].

An example of the ability of the tool to classify the features of the microstructure of dentin is shown in Figure 1-14.

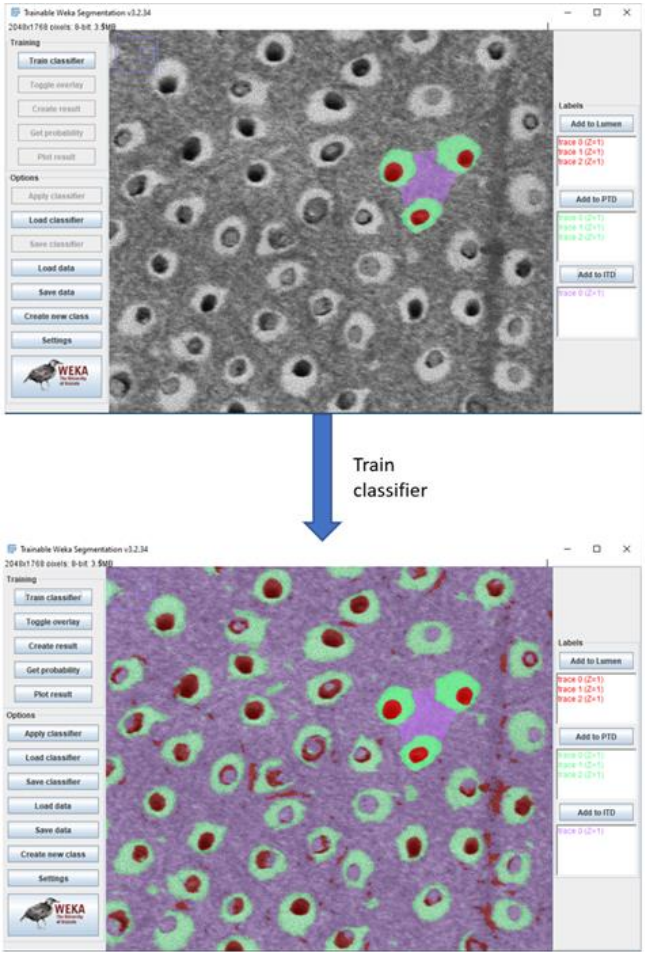

Figure 1-14. Segmentation of an SEM image (at a normalized distance of 0.12 from the DEJ) using "Trainable Weka Segmentation"

As seen in this figure, due to polishing artifacts on the ITD and the occasional filling of tubule lumens with polishing debris or odontoblast processes, the segmentation was not ideal. Some tubule lumens were also classified as ITD. To get a better-classified image, in some cases further labelled regions were chosen for each constituent, and the classifier was retrained.

The SEM images have noise, especially the “salt-and-pepper” type. In this work, the median filter was used to reduce the noise. It was applied on segmented images and not on raw SEM images because it partially attenuates the texture of the image. As explained before, the texture of the image is useful for segmentation.

Further edits were done with the software "GIMP": Each segmented image was put as a layer on the original image and was manually edited. The steps of this protocol are shown in Figure 1-15.

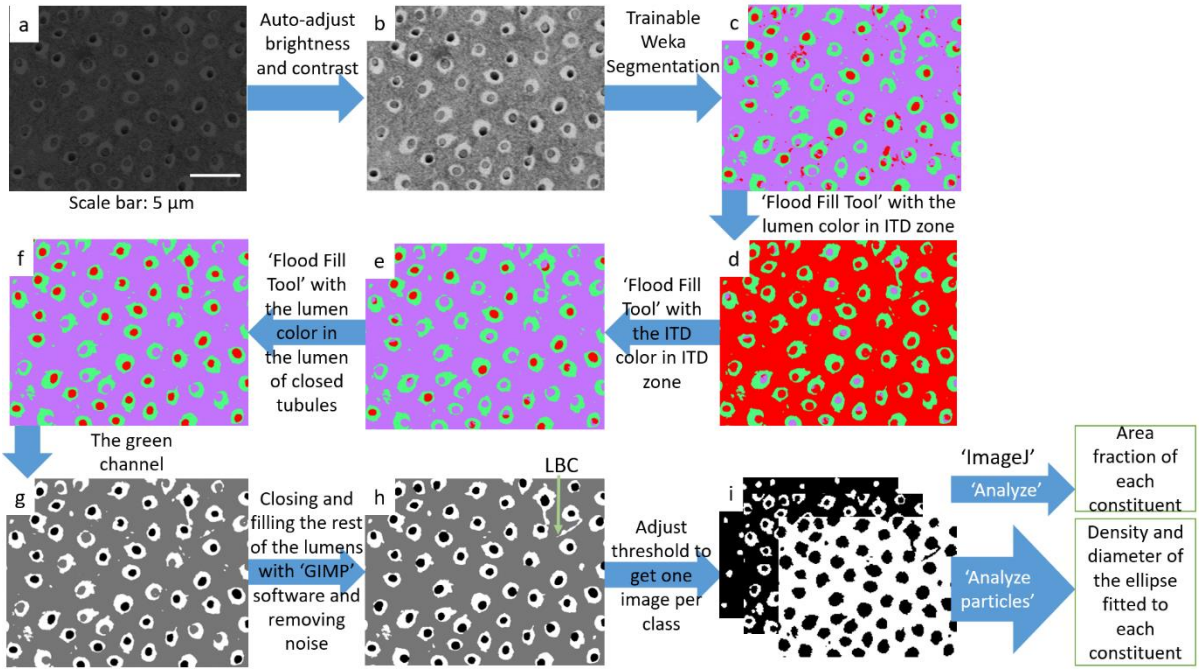

Figure 1-15. The steps of SEM image treatment and analysis at a normalized distance of 0.12 from the DEJ (Source: author)

Measurement of the morphological features

In this section, methods are presented to measure the morphological properties of the microscale features of dentin. As shown in Figure 1-15.h, apart from the tubules, bright features are visible on some of the images that are smaller than tubules and usually show no visible lumens (indicated by a green arrow). We assume that these features are lateral branch collars (LBCs) and that their lack of lumen is due to the resolution of the images. This section describes a method to quantify them together with the tubules. The morphological properties were measured on the segmented binary images (Figure 1-15.i).

Area fractions

The area fractions of different constituents give an estimate of their volume fraction. The area fractions in binarized images were measured using the software ImageJ (command "Measure"). The area fractions were measured on images with a size representative of the dentin microstructure called Representative Area Element (RAE). Indeed, the size of the analyzed image has to be large enough to include a sufficient number of entities of the various dentin constituents to represent it on average.

To estimate the RAE for measuring a stable value for the area fractions of the sample, a MATLAB code was written, which works by measuring the area fraction of the constituent in a growing square-shaped frame in the image. The measured area fraction is plotted versus the size of the frame, and once its value stabilizes, it means that the frame is big enough to be representative of the microstructure.

In Figure 1-16, the measurement of porosity is plotted for three sample SEM images (“E”, “M”, and “P”). The minimal area of the microstructure for which the porosity becomes stable is in the range 3000 to 4000 μm^2, which corresponds to a length in between 55 and 64 µm, a size much higher than the size of the constituent entities.

It was concluded that the size of the SEM images (121x104 μm^2) is representative for porosity measurement. The fact that the asymptotes of the plots in Figure 1-16 do not become completely horizontal in their progress is probably due to the global gradient of porosity observed from the DEJ to the pulp. This small slope was thus neglected, and the analysis is taken on the whole SEM images.

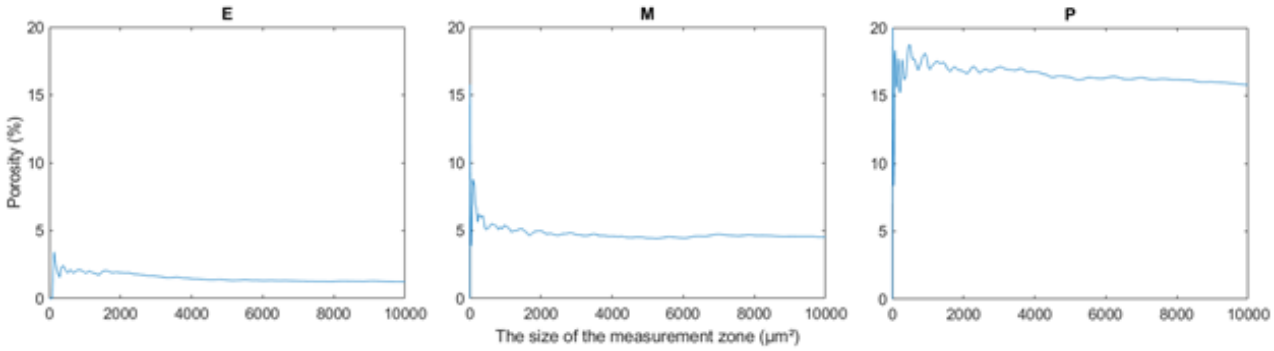

Figure 1-16. Measured porosity versus the size of the measurement zone. (Normalized distance for ‘E’, ‘M’ and ‘P’ are respectively 0.12, 0.45 and 0.83 (Source: author)

Diameter of the constituents

Another important morphological parameter measured is the size of the entities. “Analyze particles” algorithm from ImageJ was used to fit ellipses on the particles and gives the minor and major diameters of the ellipses.

Density of the features

The density of the tubules called tubular density is defined as the number of tubules per unit area. It was estimated by the command “Analyze particles” of the software ImageJ on the binary images. This command involves different tools to track and count the particles.

Distinguishing LBs

In the SEM images of dentin, some observed features are smaller than tubules. It is assumed that they are the dense collars of LBs as pointed out briefly by Zanette et al. and Nanci ([29] and [11]). The lumens of the LBs, however, could not be detected because of the resolution of images.

The diameters of LB collars were measured from the SEM images. Distinguishing the LBs from other entities (tubules or noise) was done using the command “Analyze Particles” and by setting an upper and lower limit for the size of particles (Figure 1-17).

The choice of these limits for each image was empirical: various limits were tested and the ones leading to the best resulting LBs were chosen by visual inspection. The LBs are studied on four images “E”, “M”, “M1” and “P” with the protocol shown in Figure 1-17.

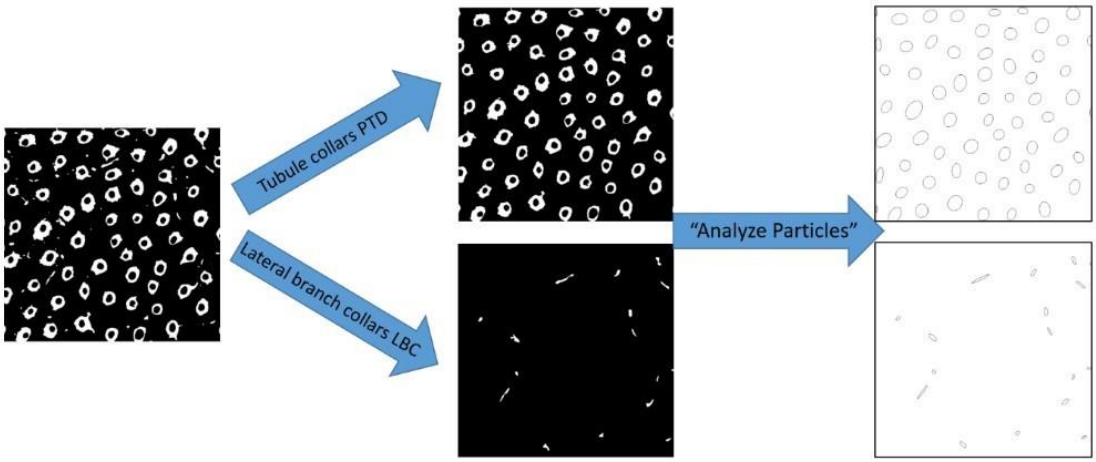

Figure 1-17. Protocol for analyzing the highly mineralized phase divided into peritubular dentin (PTD) and lateral branch collars (LBCs). "Analyze Particles" fits ellipses on the tubules and LBs to give an estimate of their dimensions. Shown on an image in "Middle dentin" (Source: author)

Estimates of the inner diameter and porosity of the LBs

As the LB lumens are not visible in the original group of images, their area fraction (porosity due to the LBs) was estimated indirectly by the following method:

1. First, the ratio of the outer to inner diameter of the LBs ($\frac{d_{LBC}}{d_{LBL}}$) was measured by analyzing another group of images of the same sample but with higher magnification (Figure 1-18) and an average ratio was calculated.

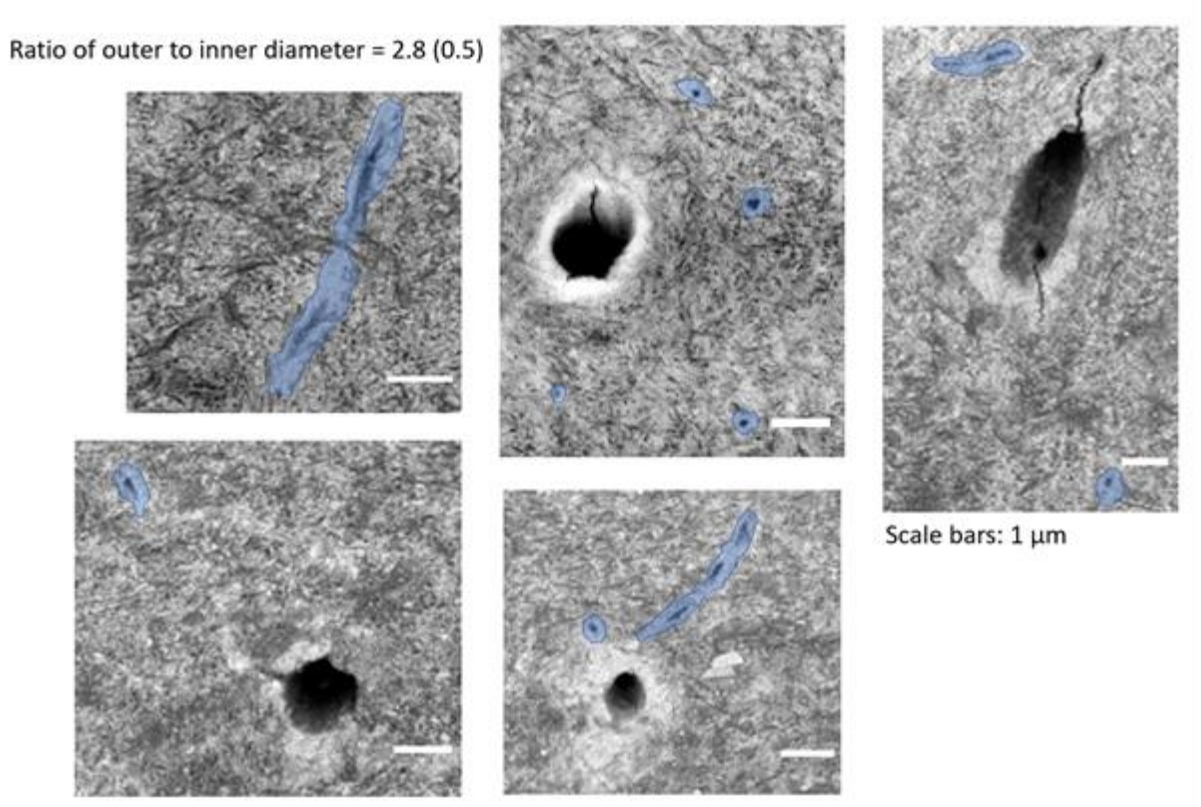

Figure 1-18. The LBs in a group of high-resolution images from the same sample (Source: author).

2. Then, the average ratio was applied to estimate the inner diameter and porosity for LBs, the lumens of which were not visible, but their outer diameters were measured by the following equation:

$$a_{LBL} = a_{LB}\left(\frac{d_{LBL}}{d_{LBC}}\right)^2 \quad (1.2)$$

where a_{LBL} is the porosity due to the LBs and a_{LB} is the whole area fraction of LBs ($a_{LB} = a_{LBL} + a_{LBC}$).

Applicability of 2D morphological measurements to a 3D microstructure

As shown in Figure 1-19, extrapolating 3D morphological parameters of a microstructure from the measurements on a 2D cross-section introduces artifacts.

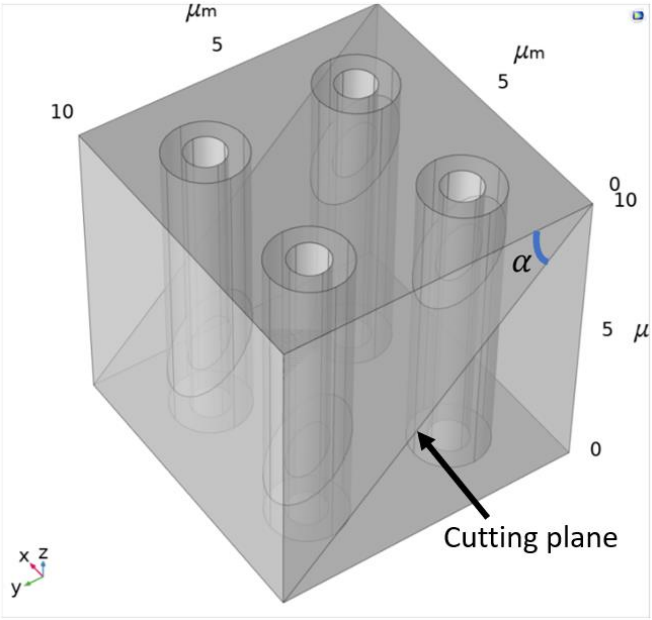

Figure 1-19. Two-dimensional sampling of the idealized 3D periodic microstructure

The various morphological properties and their artifacts due to extrapolation from 2D to 3D are discussed below.

Area fraction. When the constituents of the microstructure are isotropic and distributed uniformly and randomly in the volume, according to Delesse's principle, the volume fractions of the constituents are equal to their area fractions in the cross-section (Mandarim-de-Lacerda, (2003) [39]).
Diameter. By assuming that the tubules and LBs are cylindrical, the minor diameter of their ellipse-shaped cross-sections is the diameter of the features (Arson et al. (2019) [40]).
Tubular density. As almost any plane has an oblique angle with the tubules, the distances between the tubules are overestimated and therefore the tubular density is underestimated.

1.3 Results and discussion

In this section, the morphological properties are presented, which were measured by the aforementioned protocols.

1.3.1 Results

Imaging the dentinal tissue

In Figure 1-20, one of the SEM images of dentin is shown as an example. The features of the microstructure can be distinguished in this image. One can also see that tubules are often occupied probably by odontoblastic processes or polishing debris. The texture of ITD is due to its nanostructure, an entanglement of collagen fibrils and HAP crystals.

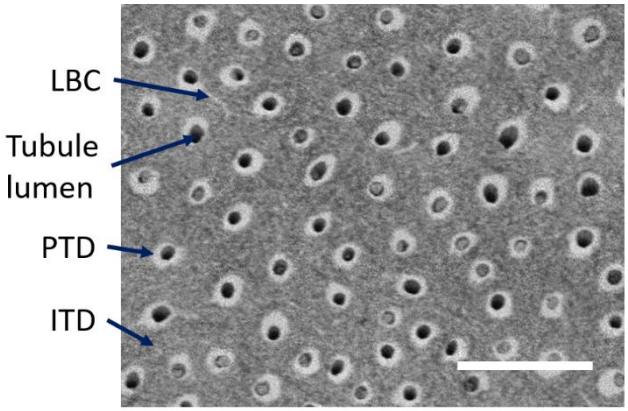

Figure 1-20. The SEM image of dentin at a normalized distance of 0.54 from the DEJ (Scale bar: 15 µm, source: author)

Estimates of the area fractions of the constituents

The changes of the area fraction of the constituents in the thickness of the dentin from the DEJ (0) to the pulp (1) are visualized in Figure 1-21. The porosity increases continuously from the enamel to the pulp, but the area fraction of HMP has its maximum approximately at the location $L_i/L=0.8$. Expression of the location "L_i" is explained in section 1.2.2.

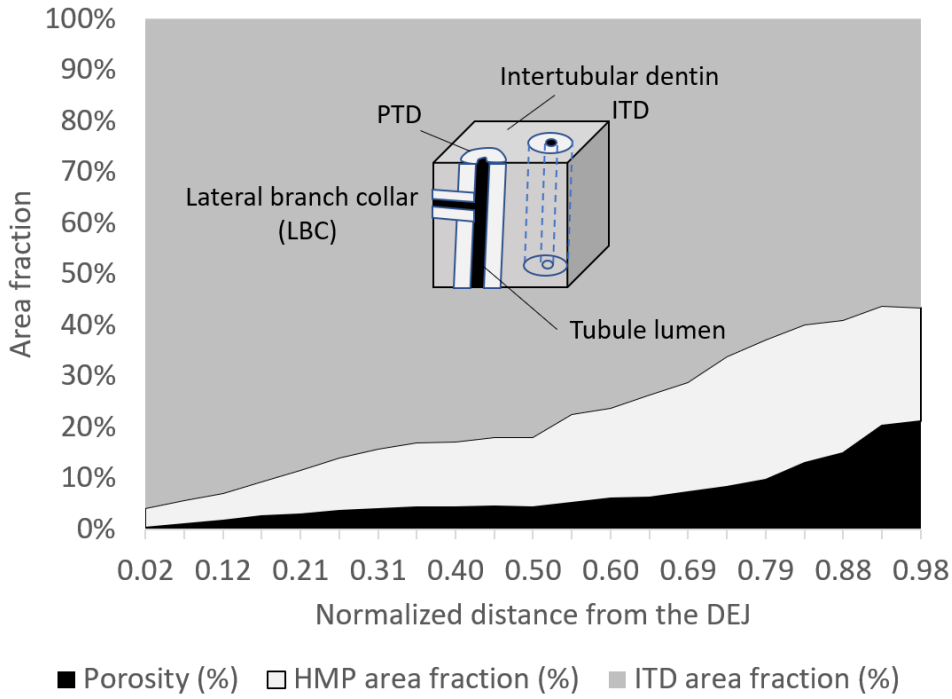

Figure 1-21. Area fraction of dentin constituents measured in the third molar of the young adult patient

The average porosity due to Tubule Lumens (f_{TL}) and tubule volume fraction (f_T) estimated from the whole row of images are given in Table 1-6.

Table 1-6. Morphological properties of the studied zone of the studied sample

Area fractions of tubules and tubule lumens in the whole studied zone	
f_{TL}	6.9%
f_T	23%

Estimates of the averaged morphological parameters of the tubules versus the location in various depths of dentin

The variation of diameter of the dentin constituents through its depth is represented Figure 1-22. In general, the average inner and outer diameters of the tubules increase from the enamel to the pulp. However, they seem to be constant between L_i/L between 0.3 and 0.8.

The average thickness of the peritubular cuffs seems to be relatively constant through the dentin except near the pulp, where a slight decrease is observed.

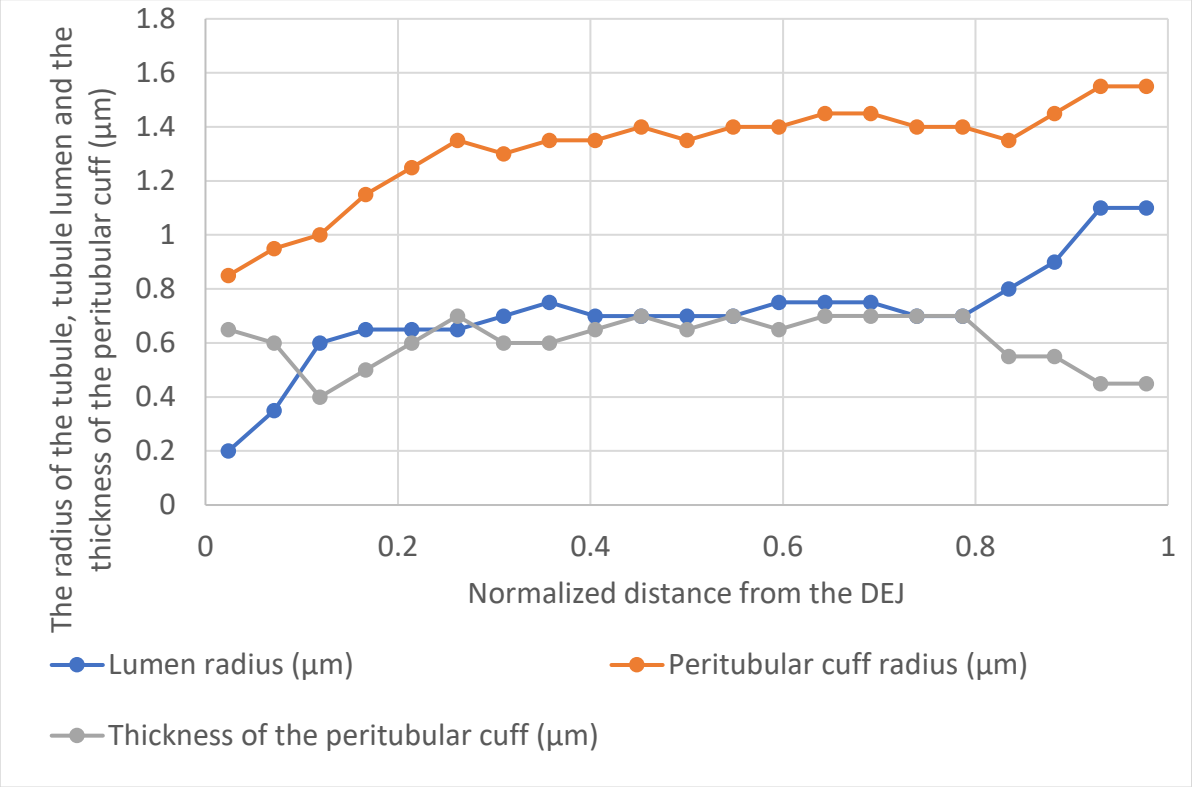

Figure 1-22. Average radius of dentin constituents versus normalized distance from the DEJ.

The variation in the number of tubules per unit area (tubular density) from the DEJ to the pulp is shown in Figure 1-23. The tubular density increases with a rate of ≈31000 (tubules/mm²)/mm up to the location 0.8 and then shows an abrupt fall.

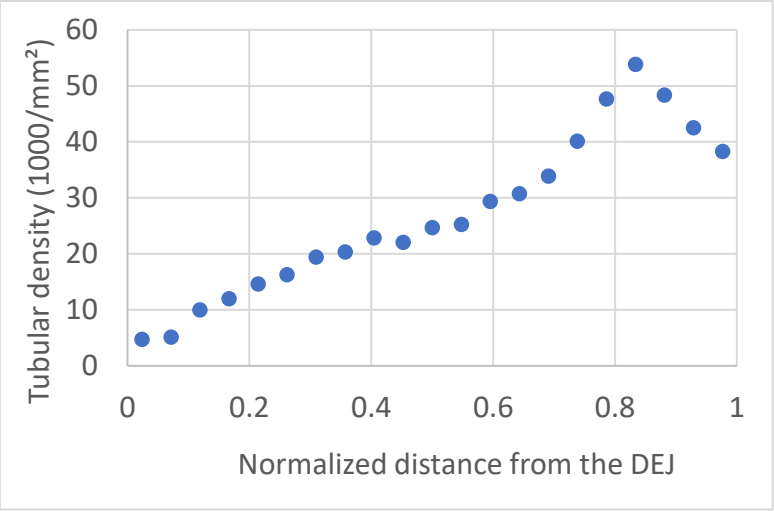

Figure 1-23. Variation of tubular density versus normalized distance from the DEJ

Characterization of the local distribution of tubules and LBs

Three SEM images -"E", "M", and "P"- were analyzed to study the density of tubules and LBs. The distribution of the diameters of the tubules and LBs are shown in Figure 1-24. Each of the histograms in Figure 1-24 shows a bimodal distribution, which is a superposition of two distributions: one for the LBs (in orange) and one for the tubules (in blue).

This figure shows that the number of tubules increases by approaching the pulp. It also shows that by moving away from the pulp more LBs are found.

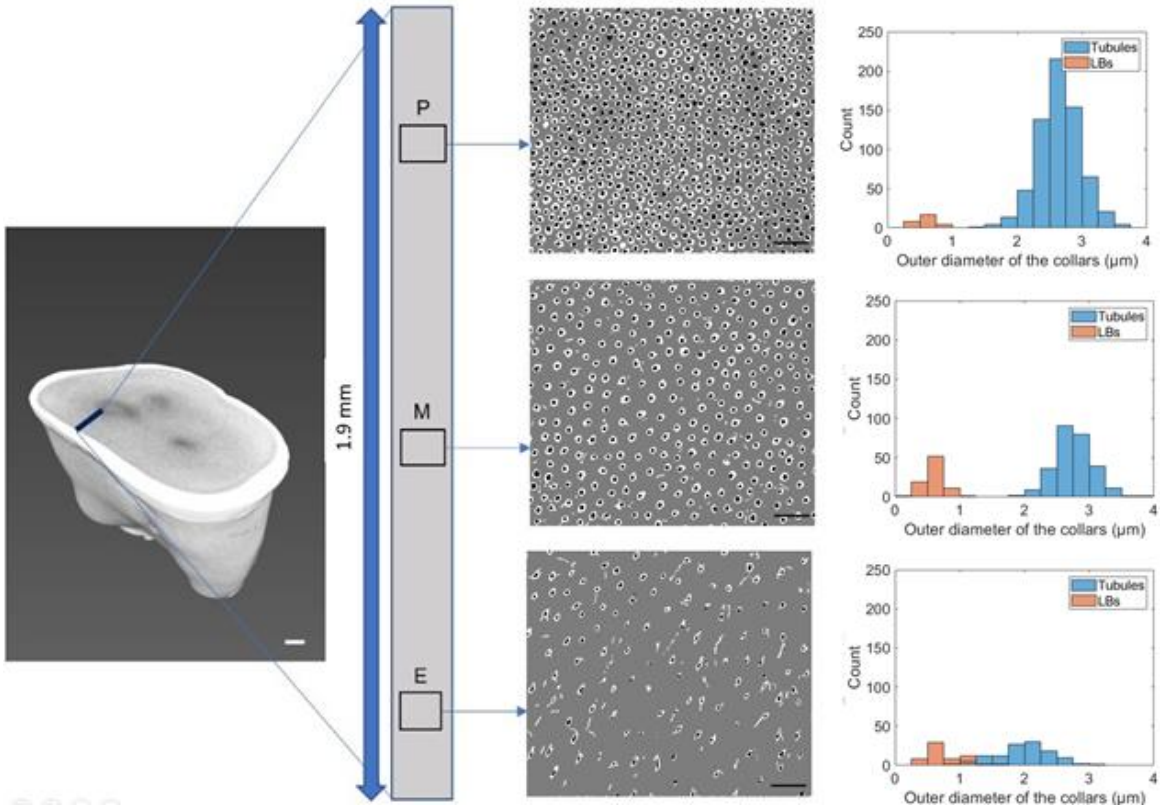

Figure 1-24. Left: the 3D image of the cut tooth (Scale bar: 1 mm). Right: Bimodal distribution of the mineralized entities in dentin (Scale bars: 15 µm), third molar, young adult patient

Near enamel, fewer tubules are detected, which is consistent with the lower tubular density in this area. On the contrary, near the pulp, the probability of finding LB is low. To better probe this difference, the probability of morphological features (instead of their number/count) has been reported in the bimodal histograms in Figure 1-25. the LBs (the modes on the left) are more probable to be observed near the enamel than elsewhere. It should be mentioned that in these normalized histograms, the area of the bins adds up to one.

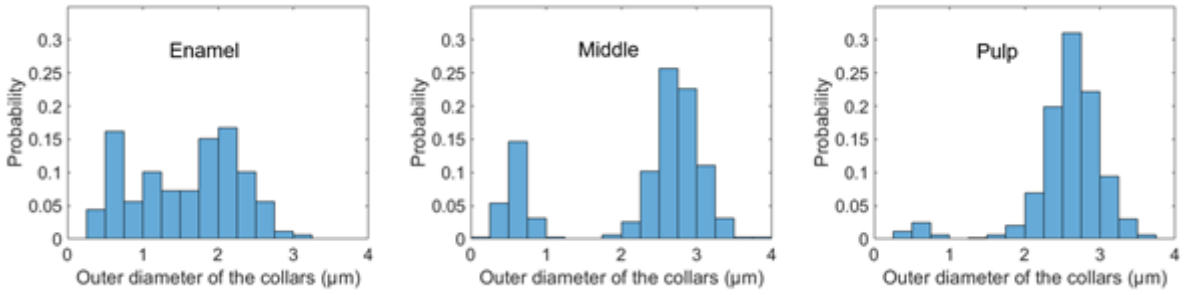

Figure 1-25. Histograms of the diameter of the mineralized collars at three locations in dentin (from left to right: near the enamel (E), in the middle (M) and near the pulp (P)).

Up to now, only LBC has been characterized. To have information about LBL, we measured the average ratio between d_{LBC} and d_{LBL}, which are the diameters of LBC and LBL respectively:

$$\frac{d_{LBC}}{d_{LBL}} = 2.8$$

The measurements were performed on images with a higher resolution (Figure 1-18). The results concerning the morphological properties of LBs are summarized in Table 1-7.

Table 1-7. Quantification of LBs with respect to the distance from the DEJ in the third molar of a young patient.

Image	Normalized distance from the DEJ	a_{LB} (%)	a_{LBL} (%)	Contribution of a_{LBL} to the local overall porosity (%)	d_{LBC} (µm)	d_{LBL} (µm)	LB density (nb/mm²)
E	0.12	0.92	0.12	7.18	0.76	0.27	4688
M	0.45	0.56	0.07	1.56	0.6	0.21	6675
M1	0.6	0.34	0.04	0.65	0.61	0.22	4529
P	0.83	0.12	0.02	0.15	0.57	0.2	2305

1.3.2 Discussion

Acquiring a group of SEM images, covering a path from the enamel to the pulp, and devising protocols for the image treatment and analysis allowed studying the morphological properties of the microstructure of dentin as a function of the location inside dentin.

Qualitative observation of the microstructure gradient

Figure 1-26 shows five images from various locations in dentin (normalized distances of 0.12, 0.45, 0.6, 0.83 and 0.98 from the DEJ). It clearly shows a huge gradient in the microstructure of dentin.

Near the pulp ("P1"), the tubule lumens are large, and the peritubular cuffs are thin. In the images "P", "M1", and "M", the inner and outer diameter of tubules are relatively constant. However, the tubular density decreases significantly from "P" to "M".

In the image "E", LBs are more visible, and the tubules obviously have smaller diameters.

The orientation of the tubules shows a gradient as well: While the tubules near the enamel are inclined with respect to the cutting plane, they are relatively perpendicular to it in the middle of the dentin sample.

Quantitative analysis will further investigate these variations in the morphological properties.

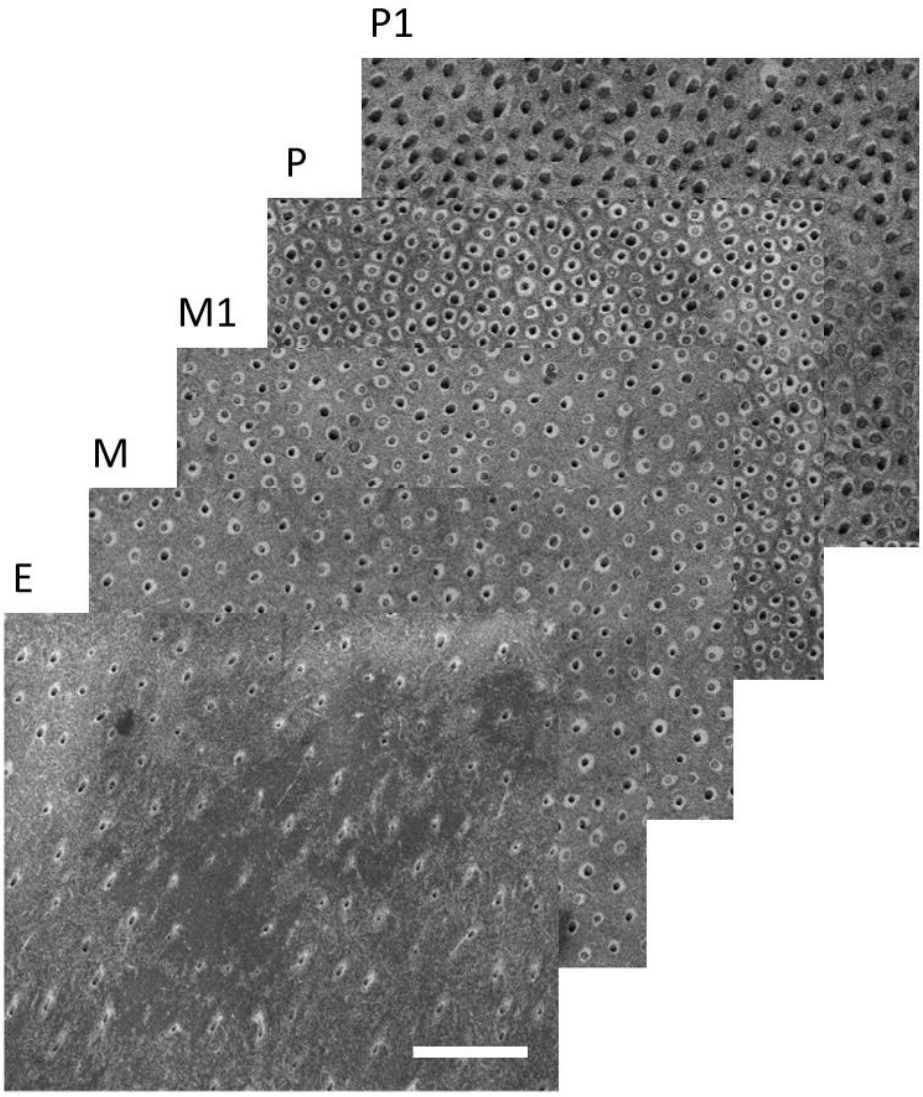

Figure 1-26. SEM images at the five chosen locations from the enamel to the pulp (Scale bar: 25 µm, source: author). Locations of "E", "M", "M1", "P" and "P1" are respectively 0.12, 0.45, 0.6, 0.83 and 0.98.

First, we will propose to revisit the different types of dentin, from mantle dentin to secondary dentin.

Mantle dentin

Let us focus on the area near enamel (next to DEJ) first. Figure 1-27 allows for investigating the morphology of the dentin microstructure near the DEJ and discussing the “mantle dentin”.

Vennat et al. (2017) [7] reported that at a distance of 5-30 µm from the DEJ the splitting of tubules into major branches occurs. In this range of distance, the microscale features of dentin seem to be different. Here, in the mentioned range of distance, more numerous and smaller features are visible, which means a splitting of the tubules.

The mantle dentin area is indicated on Figure 1-27, we see that its thickness varies from one paper to another. The smallest estimations of the thickness of mantle dentin are similar to the thickness of the zone where the tubules split. From the morphological point of view taken in my work, the mantle dentin can be supposed to correspond to the “messy” area of roughly 30 µm from the DEJ. There we can only distinguish various branches and no tubules. Then after those 30 µm, tubules are formed and are linked together by numerous and smaller lateral branches.

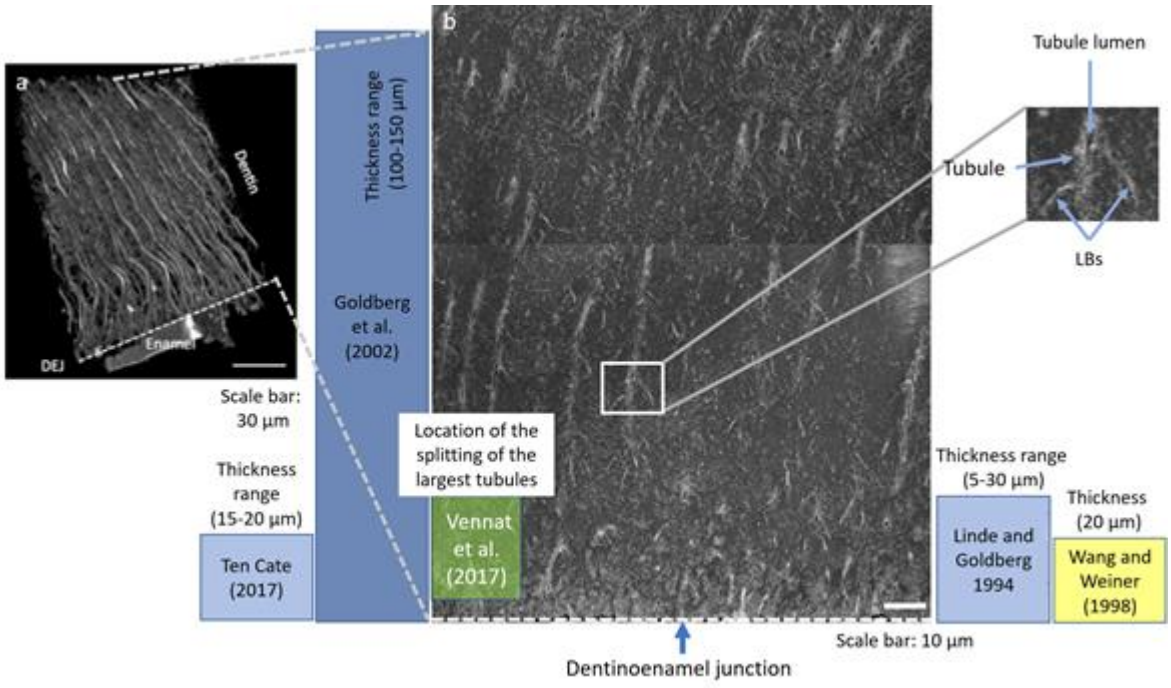

Figure 1-27.a) 3D CLSM reconstruction of the porosity of dentin near the DEJ. b) The SEM images near the DEJ.

Middle dentin

On Figure 1-22, a region is observed where the average inner and outer diameters of the tubules remain relatively constant. This result is in accordance with our qualitative observations (Figure 1-26).

So, a criterion can be proposed to define middle dentin instead of using this term with no clear delimitation of the area: it is the area where the diameters relative to tubule microstructure are stable, indicated on Figure 1-28.

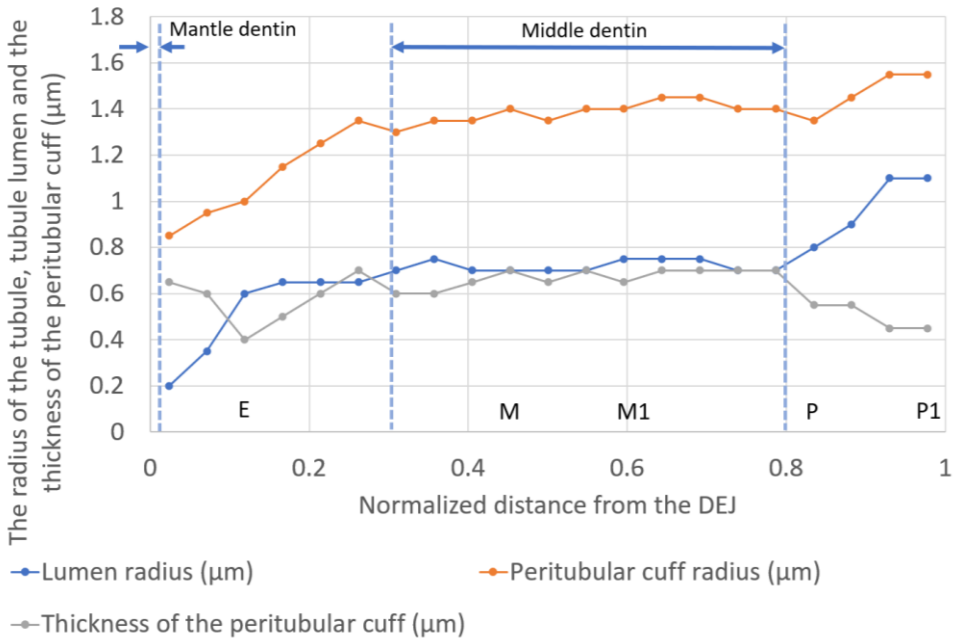

Figure 1-28. The local variation in the inner and outer diameter of tubules from DEJ to pulp. Proposed definition of middle dentin

Secondary dentin

The third type of dentinal tissue in healthy dentin is secondary dentin, which is located near the pulp (Figure 1-8).

The observed decrease in the tubular density near the pulp (Figure 1-23) was an unexpected result. However, as explained in section 1.1.4, apart from an actual change in the number per area of tubules, a variation in the angle between the cross-section and the tubules causes an apparent difference in the tubular density. This is further investigated in Figure 1-29, where the five previously introduced images (‘E’, ‘M’, ‘M1’, ‘P’, and ‘P1’) are marked on the plot.

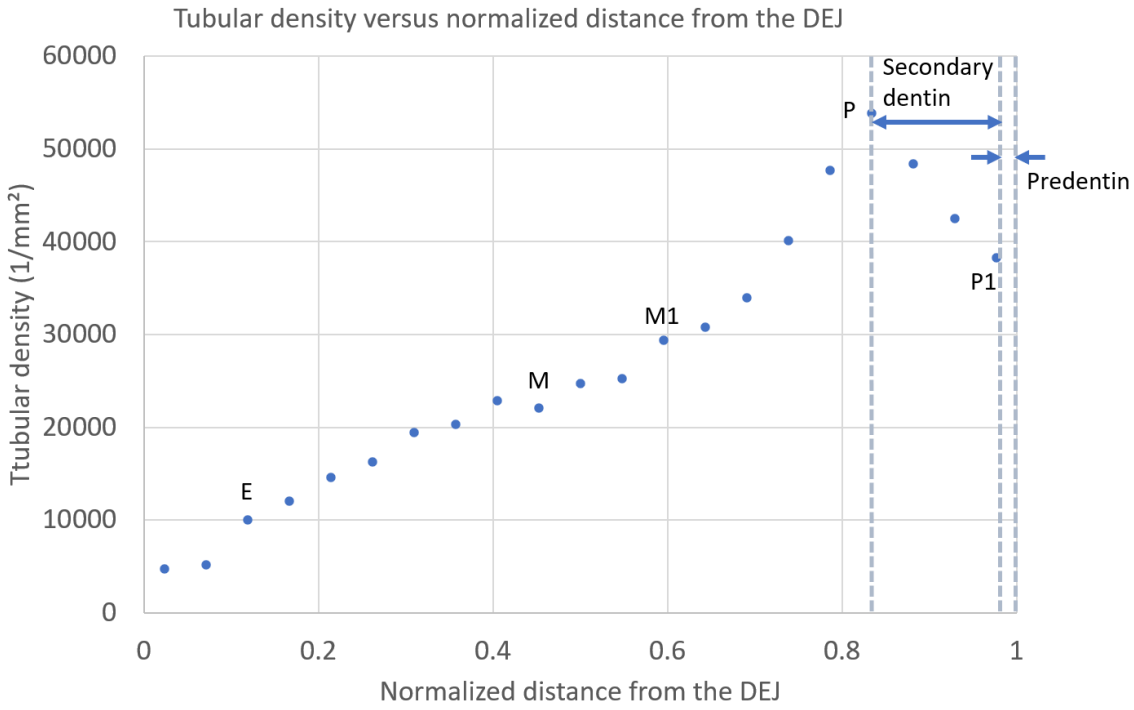

Figure 1-29. Estimation of the secondary dentin (≈280 µm) based on the variation in the tubular density. Thickness of predentin is estimated from the paper by Couve (1987) [41].

It is known that tubules in the secondary dentin change orientation. Therefore, the final 20% of the dentin thickness is assumed to be secondary dentin and predentin. Predentin is assumed to be approximately 40 µm thick [41]. Therefore, the remaining 280 µm corresponds to the thickness of secondary dentin, which is an acceptable estimation [42].

On the images belonging to this secondary dentin zone, it is observed that some tubules do not have a peritubular cuff (Figure 1-30).

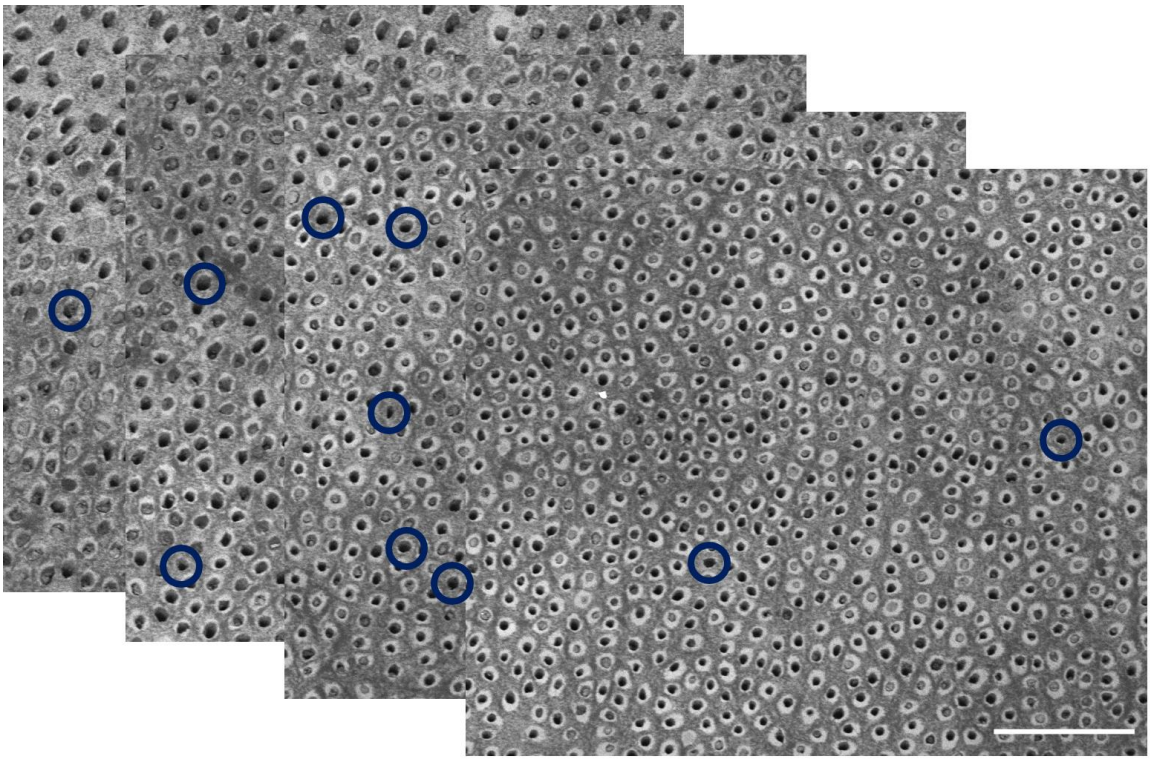

Figure 1-30. The four images that are estimated to represent the secondary dentin (in a range of normalized distance from 0.8 to 1 from the DEJ). Some tubules with very thin or no peritubular cuffs are marked. (Scale bar: 25 µm)

Quantification of the characteristics of LBs

For the first time, a SEM image analysis has been led to quantify the characteristics of LBs all through the dentin.

First, it should be remembered that among various types of LBs, the microbranches are too small to be resolved in the acquired SEM images. Therefore, the studied LBs in this thesis are only the fine and major branches according to the classification by Mjör & Nordahl, (1996) [9].

LBs were observed through the whole dentinal tissue thanks to their collars. We indeed observed a bright collar surrounding LBL (visible in Figure 1-18), which is scarcely discussed in the literature: Nanci (2017) [11] and Zanette et al. (2015) [29] briefly mentioned the LBs and their mineral collars. However, to our knowledge they have never been quantified even if they could play a role in dentin's mechanical properties. In our high-resolution images, we estimated the ratio between LBL and LBC diameters and then observed and quantified LBCs from SEM images that have a larger field of view. The estimated ratio of diameters helped with estimating the porosity due to the LBs in the latter group of images.

In comparison with the tubules, the density of LBs is more difficult to define on 2D images cut perpendicular to the principal axes of tubules. Contrary to the tubules, which are approximately regular and parallel, LBs are positioned in various and relatively random orientations. Despite this issue, the proposed protocol allowed to distinguish their collar and to measure their density for the first time all through the dentin, which varies from 6700 to 2300 nb/mm² from the DEJ to the pulp. The density of tubules shows an inverse trend (Figure 1-24), which agrees with Mjör & Nordahl (1996) [9].

The LBL area fraction (a_{LBL}) is relatively low (inferior to 1%) but increases towards DEJ, with its contribution to the overall porosity also increasing.

The porosity due to the LBs was measured to be 0.12% at ~200 µm from the DEJ. However, Vennat et al. (2017) [7] measured an overall porosity of 1.2% in the 350 µm zone of dentin below the DEJ, which leads to an estimation 0.4% of porosity due to LBs. The order of magnitude of both studies are consistent and our results may underestimate the LB contribution due to the 2D aspect of our study.

Even if the contribution of LB to porosity is decreasing towards the pulp cavity, numerous LBs remain in middle dentin and represent a porosity of roughly 0.5% corresponding to a contribution of 0.15 to 1.65 % of the local overall porosity.

Near pulp cavity, the number of LBs decreases drastically, in a way that no LBs are detected on the image nearest to the pulp.

1.4 Conclusion and perspectives

The goal of this investigation was to characterize and measure the variations in the microstructure of dentin and consequently in its morphological properties thanks to SEM images. A main achievement is the identification and quantification of the LBs that have been classified by Mjör & Nordahl in 1996 but not fully characterized since then to our knowledge.

First, an imaging protocol was designed to image the dentinal tissue by including its various types. The BSE imaging mode was chosen in order to distinguish the morphological features of the microstructure. Images from DEJ to pulp cavity have been obtained on a healthy third molar tooth from a young adult.

To quantify the microstructure, the images were treated (segmented into the microscale constituents of dentin: ITD, PTD, TL and LBs). An image treatment protocol was designed to automate the treatment of BSE mode SEM images from the enamel to the pulp and to analyze a large group of images. It enables segmenting images and separating the areas associated with the different constituents.

Then, an image analysis protocol is proposed that enables characterizing the dentinal tissue and its constituents. The constituent diameters, area fraction, density have been assessed. In particular, this protocol characterizes the LBs, which are studied for the first time with such detail. This study enables us to revisit the different zones of dentin. First, concerning mantle dentin, based on a morphological criterion (it ends where major branches are fused together), it consists of an area of roughly 30 µm (which is consistent with the literature). Within the studied sample, there is a relatively large zone (normalized distance 0.3 to 0.8) where the average dimensions of tubules remain almost constant even though their density varies. It can be proposed as a criterion to define “middle dentin”. Secondary dentin has been detected thanks to its tubules orientation change and is roughly 280 µm deep.
A novelty of this study is the quantification of the LBs at three locations: near DEJ, in middle dentin and near the pulp. The considered LBs do not take into account microbranches (branches with a diameter of less than 200 nm) due to the resolution limit of our SEM

images. The first qualitative observation is that LBs have a dense collar thanks to which we can detect them on our SEM images. We studied their distribution through the depth of dentin. The number of LBs becomes more and more important by approaching the enamel. The LBs' contribution to the overall porosity rises drastically near DEJ. The diameter of LBC is roughly 0.6 µm and is decreasing slightly from pulp to DEJ.

Now that the microstructure has been quantified through the depth of the tissue, the next step is to probe how the microstructure and in particular the LBs affect the mechanical behavior of dentin depending on the location. This unprecedented data is used as entry data for a mechanical model of the dentin proposed in Chapter 3. The local mechanical properties are obtained by nanoindentation (Chapter 2) and the treated images are used to plan those tests.

The protocols of acquisition and analysis of images developed in this thesis can be performed on other locations in dentin. Cervical region of coronal dentin is studied here, but there is also interest in studying radicular dentin and other regions of coronal dentin.
Another path of inquiry is to investigate the microstructure of teeth with various ages and pathologies to better understand the implied changes in morphology (and perhaps propose more adapted restorations protocols).

To go further in LB characterization, it would be interesting to investigate their chemical composition and nanoscale organization. This could be done by a study of Energy-dispersive X-ray spectroscopy by SEM and TEM.

2 Nanoindentation study on dentin

The mechanical properties of the constituents (or phases) of dentin at the microscale (PTD and ITD) are required for the numerical micromechanical model of dentin.

The constituents of dentin at the microscale are particularly challenging to be mechanically characterized given their small dimensions, especially for the thin PTD cuffs that are only around 0.5 μm thick. The issue is less severe for ITD because its zones are generally larger than PTD, but even these zones have small dimensions (of typically 2 μm) near the pulp. Another challenge is the local variability of the microstructure of dentin (and consequently the local variability of the properties of its constituents).

Local mechanical characterization of the *constituents* of microstructure is usually done by indentation tests (micro- or nanoindentation, depending on the size of the constituents, or by Atomic Force Microscope (AFM) indentation tests for small sizes). Apart from characterizing the constituents, nanoindentation testing is also used to identify near-surface *macro* (or homogenized) properties of the heterogeneous materials. In this case, the size of the indent area is bigger than the size of the constituents.

These techniques are summarized in the literature review of this chapter. Then, the results of the indentation studies on the *constituents of dentin*, as well as on *the dentin as a homogenized composite* are reviewed.

Two groups of indentation tests were carried out in this thesis: one group for measuring the elastic modulus and hardness of the dentin constituents (Figure 2-1.a) and another for measuring homogenized elastic modulus and hardness for dentin.

1) The first group of nanoindentations (Figure 2-1.a) was carried out using the known rules of the "statistical grid indentation technique" (Constantinides et al. (2006) [43]) and an image analysis tool called "Virtual Nanoindentation" (VN). The "VN" tool, which simulates the nanoindentation results of heterogeneous materials, verifies that the plan of nanoindentation experiments gives valid results.
2) A second group of deeper nanoindentation experiments (Figure 2-1.b) was performed to study the variation of the dentin modulus as a homogenized composite. The "VN" tool was used to simulate these deep nanoindentations as well.

Both groups of the measured elastic properties are useful because:

1) The experimental *local* properties of the constituents are *input data of the micromechanical model*.
2) The experimental *macro* (or homogenized) properties are the proper data to *validate the homogenized properties computed from the simulations, namely the output data of the micromechanical model*.

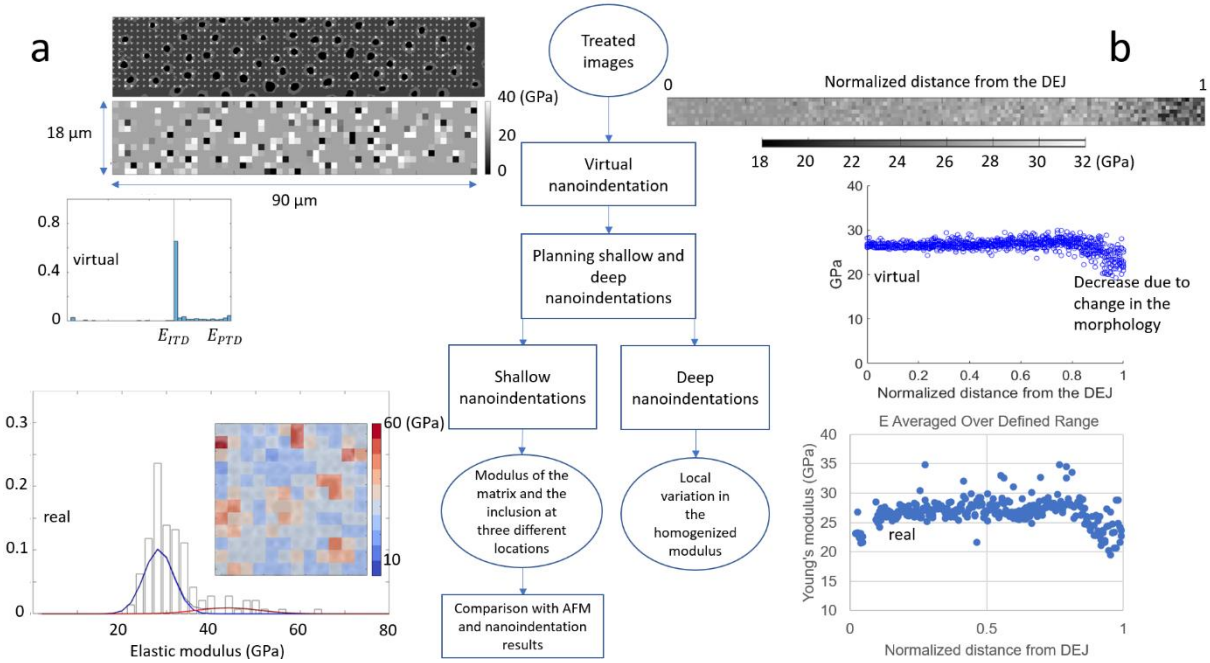

Figure 2-1. The schema of the present chapter a) the steps for characterization of dentin constituents by shallow nanoindentations, b) the steps of characterizing dentin as a composite of ITD, PTD and void by using deep nanoindentations.

2.1 Review of the indentation techniques and application to dentin characterization

2.2 Principle of indentation

The principle of indentation techniques consists of pressing a hard tip with known mechanical properties into the material being tested, recording the load-depth curve (Figure 2-2.a) and measuring geometrical parameters of the imprint.

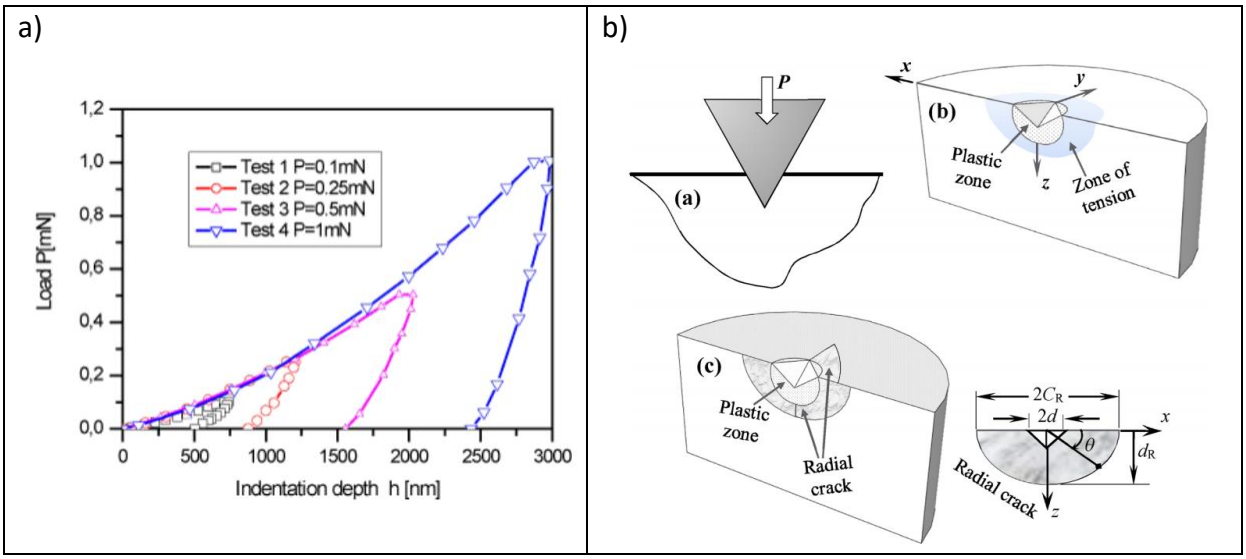

Figure 2-2.a) load-displacement curves of nanoindentation tests with various depths [44], *b) Schematic of Vickers indentation, plastic zone, and radial crack formation below the indenter* [45].

In most cases, the deformation in the specimen under the indenter involves both elastic and plastic deformations (Figure 2-2.b). By having assumptions about the nature of the mechanical behavior of the material, different mechanical properties can be identified, most famously the hardness and the elastic modulus (Fischer-Cripps, (2002) [46]). However, other

mechanical properties can be identified by nanoindentation such as yield stress, strength, viscoelastic properties, and fracture toughness, as well as internal residual stresses. However, measurement of mechanical properties by nanoindentation is known to have artifacts further discussed in section 2.4.

The hard indenter tip, explained in the principle of nanoindentation, may come in several shapes: flat, spherical, three-sided (Berkovich), four–sided pyramidal (Vickers), and so forth (shown in Figure 2-3).

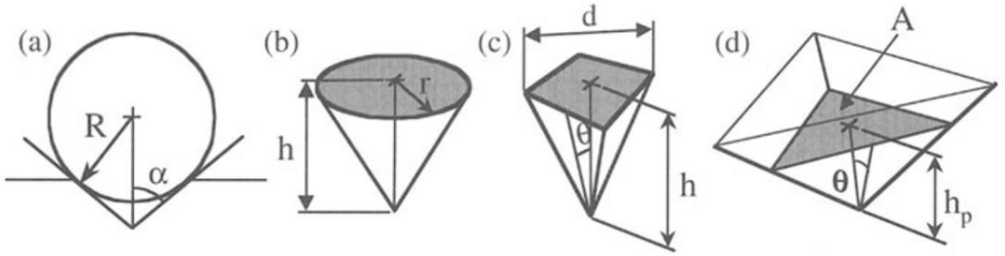

Figure 2-3. Various indenter tips: a) Spherical, b) Conical, c) Pyramidal, d) Berkovich (adapted from Fischer-Cripps, (2002) [46])

Choice of an indenter tip among these tips depends on the expected property from the nanoindentation experiment. For example, for measuring the fracture toughness, the tested material needs to be cracked and therefore sharper indenter tips e.g., Vickers indenter tip are used [46].

For measuring properties like yield strength, work hardening rate, and residual stress the spherical indenter tip is used, because in the beginning this tip causes only elastic deformation in the specimen and not immediately plastic deformation (Park & Pharr, (2004) [47]).

Indentation of a specimen involves soliciting a certain volume in the depth (penetration *h*) with a load (*F*). Indentations are usually divided into three classes according to the ranges of load and penetration of the tip (Table 2-1).

Table 2-1. Hardness testing scales defined by ISO 14577-1 [48]

Scale	Load range	Penetration range
Macro range	$2 < F < 30000$ N	Not specified
Micro range	$F < 2$ N	$h > 0.2$ μm
Nano range	Not specified	$h < 0.2$ μm

Nanoindentation is specified as an indentation test whose depth is less than 0.2 μm, but in practice, nanoindentation tests with depths of up to 1 μm are reported (Van Meerbeek et al. (1993) [49]). As mentioned in the ISO norm, "*for the nano-range, the mechanical deformation strongly depends on the real shape of indenter tip and the calculated material parameters are significantly influenced by the contact area function of the indenter used*". Therefore, particular attention must be paid to the results obtained by nanoindentation.

The interest of testing at different scales in a heterogeneous material is shown in Figure 2-4, which shows the various indentation zones of various scales on a polycrystalline material. An indentation in each scale results in a characterization in that scale: For example, the indentations whose imprints are shown in Figure 2-4.c characterize individual crystals, while the one shown in Figure 2-4.a characterizes a group of crystals in a homogenized way.

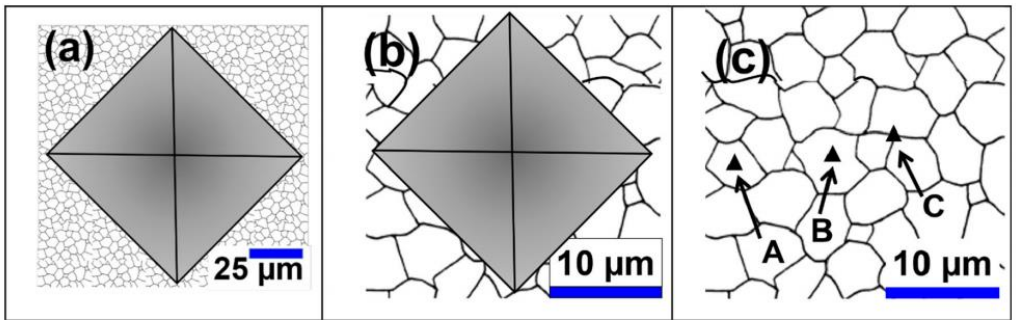

Figure 2-4. Schema of indentation hardness of a polycrystalline material at a) macroscale; b) microscale; and c) nanoscale after Broitman, (2017) [50]

2.2.1 Berkovich tip

In this thesis, a Berkovich tip was used. A few reasons for choosing this indenter are explained in section 2.6.4. In Figure 2-5.a a schema of a Berkovich indenter, together with its imprint, on the surface of dentin is shown.

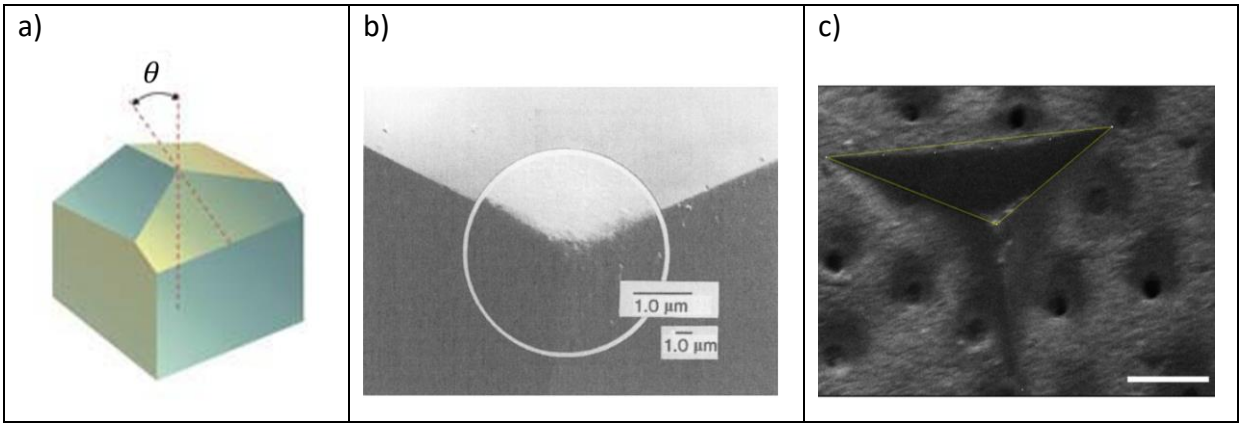

Figure 2-5.a) A schema for Berkovich tip (θ=65.27° for modified Berkovich tip) (image from Wikipedia), b) The tip of a Berkovich indenter with a radius in order of 100 nm [46]*, c) SEM image of an imprint that a Berkovich tip has left on dentin (Scale bar: 5 µm)*

Figure 2-5.b shows that the nanoindenter tip is blunt at a very small scale. To quantify this bluntness, a tip radius is defined, which is shown by R and has a typical value of 50-100 nm for a Berkovich tip [46]. Together with the roughness of the sample, this bluntness affects the results of nanoindentation, which is further explained in section 2.4.

As visible in Figure 2-6.a, the projected contact area of an indent by a Berkovich indenter is an equilateral triangle (which is visualized with its dimensions in Figure 2-6). As shown in Figure 2-6.a the side length of this triangle ('s') according to Wimmer et al. (1997)[51] is:

$$s = 7.5h_p, \tag{2.1}$$

where h_p is the penetration depth (Figure 2-3.d).

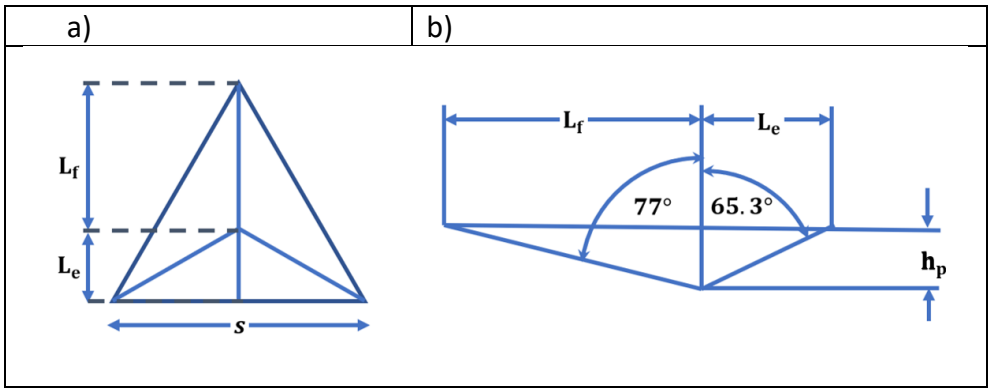

Figure 2-6.a) The contact area of a Berkovich tip, b) The side view of a Berkovich tip (adapted from Wimmer et al. (1997) [51])

2.3 Analysis of Depth Sensing Indentation (DSI)

In common indentation tests, the deformation of the material is characterized by inspecting the specimen surface and measuring the residual imprint area "*A*". Figure 2-5.c shows an example of an indented specimen. Without measurement of the depth, the recording of the maximum load and the measurement of the imprint area allow only to obtain the hardness, a property that depends on the shape of the tip.

In recent decades, a new generation of indenter devices has been created, namely the Depth Sensing Indentation (DSI), where the load '*P*' and the displacement '*h*' are continuously recorded with a high precision (Fischer-Cripps, (2002) [46]). Loading paths that are applied in DSI are similar to those followed in more conventional tests.

- The **Unloading Method** is the classical nanoindentation method to measure Young's modulus of the indented specimen. Contact stiffness (the slope S shown in Figure 2-7.a) is measured at the beginning of the unloading, and the elastic modulus is derived from it.
- The **Continuous Stiffness Measurement** (CSM) method consists in applying an oscillatory loading path and continuously measuring the modulus during penetration. For this purpose, a low-magnitude harmonic oscillation (with a frequency of 45 Hz in our tests) is superimposed on the primary load signal. A schematic load-displacement curve of such an experiment is shown in Figure 2-7.b.

The results from CSM method are less affected by time-dependent phenomena like viscoelasticity, thermal drift, or time-dependent plasticity, which are known to affect the nanoindentation tests (Oliver & Pharr, (2004) [52]). This is because of the high frequency of the oscillatory load.

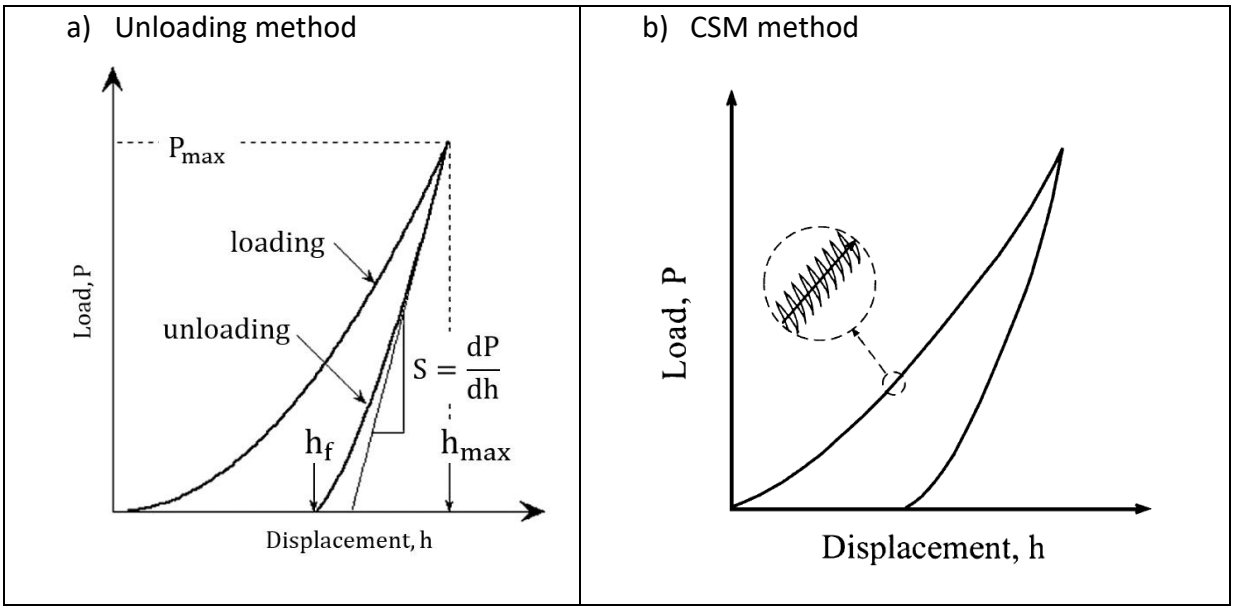

Figure 2-7. Compliance curves of depth sensing indentation tests, a) Schematic load-displacement curve of an indentation test by unloading method according to Oliver and Pharr (2004) [52]*, b) Schematic load-displacement curve of CSM method (Li & Bhushan, (2002)* [53]*)*

The most common mechanical characteristics that can be identified from the load-depth curves and the measured contact area are the hardness (*H*) and the elastic modulus (*E*) [52].

2.3.1 Hardness

Hardness is the usual and first characteristic of a material identified by this technique. It is equivalent to the average pressure under the indenter tip and characterizes the resistance to indentation [54]. However, it is not a fundamental physical property of the material [55]. It is obtained by measuring the depth of the indenter or the indentation area (area of contact) for a fixed load.

For example, the hardness is estimated as the indentation load P_{max} divided by the projected area A_P of the indentation imprint [52]:

$$H = \frac{P_{max}}{A_P} \tag{2.2}$$

where for a spherical indenter, A_P is measured as following:

$$A_P = \pi a_c^2 \tag{2.3}$$

in which a_c is the radius of the circular imprint. For tips of other shapes A_P has to be estimated by other equations (as shown in Figure 2-8.a, b, c, and d).

At the time when this technique was new, however, the projected area was not measured. The area of the curved imprint surface was measured, and the load was divided by this area (for measuring the Brinell hardness number).

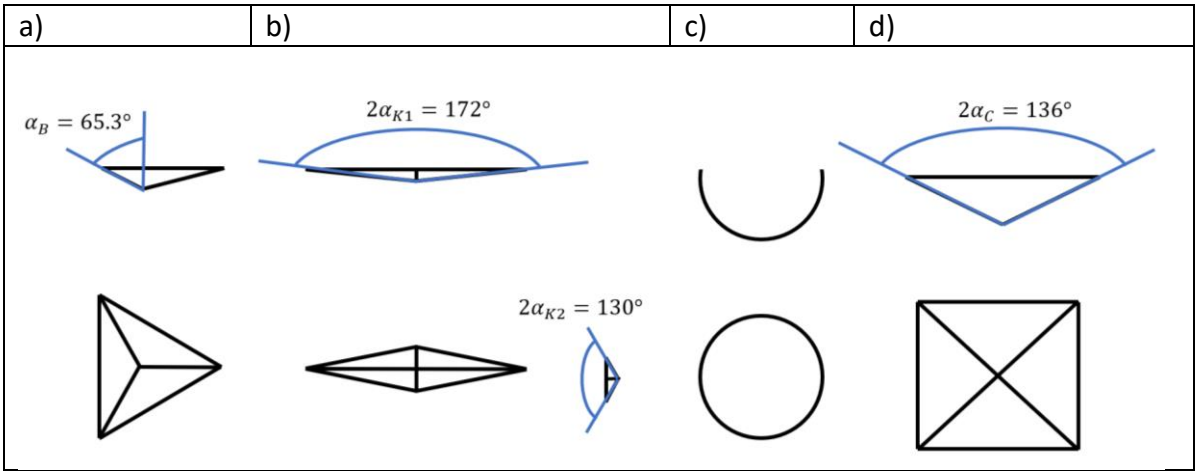

Figure 2-8. the side view of various tips above their imprint areas: a) Berkovich, b) Knoop, c) Spherical d) Vickers

The projection area A_p depends on the shape of the tip and is defined in terms of the penetration depth h_p (Figure 2-3.d).

$$A_p = f(h) \tag{2.4}$$

For an ideal Berkovich indenter ($\alpha = 136°$), the projected area A_p is given as (Fischer-Cripps 2002 [46]):

$$A_p = 3\sqrt{3}\tan^2(\alpha_B)\,h^2 = 24.56h^2 \tag{2.5}$$

for a Knoop indenter:

$$A_p = 2h^2 \tan\alpha_{K1} \tan\alpha_{K2} \tag{2.6}$$

and for a Vickers indenter:

$$A_p = 3\sqrt{3}\tan^2(\alpha_C)\,h^2 = 24.504h^2 \tag{2.7}$$

where α_B, α_{K1}, α_{K2}, and α_C are the angles shown in Figure 2-8.

2.3.2 Elastic modulus

The identification of Young's modulus of the homogeneous isotropic elastic material is based on the Boussinesq problem (1882) [56], which consists of finding the deformation and stress distribution throughout an elastic half-space when subjected to an arbitrary distribution of surface tractions. The formal solution is not in closed form, making it intractable for many real problems except for particular contact geometries such as circular contact areas subjected to uniform pressure, uniform displacement, and Herz pressure.

In the indentation literature, the most cited model for elastic contact is due to Sneddon, which considers two half-infinite bodies in contact on a plane surface. An arbitrary function $f(r)$ describes the normal separation [57].

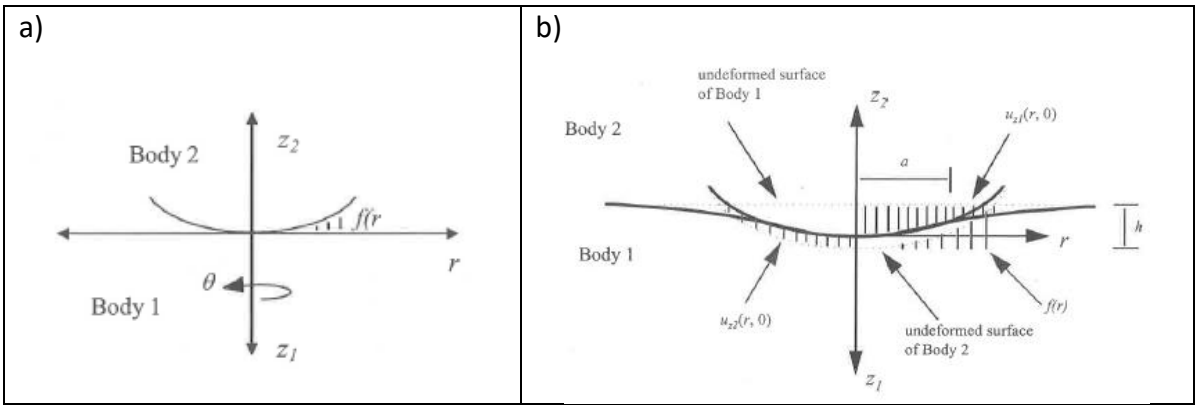

Figure 2-9.a) Contact geometry when bodies are just touching b) Two bodies deformed as a result of normal load P (Agilent technologies)

Sneddon derived a general solution of the Boussinesq problem in the form of Hankel transforms of a function, which allows expressing both the depth of penetration h and the load P

$$h = \int_0^1 \frac{f'(x)dx}{\sqrt{1-x^2}}, \qquad P = 4Ga(1-\nu)^{-1} \int_0^1 \frac{x^2 f'(x)dx}{\sqrt{1-x^2}} \tag{2.8}$$

where G and ν are respectively the rigidity modulus and the Poisson ratio with the boundary conditions:

$$\sigma_{\rho z}(\rho, 0) = 0, \qquad u_z(\rho, 0) = h - f\left(\frac{\rho}{h}\right), \qquad 0 \le \rho \le a \tag{2.9}$$

and

$$\sigma_{zz}(\rho, 0) = 0, \qquad \rho \ge a \tag{2.10}$$

where ρ is the radial distance from the indenter axis. He proposed solutions for special shapes of punch. For example, for a conical punch of semi-vertical angle θ (Figure 2-10), where $f(x) = a\tan(\theta)\, x,$ the load-depth function is parabolic.

$$P = \frac{4G\cot(\theta)}{\pi(1-\nu)} a^2, \tag{2.11}$$

which for an isotropic material can be written as:

$$P = \frac{2E\cot(\theta)}{\pi(1-\nu^2)} a^2, \tag{2.12}$$

As the contact area is a nonlinear function of the indenter depth ($A = g(h_c)$), this partially explains the nonlinear behavior (load-depth) observed during the unloading of the indenter (Figure 2-7).

The distribution of pressure under the punch, which is not uniform, is given by the following relation:

$$\sigma_{zz}(\rho, z = 0) = -\frac{2Gh}{(1-\nu)\pi a} cosh^{-1}\left(\frac{a}{\rho}\right), \qquad 0 \le \rho \le a, \tag{2.13}$$

In addition, Figure 2-10.b shows the distribution of the normalized normal stress in the volume of the elastic material tested for a conical tip (which is similar to a Berkovich tip and is schematically shown in Figure 2-10.a), computed from the Boussinesq solution. In the depth, the material is sensitive to the load up to a distance of 3 to 4 times the size of the imprint (considering the stress is lower than 5% of the normal pressure applied at the surface). In the transverse direction, the distance is smaller, approximatively 2 to 3 times. These sizes have to be compared with the sizes of the constituents of the microstructure if the material is heterogeneous and with the distance between two indentations to avoid any mechanical interaction.

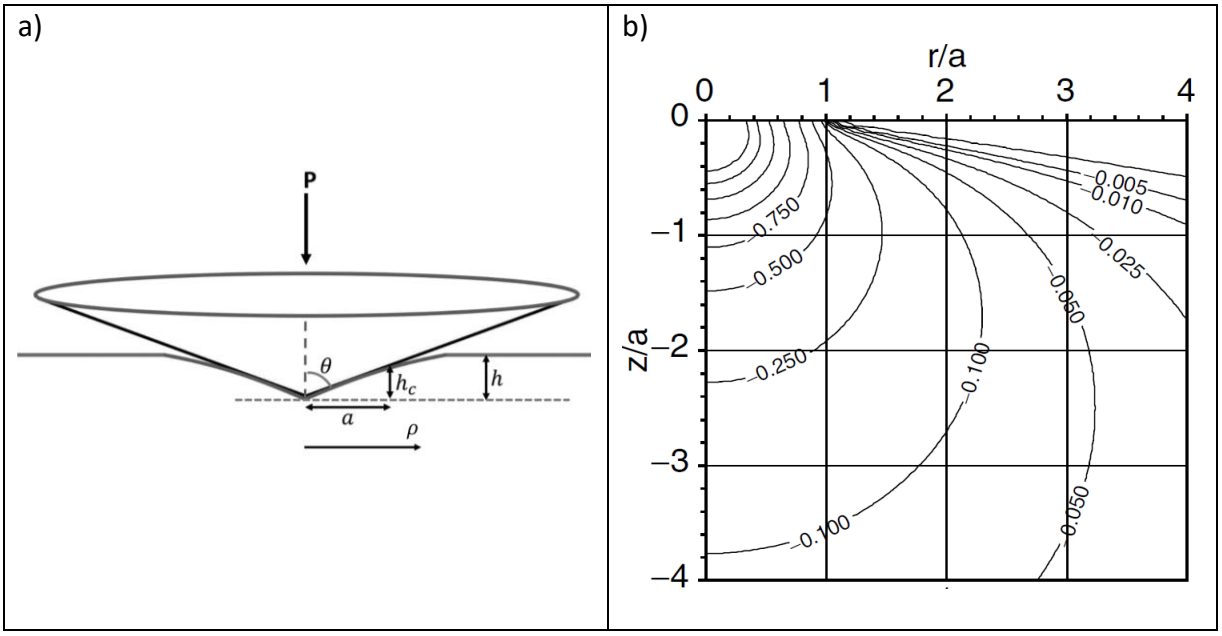

Figure 2-10.a) schema of a conical indenter tip. b) Contours of normalized normal stress due to a conical indenter [58]. *'a' is the contact radius, 'r' is the distance from the axis of symmetry and 'z' is the depth into the specimen.*

The above solution for analyzing indentation considers that the medium tested remains elastic during loading. However, it is well known that a plastic volume occurs below the tip during the loading. This elastic contact solution is applied to the problem of nanoindentation by assuming elastic recovery at the beginning of the nanoindenter's unloading. That is why the contact stiffness (S in equation 2.14 and Figure 2-7.a) is measured at the beginning of unloading, usually one-third of the maximal load.

The Sneddon solution also allows defining the reduced elastic modulus E^* from the unloading part of the $P - h$ curve shown in Figure 2-7.a:

$$E^* = \frac{S}{2\beta}\sqrt{\frac{\pi}{A}} \tag{2.14}$$

In this expression, $S = \frac{dP}{dh}$ is the elastic contact stiffness, A is the contact area, and β is a correction factor.

The reduced elastic modulus is associated with the elastic deformation of both the indenter and the specimen so that it can be related to the elastic parameters of both materials [46]:

$$\frac{1}{E^*} = \frac{1-\nu_s^2}{E_s} + \frac{1-\nu_i^2}{E_i} \tag{2.15}$$

where E_s and ν_s are, respectively, Young's modulus and Poisson ratio of the specimen material, and E_i and ν_i are, respectively, Young's modulus and Poisson ratio of the indenter material.

For non-conical indenter tips, a correction factor β [52] is added to the original Sneddon's solution to estimate the reduced modulus. For a Berkovich tip, the correction factor β is 1.034 [46].

Both methods of nanoindentation "Unloading method" (UM) and "Continuous Stiffness Measurement" technique (CSM) use this assumption.

2.4 Errors and artifacts in nanoindentation testing

Some well-known phenomena affecting nanoindentation measurements are introduced in the following subsections ([46], [59]).

2.4.1 Edge effect

The formulae to identify the properties from nanoindentations are established by considering pressing a tip on an infinite half-space. If a free edge is near an indentation, it affects the results. By theoretical and experimental studies on nanoindentation tests carried out near free edges, Jakes and Stone, (2011) [59] investigated the ratio of the measured properties affected by the edge, Youngs's modulus E^u_{eff} and hardness H^u_{eff} to the real ones (respectively E^∞_{eff} and H^∞_{eff}). They summarized their results in Figure 2-11. In these diagrams, the *x*-axis is $A^{\frac{1}{2}}/d$, which is a normalized ratio between the indent size (contact area) to the distance from the edge of the sample.

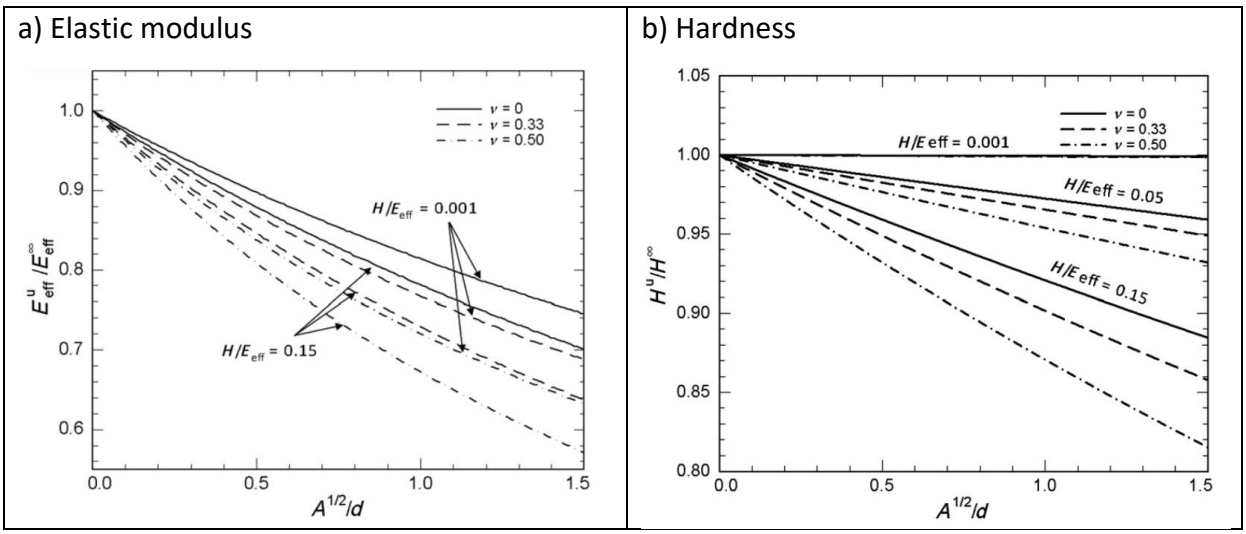

Figure 2-11. The ratio of uncorrected property near an edge to the real property (Jakes and Stone, (2011) [59]*)*

They show that at the same distance from the free edge and on the same material, shallower and therefore smaller indents are less affected than deeper indents.

As remarked in the explanation of Figure 2-10.b, the stress around the indenter is significant up to an average distance of 2 to 3 times the contact radius from the indentation location.

This corresponds approximately to a $A^{\frac{1}{2}}/d$ equal to 1.2. For this value of the parameter, the edge effect might lower the measured elastic modulus up to 35%.

A lower Poisson ratio of the material understandably decreases the edge effect. This is because a lower Poisson ratio means a smaller lateral effect for a normal load (this will be discussed further in section 2.7.5).

2.4.2 Sink-in and Pile-up

Sink-in and Pile-up occur when there is a difference between the penetration depth and contact depth of the indenter tip. These artifacts introduced error in the estimate of the contact area calculated from the penetration depth.

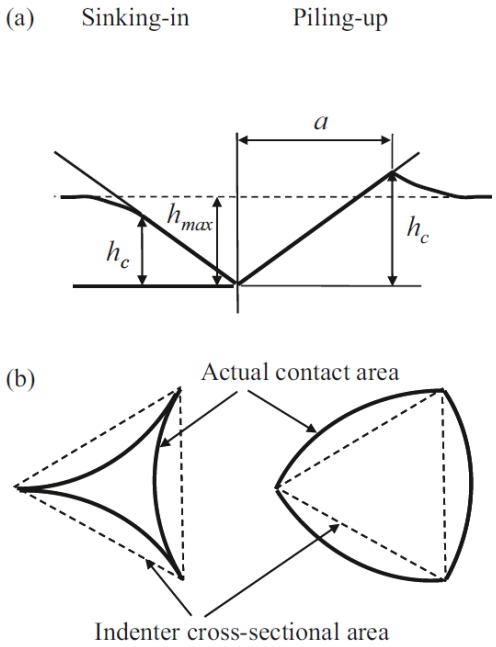

Figure 2-12. Sinking-in and Piling-up (Fischer-Cripps (2002), [46]*)*

2.4.3 Sample preparation and storage

Nanoindentation probes the outer layer of a material, yet the measured properties are attributed to its bulk. So, any part of preparation (e.g., polishing) or storage of the sample that affects the outer layer of the material affects the nanoindentation characterization of that material.

Effect of Roughness (determined by polishing)

For the Berkovich indenter, the nanoindentation results are less sensitive to the roughness of the sample surface than for indenter tips that are not sharp [46]. The surface roughness, however, can affect the indentation at low depths anyway. A parameter α is defined to quantify this effect [46].

$$\alpha = \frac{\sigma_s R}{a_0^2} \tag{2.16}$$

where σ_s is the asperity height, R is the nanoindenter tip radius and a_0 is the contact radius for a smooth surface (shown in Figure 2-10.a).

It is stated that roughness is not important if $\alpha < 0.05$ [46], which for a given nanoindenter tip and depth of indentation means a maximum allowable asperity height.

$$\sigma_s < \frac{0.05 a_0^2}{R} \tag{2.17}$$

As the asperity height is determined by the degree of polishing, this equation is useful to define the adequate protocol for polishing the sample surface for nanoindentation tests.

Dehydration

For materials whose microstructure and consequently the mechanical properties are sensitive to humidity, such as cementitious material or bone, attention must be paid in the preparation of the sample tested. The effect of dehydration was studied by Guidoni et al. (2010) [60] on bone, a biomaterial close to dentin. The researchers observed a 40% increase in the measured modulus of bone by dehydration. It is hypothesized that this considerable increase is due to the interpeptide bonds that form between collagen molecules only in the absence of water. This hypothesis is supported by the shrinkage of bone due to dehydration. These results, although obtained for bone, are due to the collagen fibrils of the bone tissue, which also exist in dentin. Therefore, the dehydration has a similar effect on the properties of dentin.

2.4.4 Time-dependent phenomena

Time-dependent phenomena are known to affect the nanoindentation results although the CSM method of nanoindentation is less affected by these phenomena. Two of them are discussed below.

Thermal drift

Thermal drift happens due to thermal dissipation in the plastic zone of the indented material below the tip which increases locally the temperature. This can lead to significant thermal expansion which causes an artifactual depth rate at a constant load. This depth rate or strain rate is indistinguishable from the effect of creep when both are present at the same time (Fischer-Cripps, (2002) [46]). Fortunately, this can be corrected (at least mitigated) by holding the load at a low constant value (only a tenth of the maximum load to avoid creep) to single out the depth rate due to the thermal drift. Another way to limit this artifact is to use CSM for measuring the elastic modulus (Li & Bhushan, (2002) [53]).

Viscoelasticity

Dentin shows viscoelastic behavior [10]. In a nanoindentation test on a viscoelastic or viscoplastic material time-dependent deformations are observed. Among the two types of loading paths to characterize the elastic modulus, CSM measurements are less sensitive to viscosity effects because the high frequency (nearly 45 Hz) and the small magnitude of the loading-unloading cycles limit the creep behavior of the material [53]. But in the unloading method, if the material exhibits high creep, negative values may be recorded for contact stiffness [46]. To prevent this artifact, the load is held at its maximum value for some time. This holding period ‘exhausts’ the material's creep potential before the measurement of the modulus, resulting in fewer errors in the modulus.

2.5 "Statistical grid indentation technique"

The theory of nanoindentation was first established for homogeneous materials. However, many of the most interesting materials tested by nanoindentation (including dentin), are heterogeneous. On heterogeneous materials, nanoindentation tests can lead to either a modulus describing the material as an effectively homogenized material, or distinct moduli that can be attributed to its constituents (PTD and ITD for dentin). This variety in results is due to the parameters of nanoindentation tests.

Nanoindentation tests are planned in the form of grids (e.g., in Figure 2-13). The parameters of these grids are number of indents (N), spacing between indents (L), and their penetration depth (h), which for heterogeneous materials are determined using the rules of "statistical grid indentation technique".

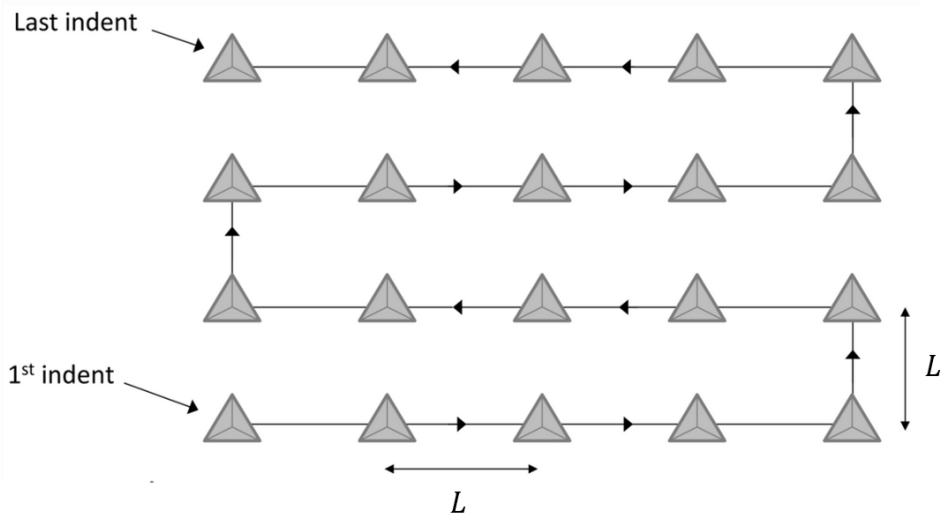

Figure 2-13. A schematic grid of nanoindentations with a spacing of 'L' between the indents. The grid is traversed in a Snake-shape order, as done by MTS/Agilent Nano Indenter (TriDiMap documentation [61]*)*

The "statistical grid indentation technique" has been developed to study the mechanical properties of materials like the CSH phase in cements that are naturally in the microscale and cannot be tested as a separate material (Constantinides et al. (2006) [43]). In the following, the recommendations of this technique for the nanoindentation parameters are explained.

2.5.1 Depth of indents

Figure 2-14.a demonstrates that the indentation depth, which determines the size of the contact area, and also the volume of the material loaded, characterizes the effectively homogenized composite or the components of the composite.

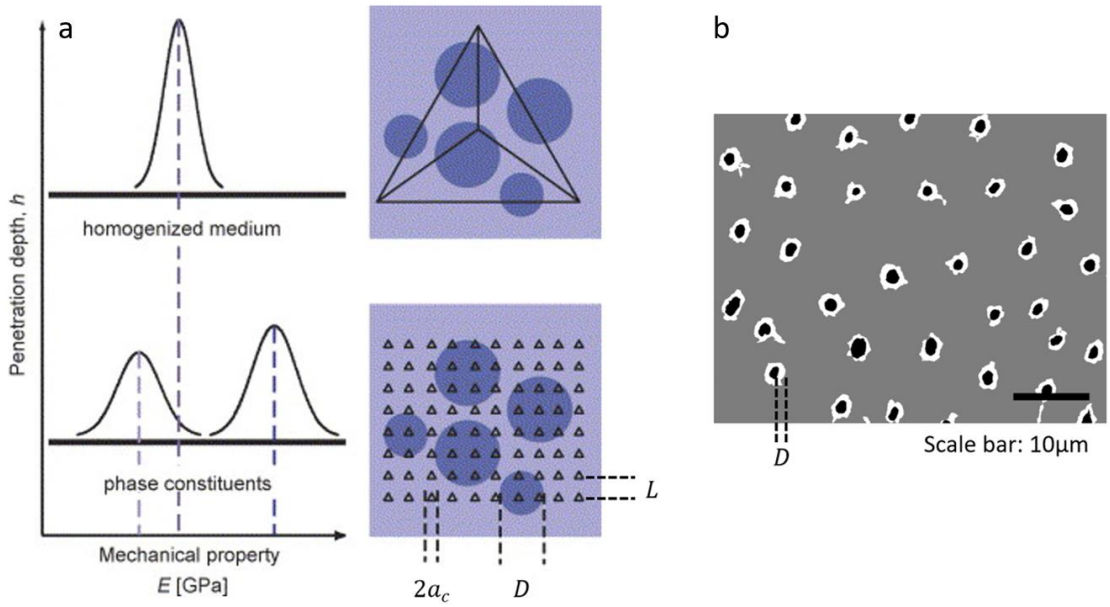

Figure 2-14.a) Impact of the penetration depth on the measured values by nanoindentation (Constantinides et al. (2006)[43]*) b) an example of the tubular microstructure of dentin is shown to give a perspective of using this method on dentin*

In what follows, h_{hom} and h_{con} represent respectively the depths needed to characterize the dentin in a homogenized way as a composite or the depth for characterizing the constituents. For measuring homogenized values, the indentation must be deeper than a certain limit [43].

$$h_{hom} > 2D \cot\theta \tag{2.18}$$

where θ is the semi-angle of the indenter tip, and D is the dimension of the microstructure feature. Therefore, the equation for a Berkovich tip ($\theta = 65.27°$) can be written as:

$$h_{hom} > 0.92\ D \tag{2.19}$$

For characterizing the phases, a rule of thumb known as 1/10-rule of Bückle exists [61]. It states that the indentation depth should be less than 1/10 of the characteristic size of the microstructure D.

$$h_{con} < \frac{D}{10} \tag{2.20}$$

2.5.2 Spacing of indents (Indentation step)

Each indent affects a zone of the material plastically within a radius R_p. Hence, to characterize the material correctly, the next indent should be done out of this plastically and permanently affected zone. In other words, the indentation step (L) should be larger than twice the plastic radius (R_p).

$$L > 2R_p \tag{2.21}$$

which for a Berkovich indenter means [61]:

$$L > 10.5h \text{ to } 21h \tag{2.22}$$

Phan and Oliver (2019) [62] tested a wide range of materials, including brittle and ductile, to conclude that a spacing of 10 times the indentation depth is enough to prevent adjacent Berkovich indentation tests from affecting the results of each other.

2.5.3 Number of indents

To capture the properties of the constituents with enough data from each of them, the number of indents (N) should be relatively high [43]:

$$L_{con}\sqrt{N} \gg D \tag{2.23}$$

Nanoindentation tests are time-consuming. Therefore, the aim is usually to satisfy this condition with indents as few as possible (not more than a few hundreds of tests in one grid).

With this background on the nanoindentation of heterogeneous materials, the nanoindentation studies on the properties of dentin are reviewed.

2.6 Review of the mechanical properties of dentin and its constituents

In nanoindentation tests, sample preparation is important. This is because of the effect of roughness on the nanoindentation results (which was explained in section 2.4.3 and should be minimized). All the studies reviewed in this section have polished the sample up to 1 µm or finer.

2.6.1 Mechanical properties of the constituents

The results of some of the literature concerning the local properties of the dentin constituents (ITD and PTD) are summarized below, data being reported in Table 2-2.

Kinney et al. (1996) [63] used AFM indentation because they could keep the sample hydrated this way. They measured the hardness (H) of both constituents of dentin (2.3±0.3 GPa for PTD and 0.5±0.1 GPa for ITD). Although they did not measure the elastic modulus in this paper, the stiffness imaging using “Force Modulation Mode” of AFM (Figure 2-15.a) showed that in the investigated zone, the stiffness of PTD is homogeneous but not the stiffness of ITD, which varies spatially (up to 40%).

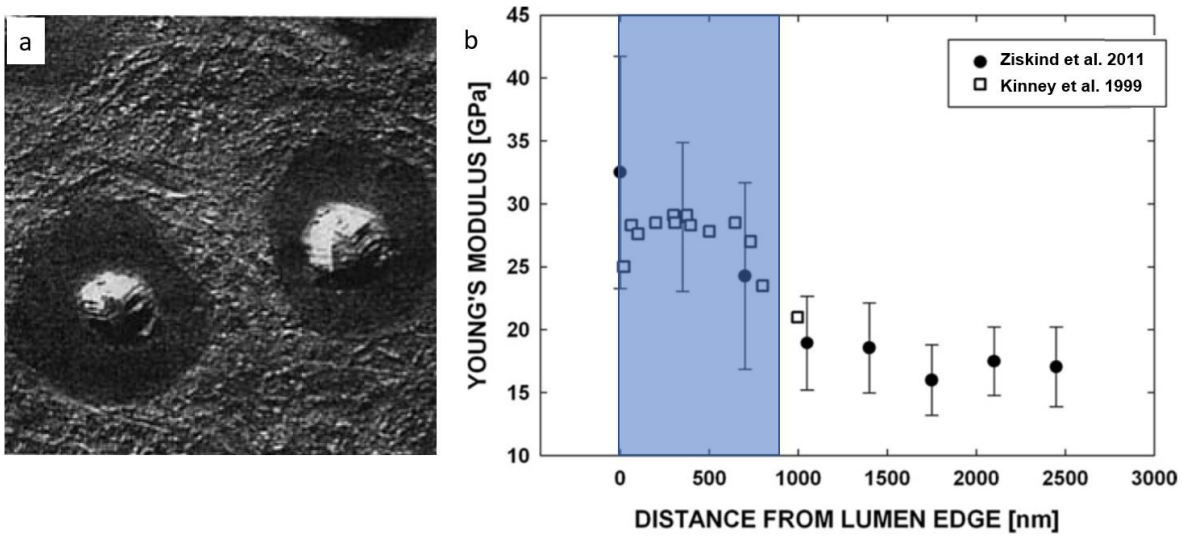

Figure 2-15.a) Stiffness image of dentin using AFM (Kinney 1996 [63]*): softer areas (ITD) are brighter and stiffer areas (PTD) are darker, (the grey levels inside tubule lumens are artifactual, because they do not have a Young's modulus), b. Comparison between the maps of Young's modulus of dentin as a function of the distance from the lumen edge in two studies. The zone associated with PTD is highlighted in blue.*

In another paper, Kinney et al. (1996) [64] indented the dentin surface by an AFM and measured the moduli by analysing the force-displacement curves. Their results are presented in Figure 2-15.b. They claimed that the stiffness of PTD does not vary from the DEJ to the pulp. This, together with the previous reviewed papers implies that PTD is homogeneous both across each tubule and throughout dentin. This homogeneity of stiffness is consistent with the simpler nanostructure and production process of PTD compared with the ITD (e.g., various ways that the collagen fibrils of ITD are positioned with respect to each other and the variety in their degree of intra- and extrafibrillar mineralization). The researchers also questioned the sufficiency of the resolution of indentation techniques for characterizing the constituents of dentin, because a nanoindentation of only 50 nm depth (a usual minimum of nanoindentation depth) samples a zone of approximately half a micrometer in extent, which often goes through both constituents. Therefore, the moduli given for PTD are probably underestimated (because of being adjacent to ITD and pores).

In their nanoindentation study on dentin, Habelitz et al. (2002) [65] studied the effect of demineralization, which happens to dentin samples because of storage in water or a solution that does not have Calcium and Phosphate ions. As shown in Figure 2-16, it causes a considerable decrease of up to 80% in the modulus in a few days. Even if the sample is stored in a suitable solution, the sample preparation steps like cutting and polishing may partially demineralize the sample.

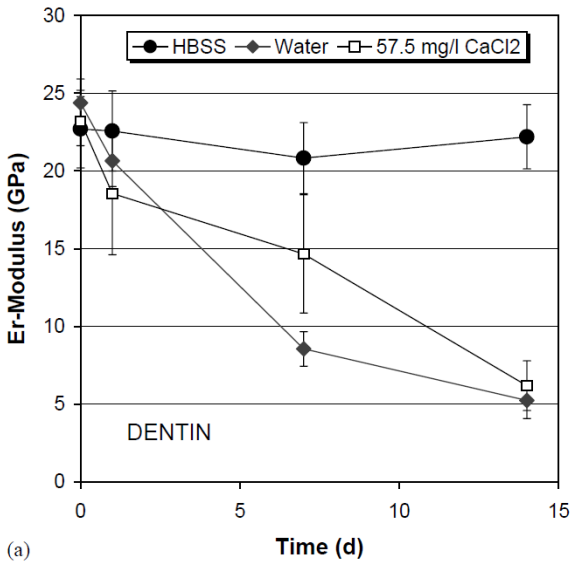

Figure 2-16. The reduction in Young's modulus of dentin due to demineralization (Habelitz et al., (2002) [65]*)*

Ziskind et al. (2011) [66] disagreed with the idea that the elastic modulus of PTD is locally homogeneous. They claimed that the PTD is stiffer near the edge of the lumen (≈40–42 GPa) and gets softer by approaching the ITD (down to ≈17 GPa). They compared their results with those by Kinney et al., (1999) [67] in Figure 2-15.b. In addition, Cohen et al. (2008) [68] previously concluded by means of FEM simulations that the varying stiffness across the PTD cannot be justified by the compliance caused by the adjacent ITD.

Anisotropy of dentin or its constituents has also been studied. Using AFM, Kinney et al., (1999) [67] observed a very slight anisotropy in ITD with a higher modulus parallel with tubules (20.3 vs 20.1 GPa). Ziskind et al. (2011) [66] used nanoindentation and observed an anisotropy, which is a little bit more pronounced. But they found the same orientation as the one reported by Kinney et al. (1999) [67] (≈22 vs 18 GPa). One particularity about these studies is that nanoindentation analysis assumes an elastic isotropic material. However, it is assumed that nanoindentations in various orientations can give an idea of the anisotropy of the tested material. The anisotropy of dentin is discussed in Chapter 3.

Table 2-2. Elastic modulus of the constituents of dentin. In the studies that have considered the viscoelastic behavior of dentin the storage modulus of dentin (E') is given.

	Indenter tip	PTD (GPa)	ITD (GPa)	Depth or load of indentation	Hydration state
Wang (2016) [24] (Nanoindentation)	Berkovich	26.7 (3.4)	16.2 (5.5)	200 nm depth	Dry
Ryou (2012) [69] (Nanoindentation and dynamic mechanical analysis (DMA))	Berkovich	E'=28.6-34.2	E'=18.1-21.6	-	Hydrated

Ziskind 2011 [66] (Nanoindentation)	Berkovich	Graded from 40-42 GPa at the lumen edge down to ~20 GPa at the interface with the ITD	~22 GPa parallel with the tubules and 18 GPa perpendicular to them	30-70 nm depth corresponding to 200-300 µN load	Dry
Balooch et al. (2004) [70] (AFM)	Cube-corner	E'=40-50	E'=17-23	2.5 µN load	Dry
Habelitz et al. (2002) [65] (Nanoindentation)	-	-	23.7±2.6	400 nm depth	Hydrated
Kinney et al. (1999) [67] (AFM indentation)	-	28.6±0.5	20.1±1.1 (perpendicular to the tubules) 20.3±0.9 (parallel with the tubules)	400 to 700 µN load	Fully hydrated
Kinney et al. (1996) [64] (Nanoindentation)	Berkovich	29.8±8.9	17.7±0.3 (near the pulp) 21.1±1.3 (near the DEJ)	50 nm depth	Dry

By reviewing the literature on the nanoindentation results on the constituents of dentin (PTD and ITD), we noticed the interest in characterizing the constituents as a function of location in dentin.

2.6.2 Homogenized mechanical properties of the dentinal composite

Mapping the local (homogenized) modulus of dentin has been of interest to researchers to better understand the tooth's mechanical response in mastication. Studies by the researchers who measure the homogenized elastic modulus for dentin are summarized in this section. In these studies (reviewed in chronological order), nanoindentation tests are deep (usually 1000 nm or more).

Van Meerbeek et al. (1993) [49] did nanoindentation tests on restored tooth. Even though their main goal was to characterize the resin-dentin bonding area, they also reported a homogenized value of 19.3±2.2 GPa for the coronal dentin itself. They did not further specify the location of their measurement in dentin.

Meredith et al. (1996) [71] derived Young's modulus from Knoop microhardness and reported relatively small values (8.7-11.2 GPa). This could be due to the storage of dentin samples in deionized water before the experiment, which is known to result in a decrease in the stiffness [10]. One interesting aspect of their paper is that they investigated the homogenized modulus of dentin for various distances from the DEJ. They observed that the dentin becomes stiffer by approaching the pulp.

Wang and Weiner (1998) [72] plotted the microhardness of dentin for the whole path from pulp to the enamel. They observed a sharp minimum in hardness values at the DEJ in the mm-scale (Figure 2-17.a). Another hardness mapping by Marshall et al. (2000) [65] showed a relatively smooth transition from the enamel to dentin in the microscale (Figure 2-17.b).

For comparison between Figure 2-17.a and Figure 2-17.b, notice that there is an approximate relation between Vickers hardness (VH) and the hardness (H):

$$H(GPa) \approx 0.0098VH\left(\frac{kgf}{mm^2}\right) \tag{2.24}$$

Therefore, the equivalent hardness in Figure 2-17.a is always lower than 1 GPa and reaches values as low as about 0.4 GPa at the DEJ. However, in the study by Marshall et al. (2000) [73] (Figure 2-17.b), the hardness of dentin at the DEJ is close to 1 GPa.

Interface with another material might have a similar effect to a free edge. Based on this, the disagreement between the two studies on the mechanical properties at the DEJ (Figure 2-17) can be explained: the artifact due to the interface with the enamel is more pronounced in the deeper microindentation tests by Wang & Weiner, (1998) [72] as it is the case for the edge effect, which is more severe the deeper the indentation is. Therefore, the deeper indentations in Figure 2-17.a are more affected and show a significant minimum at the DEJ interface.

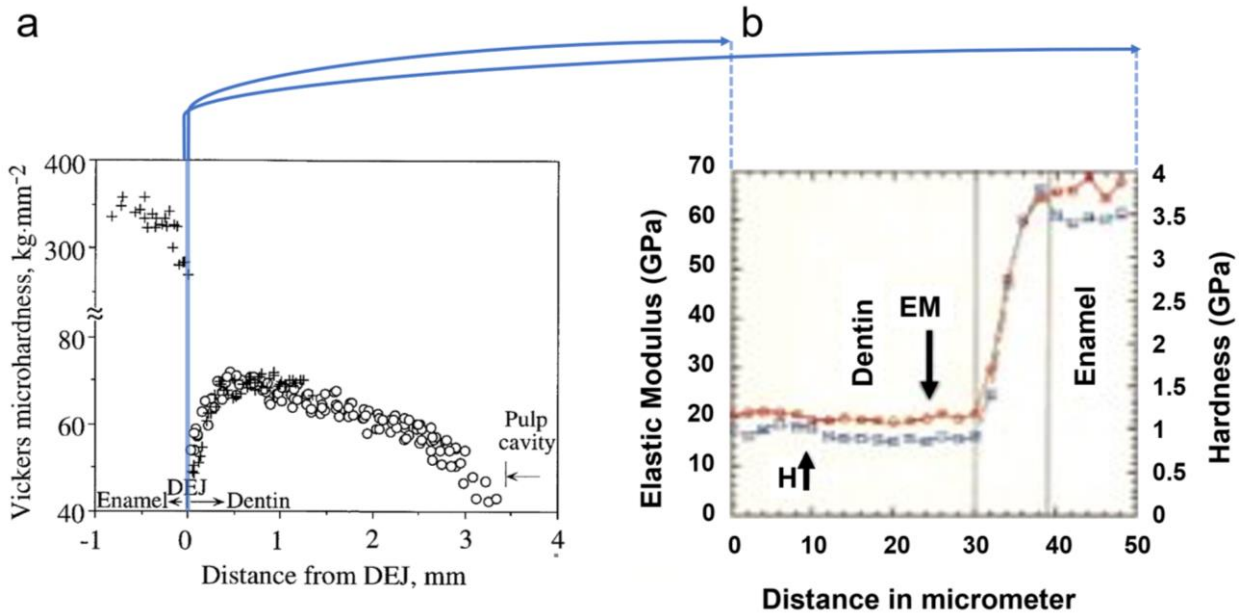

Figure 2-17. Comparison between the map of mechanical properties mapped by Wang and Weiner (1998) [72] *('a') and Marshall et al. (2000)* [73] *('b').*

One study that especially considered the effect of dehydration and also demineralization on dentin, was the one by Fong et al. (2000) [74] who kept the dentin samples moist in a solution (Phosphate buffer saline) that did not demineralize them. The authors minimized the exposure of the samples to air to the 45 minutes of nanoindentation test. Even during the test, the air had a humidity of 80-100%. By preventing both demineralization, which

softens the dentin and dehydration, which hardens it, this study has reported the highest homogenized modulus for dentin in Table 3-3. This probably means that the other studies (reporting smaller moduli) are generally more affected by demineralization than by dehydration.

Angker et al. (2003) [75] showed that Young's modulus of dentin is highest in the middle part of dentin and decreases slightly near the DEJ and considerably near the pulp. This difference in the decreases near pulp and enamel is in contrast with the study by Wang and Weiner (1998) [72], who observed rather equal decreases at those locations (Figure 2-17.a).

Wang et al. (2018) [76] too mapped the elastic modulus of a tooth. Their main interest was the DEJ, therefore they did not indent throughout the dentin. As visible in Figure 2-17.b, they observed a smooth transition between the enamel and dentin (like Marshall et al. (2000) [73]).

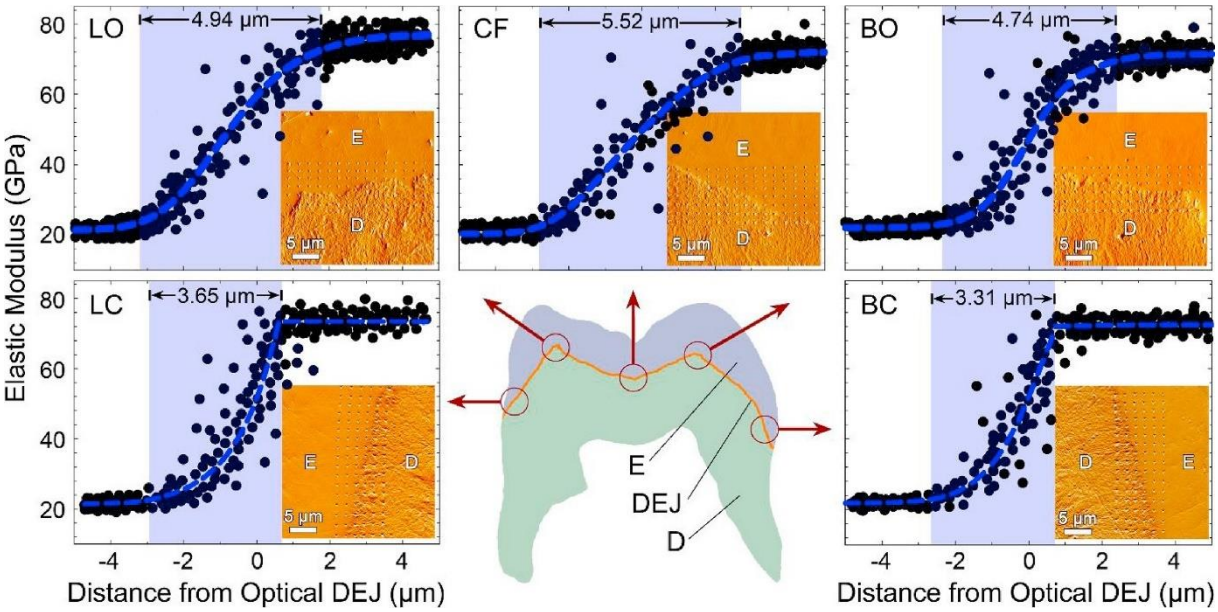

Figure 2-18. Elastic modulus maps of tooth across DEJ at various locations of a tooth. Wang et al. (2018) [76]

The above-mentioned studies are summarized in Table 2-3.

Table 2-3. The homogenized Young's modulus of dentin in the literature

	Indenter tip	Homogenized Young's modulus (GPa)	Depth of indentation (nm)	Hydration state
Angker et al. (2003) [75]	Berkovich	Superficial: 16.91±3.85 Middle: 17.06±3.09 Deep: 11.59±3.95	1312.5±292.2 1424.9±321.3 1931.1±534.6	Hydrated
Marshall et al. (2000) [73]	-	19.65 [18.61, 20.69]	-	Hydrated
Fong et al. (2000)	Berkovich	24.8±1.4	~100	Kept hydrated

[74]		(averaged)		up to the testing
Xu et al. (1998) [77]	-	20±2	-	Kept hydrated up to the testing
Meredith et al. (1996) [71]	-	8.7±11.2	-	Hydrated
Van Meerbeek et al. (1993) [49]	Triangular diamond tip	19.3	Up to 1000	Air-dried

2.6.3 Homogenized mechanical properties of the dentinal composite by other methods

In this subsection, a few other studies are summarized that have characterized the dentin as a homogenized material. Two groups of studies are reviewed:

1) Resonant Ultrasound Spectroscopy method: This method, despite its relatively precision, does not give results that represent the normal elastic behavior of dentin in strain rates of everyday functioning. This is due to the method's high strain rate, which does not activate the creep. This is shown in the high range of moduli that are summarized in Table 2-4 and use the RUS method (23-26.5 GPa).
2) Compression and tension tests: Results from three compression tests and three tension tests are also reviewed. The range of homogenized elastic modulus from these studies (approximately 10-18 GPa) is close to the range given by nanoindentation results (approximately 9-20 GPa, as shown in Table 2-4).

Table 2-4. Characterization of dentin as a homogenized composite by various mechanical methods

Method and Researchers	Homogenized Young's modulus (GPa)	Hydration state	Dimensions of the sample	Conclusion
RUS, Wang (2014) [24]	$E_l = 23.01 \pm 1.69$ GPa $E_t = 23.32 \pm 1.83$ GPa	Hydrated	~3x1x1 μm^3	Elastic properties are close to isotropic
RUS, Kinney et al. (2005) [78]	$E \approx 26.5$ GPa $G \approx 10$ GPa	Rehydrated prior to the test	~1.7x1.1x0.8 μm^3	No significant difference between the elastic and shear moduli of transparent and normal dentin
RUS, Kinney et al. (2004) [79]	$E_l = 23.2$ GPa $E_t = 25$ GPa $E_{dried} = 28.1$ GPa $\nu_{21} = \nu_{31} = 0.29$	Rehydrated prior to the test	~1.7×1.1×0.8 μm^3	Small transverse anisotropy that disappears by drying the sample
Compression, Wang (2014) [24]	16.66 (5.06) GPa and 17.78 (5.04) GPa (for load and unload)	Hydrated	~3x1x1 μm^3	The humidity has no clear influence on the modulus.

Compression, Jantarat et al. (2002) [80]	13.3±1.3 GPa	Hydrated	Hollow cylinders : Outer diameter: 3.5 µm Inner diameter: 1.5 µm Length: 6-10 µm	
Compression, Palamara et al. (2000) [81]	$E_l = 10.7 \pm 2.4$ GPa $E_t = 11.9 \pm 3$ GPa $E_{45} = 7.7 \pm 0.7$ GPa	Rehydrated	1.5x1.0x1.0 μm^3	There was no significant difference Between [Young's modulus] 0° and 90° but there was between 0° and 45° and between 45° and 90°
Tension, Sano et al. (1994) [82]	13.7 (3.4) GPa	Hydrated	Cross-section area 0.5x0.55 μm^2	Slightly higher Young's modulus for Coronal dentin.
Tension, Currey and Brear, (1990) [83]	9.2 GPa	Hydrated	Not mentioned	Linear relationship between hardness and Young's modulus
Tension, Lehman (1967) [84]	11.0 GPa Improvement by Kinney et al. (2003): 16.9 GPa	Hydrated	Hollow cylinders : Outer diameter: 3.2 µm Inner diameter: 1.9 µm Length: 4.4 µm	

2.6.4 Lessons learned from the nanoindentation review on dentin

Nanoindentation allows to identify the local elastic properties of the dentin constituents as well as the homogenized elastic modulus of the dentin. To have an idea of the size of nanoindentation tests in the reviewed studies, their approximate indentation areas are visualized on a treated image of dentin in Figure 2-19.

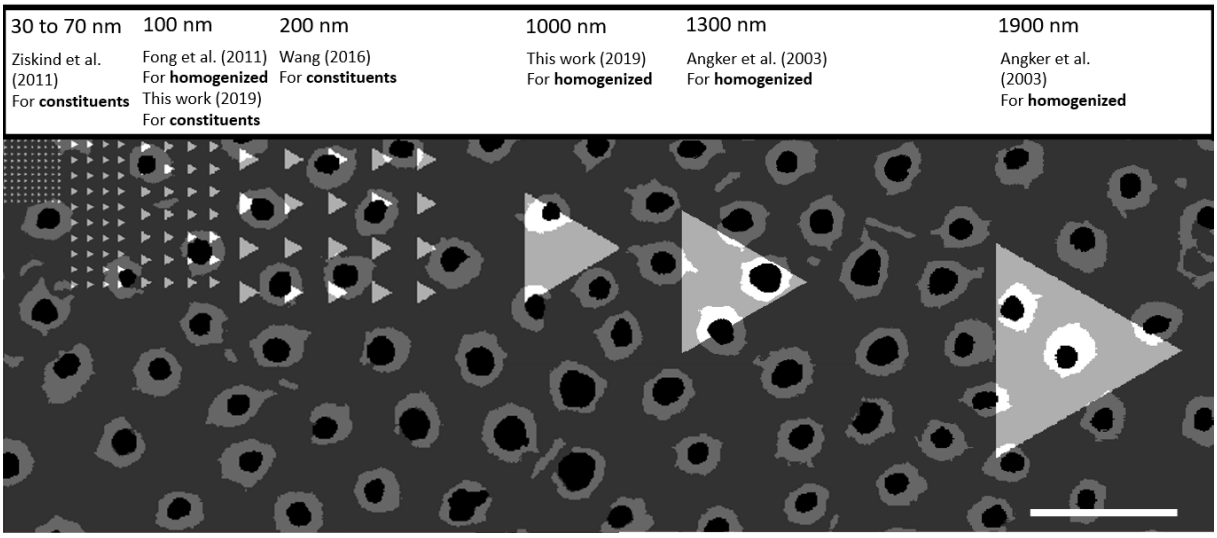

Figure 2-19. Schematic visualization of the indent size in studies that have used Berkovich tip on the microstructure of dentin (SEM image at normalized distance 0.6 from the DEJ) (Scale bar: 10 µm)

Nanoindentation tests from available studies indicate a Young's modulus ranging from 20 to 50 GPa for the PTD, and 16 to 24 GPa for the ITD. The values reported for the homogenized dentin are close to the range reported for the ITD.

Reviewing these studies has outlined some points that help to better investigate the properties of dentin in our study.

1) Choice of the indenter tip

Most of the previous studies have used a Berkovich tip. The use of Berkovich tip in this thesis permits the comparison of the results with those of the literature. In addition, the sharpness of Berkovich tip makes it more suitable for shallow indentations. This is especially important because shallow nanoindentations are needed to study the constituents of dentin.

Sharpening is however required for the indenter tip after many tests due to wear. In this case, Bekovich is a better choice than 4-sided pyramid indenter tips. This is because the three sides of the Berkovich tip necessarily intersect at one point. But the four sides of a Knoop or Vickers tip are more likely to intersect in a line than in a point, which makes their sharpening challenging. Another reason for choosing a Berkovich tip to characterize the constituents of a composite material is that it more probably affects only one of the constituents. By studying thin films on substrates, Sakharova et al. (2009) showed that among three indenter tips (Vickers, Berkovich, and conical), Berkovich shows the least effect of the substrate on the plastic deformation of the specimen.

2) Demineralization effect

The significant effect of demineralization on the mechanical behavior highlights the necessity to keep the dentin sample in a suitable solution before testing. The sample in this thesis was kept in Ringer's solution, which contains Calcium ions and has been used for storing calcified tissues in previous studies (e.g. by Burstein et al. (1972) [85]).

3) Loading protocol

Based on the points learned from the previous studies, The loading protocol of nanoindentation tests is designed in a way to minimize the effect of time-dependent phenomena.

To plan shallow nanoindentations for characterizing the constituents the *Statistical Grid Indentation Technique* was used in this thesis. The grid of nanoindentation tests adopted is detailled in section 2.7.3.

4) Local variation of properties in dentin

The mechanical properties (and the morphology) of the constituents of dentin vary locally in dentin. Even if some researchers do not agree with local variation in the mechanical properties of PTD, the surveyed papers agree that the properties of ITD do vary throughout dentin. Consequently, multiple locations inside dentin should be chosen to take account of this variation.

2.7 Characterization of dentin by nanoindentation

2.7.1 Nanoindentation instrument

The MTS Nano Indenter XP available at the lab MSSMat (Figure 2-20) is equipped with a Berkovich tip. It has a force sensor resolution of 10 nN and a depth sensor resolution of 0.01 nm. With such high resolutions, it provides both CSM and unloading measurements of Young's modulus and hardness of the specimen. A lateral motion stage allows the sample to move between the microscope and the indenter, so that the nanoindentation location can be visualized first.

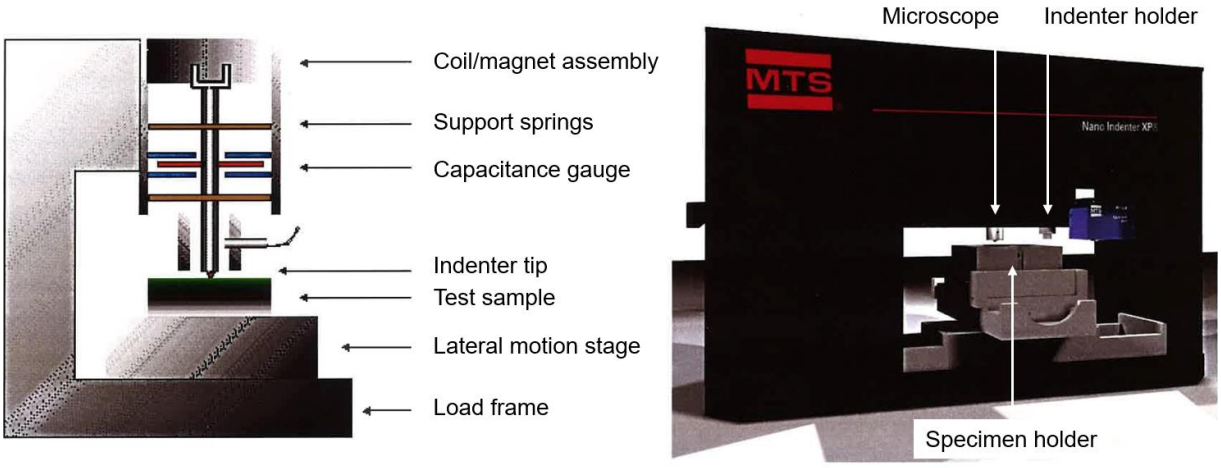

Figure 2-20. Schema and 3D reconstruction of the nano indenter (Customer care kit of the Nano Indenter)

To reduce the acoustic disturbances, the Nano Indenter is positioned inside an isolation cabinet (Figure 2-21) and for minimizing the transmitted mechanical vibrations, it is mounted on an anti-vibration table.

Figure 2-21. The isolation cabinet of the Nano Indenter XP

2.7.2 Sample preparation

The same dentin sample described in chapter 1, which was polished with abrasive papers and diamond suspensions up to 1 µm is used for nanoindentation. The sample was dehydrated by bathes of alcohol for SEM imaging and then rehydrated in Ringer's solution before the nanoindentation testing (Figure 2-22). It was kept in Ringer's solution, which contains Calcium ions and has been used for storing calcified tissues in previous studies (e.g. by Burstein et al. (1972) [85]).

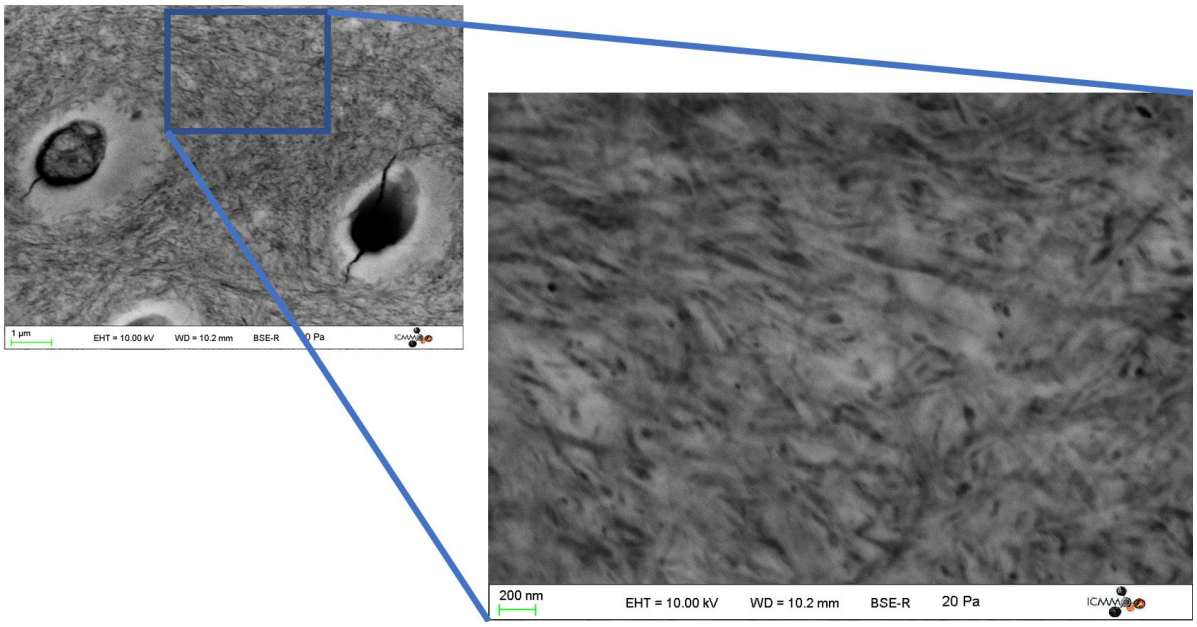

Figure 2-22. The surface of the dentin. The fibrillar pattern visible in the image represents the collagen fibrils. (Source: author)

2.7.3 Recommendation of parameters using "statistical grid indentation technique"

Chen and Vlassak (2001) [86] mentioned that such characterization of phases by statistical grid indentation technique is valid only if the ratio of the elastic moduli of the phases is between 0.2 and 5. Otherwise the indentations on each phase are affected by the adjacent phases. Even though this assumption is established by studying a specific morphology of microstructure (thin films on substrates), this rule is assumed to be a good first guess for other microstructure morphologies as well.

Fortunately, the elastic modulus ratio between the ITD and PTD satisfies this condition. Therefore, this technique was used to recommend the nanoindentation parameters.

Depth of indentations

For a 0.5 µm average value of the peritubular cuff thickness taken as the microstructure size D, equations 2.19 and 2.20 lead to respectively:

$$h_{hom} > 460\ nm \tag{2.25}$$

$$h_{con} < 50\ nm \tag{2.26}$$

50 nm is a shallow depth for nanoindentation. Hence, the effect of roughness of the sample should be verified before performing nanoindentations with such depth.

Even though the roughness of this sample is not measured, it can be estimated to be no more than the radius of collagen fibrils (≈ 50 nm according to Bertassoni et al. 2012) because collagen fibrils are visible on the polished surface of the dentin sample (Figure 2-22).

The minimum depth of indentation can be determined from equation 2.17. This equation should be adjusted for the Berkovich tip. The radius of the Berkovich tip (R) is 50-150 nm[58] and is assumed to be 100 nm for the Berkovich tip used in this thesis. And a_0 (the contact radius for a smooth surface) for a Berkovich indenter is equal to 3.5 times the penetration depth. These result in:

$$\sigma_s < \frac{0.05(12.25h^2)}{100} \tag{2.27}$$

Consequently, nanoindentations of 50 nm depth would allow asperity heights of only 15.3 nm. Such a low asperity height cannot be assumed for this dentin sample. However, by increasing the indentation depth to 100 nm, the maximum allowable asperity height will be ≈ 61 nm (comparable to the roughness estimation of the sample in this thesis).

Therefore a 100 nm-depth is chosen for shallow nanoindentations on dentin.

$$h_{con} = 100\ \text{nm} \tag{2.28}$$

The depth for deep nanoindentations can be concluded with less complication from the equation 2.25:

$$h_{hom} = 1000\ \text{nm} \tag{2.29}$$

Spacing

An average between the limits given in equation 2.22 is chosen in this thesis:

$$L_{con} = 15 \times h_{con} = 1.5\ \mu m \tag{2.30}$$

$$L_{hom} = 14 \times h_{hom} = 14\ \mu m \tag{2.31}$$

Number

For each of the three locations in dentin, $N = 720$ is chosen as the number of the shallow nanoindentation tests, which by considering the above-given 1.5 µm as the spacing and 0.5 µm as the feature size satisfies the equation 2.23.

$$L_{con}\sqrt{N} = 1.5\sqrt{720} \gg 0.5 \tag{2.32}$$

2.7.4 Planning the shallow and deep nanoindentation grids on the dentin sample

Three shown locations in Figure 2-23 are chosen for nanoindentation tests to take account of the local variation of the properties. Section 2.5 has given recommendations for the parameters of the nanoindentation grids.

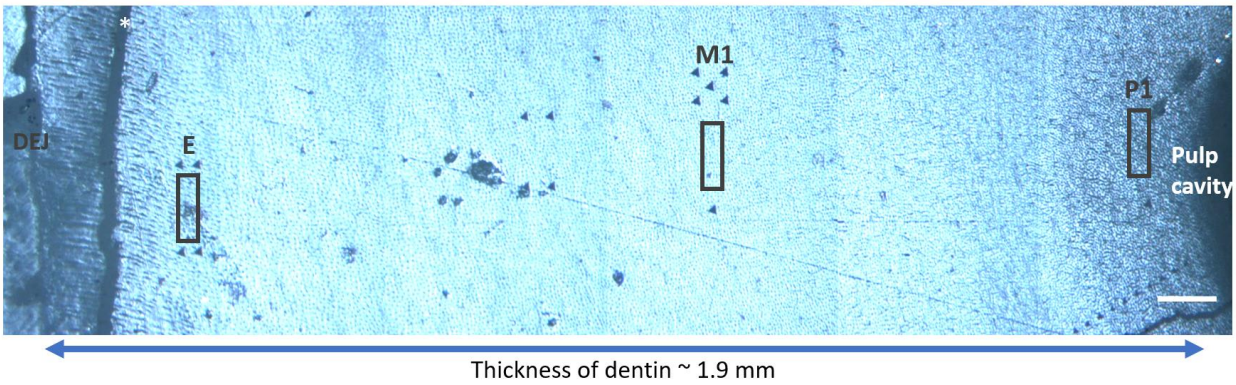

Figure 2-23. Optical microscope image of the surface of dentin. 'E', 'M1' and 'P1' show the locations of nanoindentation. The '' on the upper left corner of the image marks a crack (scale bar: 100 µm)*

2.7.5 "Virtual Nanoindentation" tool

For a material like dentin, in which the microstructure dimensions vary locally the ideal depth of indentation may vary as well. For such a case, it would be more practical to locally investigate the image of the microstructure instead of deciding based on measuring the dimensions of the microstructure, which continuously vary. For this goal, an image analysis tool was developed called 'Virtual Nanoindentation', abbreviated as the 'VN' tool. This tool will be used for *verifying* the above-given parameters that resulted from the rules of "statistical grid indentation technique".

The 'VN' tool is developed in the framework of MATLAB software. It gets as input the treated image of the material surface and a given set of parameters for a nanoindentation grid and provides answers to the following questions:

1) How heterogeneous or homogeneous the results of a grid indentation would be. If it would give one homogenized modulus for the composite or distinct values for the constituents.

2) The degree to which the map of nanoindentation results would reveal or 'image' the composite microstructure.

To illustrate the concept of the 'VN' tool consider the imaginary two-phase composite (Figure 2-24.a) and its microstructure, which is like what is usually used to explain the concept of the 'statistical grid indentation technique' ([43], [61]).

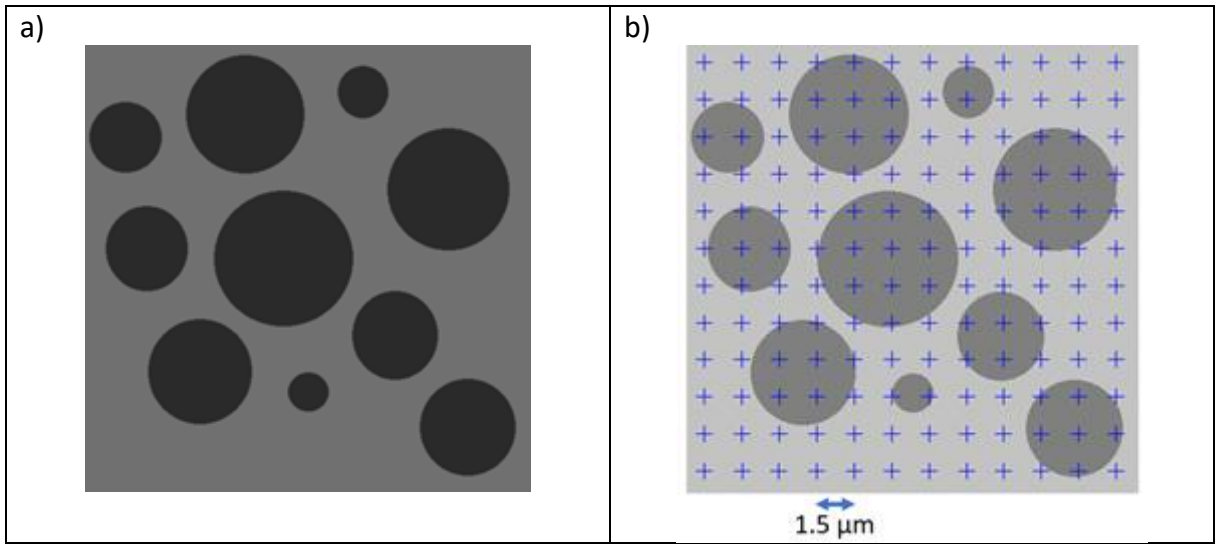

Figure 2-24.a) Microscopic image of an imaginary composite used to test the "VN" tool, (Scale bar: 2 µm) b) A schema of the microstructure with grey levels that represent first guesses for Young's moduli of the constituents. The planned grid of nanoindentations is marked on the microstructure.

One should set the grey level of each constituent equal to a first guess for its Young's modulus (Figure 2-24.b). A first guess because the 'Virtual Nanoindentation' is performed in the planning of and before the nanoindentation tests, which measure the true moduli.

By giving the supposed depth of the nanoindentation (e.g., 100 nm), the recommended spacing between indents results from equation 2.22 (e.g., 1.5 µm spacing for 100 nm depth). Next, the locations on the image with the advised spacing are chosen. The grid of nanoindentation is shown in Figure 2-24.b with the mentioned spacing.

Then, the indentation locations on the image are framed in frames that describe the contact area between the sample and the Nanoindenter tip for the prescribed indentation depth. For a Berkovich tip these areas are equilateral triangles (described in section 2.2.1 and visualized in Figure 2-25).

Here for simplification, the total depth of 100 nm is assumed to be the same as the contact depth h_c (i.e. neither sink-in nor pile-up). For the above-mentioned matrix of indents, the contact areas are demonstrated in Figure 2-25. The environment around indents is darkened for better visualization.

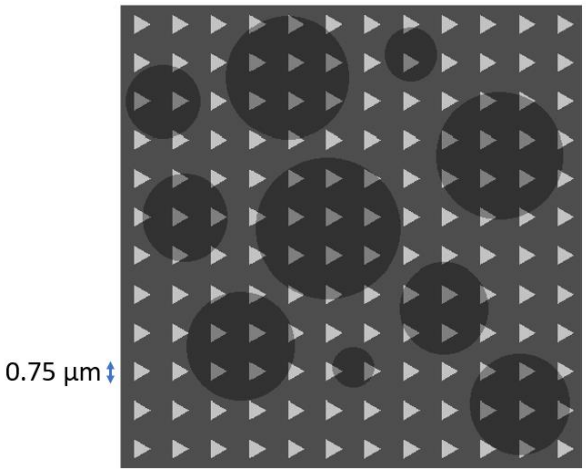

Figure 2-25. The approximate contact areas of 100 nm depth Virtual Nanoindentations

To estimate the elastic modulus for each nanoindentation test and more generally for the whole composite (shown in Figure 2-24.a), mechanical and morphological assumptions and analysis are done. It is assumed that the visible microstructure extends perpendicularly into the visible surface (Figure 2-26).

It is known that the volume stressed by the indenter extends both in the depth and in width as shown in section 2.3.2 and Figure 2-10.b, the stresses diminishing with the distance to the indenter tip. This complicates making a refined estimate of Young's modulus of the composite. Nevertheless, we assume that the Voigt rule of mixture of *n* phases applies to estimate the homogenized Young's modulus E_{Voigt} of the sample in the orientation normal to the surface:

$$E_{Voigt} = \sum_{i=1}^{n} f_i E_i = \sum_{i=1}^{n} a_i E_i \tag{2.33}$$

where f_i indicates the volume fraction of phase i, $a_i$its area fraction seen on the surface and E_i its Young's modulus. For a microstructure with parallel parts, which are not parallel with the surface of the material, $f_i = a_i$.

It should be mentioned that this simplified estimate considers perfect bonding between the phases and does not take the effects from the interface into account.

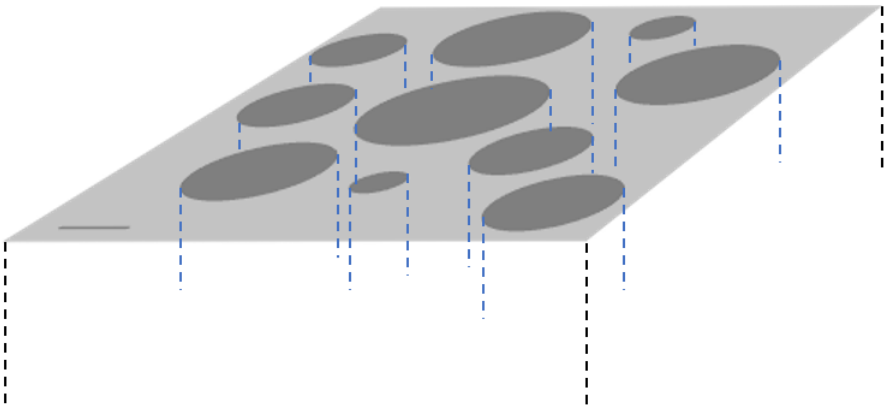

Figure 2-26. Normal extension of the microstructure into the material

Another underlying assumption of this estimate is that the affected zone is vertically located beneath the indentation contact. However, this is only correct if a vertical deformation in the surface of the specimen only causes vertical deformations in the bulk of the specimen. This is equivalent of having a Poisson's ratio of zero. For other values of Poisson ratio (which are more realistic), the affected zone will increase in size by going deeper from the surface of the specimen, and will form a spherical shape (as suggested by Figure 2-10.b).

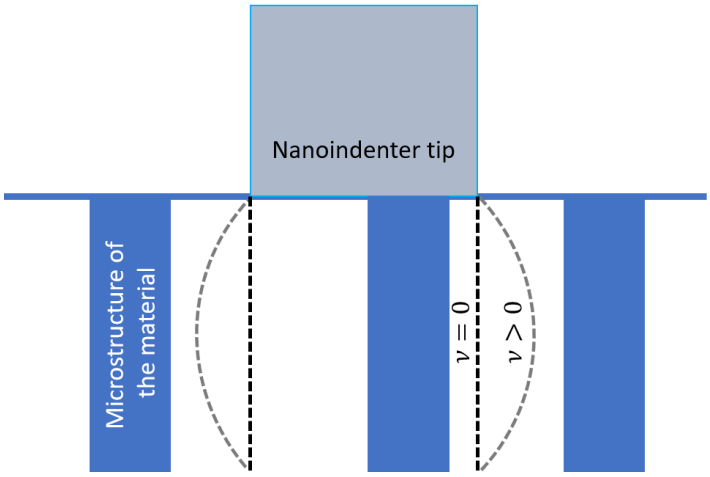

Figure 2-27. The affected zone of the material by an indentation

Equation 2.33 estimates the modulus of the composite in a specified zone. It can be used both for the whole surface of the specimen (Figure 2-28) or the contact area of one nanoindentation test. Figure 2-28 shows the projected contact area of a 1 µm deep nanoindentation on the sample.

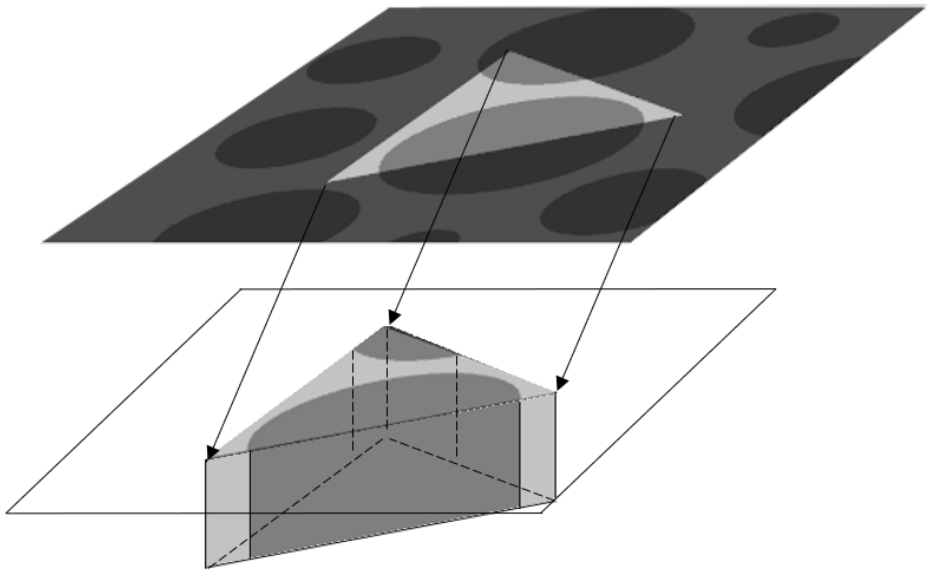

Figure 2-28. The zone of interest for a 1 µm depth indent, perpendicular to the surface

Mapping the estimated moduli

The "VN" tool averages the grey level of the pixels in each contact area, attributes the result to the indented location, and maps the estimated moduli.

The Young's modulus E_{Voigt} is then calculated by averaging the grey level (of the pixels inside each zone of interest (ZOI).

$$GL_{ZOI} = \frac{1}{N_{ZOI}} \sum_{i \in ZOI}^{N_{ZOI}} GL_i \tag{2.34}$$

where GL_i is the grey level of the pixels $i \in [1, N_{ZOi}]$ included in the ZOI, and GL_{ZOI} the average grey level of the ZOI.

If all pixels of a ZOI have the same grey level, the ZOI defines a monophase area.

$$E_{ZOI} = E_{con} \tag{2.35}$$

where E_{con} is the elastic modulus of the constituent. For the sample grid indentation being discussed, the map of the estimated moduli is shown in Figure 2-29.a.

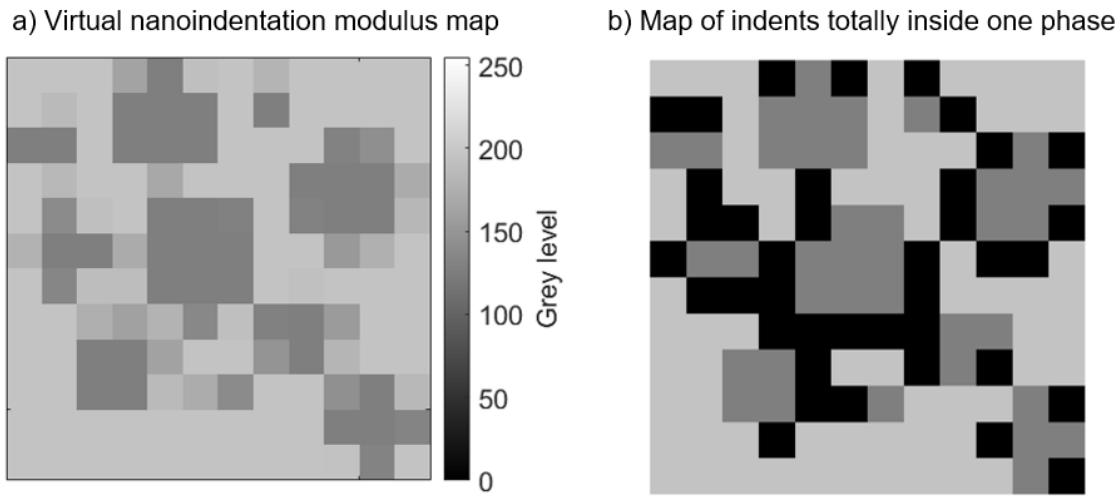

Figure 2-29.a) Map of the "Virtual Nanoindentation" results, b) The map of indentations that are totally inside one phase. The multiphase indents are shown in black.

Monophase and multiphase indents

The "monophase" and "multiphase" indents are two useful elements in analyzing the "VN" tool results. Monophase indents are those that only indent one of the phases and as result give the Young's modulus of that phase. Their distributions in the map are shown in Figure 2-29.b. "Multiphase" indents are those, where the indenter touches more than one phase. These indents are absent from the map in Figure 2-29.b.

Heterogeneity or homogeneity of the results

The degree of heterogeneity or homogeneity of the results of a grid of virtual nanoindentations is best visible on a histogram. The distribution of the grey level (equal to Young's modulus) from the above "VN" map is visualized in Figure 2-30. The Young's modulus for the whole composite (E_{hom}) (also calculated by the equation 2.34) is shown by a vertical dashed line.

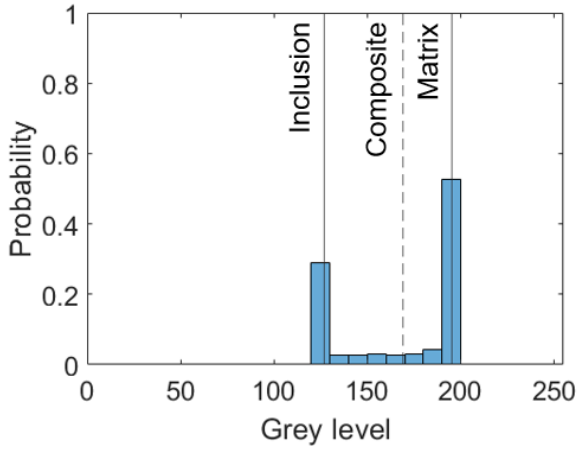

Figure 2-30. The histogram of the imaginary nanoindentation results

Investigating the effect of the depth of indentation

To visualize the effect of variation in the nanoindentation depth, 'Virtual Nanoindentation' tests were done with various depths but with the same number of pixels in the grid (25x25).

Equal numbers of indents are chosen to allow a comparison between the results for various depths of indentation. If the dimensions of the image do not allow the required number of the indents, the image is repeated periodically.

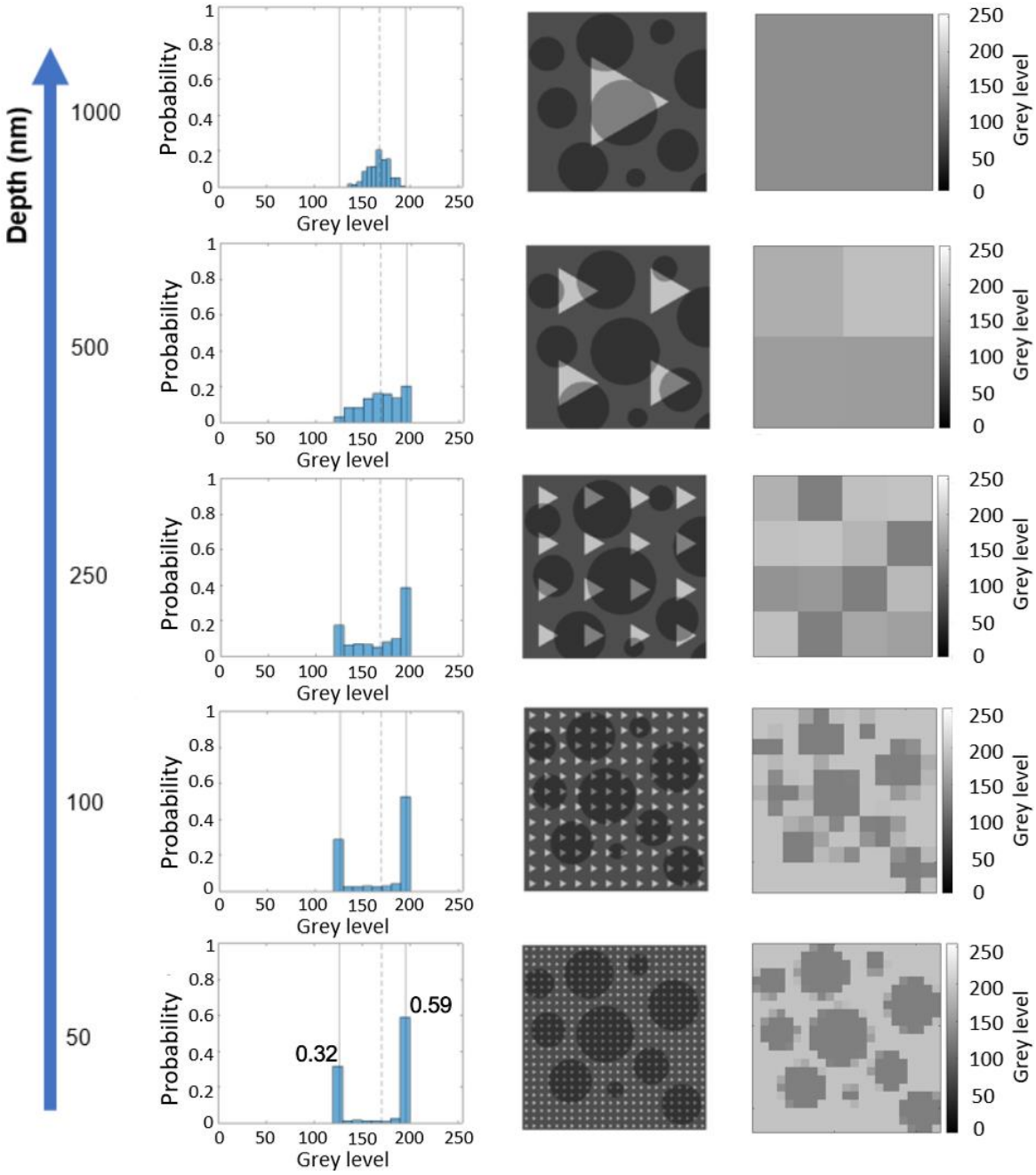

Figure 2-31. Histograms of Virtual Nanoindentations with a grid of 25x25 pixels on the same composite material for various depths.

It is observed as expected, that distributions with the most distinctive monophase peaks are the result of the shallowest virtual nanoindentations (50 nm in Figure 2-31).

By decreasing the depth of nanoindentations and refining the indentation grid (moving downward in Figure 2-31), more indents become monophase. And the fraction of indents in each phase converges to the area fraction of that phase. This is shown by studying Figure 2-31 and measuring the area fractions of the phases by the software ImageJ (Table 2-5).

Table 2-5. percentage of indents that are only in one constituent of the microstructure (compared with the area fraction of the constituents)

Indent depth	Indents only in the inclusion	Indents only in the matrix
	39.4 % (area fraction)	60.6 % (area fraction)
50 nm	31 %	58 %
100 nm	24 %	45 %
250 nm	10 %	20 %
500 nm	0.2 %	5.7 %
1000 nm	0 %	0 %

The deepest virtual nanoindentations (up in the diagram shown in Figure 2-31 associated with 1 µm depth) show one peak for the multiphase indents. Therefore, it is concluded that for this microstructure, 1 µm depth is enough to give homogenized values for the elastic modulus.

Performance of the "VN" tool

For composites having constant sizes microstructure features that are distributed uniformly everywhere, the usual rules of thumb (explained in section 2.7.3) define the recommended depth and spacing of nanoindentations. But if the sizes and density of the features vary spatially (as they do for dentin), determining the grid parameters is more complicated.

The "VN" tool helps to predict if the results describe the properties of the constituents of the composite or if they characterize the whole composite in a homogenized manner.

This estimation helps to predict whether the results describe the constituents of the composite or represent the whole composite in a homogenized manner.

2.7.6 Application of the "VN" tool to dentin

The "VN" tool was applied on dentin to plan the nanoindentation tests (or verify an already planned grid of nanoindentation). The input data were the treated SEM images presented in Chapter 1. In the case of the SEM images of dentin in the BSE mode (Figure 2-32.a), the grey level of the pixels in the image was already related with Young's modulus of the material because heavier elements are imaged brighter and cause a higher stiffness as well. Because dentin is nonconductive, there will be a charging effect in the image. And this, together with other artifacts observed on the images (contamination, polishing scratches, etc.) would cause significant errors when using the VN tool to estimate Young's modulus or the area fraction. That is why the segmented images of dentin are chosen for virtual nanoindentation (and not the untreated BSE mode images). The chosen assigned moduli for ITD and PTD are respectively 26 and 40 GPa.

As an example, the image 'M1' from Chapter 1 is shown in both original (Figure 2-32.a) and segmented versions (Figure 2-32.b).

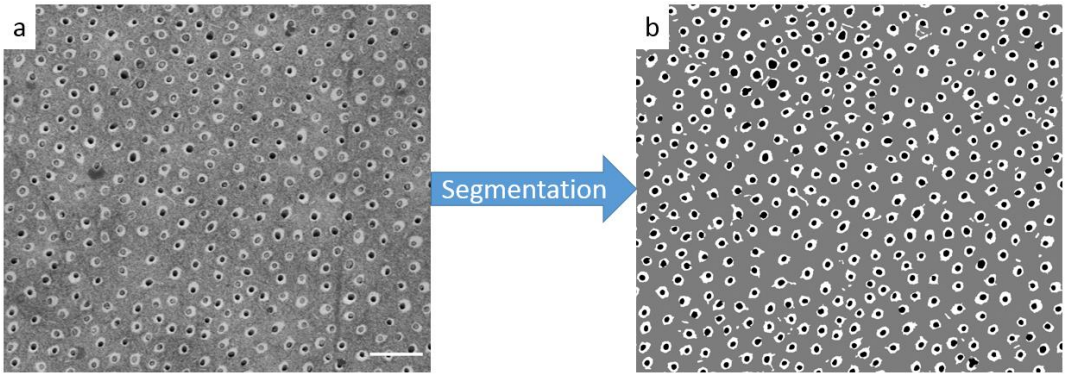

Figure 2-32.a) The image 'M1' in its original format (at a normalized distance of 0.6 from the DEJ and with a scale bar of 15 µm), b) The same image segmented by following the protocol of image treatment explained in Chapter 1

The "VN" tool performs shallow and deep virtual nanoindentations (with the designed grid parameters) on the segmented dentin images.

Shallow Virtual Nanoindentations: how well will we probe the microstructure by indentation?

Virtual nanoindentations with 100 nm depth were performed on 3 locations across dentin to take account of the variation in its microstructure. These three locations are shown on the sample in Figure 2-33, and are named 'E' for enamel, 'M1' for middle and 'P1' for pulp. These are the same locations where the real nanoindentations will take place.

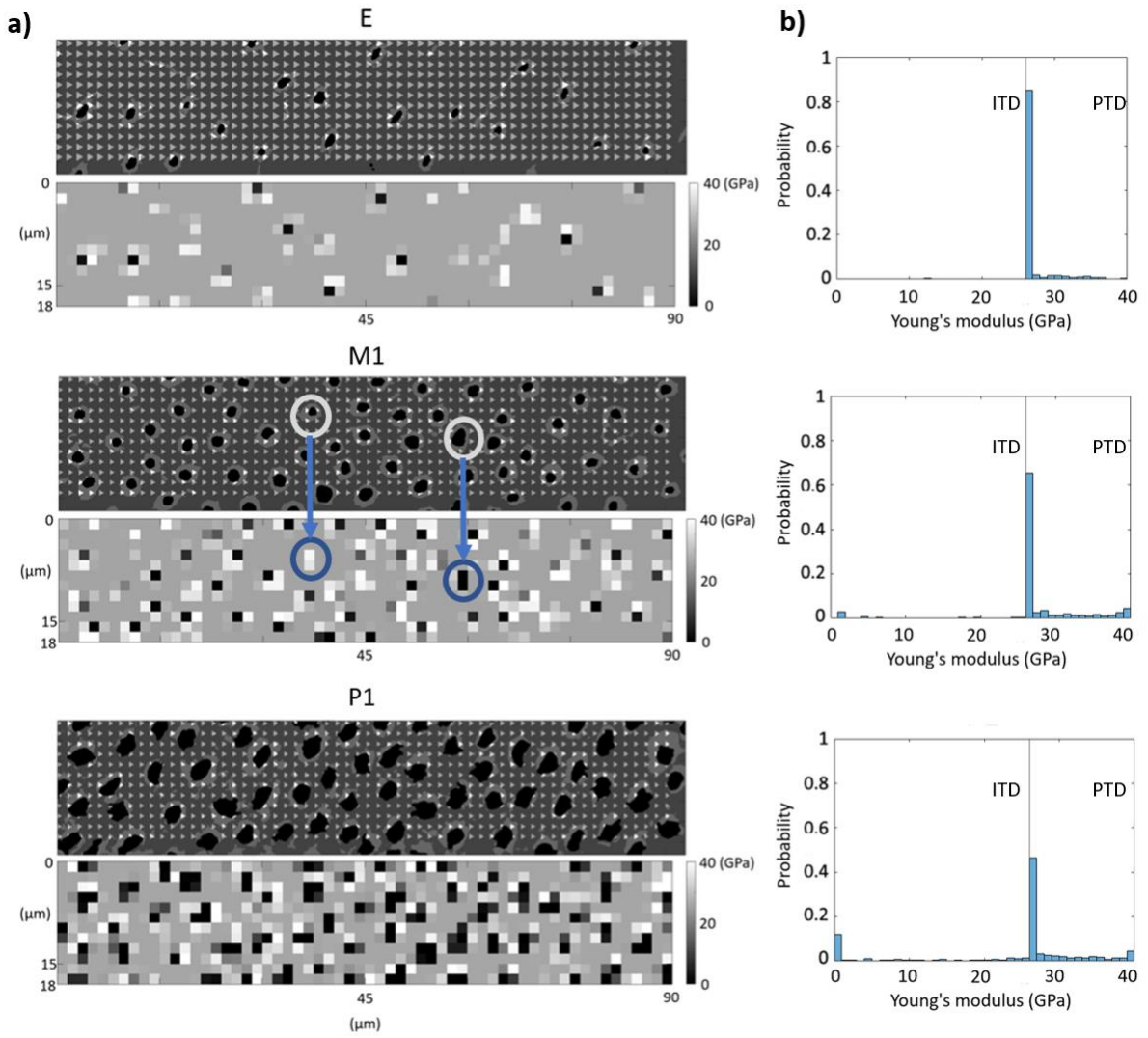

Figure 2-33.a) Grids of Virtual Nanoindentations with a depth of 100 nm, at three locations: near the enamel ('E'), in the middle ('M1') and near the pulp ('P1') b) Histograms of Virtual Nanoindentation results in the same three locations in dentin

The modulus maps below each of the segmented images (Figure 2-33.a) show that a matrix of 100 nm deep nanoindentations with a spacing of 1.5 μm between the indents might miss some details of the microstructure. For example, the encircled zones in "M1" demonstrate cases where indentations have missed one of the three phases and therefore have shown non-adjacent constituents to be adjacent ones.

The shallow virtual nanoindentations estimate the possibility of distinctively characterizing each constituent of dentin. This is done by investigating the histograms of the virtual nanoindentation results. In Figure 2-33.b, the histograms at the three locations in dentin show the distribution of the moduli that are estimated by the "VN" tool. It is observed that in all of the three locations, there are enough indentations in the ITD to characterize it, i.e. there is a recognizable peak around $E_{ITD} = 26\ \mathrm{GPa}$ in each of the three histograms. Even near the pulp where the ITD zones are narrower, more than 39% of the nanoindentations are totally inside ITD. On the contrary, indents that are purely inside PTD are scarce everywhere (always less than 4%), and especially near the enamel (only 0.7%). Therefore, the obtained data points are not sufficient to reliably characterize PTD.

Table 2-6. Percentage of the monophase indents

	E	M1	P1
Percentage of indents that are totally in ITD	86	59.9	39.4
Percentage of indents that are totally in PTD	0.7	2.6	3.1

This leaves us to reconsider the equation 2.19 that was used to validate the chosen number of indents. In that equation, the size of the microstructure feature (D) helps to verify if the number of indentations is enough for characterizing the constituents. This equation is almost as valid at the location 'E' as it is at locations 'M1' and 'P1'. This equal validity is because the feature size (the thickness of the peritubular cuff) is relatively constant in the three locations (as seen in chapter 1, it is 0.4 µm in 'E', 0.65 µm in 'M1', and 0.45 µm in 'P1'). But while the indents in 'M1' group seem to characterize PTD with relative success, the same number of indents in 'E' are not enough to do so.

A suggested modification to the rule of thumb regarding the number of indents

Therefore, the equation should be modified by redefining 'D', which is the size of the microstructure feature. If 'D' indicates only the microstructure feature size (tubule size in this case), the required number of the indents does not vary by a variation in the tubule density. But it does vary if 'D' is redefined to be not only the tubule size but also the typical dimension of the ITD matrix -i.e., the typical distance between tubules-. This new definition of the microstructure feature is named D_{num}, to remind its role in defining the needed number of indents.

$$D_{num} = \max(D, \text{typical distance between features}) \tag{2.36}$$

$$L_{grid}\sqrt{N} \gg D_{num} \tag{2.37}$$

Then the equation will predict more indents near the enamel because of greater distances between tubules. However, D in equations 2.19 and 2.20 (prescribing the depth and spacing of indents) does not need to be modified, because there it is the smallest dimension of the microstructure features (tubules or the matrix between them) that should define the depth of nanoindentation to prevent probing zones of material that go through multiple constituents.

Another suggestion for characterizing a scarce feature in the microstructure: pointed nanoindentations

Increasing the current number of the indents (720 at each location) might not be practical. Another way to tackle characterizing a scarce feature of the material is *pointed nanoindentations* (i.e., indentations that are not in a grid but are individually planned and performed on the feature in question).

2.7.7 Effective stiffness of dentin: what is the prediction of the "VN" tool for the homogenized modulus of the dentinal tissue depending on location?

Due to the spatial variation of the morphology of dentin, the homogenized mechanical properties vary across the sample even if the properties of the constituents would stay the same everywhere. To investigate this, deep virtual nanoindentations were done on a stitched version of the segmented images of dentin from the DEJ to the pulp. The stitched image is shown in Figure 2-34.a.

A 7x147 matrix of virtual nanoindentations with the suggested grid parameters for deep nanoindentation (1 µm depth) was done on the stitched treated image, which extended from the enamel to the pulp. The resulting map is shown in Figure 2-34.b.

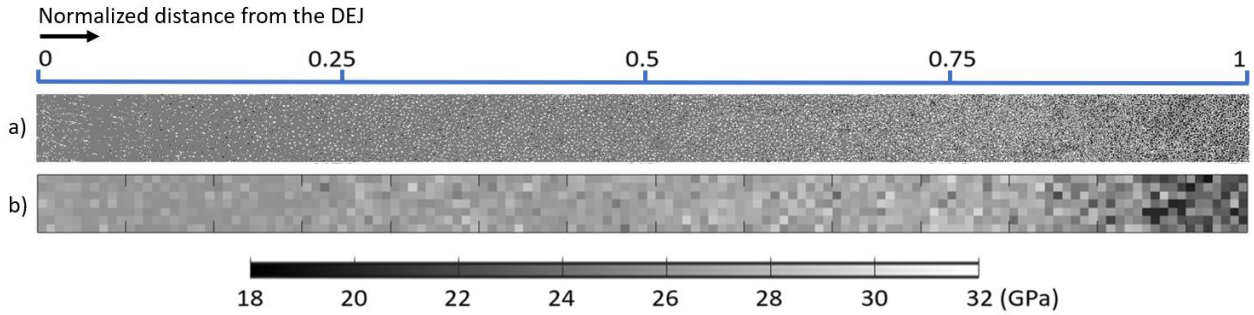

Figure 2-34.a) SEM image treated with the protocol proposed in Chapter 1, b) Resulting 'VN' test using $E_{PTD} = 45\ GPa$, $E_{ITD} = 30\ GPa$, and $E_{lumen} = 0\ GPa$ as grey levels

These results are plotted versus the normalized distance from the DEJ in Figure 2-35 to study the spatial variation of virtual nanoindentation results from the DEJ to the pulp.

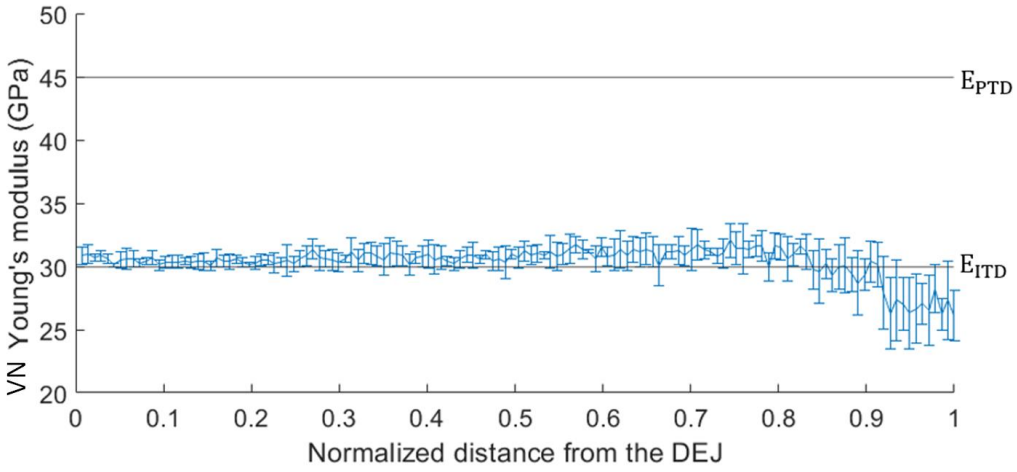

Figure 2-35. Deep virtual nanoindentation Young's modulus with respect to normalized distance from the DEJ. 7 data at each location give the mean and the SD.

In this plot (Figure 2-35), the homogenized Young's modulus (E_{Voigt}) decreases near the pulp. As this is simulated by the "VN" tool, this variation in the estimated modulus is only due to a variation in the area fractions (a_i) of the constituents. In the previous chapter, it was claimed that there is secondary dentin. Before continuing the study of the dentin sample at hand, an inquiry using the "VN" tool was done on the sclerotic dentin (explained in the introduction).

Studying sclerotic dentin by the "VN" tool

In the same way that the "VN" tool was used above to study the variation of the homogenized modulus of normal dentin, it was used to study the Young's modulus of sclerotic dentin. A fully sclerotic dentin was simulated by artificially filling up the tubule lumens (in the same treated SEM image that used in the previous subsection) with a material that had the same Young's modulus (the same grey level for the "VN" tool) as PTD.

The results (Figure 2-36) suggest that the elastic modulus of dentin in sclerotic and non-sclerotic states will have reverse trends near the pulp (normalized distance of 0.8 to 1 from the DEJ): the first increases by approaching the pulp, while the second decreases. Validation of this preliminary result needs testing a sample of sclerotic dentin.

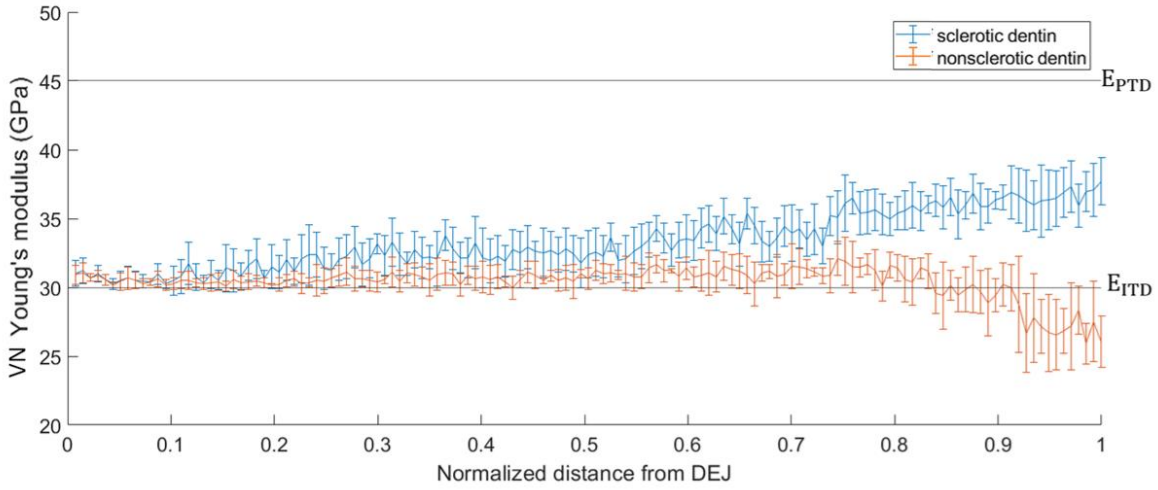

Figure 2-36. Comparison of 'Virtual Nanoindentation' modulus of sclerotic and non-sclerotic dentin with respect to normalized distance from the DEJ. 8 data points at each location give the mean modulus and the SD.

Limitations

A limitation of this tool for studying porous materials is the possibility of estimating zero modulus for some nanoindentations (visible in the modes of zero in the 2nd and 3rd histograms in Figure 2-33). If the projection of the nanoindentation contact area is small enough, it can completely fit inside the pores. In this case, the average grey level is zero (which means black). But if the nanoindenter tip enters a pore in a real nanoindentation, there might be a problem in surface detection for the nanoindenter, which leads to NaN as the result or the nanoindenter may measure a nonvalid value due to bad surface detection. In the case where the nanoindentation partially covers a pore, the effect of the pore in the virtual nanoindentation will be a weighted averaging of zero in the homogenized modulus. But, in reality, the material next to the pore may bend under the pressure of the tip (which is not in the theory of nanoindentation). And this might introduce errors to the estimation by the "VN" tool.

Despite these limitations, we can argue that the "VN" tool is an interesting and useful tool to plan nano-indentation tests on graded heterogeneous materials.

2.7.8 Conclusion

A view of the capabilities of the nanoindentation method and the specific challenges of testing the dentinal tissue allows us to give recommendations for the indentation parameters. By taking these recommendations into account, the characterization of dentin can begin. The sample and the instrument used in this thesis are introduced and then tests are done for this objective. The results are analyzed using the 'VN' tool.

Nanoindentation tests

Thanks to the "VN" tool, we better foresee what can be expected from different nanoindentation tests. Keeping in mind the phenomena that cause artifacts in nanoindentation tests, the loading protocol was defined to minimize and correct their effect. Especially, the effect of creep and thermal drift were considered.

Loading protocol of nanoindentation tests

The loading path used is shown in Figure 2-37. For both shallow and deep nanoindentations, first the indenter is positioned on the surface and the load is applied with a constant displacement rate. After reaching the planned depth, the load is held constant for 10 s. The longer this loading/holding time is, the better the viscous effects on the results are eliminated [87].

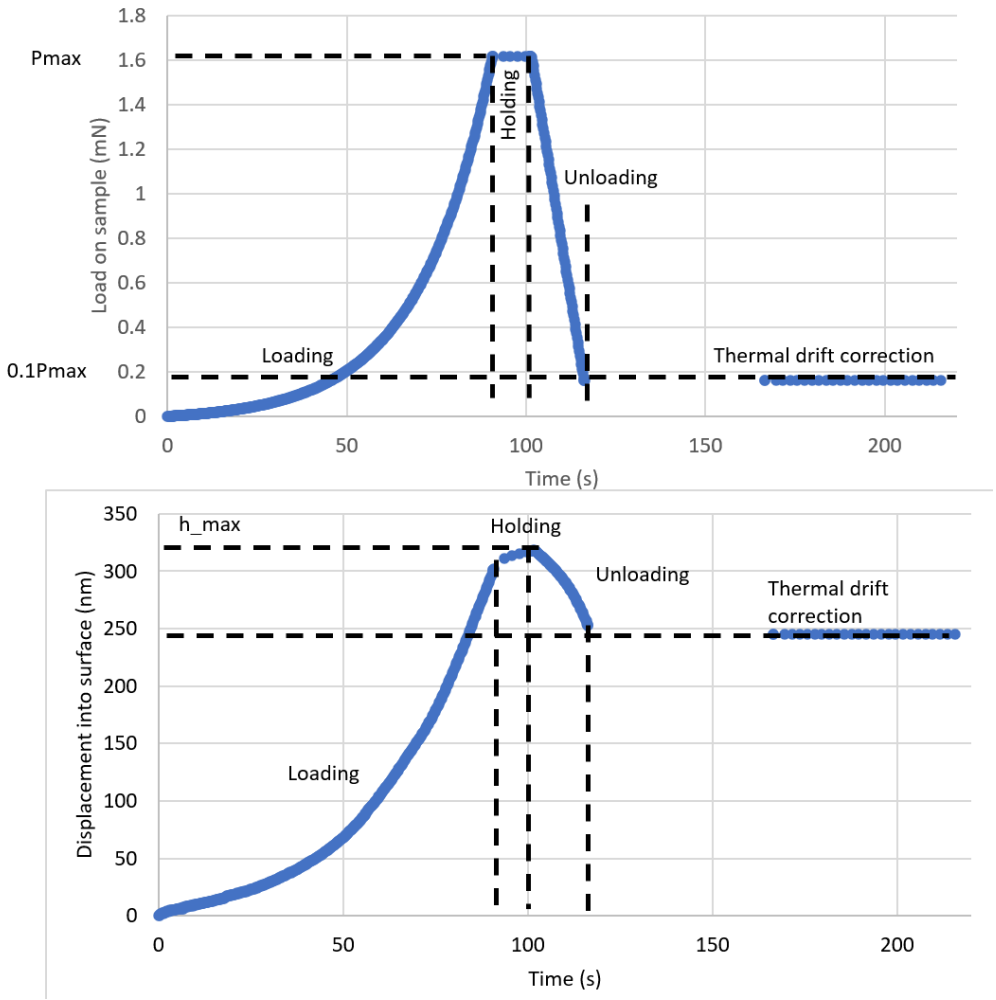

Figure 2-37. Loading protocol with a first holding for exhausting the creep and a second holding for thermal drift correction

Then, for correcting the effect of thermal drift, the load is decreased until a tenth of its maximum magnitude and is held constant. Holding a bigger load for a long time would cause creep. After waiting 100 s to let the thermal drift sink below a certain value ($\dot{\epsilon} < 0.05\ s^{-1}$), the next test is done.

The format of the results

The software of the Nano Indenter saves the results from each nanoindentation grid in an Excel file, which includes the results of each nanoindentation test together with a summary of all tests. It eliminates the results of inappropriate tests. Inappropriate tests are those in which the contact between the indenter and the specimen are not established properly.

Shallow nanoindentations for the constituent values

Shallow nanoindentations were performed and analyzed, which aim to measure the moduli of the dentin constituents (ITD and PTD). The results (in the format of Excel files) were analyzed with the MATLAB toolbox "TriDiMap". The analysis that was done before by the "VN" tool helped to evaluate the results.

The TriDiMap MATLAB toolbox is designed to analyze the results of nanoindentation tests (Mercier 2016). The reader is referred to its documentation [61] for getting to know its versatile capabilities. Most interestingly for this research, it maps and deconvolutes the nanoindentation results.

Mapping the nanoindentation results

The modulus maps of the group "M1" (including 5 grids of 12x12 pixels each) are shown in Figure 2-38 together with the optical microscopy images of the imprints of the nanoindentations.

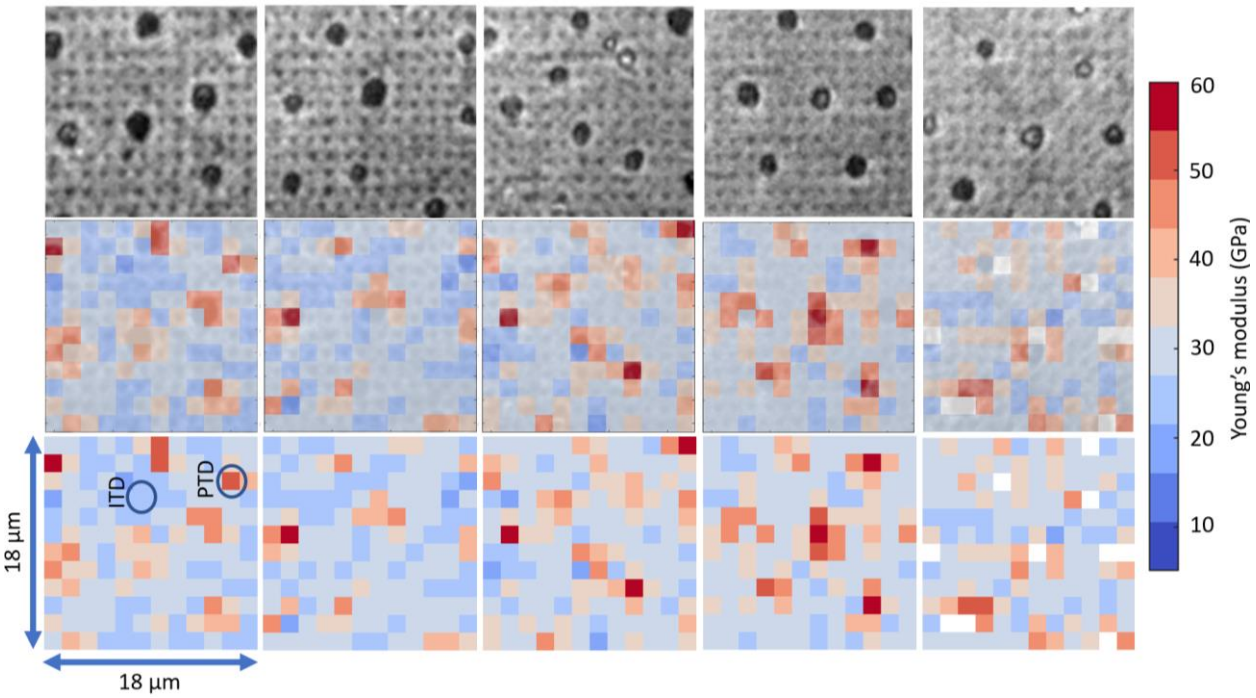

Figure 2-38. Visualization of the group "M1" of nanoindentations. 1st row: The optical microscopy images of the indented locations, 2nd row: Young's modulus maps superposed on the optical microscopy images, 3rd row: Young's modulus maps of the TriDiMap toolbox.

Figure 2-38 shows a match between the locations of tubules on the optical microscopy images and the higher values on Young's modulus maps. As seen, the resolution of these maps is sufficient to observe higher moduli for the tubules, but not to investigate the possible variation in the PTD modulus with respect to the distance from tubule lumen.

One nanoindentation on each of the phases is chosen (encircled in Figure 2-38) and their load-displacement curves are shown in Figure 2-39 as typical examples of indents in ITD and PTD.

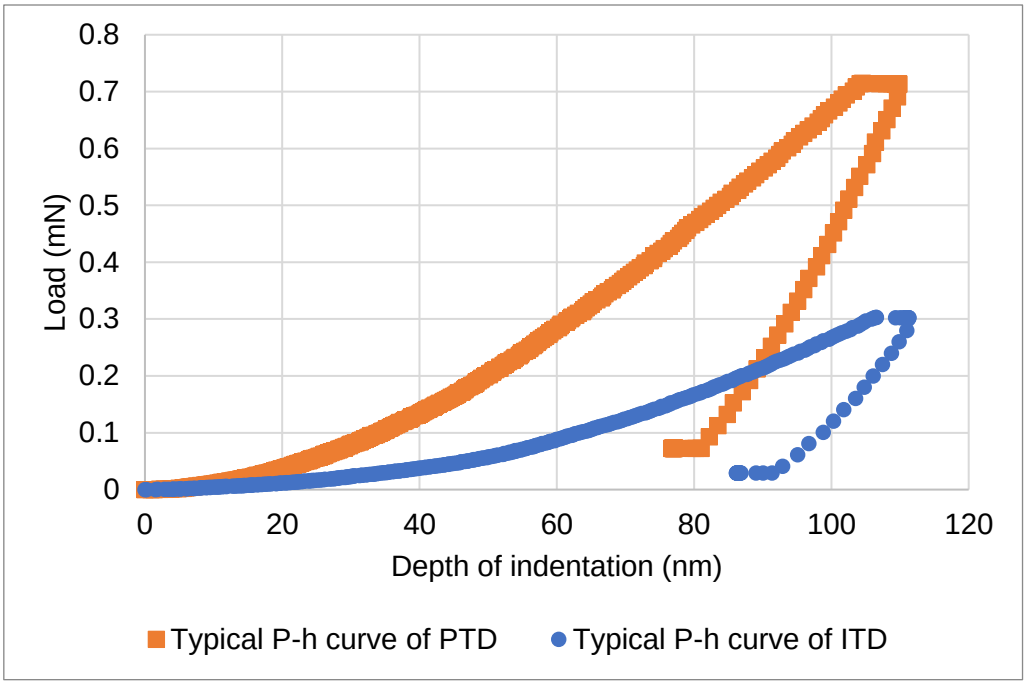

Figure 2-39. Typical load-depth curves for ITD and PTD

In the next subsection, TriDiMap will be used to deconvolute the nanoindentation results and to give distinct values for the moduli of ITD and PTD.

Deconvolution method of the results

In order to get distinct Young's moduli for ITD and PTD, the "Deconvolution technique" implemented in the TriDiMap toolbox ([61]) was applied on each of the 3 groups of nanoindentation tests ("E", "M1" and "P1"). The histogram of the nanoindentation results was deconvoluted into two phases (PTD and ITD) by assuming a normal distribution for each phase (Figure 2-40).

In what follows the formulae for a normal distribution are given by equations 2.38-2.39. Then a distribution of m phases is introduced by superposing m normal distributions. Next, a minimization is introduced that finds the closest m-phase normal distribution with the experimental data and finally, using the mentioned minimization, the experimental data will be deconvoluted into a given number of phases.

The equation of normal distribution of the mechanical property x of phase r is:

$$p_r(x) = \frac{1}{\sqrt{2\pi s_r^2}} \exp\left(\frac{-(x-\mu_r)^2}{2s_r^2}\right) \tag{2.38}$$

here μ_r is the mode or the mean of the phase r and s_r is the standard deviation of that phase.

$$\mu_r = \frac{1}{N_r}\sum_{i=1}^{N_r} x_i \; ; \; s_r^2 = \frac{1}{N_r - 1}\sum_{i=1}^{N_r}(x_i - \mu_r)^2 \tag{2.39}$$

In the equations above, N_r is the number of the data points belonging to the phase r. With the constraint that the sum of the data points of all phases (N_{exp}) is the total number of experimental data.

$$N_{exp} = \sum_{r=1}^{m} N_r \tag{2.40}$$

Given that $f_r = \frac{N_r}{N_{exp}}$ is the fraction of the data points attributed to the phase r, the superposition of m normal distributions (for m phases) will be:

$$C(x) = \sum_{r=1}^{m} f_r p_r(x) \tag{2.41}$$

By minimizing the difference between the experimental histogram (p^{exp}) and the superposition of the normal distributions ($C(x)$), the best approximation of the latter will be found.

$$\min \sum_{i=1}^{N^{bins}} \left[\left(p_i^{exp} - C(x_i) \right) p_i^{exp} \right]^2 \tag{2.42}$$

The results of deconvoluting the experimental nanoindentations are discussed in the next section.

The deconvolution results

The deconvolution from the TriDiMap toolbox was applied to the modulus measurements from the three nanoindentation groups (near the enamel ("E"), in the middle ("M1") and near the pulp ("P1")). The deconvolution is illustrated for one of the three locations ("M1") in Figure 2-40. The results of the deconvolution at all of the three locations are summarized in Table 2-7.

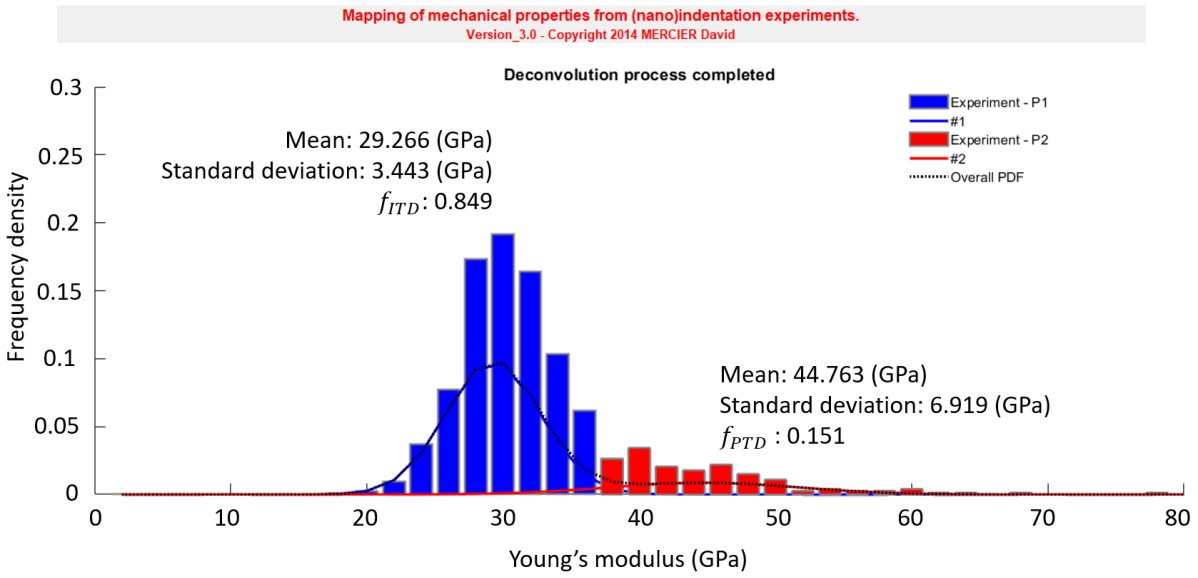

Figure 2-40. Bimodal histogram of the nanoindentation results (indenter depth 50 nm) and its deconvolution into two modes

Table 2-7. Experimental values for the elastic moduli of PTD and ITD distinguished by deconvolution. For comparison, the area fraction of each phase and the fraction of Virtual Nanoindentations (indenter depth ??? nm) totally inside that phase are also tabulated.

Normalized distance from the DEJ	method	Constituent	Average modulus in GPa (SD)	Data fraction of deconvoluted phases	Area fraction	Fraction of indents totally in one phase according to the "VN" tool
0.12 (E)	CSM	ITD	30 (4)	0.98	0.93	0.86
		PTD	44 (5)	0.02	0.05	0.007
		Tubule lumen	-	-	0.02	0.003
0.59 (M1)	CSM	ITD	29 (3)	0.84	0.76	0.597
		PTD	45 (7)	0.16	0.18	0.026
		Tubule lumen	-	-	0.06	0.021
0.97 (P1)	CSM	ITD	33 (6)	0.92	0.57	0.394
		PTD	53 (8)	0.08	0.22	0.031
		Tubule lumen	-	-	0.21	0.115

Hardness values of the dentin constituents (deconvoluted from shallow nanoindentation results) in the same three locations are summarized in Table 2-8.

Table 2-8. Experimental values for the hardness of PTD and ITD distinguished by deconvolution

	ITD	PTD
E	0.96 GPa	1.6 GPa
M1	0.91 GPa	1.61 GPa
P1	1.25 GPa	2.16 GPa

There are significant differences between the hardness values measured here and in the paper by Kinney et al. (1996). First, they observed a relatively constant hardness for PTD throughout dentin, while here the PTD is significantly harder near the pulp. The hardness of ITD measured here is higher near the pulp, but Kinney et al. (1996) reported a higher stiffness near the enamel.

Also, this measurement differs from the study by Kinney et al. (1996) in the difference between the hardness of the constituents. They reported a hardness of PTD about four times bigger than that of ITD, but here a ratio of less than two is observed.

Analysis of the experimental nanoindentation results by studying virtual nanoindentations

In the two following subsections, the histogram of virtual nanoindentations at "M1" (Figure 2-33, the histogram in the middle) and the histogram of the experimental data at the same location (Figure 2-40) are compared in two aspects: number of peaks in the histogram and the degree of scatter in data.

Number of peaks in the histogram

"VN" results at "M1" have three visible modes for the indents inside the three constituents of dentin microstructure (PTD, ITD and lumen). One might expect separate modes for these multiphase indents (e.g. a peak for the indents on PTD and ITD). However, as visible in Figure 2-33, the multiphase *virtual nanoindentations* do not form separate modes in the histogram.

On the other hand, the measured moduli from *experimental nanoindentations* are deconvoluted into two groups of results for PTD and ITD. Contrary to virtual nanoindentations, the experimental nanoindentations in lumens result in NaN or a value other than zero (as visible in the maps in Figure 2-38). Therefore, there is no measured modulus of 0 GPa and no peak in the histogram at 0 GPa.

The histogram shown in Figure 2-40 could also be deconvoluted into more than two modes to take account of multiphase indents (TriDiMap lets the user choose the parameter "m" in equation 2.41). But it is important to notice that such a multiphase peak must have also existed in the histogram of virtual nanoindentations (Figure 2-33) because they take into account multiphase indents. Even if an extra peak exists in the histogram of experimental nanoindentation results, it may be due to damaged material (as explained in the paper by Furin et al. (2016) [88] for the case of nanoindenting bone tissue) and may not be necassarily attributed to the multiphase indents.

The scatter of the data

In comparison with the histogram of the virtual nanoindentations at "M1" (Figure 2-33, the histogram in the middle), the histogram of the experimental nanoindentations at the same location (Figure 2-40) shows significantly more scatter. The scatter of experimental nanoindentation data is explained for different reasons:

1) *Variation inside each phase*. This variation is not considered in the current application of the "VN" tool, because each phase has a uniform grey level in the input treated images.
2) *Variation in results because of multiphase indents*. This is the only kind of variation simulated by the virtual nanoindentations. It causes the data points that stand between the peaks of phases in the histogram of virtual nanoindentation results (as shown in histograms in Figure 2-33).

3) *Variation due to damaged material*. The part of the sample surface that is damaged due to sample preparation or the indentation process itself, shows a smaller modulus than the intact material (Furin et al. (2016) [88]).

Virtual nanoindentation results, which only have the second type of variation, are much less scattered than the experimental data. Therefore, the significant scatter in the experimental data, should be mainly explained by the first and third kinds of the variation in results.

Deconvolution of "Virtual Nanoindentation" results

To test the effect of the multiphase indents on the deconvolution, the deconvolution was also performed on the results of the "VN" tool. In other words, is it possible to get the constituent moduli that were given as input to the "VN" tool if one deconvutes the "VN" results?

This is done below on "VN" results, which took as input the constituent moduli that resulted from deconvolution of experimental results.

Table 2-9. Distinct deconvoluted elastic moduli from Virtual Nanoindentation

Location	Constituent	Input of "VN" from real shallow nanoindentations	Output of "VN" by deconvolution (SD)
0.12 (E)	ITD	30	31 (2)
	PTD	44	43 (1)
0.59 (M1)	ITD	29	29 (1)
	PTD	45	40 (4)
0.97 (P1)	ITD	33	34 (1)
	PTD	53	47 (5)

As the results in Table 2-9 show, the output results of ITD seem acceptable in all three locations, but the deconvoluted moduli for the PTD become more erroneous and underestimated by moving away from the enamel. This is because of the scarcity of the data for the PTD peaks and the fact that PTD is always adjacent to something less stiff: ITD or lumen. Therefore, the multiphase data points always have smaller moduli than the PTD (an asymmetric distribution). Deconvolution assumes a symmetric (normal) distribution and therefore shifts the PTD mode to the left (smaller values). The same has been the case for the experimentally measured elastic modulus of PTD.

Conclusion of the analysis of deconvoluting the results

The multiphase indents, even though numerous (roughly 0.36 of the total at the location "M1") are distributed in a relatively uniform way between the monophase modes and do not form extra peaks in the histogram of virtual nanoindentation results. Therefore, they cannot explain the scatter in experimental results (as for example visible in Figure 2-40). Therefore, a significant part of the scatter in the nanoindentation results of dentin, is due to variation inside each phase and the possible damage that happens to the material.

Comparison with the results given in the literature

In this part, we show results from virtual nanoindentation tests in order to estimate the Young's modulus of dentin constituents at different locations in the dentinal tissue as well as the local variation of the results due to the spatially variation of the microstructure.

For ITD, Young's modulus ranging between 29 and 34 GPa was measured. It is higher than the previously reported values (summarized in Table 1). The reason could be that our sample was dehydrated by alcohol bathes and drying is known to increase the elastic stiffness of dentin. But other studies that report testing dry samples only mean that their sample is air-dried (i.e. they have not dried their samples with a systematic protocol). It might be that drying the sample by alcohol bathes is more efficient than air-drying and therefore stiffens the dentin more.

For PTD, Young's modulus ranging between 44 and 53 GPa was obtained. It is higher than most of the previously reported values (summarized in Table 1) but is comparable with the value given by Balooch et al. (2004) [70]. The fact that contrary to the ITD, our measured moduli for the PTD are not the maximum values is consistent with the claim by Kinney et al. (1999) [67] that dehydration affects only the ITD.

In conclusion, the constituent moduli measured in this chapter are relatively high and this could partially be attributed to the dehydration of the sample for the SEM imaging.

2.7.9 Deep nanoindentation for homogenized values

Deep nanoindentations with the prescribed spacing are done throughout the dentin specimen shown in Figure 2-23. These tests estimated the homogenized Young's modulus of the dentin. In Figure 2-41, the deep nanoindentation results are overlaid on the area fraction plot from Chapter 1 (section 1.3.1). This figure visualizes the potential relation between the elastic modulus of dentin and its morphological properties (in this case the area fractions of the constituents).

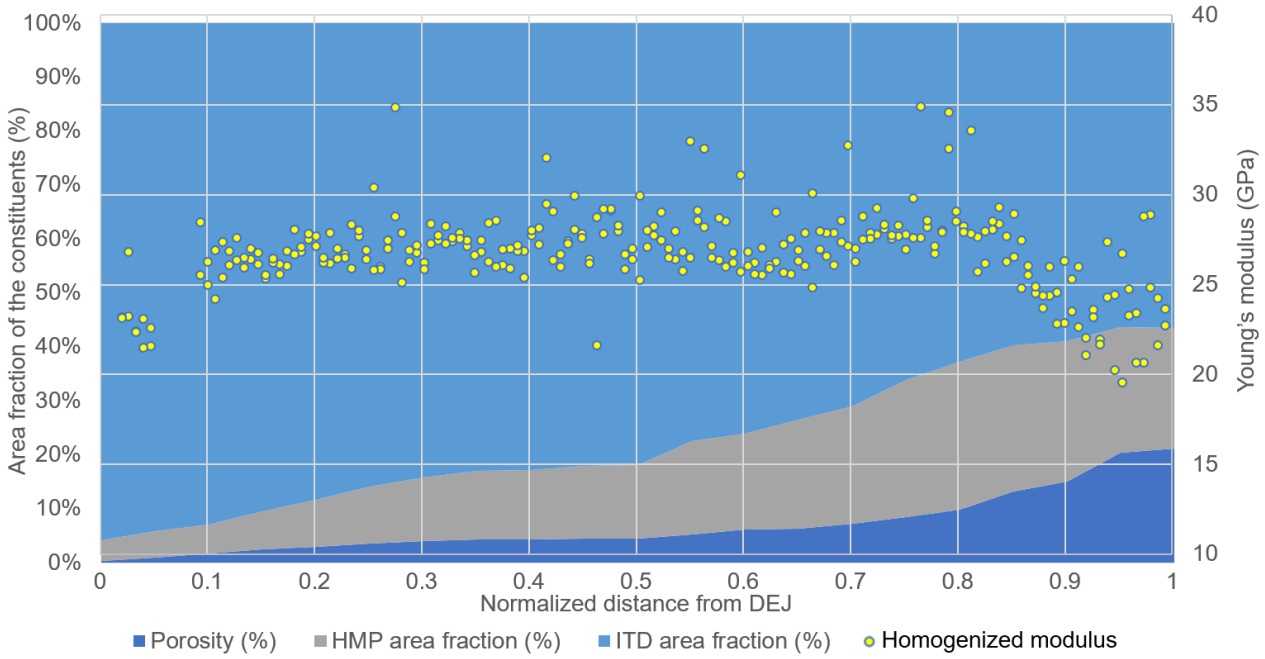

Figure 2-41. Local variation (from the DEJ to the pulp) of the homogenized Young's modulus of dentin as a composite of ITD, PTD and void

The crack on the sample surface (visible in Figure 2-23 near the DEJ and around 50 µm wide) caused a few erroneous values that are removed in the plot. Similarly, because of the possible effect of the interface between enamel and dentin, the first few nanoindentations in 42 µm distance of the DEJ were ignored.

Despite the variation in the microstructure, dentin shows a rather constant Young's modulus (27.6±1.7 GPa) over a big range of normalized distance (0.2-0.8). Interestingly, this is the same zone that is named 'Middle dentin' in Chapter 1. The modulus decreases significantly near the enamel (mantle dentin), and especially near the pulp (secondary dentin). This means that the stiffness might be a good indicator to define the dentin types.

The decrease in modulus near the pulp is also observed in the virtual nanoindentation results. This co-occurrence means that the *variation of the constituent contents* (which is taken into account by the "VN" tool) *can explain the decrease of the elastic modulus near the pulp*.

With the same argument, the decrease in the modulus near the enamel (within 0.2 normalized distance) cannot be explained by a variation in the area fractions of the constituents (because it does not have a parallel in the virtual nanoindentation results). Therefore, it should be because of the existence of the mantle dentin and the less-mineralized soft zone mentioned in Chapter 1.

2.7.10 Summary of the nanoindentation results

To have a comprehensive view of the nanoindentation results for constituents and homogenized values, they are plotted together in Figure 2-42.

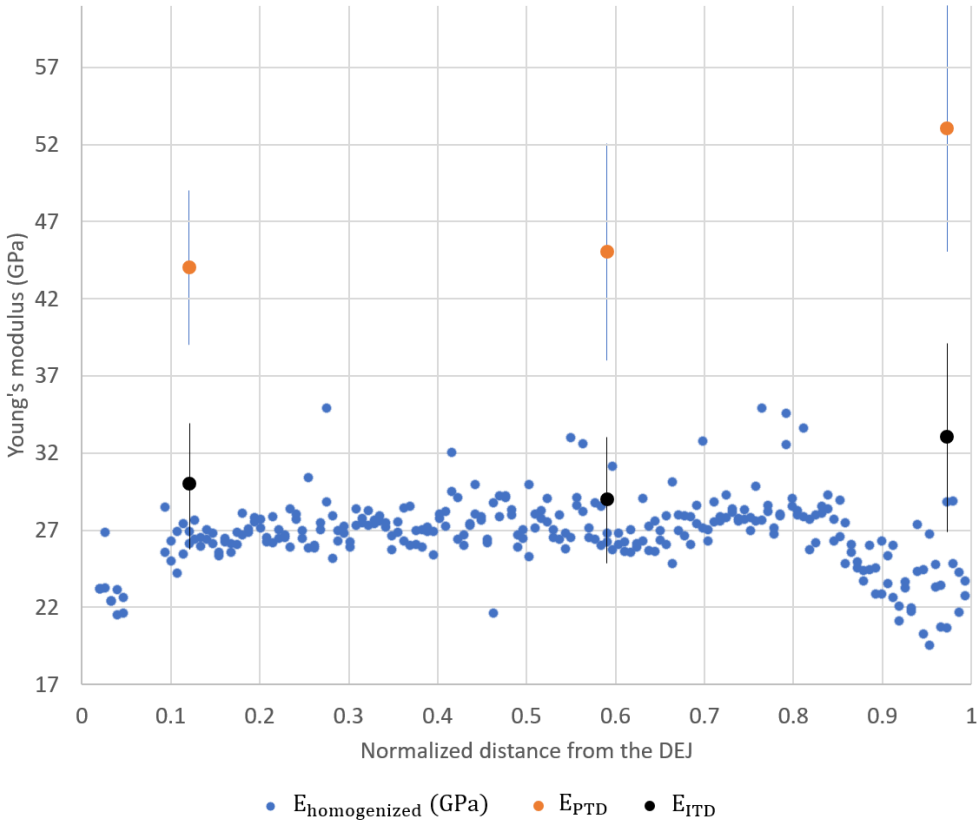

Figure 2-42. Shallow and deep nanoindentation results versus normalized distance from the DEJ

At the three locations near the enamel, in the middle and near the pulp, we obtained respectively values of 44, 45, and 53 GPa for PTD and values of 30, 29, and 33 GPa for ITD. In comparison with the literature, these values are high, which is partially due to the dehydration of the sample.

The homogenized modulus of dentin (blue points on Figure 2-42) is close to the modulus of the intertubular matrix (black points on Figure 2-42). However, the moduli of the homogenized dentin and ITD diverge, especially near the pulp. There, the porosity becomes significant enough to get the homogenized modulus even lower than the modulus of the ITD matrix. The same phenomenon was observed in virtual nanoindentation results (Figure 2-35).

Another issue of interest is comparing the trend of the homogenized modulus in virtual and real nanoindentations. The trend of virtual deep nanoindentations (Figure 2-35) successfully imitates the real deep nanoindentations (Figure 2-42) in two aspects:

1) being relatively constant in the middle part of dentin
2) decreasing by approaching the pulp.

These similarities mean that in these dentin regions (near the pulp and in the middle), the contents or volume fractions of the constituents are the decisive factors for the magnitude of homogenized elastic modulus in dentin. However, near the enamel, it is not the constituents' contents that causes a decrease (because it would be predicted by the "VN" tool). Therefore, it should be a decrease in the moduli of the constituents.

Artifacts of nanoindentation on dentin

For some of the artifacts that affect the nanoindentation results, precautions have been taken. *Thermal drift* and *viscoelasticity* were prevented from affecting the results by designing the loading protocol, i.e., setting holding periods. *Demineralization* was avoided by storing the sample hydrated in a suitable solution during its preparation. But *dehydration* was done before the experiment as a requirement for SEM imaging, and apparently, its effect was not fully reversed by rehydration in Ringer's solution. Finally, setting a lower limit for the nanoindentation depth prevented the *roughness* of the sample from affecting the measurements.

The other two artifacts are investigated in the following subsections: free edge effect and sink-in (or pile-up).

Free edge effect

The free edge effect is interesting in this study because dentin has a free edge at the border with the pulp cavity (Figure 2-23). Therefore, the edge effect was checked for the *deep nanoindentations* because of a bigger imprint area (A).

The Poisson ratio of dentin is usually accepted to be around 0.3. Furthermore, the ratio $\frac{H}{E_{eff}}$ is around 0.05 in the present measurements. With these assumptions and with the help of Figure 2-11, it is concluded that the error due to the 'Edge effect' will be less than 10 percent already from the second deep indentation (~20 µm distance from the DEJ), and it will be less than 2 percent from the 6th (~80 µm from the DEJ). Again, it is reminded that the indents closer than 42 µm to the edge were ignored anyway. Therefore, it is safe to neglect this artifact.

Sink-in or pile-up

Sink-in or pile-up of dentin under nanoindentation has not been usually reported. However, two arguments play in favor of sink-in:

1) The contracting volumic deformation of calcified tissue: According to Tai et al. (2006) [89] the porosity of dentin leads to an irreversible volumic contraction in the compacted zone under the indenter tip, which causes sink-in.
2) Sink-in is the usual behavior for strain-hardening materials [46], which is observed in dentin (An & Zhang (2017) [90]).

By imaging the indented surface using SEM, it was verified that the nanoindentations had caused sink-in. If pile-up was observed, a correction of results should have been applied. However, the observation of sink-in in Figure 2-43 shows that the use of Oliver Pharr method has been justified, and no correction is needed, according to Cheng & Cheng (2004)[91].

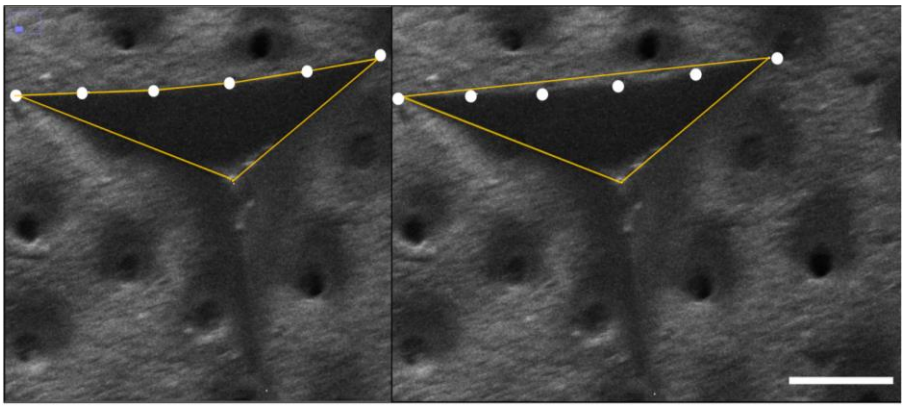

Figure 2-43. The yellow frame on the figure left illustrates one-third of the actual contact area of the indent and the one on the right one third of the ideal contact area (scale bar: 5 µm)

2.8 Conclusion

Nanoindentation was used to assess the stiffness of the dentin's constituents. Because dentin shows a gradient of micro- and nanostructure and, consequently, its mechanical properties, nanoindentation tests were performed on three different locations (i.e., near the enamel, in the middle, and near the pulp) to probe this variation.

The grids of nanoindentations were planned using rules of thumb that exist in the "statistical grid indentation technique". One of these rules (the one about the number of indents) was modified for the case of a composite with a continuous matrix in between the features (e.g., dentin).

To simulate the results of nanoindentation grids, the "VN" tool was developed. The "VN" tool, a simple and straightforward tool based on the "Voigt" upper bound, allows estimating if a given indentation depth will measure either distinct moduli for the constituents or a homogenized modulus for the composite. Contrary to the known rules of the "statistical grid indentation technique", this tool does not need the dimensions of the microstructure features as input. A treated image of the microstructure is enough.

Application of the "VN" tool to shallow nanoindentations showed that nanoindentations of 100 nm depth could characterize ITD at every location, but PTD is challenging to characterize because it is scarce, especially near the enamel. There, even as many as 720 indentations would give only around five indents that are totally inside PTD, which is not enough and leads to an inaccurate Young's modulus for PTD.

The "VN" tool was also used to simulate deep nanoindentations that are expected to result in homogenized elastic moduli for the composite.

Measuring the elastic moduli of PTD and ITD was the primary goal of this chapter. Shallow nanoindentations (planned by the "statistical grid indentation technique" and verified by the "VN" tool) were performed, and the "TriDiMap" toolbox deconvoluted the results for each constituent.

Deep nanoindentations throughout the dentin were done too and revealed the general trend of the homogenized Young's modulus of dentin as a composite. The trend was similar to that of the virtual deep nanoindentations. This similarity means the superior effect of the

factor that the “VN” tool takes into account (the area fraction of the constituents) compared with the factors that it cannot take into account (damage to the constituents, variation inside constituents).

2.9 Perspective

In this chapter, we proposed a nanoindentation protocol based on admitted rules and the findings of a new proposed tool (the “VN” tool). We obtained interesting results, but a few improvements can be proposed.

2.9.1 Improving what is already done

To overcome the difficulty of characterizing the PTD (due to its scarcity), pointed nanoindentation tests are suggested.

Changing the nanoindenter tip is another possibility. If the goal is to map the modulus of the material with a good resolution, the cube-corner tip allows a smaller spacing between indents with the same nanoindentation depth. That is because it has a smaller plastic radius. Although this tip is more often used for studying inelastic phenomena and cracks, the cube corner indenter performs well for measuring the elastic modulus.

Another point that could be improved for further study is the hydration state of the sample. Most importantly, a hydrated sample is closer to the in-vivo state. Therefore, it is preferable first to indent the sample and then dehydrate it for SEM imaging.

2.9.2 Further steps

One aspect that was not experimentally investigated in this nanoindentation study was the anisotropy of dentin. Nanoindentation was always done perpendicular to one cross-section plane (Figure 22), which, as discussed, has a varying angle with the tubules. It will be interesting to indent dentin parallel and perpendicular to tubules with shallow and deep nanoindentations to study the anisotropy of the constituents and the dentin composite, respectively. This task will undoubtedly be challenging, mainly because it will require polished surfaces of dentin that are perpendicular to each other.

Another question to investigate before attributing the measured moduli to dentin is the following: by nanoindentation, only the outer layer of the material is examined, while the resulting properties are attributed to the bulk material. Therefore, tests on a bulk material (like micro-tensile or micro-compression tests) can complement these experimental data.

3 A micromechanical model of dentin

3.1 Introduction

In this chapter, a modified micromechanical model of dentin is presented, which is based on the model developed by Vennat et al. (2021) [92]. The modified model is built at a relevant scale, where the main features of the microstructure, namely the tubules and their lateral branches appear. In the original model [92], my contribution was in the image analysis section, which resulted in the geometry used in the simulation. The mentioned model was implemented in a FEM code and allowed investigating the macroscopic elastic behavior of dentin and estimating the local stress concentration occurring around the tubules. The modified model is implemented in a module of COMSOL called “Cell Periodicity”.

The model is based on the morphological data achieved in Chapter 1 and the mechanical properties for the constituents measured by nanoindentation as explained in Chapter 2. These experimental steps together with other steps of the thesis are visualized in Figure 3-1.

First, using the morphological properties of the dentin microstructure presented in Chapter 0, a simplified description of a representative volume element (RVE) is defined (Figure 3-1.c). To account for the spatial variation of the microstructure, three RVEs were built corresponding to three different specific areas: near the enamel, in the middle dentin, and near the pulp. For completing the input data of the numerical model, Young’s moduli of the constituents determined by nanoindentation have been introduced. The simulations lead to the assessment of dentin’s local effective stiffness matrix (Figure 3-1.c) and the highlighting of the overstress locations (Figure 3-1.d). They allowed a better understanding of the influence of dentin microstructure on its mechanical behavior. The resulting stiffness matrix fully describes the local elastic properties of dentin. For instance, its Young's and shear moduli in various orientations, and the degree of the elastic anisotropy of dentin are assessed. The analysis went further by discussing the sensitivity of the elastic properties to following parameters:

- Young’s modulus of the peritubular collars,
- The occlusion of the tubules due to sclerosis,
- The anisotropy of the intertubular dentin (ITD).

Besides, studying the stress distribution of dentin gives an idea of its fracture behavior. For example, locations of higher stress concentrations can be recognized where fracture might initiate.

In the following, first, micromechanical studies of dentinal tissue are reviewed. Then, the micromechanical model used in this thesis is described, and the results of simulations are discussed. The review focuses on the elastic properties because the stress distribution in dentin has been little discussed in the literature.

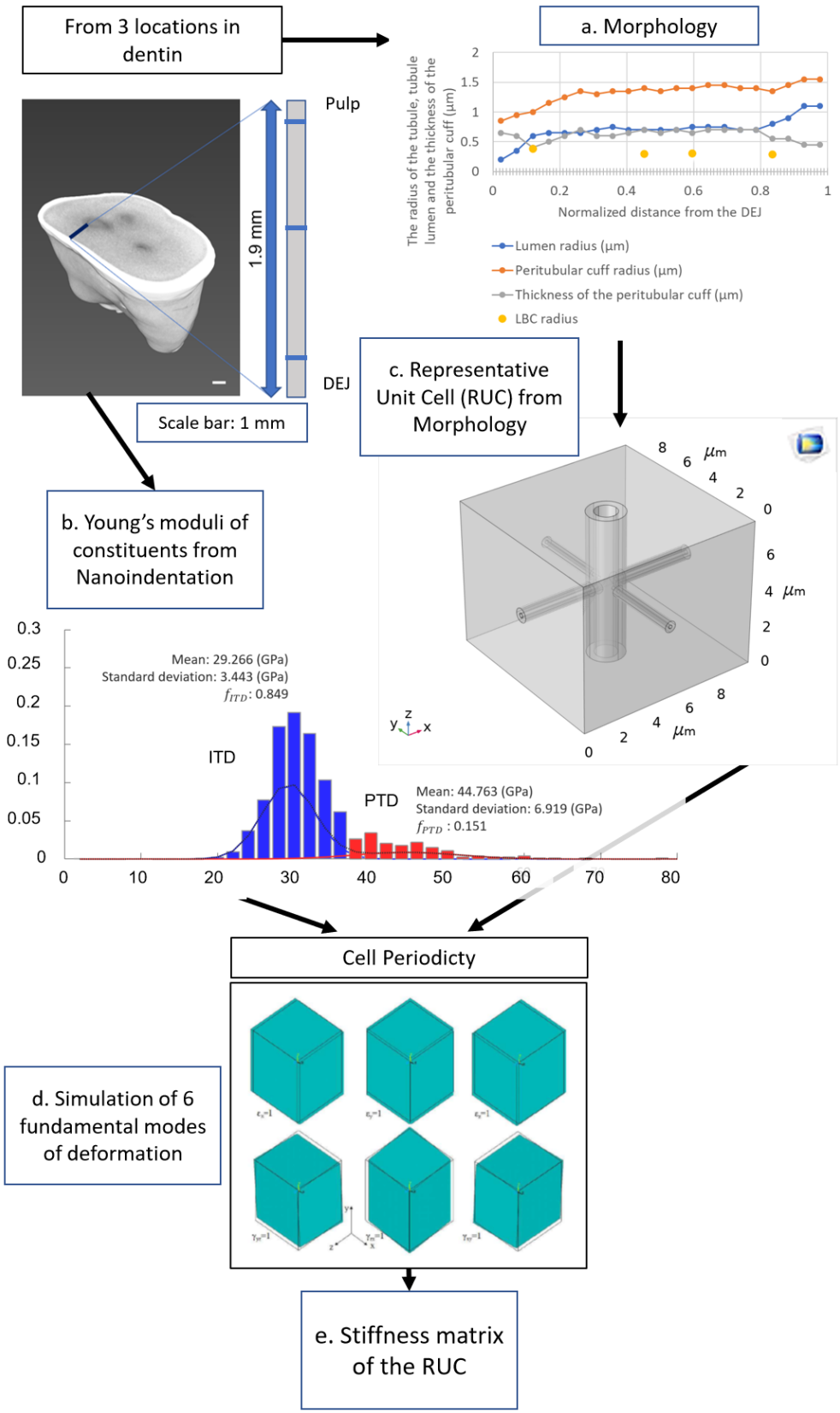

Figure 3-1. Schematic view of the numerical and experimental steps in this thesis, a) a diagram representing the measured morphological properties as a function of the location in dentin, b)

3.2 Dentin micromechanical models

Micromechanics is a field of study that investigates the overall response of heterogeneous materials knowing the geometries and mechanical properties of the constituents. The method that allows predicting the overall response from the local geometry and mechanical properties is called homogenization [93]. As this thesis does not aim to develop new micromechanical models, the theory of micromechanics is not recalled here. Only the useful Reuss and Voigt bounds for elastic moduli, which are reference points, are reminded. Then the proposed micromechanical models of dentin are reviewed.

Theoretical analyses of heterogeneous materials have provided rigorous bounds for the estimation of the elastic properties -i.e., bounds that must be always satisfied-. The simplest bounds are called Voigt and Reuss bounds. They give effective estimates of the shear and bulk moduli (*G* and *K*, respectively). A similar approach can be applied to define upper and lower estimates for Young's modulus when the phases and the homogenized medium are isotropic. In those cases the estimates derive from the rule of mixtures (E_V and E_R), and can be applied on a material with constituents, which are perfectly bounded together.

Voigt model:

The Voigt model, considering that all phases of the composite are subjected to the same uniform axial strain, permits to define E_V, which is an upper bound for the overall modulus of a heterogeneous material. It is stated below for the constituents of dentin:

$$E_V = f_{Lumen}E_{Lumen} + f_{HMP}E_{HMP} + f_{ITD}E_{ITD} \tag{3.1}$$

where f is the volume fraction, E is the elastic modulus, and the indices $Lumen$, HMP, ITD represent respectively the lumens of the tubules and the lateral branches (LBs), the highly mineralized phase including peritubular cuffs and lateral branch collars (LBCs), and the intertubular dentin (ITD).

In the case of a matrix reinforced by monodirectional fibers, this bound is very close to Young's modulus of the homogenized medium in the direction of the fibers, which is also called longitudinal modulus E_l.

Reuss model:

The Reuss model, considering that all phases of the composite are subjected to the same uniform axial stress, permits to define E_R a lower bound for the overall modulus of heterogeneous materials. It is stated below for the constituents of dentin:

$$\frac{1}{E_R} = \frac{f_{Lumen}}{E_{Lumen}} + \frac{f_{HMP}}{E_{HMP}} + \frac{f_{ITD}}{E_{ITD}} \tag{3.2}$$

However, this bound is not of interest for dentin because if $E_{Lumen} = 0$, then $E_R = 0$. Therefore, as proposed in Vennat et al. (2021), a modified version of E_R is derived.

"Modified" Reuss model, E_R^* for the porous microstructure of dentin:

$$E_R^* = \frac{1}{\frac{f_{ITD}}{E_{ITD}} + \frac{f_{Tubule}}{E_{Tubule}}} \tag{3.3}$$

where $E_{Tubule} = \frac{f_{PTD}}{f_{PTD}+f_L} E_{PTD}$, which is estimated from the Voigt rule of mixture for the tubules without the intertubular matrix.

This modified Reuss model does not give an absolute minimum for the modulus of heterogeneous material. Its validity is further discussed in section 3.4.1.

In a matrix reinforced by monodirectional fibers, the Reuss model E_R is close to Young's modulus of the homogenized medium in the direction perpendicular to the fiber axis E_t. Hence, the modified Reuss estimate, E_R^* can be compared with transverse Young's modulus in the direction perpendicular to the tubules (E_t).

Apart from Voigt and Reuss model estimates, there exist other bounds that are more restrictive for the shear and bulk moduli, such as Hashin-Shtrikman bounds [94]. These bounds are used for heterogeneous material that have inclusions with geometries like spheres, spheroids, cylinders, or hollow cylinders studied by Hashin & Rosen (1964) [95]. However, these are not discussed in this chapter.

Finite element method (FEM) and X-ray computed tomography (CT) have widened the horizons of the micromechanics field. On one hand CT permits to get information about the topology of the microstructure and the inner material composition. Tools are available to transform the 3D CT images into FEM meshes. On the other hand, by FEM, microstructures with more complex geometries can be modelled and homogenized [93]. In the following section, the micromechanical studies using FEM on dentin are reviewed.

3.2.1 Micromechanical models of dentin

Several studies have been dedicated to the development or use of mechanical models of the tubular structure of dentin. In this review, the emphasis is placed on two aspects of their results:

- The elastic anisotropy that results from each model: its orientation and degree defined by the ratio d of the longitudinal Young's modulus E_l divided by the transverse Young's modulus E_t: $d = E_l/E_t$ (the longitudinal and transverse orientations l and t are shown in Figure 3-2).

- The spatial variation in the stiffness with respect to the distance from the DEJ.

These main points are summarized in Table 3-1.

Kinney et al. (1999) [67] used a generalized self-consistent model of cylindrical inclusions embedded in a homogeneous and isotropic matrix phase to characterize the dentin structure. This model permits to estimate the overall elastic stiffness matrix, which is

transverse isotropic. The authors concluded that the ITD dominates the mechanical properties of dentin and that the elastic anisotropy of dentin is negligible.

Qin and Swain (2004) [96] extended the dilute micromechanical model of Hashin and Rosen (1964) [95], considering a multi-layer reinforcement. This model included the fluid (liquid or gas) inside the tubules. They observed a gradual decrease of mechanical properties by moving away from the pulp. About anisotropy, they found the elastic modulus to be higher in the direction parallel to the tubule axis ($E_l > E_t$), where E_l is the longitudinal elastic modulus and E_t is the transverse elastic modulus.

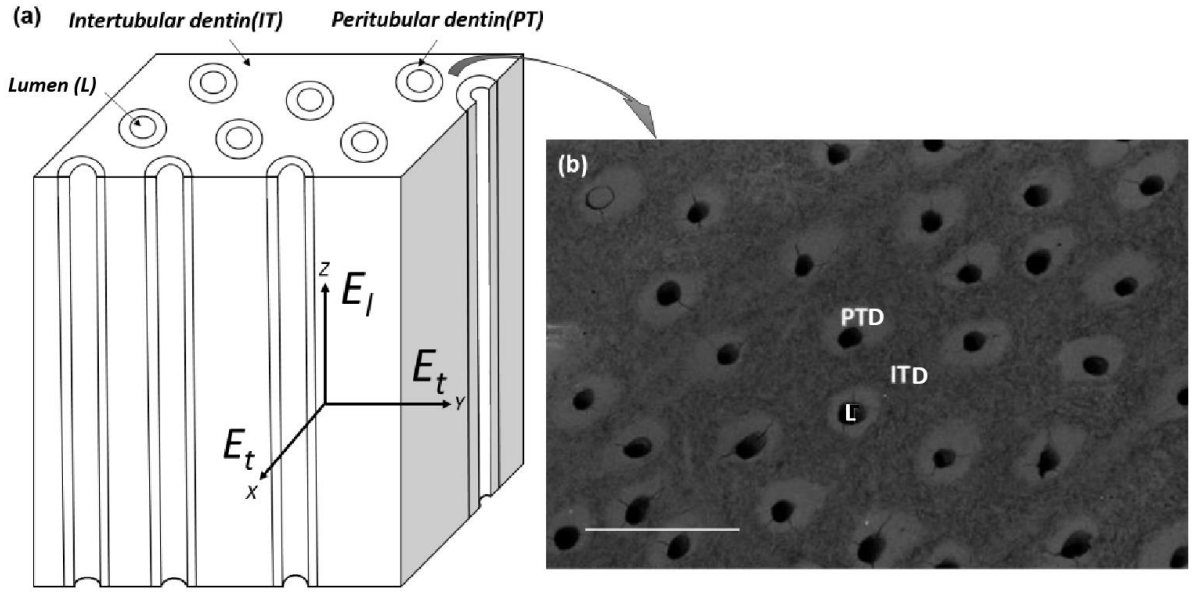

Figure 3-2.a) Dentinal structure: the directions of longitudinal modulus (E_l) and transverse modulus (E_t). b) Scanning electron microscopy image from the top view of dentin, with the identification of regions of peritubular dentin (PTD), intertubular dentin (ITD), and a lumen (L). (Scale bar: 10 µm), images adapted from Wang et al. (2015)

This orientation of anisotropy is typical for studies that only consider the tubular *microstructure* of dentin (Figure 3-2.a) and assume isotropic elasticity for the micro-constituents and do not consider the *nanostructure* of dentin (Figure 3-3). It is because by assuming homogeneous isotropic constituents at the microstructure, dentin's representative volume element is always stiffer parallel with the axis of tubules. The simple rule of mixtures can explain this anisotropy orientation.

However, if a multiscale model is studied, which beside the microstructure includes the nanostructure or its effects, the orientation of elastic anisotropy is not known before modelling. This unpredictability is because the nanoscale reinforcements in ITD are the mineralized collagen fibrils, which are perpendicular to tubules in many places [12] as visualized in Figure 3-3.

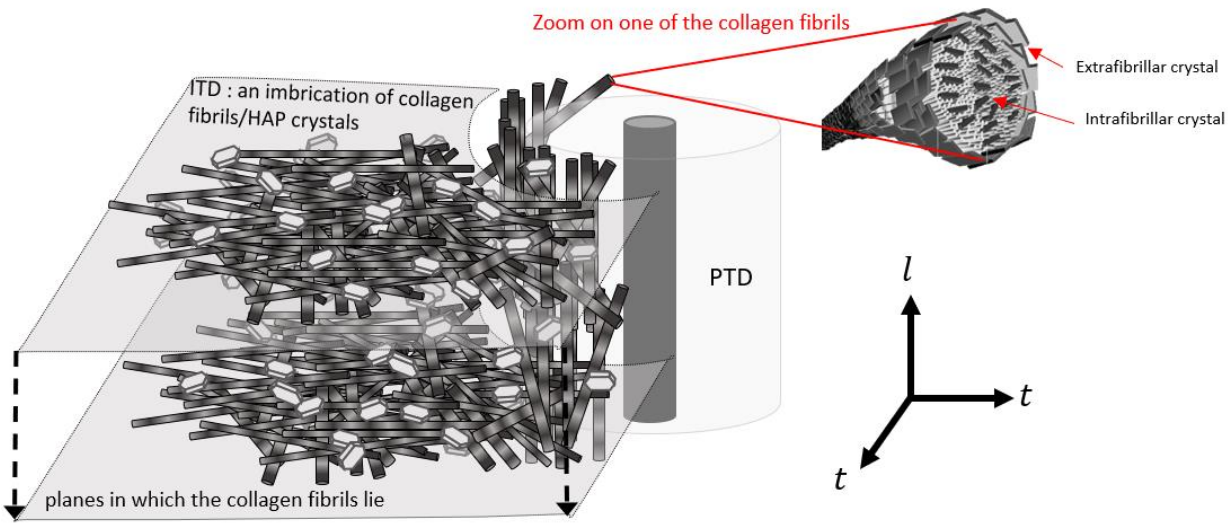

Figure 3-3. Schematic view of the planar nanostructure of ITD, with collagen fibrils that lie in plane perpendicular to the tubules (Courtesy of Dr. E. Vennat)

If the collagen fibrils, which reinforce the intertubular dentin in the transverse plane, outperform the tubules, which reinforce the dentin in the longitudinal direction, then the dentin as a homogenized composite will be stiffer in the transverse orientation. This anisotropy orientation ($E_t > E_l$) is observed near the enamel by Bar-On & Wagner (2012) [97]. They modelled the nanoscale entanglement of collagen fibrils and HAP for the first time. The anisotropy of their model decreased by approaching the pulp. The homogenized modulus in their model was higher near the pulp, which accords with Qin and Swain (2004) [96].

Yoon (2013) [98] combined several micromechanical models to account for the complex hierarchical structure of dentin at the microscale and nanoscale to estimate the effective elastic properties. One of his model's specificities was that he considered variation in the shape of the HAP crystals. This variation is observed in the dimensions of the Hydroxyapatite nanocrystals from the DEJ to the pulp. He found a more pronounced anisotropy near the enamel and a higher transverse modulus than the longitudinal modulus.

Vennat et al. (2017) [7] used FEM simulations to investigate the microstructure's role in dentin's mechanical properties. They concluded that the PTD is there to compensate for porosity's detrimental effect by alleviating the stress concentrations.

A common aspect of all these studies is that they did not consider the lateral branches of the tubules. For the first time, Vennat et al. (2021) [92] accounted for the LBs and their collars in a model, developed in the framework of micromechanical models in periodic media ([99],[100]). Their model overcomes certain limitations of the previous approaches and computed the effective homogenized orthotropic elastic properties of dentin. It has been concluded that the LBs do not affect the elastic stiffness of dentin. However, the LBs influence the fracture behavior of dentin because the LBs cause stress concentration factors as high as 6 at the connection points with the tubules. This is twice the stress concentration factors only due to tubules or lateral branches away from the tubules.

The main conclusions of the mentioned studies are summarized in Table 3-1. In this table, the degree of anisotropy of dentin, d, is defined by the ratio $\mathrm{E}_l/\mathrm{E}_\mathrm{t}$.

Table 3-1. Summary of the results of micromechanical models of dentin in the literature

	Young's modulus/ (Shear modulus)	Anisotropy	Graded stiffness	Considered scale(s)
Kinney et al. (1999) [67]	E~16 GPa/ (G ~ 6.2 GPa)	Negligible anisotropy	Stiffer by moving away from mantle dentin	Microstructure
Qin & Swain (2004) [96]	Near the enamel: E_l=22.5 GPa, E_t=22 GPa Near the pulp: E_l=28 GPa, E_t=24.5 GPa	$\mathrm{E}_l > \mathrm{E}_\mathrm{t}$ Near the enamel: $d = 1.02$ Near the pulp: $d = 1.14$	Stiffer near the pulp	Microstructure
Bar-On & Wagner (2012) [97]		Near the enamel (Low f_T): $\mathrm{E}_l < \mathrm{E}_t \Rightarrow d < 1$ Near the pulp (High f_T): $\mathrm{E}_l > \mathrm{E}_t \Rightarrow d > 1$	Stiffer near the pulp	Nano- and microstructure
Yoon (2013) [98]	Near enamel (plate-like crystals): 20.7 GPa, 23.2 GPa, 25.3 GPa Near pulp (needle-like crystals): 21.0 GPa, 23.4 GPa, 23.1 GPa	$\mathrm{E}_l < \mathrm{E}_t \Rightarrow d < 1$ (more pronounced near enamel)	Stiffer near the pulp	Nano- and microstructure
Seyedkavoosi & Sevostianov (2019) [101]	E_l: 44.5 GPa E_t: 41.6 GPa	$\mathrm{E}_l > \mathrm{E}_\mathrm{t}$ $d = 1.07$	Not studied	Nano- and microstructure
Vennat et al. (2021) [92]	E_l: 21.7 GPa E_t: 20.6 GPa	$\mathrm{E}_l > \mathrm{E}_\mathrm{t}$ $d = 1.05$	Stiffer near the enamel	Microstructure

One noticeable common point revealed in this table is that the elastic anisotropy is relatively low and has various orientations in various studies.

3.3 A recent micromechanics model for dentin

This section summarizes the main elements of the numerical micromechanical model that was used in this thesis. The reader is invited to read the paper by Vennat et al. (2021) [92] for more details.

The periodic cells corresponding to the three considered areas are built based on the observation of the dentin and the morphological data presented in Chapter 1. The cells

comprise tubule lumens (TL), peritubular dentin (PTD), lateral branch lumen (LBL), lateral branch collars (LBC), and intertubular dentin (ITD). This model is implemented in the software COMSOL 5.5.

3.3.1 The geometry of the periodic cell

The morphological properties measured from 2D SEM images are used to define an elementary unit cell of dentin. The unit cell consists of a tubule (T=Tubule Lumen + PTD) along one axis, and four lateral branches (LB=LBL+LBC) perpendicular to it along the other two axes.

By periodically repeating, the repeated unit cell (RUC) generates a periodic microstructure, which is consistent to model a type of dentin observed in a certain volume and at a certain location where the tubule orientation does not vary. Because the tubules are assumed to be positioned on a square lattice as explained in Chapter 1, this repeated unit cell has the form of a brick (Figure 3-4).

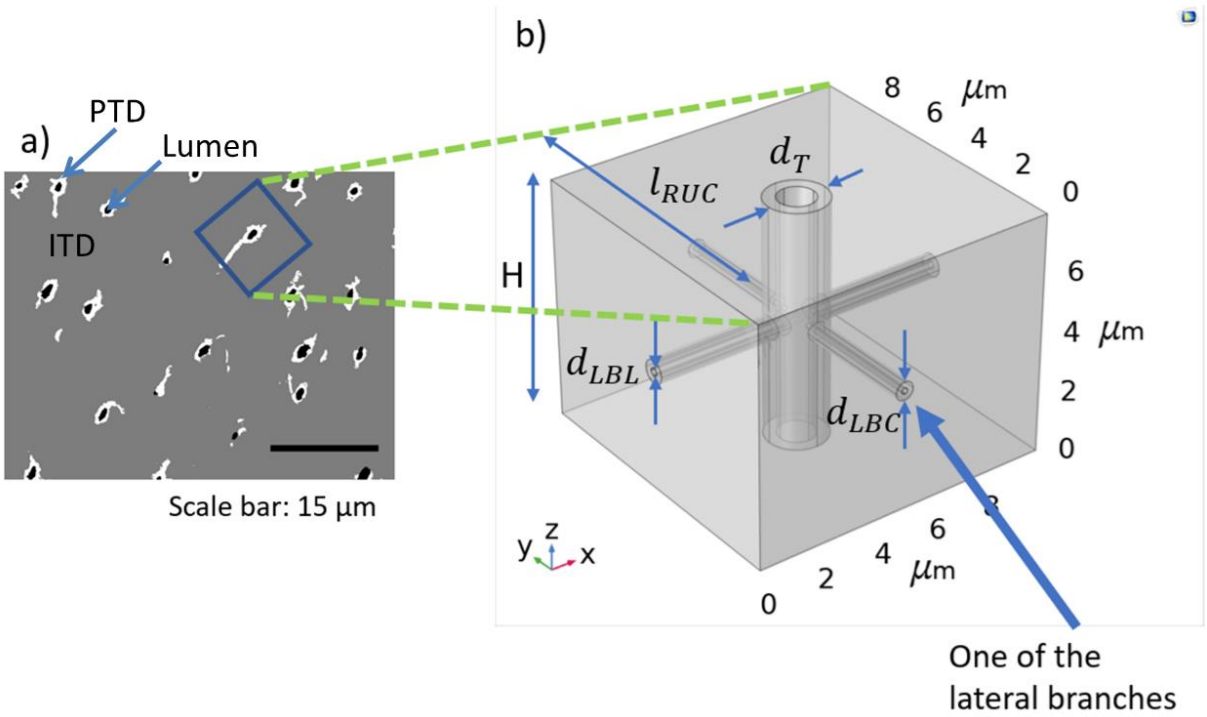

Figure 3-4. Defining a «Repeated Unit Cell » of dentin's microstructure using its morphological properties (Source: author)

The method for estimating the parameters of this geometry is as follows:

The inner and outer diameters of the tubules and the LBs were measured from the SEM images. The side length of the RUC (l_{RUC}) on the other hand, was derived from other morphological parameters. This was done by noticing the fact that the area of the dentin microstructure that includes only one tubule is equal to the inverse of the tubular density ρ so that:

$$l_{RUC} = \sqrt{\frac{1}{\rho}} \tag{3.4}$$

where ρ is number of tubules per unit surface perpendicular to the tubules axes.

Estimating the height of the RUC (H) was done by assuming that the area fraction of LBs visible in the 2D plane (a_{LBs}) and the volume fraction of the LBs are equal. This is according to the Delesse principle, which is explained in Chapter 1 [39]. Therefore, the volume fraction of the LBs (f_{LBs}) is estimated. This estimation is done using the parameters shown in Figure 3-4.b, and is set equal to the area fraction of the lateral branches (a_{LBs}):

$$a_{LBs} \approx 2\frac{\frac{\pi d_{LBC}^2}{4}(l_{RUC} - d_T)}{l_{RUC}^2 H} \tag{3.5}$$

where the variables are introduced in Figure 3-4.

It is reminded that the lumens of the lateral branches (LBLs) are not visible in the SEM images, therefore the area fraction of the bright features, which are the mineralized collars of the LBs, were attributed to the whole LBs (f_{LBs}).

The equation above can be reformulated as:

$$H \approx \frac{\pi d_{LBC}^2 (l_{RUC} - d_T)}{2 l_{RUC}^2 f_{LBs}} \tag{3.6}$$

The estimated dimensions for three RUCs are given in Table 3-2:

Table 3-2. Dimensions of the RUCs that are studied. The images in the first column are named as in Chapter 2.

Images: (Normalized distance from the DEJ)	$\rho\ (\frac{1}{mm^2})$	l_{RUC} (µm)	H (µm)	d_{LBC} (µm)	d_{LBL} (µm)
E (0.12)	10013	10	10.7	0.76	0.27
M1 (0.6)	29402	5.8	14.8	0.6	0.15
P1 (0.96)	38303	5.1	5.1	Not detected	Not detected

The three RUCs studied in this chapter are shown in Figure 3-5.

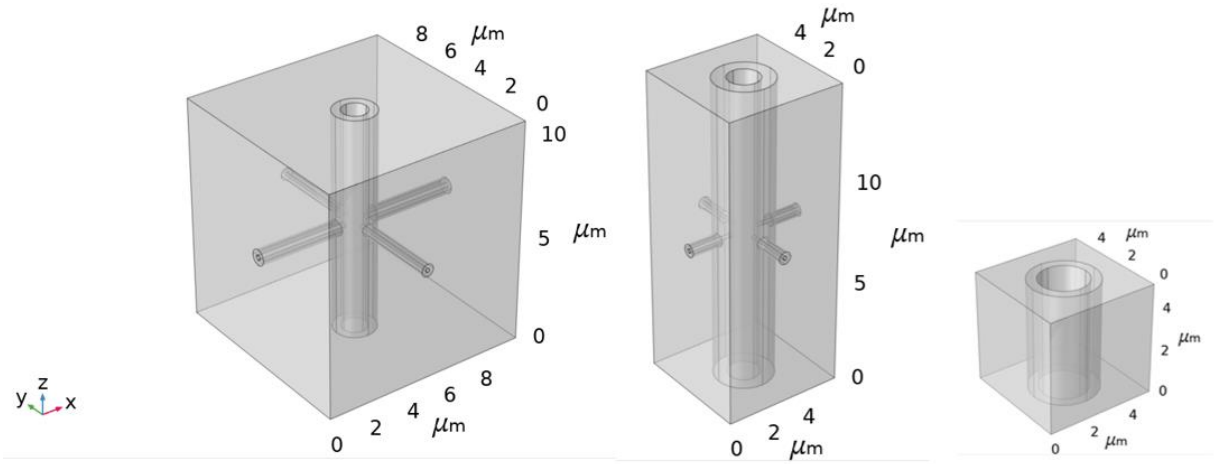

Figure 3-5. Three RUCs near the enamel, in the middle and near the pulp from left to right.

3.3.2 Elastic properties of the constituents

The constituents of dentin are assumed to have elastic isotropic properties. The values for Young's moduli of the PTD (E_{PTD}) and the ITD (E_{ITD}) are taken from Chapter 2 and are recalled in Table 3-3. The Poisson ratios of the constituents are assumed to be 0.3, which is a common assumption.

Table 3-3. Elastic moduli of the constituents of dentin and the Poisson ratio used: Input of the micromechanical model

RUC (Normalized distance from the DEJ)	E_{PTD}	E_{ITD}	ν_{PTD}	ν_{ITD}
E (0.12)	44 GPa	30 GPa	0.3	0.3
M1 (0.6)	45 GPa	29 GPa	0.3	0.3
P1 (0.96)	53 GPa	33 GPa	0.3	0.3

3.3.3 Equations and periodic boundary conditions

The calculations were based on the Elementary Volume Approach ([92]). In this approach, the macro-strains $\bar{\boldsymbol{\varepsilon}}$ and macro-stresses $\bar{\boldsymbol{\sigma}}$ are defined by averaging the resulting strains $\boldsymbol{\varepsilon}$ and stresses $\boldsymbol{\sigma}$ over the volume $\boldsymbol{V}$, respectively:

$$\bar{\boldsymbol{\varepsilon}} = \frac{1}{V}\int_V \boldsymbol{\varepsilon}\, dV \tag{3.7}$$

$$\bar{\boldsymbol{\sigma}} = \frac{1}{V}\int_V \boldsymbol{\sigma}\, dV \tag{3.8}$$

where V is the volume of the repeated unit cell (RUC). In equations 3.7 and 3.8, the local strain $\boldsymbol{\varepsilon}$ is kinematically admissible and the local stress $\boldsymbol{\sigma}$ is statically admissible.

The relation between the macro-strains and macro-stresses determines either the equivalent matrix of stiffness or the equivalent matrix of compliance. The following average theorems allow connecting the average quantities to the boundary conditions:

- The average stress theorem: when at each point of the boundary surface S, the traction vector $\boldsymbol{T}_0 = \boldsymbol{\sigma}_0 \boldsymbol{n}$ is applied with a constant $\boldsymbol{\sigma}_0$, and $\boldsymbol{n}$ is the outer normal unit vector, it results:

$$\bar{\boldsymbol{\sigma}} = \boldsymbol{\sigma_0} \tag{3.9}$$

Although the local stress inside the RUC is not uniform.

- The average strain theorem: when at each point of the boundary surface S, the displacement vector $\boldsymbol{u}_0 = \boldsymbol{\epsilon}_0 \boldsymbol{X}$ is applied with a constant $\boldsymbol{\epsilon}_0$ and $\boldsymbol{X}$ is the global coordinate, it results:

$$\bar{\boldsymbol{\epsilon}} = \boldsymbol{\epsilon_0} \tag{3.10}$$

Although the local strain inside the RUC is not uniform.

To apply the average strain theorem to periodic medium, the displacement vector $\boldsymbol{u_0}$ is decomposed as:

$$\boldsymbol{u_0}(\boldsymbol{X}, \boldsymbol{x}) = \boldsymbol{\epsilon_0 X} + \boldsymbol{u}^*(\boldsymbol{x}) \tag{3.11}$$

where $\boldsymbol{\epsilon_0}$ is a constant and $\boldsymbol{x}$ is the local coordinate in the RUC and $\boldsymbol{u}^*$ is a periodic vector depending on the local coordinate.

In practice, considering the RUC defined in Figure 3-6, for two opposite surfaces S_{src} and S_{dst}, the equations follow:

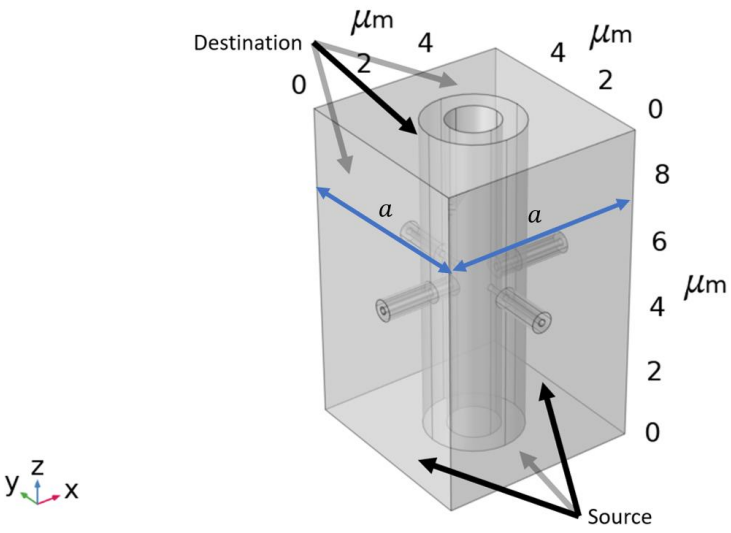

Figure 3-6. Defining source and destination faces for the boundary conditions of the RUC

$$\boldsymbol{u}_{src} = \bar{\boldsymbol{\varepsilon}} \boldsymbol{X}_{src} + \boldsymbol{u}^* \tag{3.12}$$

$$\boldsymbol{u}_{dst} = \bar{\boldsymbol{\varepsilon}} \boldsymbol{X}_{dst} + \boldsymbol{u}^* \tag{3.13}$$

By subtracting the 3.12 and 3.13 equations, the constraint 3.14 is resulted:

$$\boldsymbol{u}_{dst} - \boldsymbol{u}_{src} = \bar{\boldsymbol{\varepsilon}} (\boldsymbol{X}_{dst} - \boldsymbol{X}_{src}) = \bar{\boldsymbol{\varepsilon}} a \tag{3.14}$$

where a is the distance between the facing sides.

3.3.4 Meshing and element type of the RUC

In the study by Vennat et al. (2021) [92] the meshing was implicit. The interested reader is referred to the paper for further information. However, in this thesis the geometry of the RUC was meshed in COMSOL explicitly and automatically by tetrahedral elements of quadratic type.

The possible presence of singularities in the geometry (distortion of the FE) might generate locally inaccurate estimations of the computed stresses. Notably at the junction between tubules and lateral branches on the one hand and on the other hand at the interface between collar and void. The mesh size can play a role in this issue. To avoid such problems, a numerical analysis was done on one of the RUCs. This analysis included various simulations with various element sizes. Because the most accurate estimate of the stress field results from the finest mesh, different computations were compared. The critical zone of the RUC is located at the interface between the mineralized collar and lumen at the connection point of tubule and lateral branch. This zone is shown in Figure 3-7 and Figure 3-8.

In particular, it is verified that the maximum Stress Concentration Factor (SCF) of the first principal stress does not vary unstably by varying the mesh size. The verification is done by comparing the SCF for various mesh sizes. The SCF for the first principal stress is defined as the local first principal stress σ_I divided by the first principal stress averaged in the volume $\bar{\sigma}_I$:

$$SCF = \frac{\sigma_I}{\bar{\sigma}_I} \tag{3.15}$$

The minimum element size as listed in Table 3-4 is defined in the software and regulates the mesh size at the interface between the lumen and collars (Figure 3-7). Hence, the minimum element size in this particular case is an indicator of the mesh size at the sensitive interface between the lateral branch lumen and lateral branch collar.

Table 3-4. Maximum SCF for various element sizes

Minimum element size (µm)	Maximum SCF of first principal stress (normal loading parallel with the LBs)
0.02	7.22
0.04*	**7.14**
0.06	5.7
0.08	7.38
0.12	7.49
0.24	6.6

* size defined for the computations

The mesh with the minimum element size of 0.04 µm (Figure 3-7) is a good compromise between the desired precision and the duration of the FE simulation. For comparison, the

mesh with a minimum element size of 0.12 is also shown in Figure 3-8, which has bigger elements.

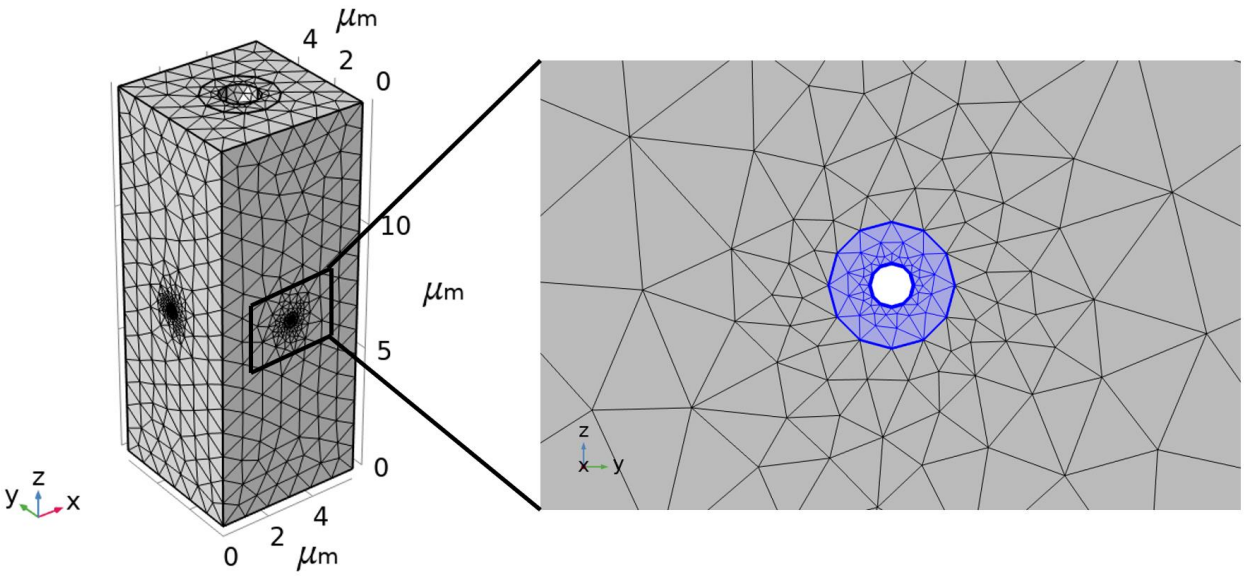

Figure 3-7. Tetrahedral mesh used for discretization of the geometry (minimum element size: 0.04 µm)

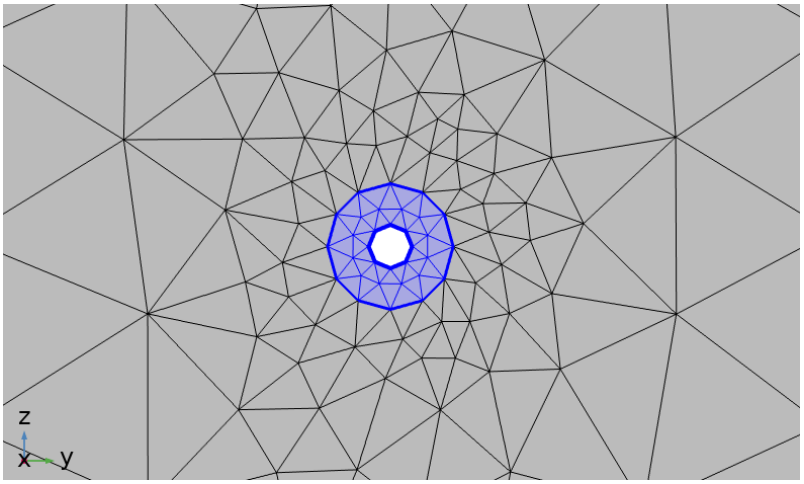

Figure 3-8. Tetrahedral mesh used for discretization of the geometry (minimum element size: 0.12 µm)

3.3.5 Six modes of deformation to identify the elastic properties

To identify the stiffness tensor $\overline{\boldsymbol{C}}$, simulation of the six modes of deformation (3 normal and 3 shear load cases) were done by applying the periodic conditions (Voigt notation adopted here):

$$\bar{\boldsymbol{\varepsilon}}_{\mathbf{1}} = \begin{bmatrix} 1 \\ 0 \\ 0 \\ 0 \\ 0 \\ 0 \end{bmatrix}, \bar{\boldsymbol{\varepsilon}}_{\mathbf{2}} = \begin{bmatrix} 0 \\ 1 \\ 0 \\ 0 \\ 0 \\ 0 \end{bmatrix}, \bar{\boldsymbol{\varepsilon}}_{\mathbf{3}} = \begin{bmatrix} 0 \\ 0 \\ 1 \\ 0 \\ 0 \\ 0 \end{bmatrix}, \bar{\boldsymbol{\varepsilon}}_{\mathbf{4}} = \begin{bmatrix} 0 \\ 0 \\ 0 \\ 1 \\ 0 \\ 0 \end{bmatrix}, \bar{\boldsymbol{\varepsilon}}_{\mathbf{5}} = \begin{bmatrix} 0 \\ 0 \\ 0 \\ 0 \\ 1 \\ 0 \end{bmatrix}, \bar{\boldsymbol{\varepsilon}}_{\mathbf{6}} = \begin{bmatrix} 0 \\ 0 \\ 0 \\ 0 \\ 0 \\ 1 \end{bmatrix}, \tag{3.16}$$

As shown in Figure 3-9, the three first load cases correspond to normal loads in respectively x, y, and z orientations. The next three load cases correspond to shear loads in respectively xy, xz, and yz planes.

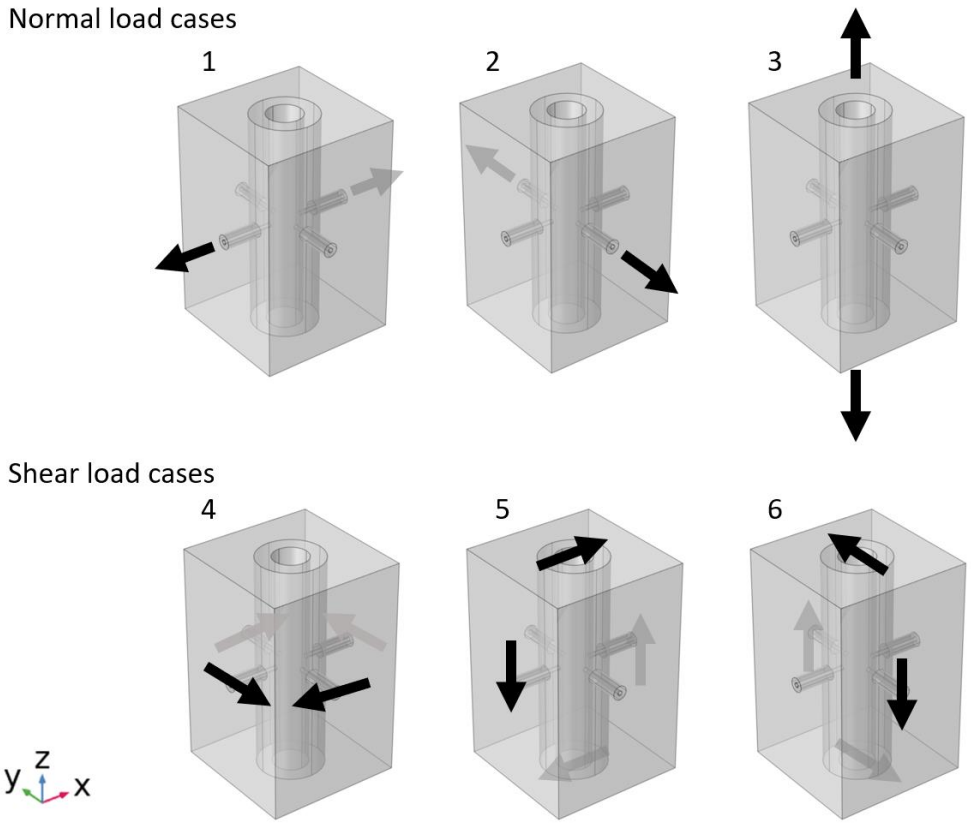

Figure 3-9. The six loadings that are used to calculate the stiffness matrix of the repeated unit cell.

From these simulations, after calculations of the average macro-stresses $\overline{\boldsymbol{\sigma}}$, the stiffness matrix $\overline{\boldsymbol{C}}$ can be determined. Then it is inversed to obtain the compliance matrix (S), as the elastic constants of an anisotropic material are more easily identified from the compliance matrix:

$$\overline{\boldsymbol{S}} = \overline{\boldsymbol{C}}^{-1} \tag{3.17}$$

By assuming transverse isotropy due to geometric symmetries visible in Figure 3-9, the homogenized repeated unit cell has a compliance matrix in the shape shown in equation 3.18. The results of the calculations are presented in the following subsections.

Dentin is considered as a transverse isotropic elastic material and due to the geometric symmetries visible in Figure 3-9, the compliance matrix written by using Voigt notation reads ([102]):

$$S = \begin{bmatrix} \frac{1}{E_t} & -\frac{\nu_{tt}}{E_t} & -\frac{\nu_{tl}}{E_t} & 0 & 0 & 0 \\ -\frac{\nu_{tt}}{E_t} & \frac{1}{E_t} & -\frac{\nu_{tl}}{E_t} & 0 & 0 & 0 \\ -\frac{\nu_{lt}}{E_l} & -\frac{\nu_{lt}}{E_l} & \frac{1}{E_l} & 0 & 0 & 0 \\ 0 & 0 & 0 & \frac{1}{G_{lt}} & 0 & 0 \\ 0 & 0 & 0 & 0 & \frac{1}{G_{lt}} & 0 \\ 0 & 0 & 0 & 0 & 0 & \frac{1}{G_{tt}} \end{bmatrix} \quad (3.18)$$

3.4 Results and discussion

In this section, the effective elastic properties of the RUCs of dentin obtained by the micromechanical model are presented. The effects of various parameters such as the lateral branches, aging, and anisotropy of the ITD on the homogenized or effective elastic properties are studied.

In addition, the stress distributions in the RUCs are presented and a focus is done to evaluate the presence of lateral branches.

3.4.1 Local variation of the homogenized elastic properties in tooth

Finite element simulation with the three RUCs related to various locations in dentin, allowed studying the local variation in the homogenized elastic properties of dentin. In Table 3-5, the identified elastic constants for the RUCs are shown.

Table 3-5. Elastic properties obtained by FE homogenization at the enamel (E), in the middle (M1), and near the pulp (P1)

	E	M1	P1
E_t (GPa)	29.3	28.3	25.5
E_l (GPa)	29.8	30.8	31.0
G_{tl} (GPa)	11.4	11.3	10.6
G_{tt} (GPa)	11.3	10.8	9.0
ν_{tl}	0.29	0.28	0.25
ν_{lt}	0.3	0.3	0.3
ν_{tt}	0.3	0.3	0.29
Degree of anisotropy ($d = E_l/E_t$)	1.02	1.09	1.22

In addition, in Table 3-6 the elastic moduli in the longitudinal and transverse orientations are compared with the Voigt (E_V) and modified Reuss (E_R^*) estimates.

Table 3-6. Measured elastic moduli from the three RUCs together with Voigt and modified Reuss estimates

	E	M1	P1
E_l (GPa)	29.8	30.8	31.0
E_V (GPa)	30.0	29.6	31.1
E_t (GPa)	29.26	28.33	25.51
E_R^* (GPa)	32.86	29.54	30.74

The data in Table 3-5 and Table 3-6 reveal several important points:

1) Young's modulus E_l in the direction of the tubules axis is less affected by the change of the microstructure (increase of 3.3%), probably because the increase in porosity is partly compensated by thickening of the peritubular cuffs.
2) Young's modulus E_t in the direction perpendicular to the tubules axis is more sentitive to the microstructure variation (decrease of 15.4%).
3) The shear moduli G_{tt} and G_{tl} decrease from the enamel to the pulp but G_{tt} is more sensitive to the microstructure (decrease of 20.4%) than G_{tl} (decrease of 7.0%).
4) G_{tt} is smaller than G_{tl} because shear in the transverse plane "tt" does not cause a longitudinal deformation in the tubule, while shear in a longitudinal plane "lt" deforms the tubule longitudinally. This order in value is the same as the one reported by Vennat et al. (2021) [92].
5) G_{tt} is smaller than G_{tl}. The shear modulus in the transverse plane is smaller because shear in the transverse plane "tt" does not cause a longitudinal deformation in the tubule, while shear in a longitudinal plane "lt" deforms the tubule longitudinally. This order in value is the same as the one reported by Vennat et al. (2021) [92].
6) ν_{tl} is smaller than ν_{lt} and ν_{tt}, which accords with the study by Vennat et al. (2021) [92], because ν_{tl} represents a case where a load in the softer orientations (transverse), induces a deformation in the stiffer orientation (longitudinal).
7) The degree of elastic anisotropy is very low near the enamel. It increases gradually when approaching the pulp. This trend confirms the observations by Qin & Swain (2004) [96].

The elastic moduli in the direction parallel with the tubules (E_l) are very close to the Voigt model (E_V), which is due to fact that for measuring the E_l the RUC is loaded parallel with the tubule as shown in Figure 3-9, load case 3. In this configuration, the microstructure is parallel with the loading except for the LBs. The fact that E_l at "M1" is higher than the Voigt bound should be due to numerical errors.

Contrary to the good performance of the Voigt bound, the modified Reuss bound does not show an acceptable performance. Especially near the enamel "E", the modified Reuss bound is higher than the Voigt bound, which is known to be the upper bound.

Therefore, for estimating the properties of dentin, only the Voigt bound is recommended, which can give an acceptable estimate for the longitudinal modulus E_l. The modified Reuss bound cannot approximate the transverse modulus with success.

Effect of the lateral branches

In this section, the effect of the LBs on the elastic properties of dentin is investigated. This is done by comparing the results of the RUC "M1" with LBs and another with the same geometry but without LBs. The results are summarized in Table 3-7:

Table 3-7. Comparison of the elastic properties obtained by FE homogenization at the location "M1" with and without LBs

	The model with LBs	The model without LBs
E_t (GPa)	28.3	28.4
E_l (GPa)	30.8	30.8
G_{tl} (GPa)	11.3	11.3
G_{tt} (GPa)	10.8	10.8
ν_{tl}	0.28	0.28
ν_{lt}	0.3	0.3
ν_{tt}	0.3	0.3
Degree of anisotropy ($d = E_l/E_t$)	1.09	1.08

The results show that the LBs do not have a significant effect on the elastic stiffness in the middle of dentin. In Vennat et al. (2021) [92], the same result is reported. This is because the volume content of the LB is very low in comparison with the matrix.

Effect of aging

To introduce the effect of aging on dentin, sclerotic dentin (explained in section 1.1.2), is modelled by filling the lumens of tubules and LBs with PTD material. The geometry of the sclerotic RUC defined at the location "M1" is shown in Figure 3-10.

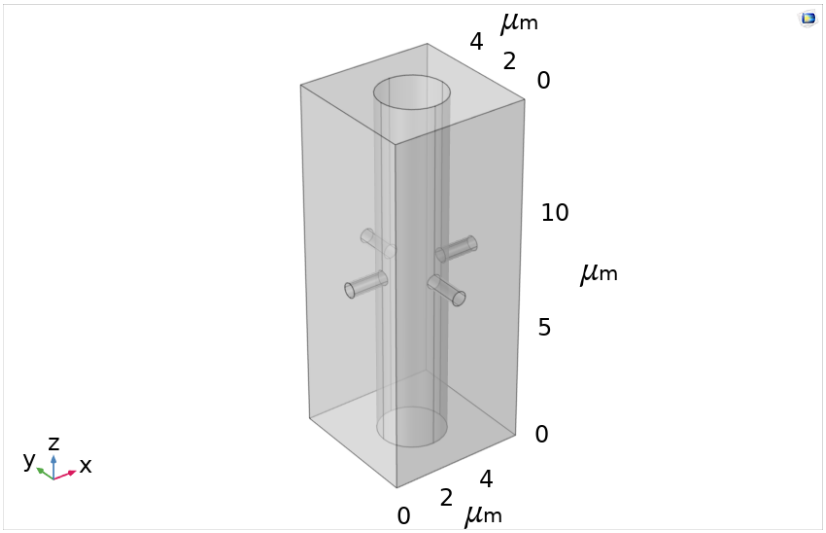

Figure 3-10. « RUC » with filled tubules and LBs to model sclerotic dentin

The results from this simulation is compared with the previous one (non-sclerotic dentin) in Table 3-8.

Table 3-8. Comparison of the results from sclerotic and non-sclerotic RUCs

	Non-sclerotic	Sclerotic
E_t (GPa)	28.3	31.0
E_l (GPa)	30.8	31.5
G_{tl} (GPa)	11.3	11.9
G_{tt} (GPa)	10.8	11.9
ν_{tl}	0.28	0.29
ν_{lt}	0.3	0.3
ν_{tt}	0.3	0.3
Degree of anisotropy ($d = E_l/E_t$)	1.09	1.02

In addition, the elastic moduli of sclerotic dentin in the transverse and longitudinal orientations are visualized in Figure 3-11. For comparison, the results from non-sclerotic RUCs of dentin are shown too.

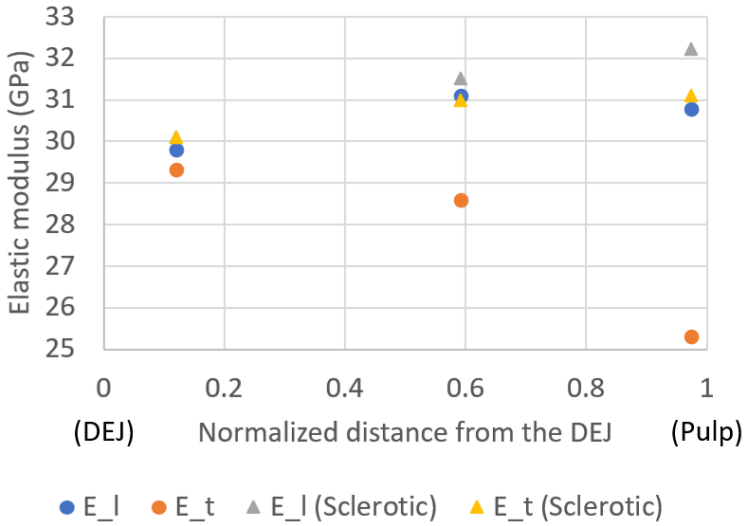

Figure 3-11. Comparison of the moduli of normal and sclerotic dentin

The degree of elastic anisotropy for sclerotic and non-sclerotic dentin are summarized in Table 3-9.

Table 3-9. Degree of anisotropy in various locations in dentin for sclerotic and non-sclerotic dentin

Degree of anisotropy	Non sclerotic	Sclerotic
E	1.22	1.04
M	1.09	1.02
P	1.02	1.00

By observing these results, two points are concluded:

- Sclerosis slightly stiffens the dentin because the voids are filled. E_l and E_t move upward as shown in Figure 3-11.

- Sclerosis slightly decreases the elastic anisotropy, especially near the pulp cavity. As shown in the same figure, E_l and E_t become closer together. The degree of anisotropy is reported in Figure 3-11.

However, Arola & Reprogel (2005) [103] do not support the stiffening of dentin due to sclerosis. This may be true, because in our model, the quality of PTD and ITD, as represented by their elastic modulus, has not varied in sclerotic dentin. Nevertheless, the minerals of ITD are reported to be dissolved during the sclerosis [16]. Besides, in our model the PTD that fills up the lumens is continuous with the cuff around it, even though in reality there is an interface between the material inside the lumen and the peritubular cuff (Figure 3-12), with a behavior not reflected in this model.

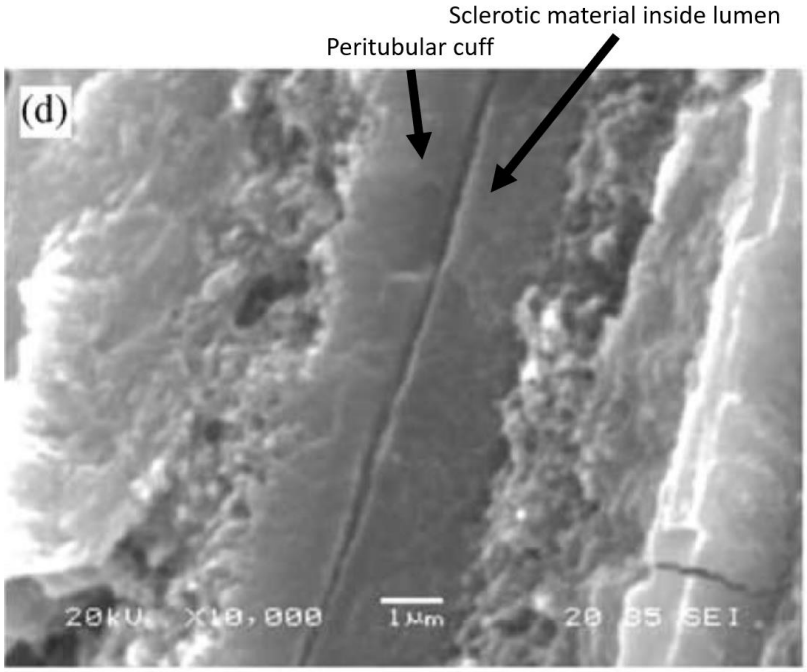

Figure 3-12. Fractured surface of sclerotic dentin [103]

Effect of the anisotropy of ITD

In this section, the effect of the anisotropy of the ITD on the homogenized dentin is shown.

As seen in section on "Local variation of the homogenized elastic properties in tooth", with elastic isotropic PTD and ITD, the tubules cause an elastic anisotropy with a higher modulus parallel with their orientation.

For having a better idea of how anisotropic the ITD is and in which direction, the degree of anisotropy, which was defined for the whole dentin and was characterized by parameter d, is also defined for ITD (d_{ITD}). d_{ITD} is bigger than one if the ITD is stiffer parallel with the tubules and is smaller than one if it is stiffer perpendicular to the tubules.

In several simulations, different degrees of elastic anisotropy for ITD in both orientations (parallel with or perpendicular to the tubules) were considered. Their effects on the homogenized Young's moduli of dentin are shown in Figure 3-13.

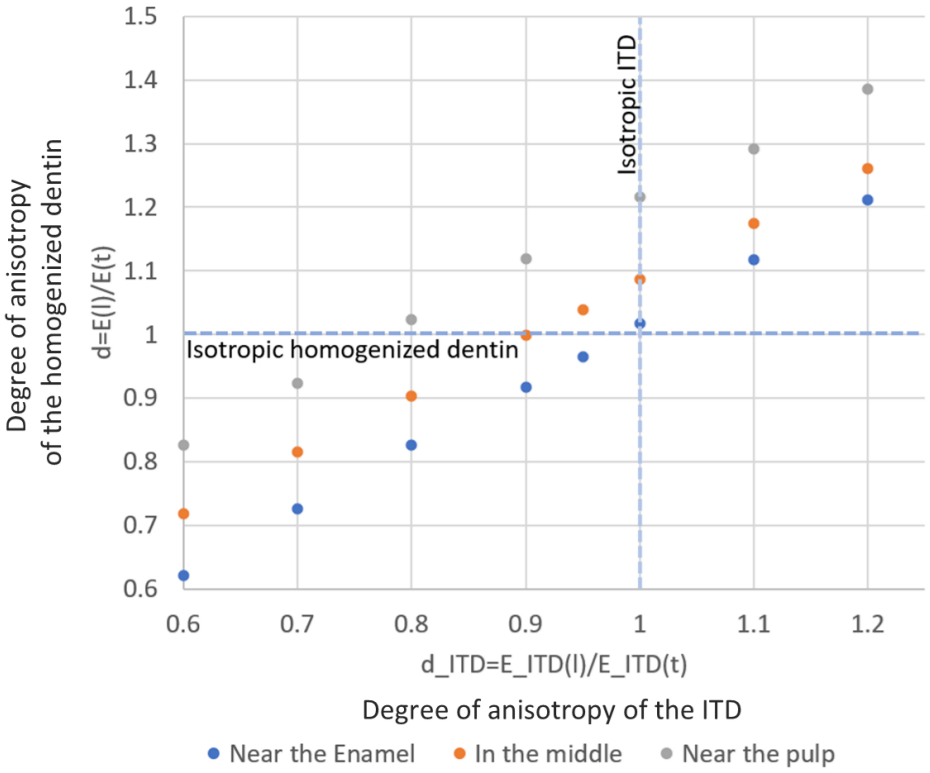

Figure 3-13. Effect of the ITD's anisotropy on the anisotropy of the homogenized dentin

In summary, the following points can be highlighted:

1) If as claimed by the experimental study by Ziskind et al. (2011) [66] ITD is stiffer parallel with the tubules ($d_{ITD} = 1.22$), then the anisotropy of ITD and tubules add up. It will be always the case that $E_l > E_t$ and $d > 1$, which is in the right side of the vertical dashed line in Figure 3-13.
2) But if the ITD is stiffer perpendicular to the tubules ($d_{ITD} < 1$), shown by the left side of the vertical dashed line in Figure 3-13, there might be different results:
    - For a low density of tubules (e.g., near the enamel), the anisotropy due to tubules is less significant and it is less probable for the anisotropy of ITD to be cancelled out. Therefore, it is more probable that $d < 1$.
    - For a higher density of tubules (e.g., near the pulp), the more significant anisotropy due to tubules is more likely to cancel out the anisotropy of ITD or even change the orientation of the anisotropy in its own favor, which leads to $d \approx 1$ or even $d > 1$.

The local variation in the elastic anisotropy that is observed here agrees with both Bar-On & Wagner (2012) [97] and Qin & Swain (2004) [96], who reported an anisotropy degree bigger than one, which increases by approaching the pulp. Figure 3-13 also explains the anisotropy stated by Yoon (2013) [98] who reported a more pronounced anisotropy near the enamel. In his study, a $d < 1$ was observed that became even smaller by approaching the enamel. The same trend is observed for the data associated with $d_{ITD} = 0.7$ in Figure 3-13.

Parametric study of the elastic modulus of PTD

As mentioned in Chapter 2, measurement of E_{PTD} is more prone to errors than E_{ITD}. The question arises that how important a change in E_{PTD} due to unrecognized errors is for the homogenized modulus of dentin. The variation in the homogenized modulus obtained by the micromechanical model considering the RUC in the middle dentin is shown in Figure 3-14.

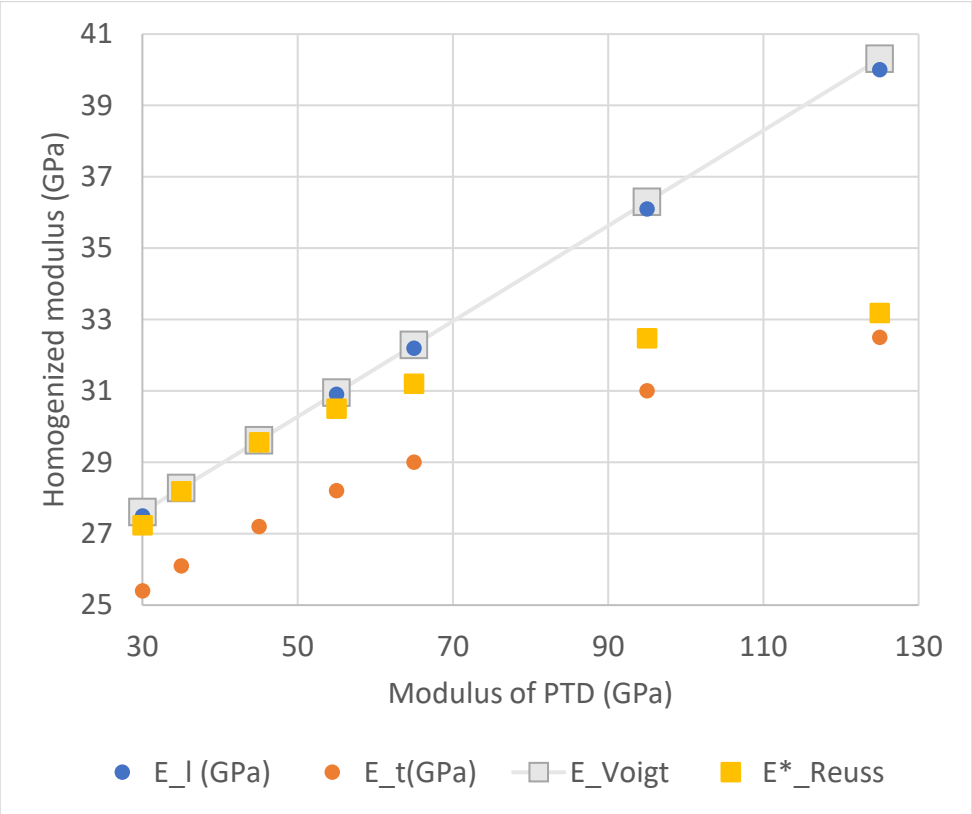

Figure 3-14. Parametric study of the modulus of PTD (Its effect on the analytical estimates and the numerically homogenized moduli)

By comparing Young's moduli resulting from various values of E_{PTD} with the experimental results discussed in section 2.6.1, the following points are noted:

- The Voigt bound corresponds well with the longitudinal modulus that is obtained from numerical simulation. This can be understood by the fact that the constituents in the RUC, have an assembly that is relatively parallel with the orientation of the acquired elastic modulus.
- As shown in Figure 3-14, the modified Reuss model is not a good estimate for E_t at reasonable values of E_{PTD} but it seems to become more acceptable E_{PTD} is unrealistically high (over 130 GPa).
- By increasing the difference between the moduli of ITD and PTD, for example varying E_{PTD} from 30 to 125 GPa, the anisotropy logically increases. The value of d increases from 1.08 to 1.23 due to tubule orientation and high stiffness of the reinforcement.

Increasing E_{PTD} to 50 GPa can be assumed acceptable because as discussed in Chapter 2, it is usually underestimated.

3.4.2 Stress concentration around tubules and especially LBs in dentin

The failure strength of many materials is sensitive to holes or notches [104]. In such cases, the stress concentration factor (SCF) around the holes should be investigated.

Analysis of stress around a cylindrical hole in a plate under tension (Kirsch's solution)

As a first step, a simplified geometry is studied (Figure 3-15), namely the stress distribution around a circular hole in a plate subjected to a uniaxial tensile loading 'σ_{inf}'. The geometrical parameters of the problem are the following: the hole has a radius of 'a' (and a diameter '$d = 2a$'). The plate has a width of 'W' and a length of 'L'. By assuming 'W' to be infinite, the well-known Kirsch's solution (1898) is obtained [105].

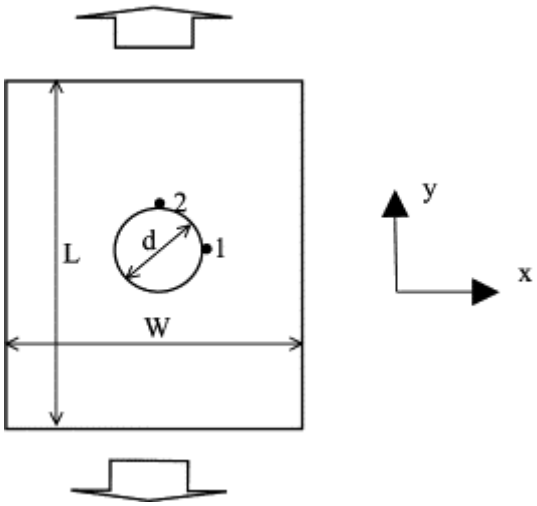

Figure 3-15. A plate with a circular hole under uniaxial tension ([104]): a) drawn of the perforated plate; b) hoop stress distribution around the hole in the semi-infinite medium

According to the Kirsch's solution, the hoop stress '$\sigma_{\theta\theta}$' is positive and the highest at point 1 in Figure 3-15, where $\sigma_{\theta\theta} = 3\sigma_{inf}$. Point 1 is at the hole interface ($r = a$) and in the plane perpendicular to the uniaxial tensile load. The hoop stress '$\sigma_{\theta\theta}$' becomes negative and compressive when it reaches the point 2: $\sigma_{\theta\theta} = -\sigma_{inf}$. The usual stress concentration factor ($SCF = \sigma_{\theta\theta}/\sigma_{inf}$) varies from +3 to –1, the critical area being the point 1. By getting far from the hole, the stresses become close to the original overall tensile stress. This case is a reference case for the following study. This solution is approximately correct if the W and L are not infinite, but W/a and L/a are high enough.

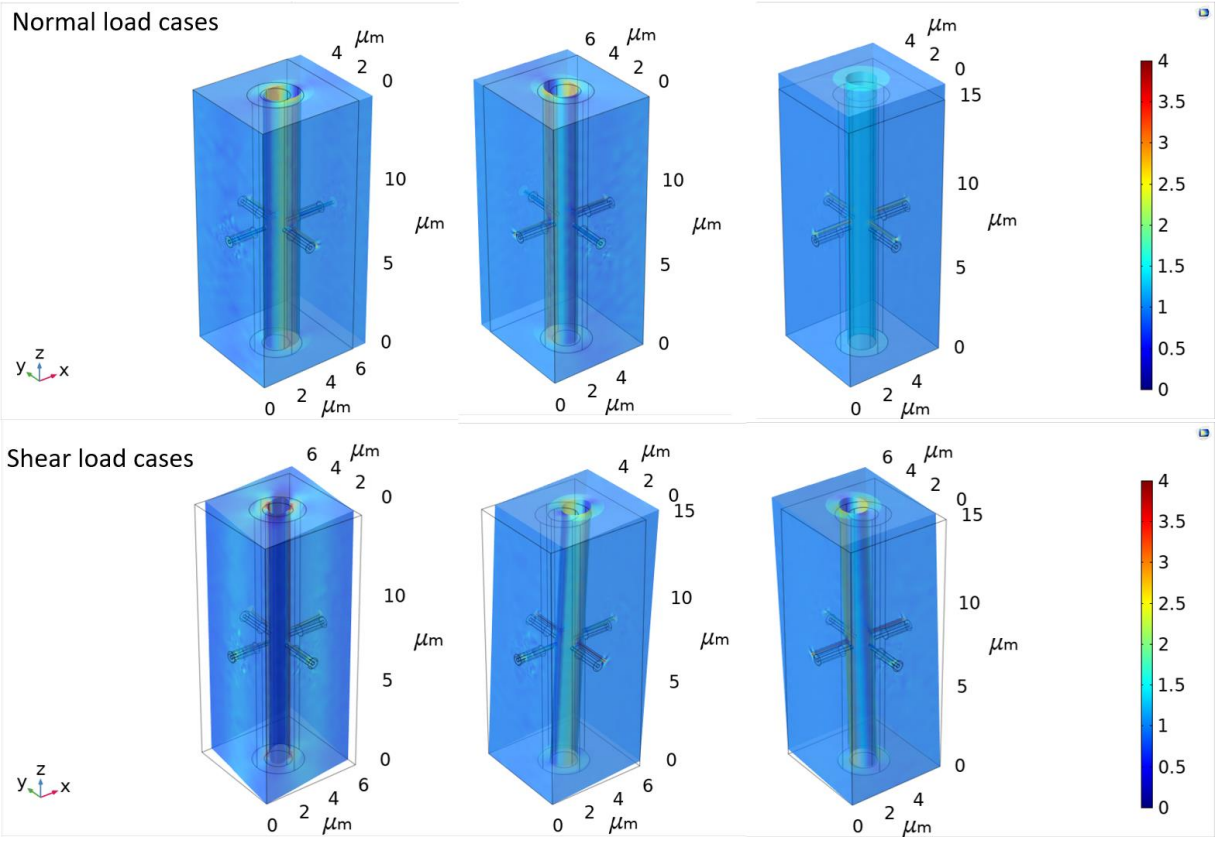

Figure 3-16. The distribution of the SCF of first principal stress in six fundamental modes of deformation (three normal and three shear load cases), RUC 'M1'

Based on what was said, for loadings perpendicular to the tubules or lateral branches, a similar stress concentration is expected around the lumens.

The distribution of the Stress Concentration Factor in the repeated unit cell: effect of the LBs

Figure 3-16 shows the distribution of the first principal stress (σ_I) in the RUC 'M1' for the six fundamental load cases.

Next, the distributions of the stress concentration factor when applying uniaxial traction in two perpendicular directions are analyzed on a plane: case 2 and case 3 shown in Figure 3-9, which are tractions in the x- or y-orientation of LBs or in the z-orientation of the tubule. The maps are shown respectively in Figure 3-17 and Figure 3-18.

The SCF of the maximum principal stress (σ_I) is plotted in Figure 3-17 on the symmetry plane of the RUC (xz) when a normal load is applied perpendicularly to it (in y-orientation). This plot reveals that the highest value of SCF is near 6.6 when the load is perpendicular to the tubule and the LBs. The maximum SCF happens at the connection point of the tubule and the LBs (Figure 3-17.a, and Figure 3-17.b).

a) b)

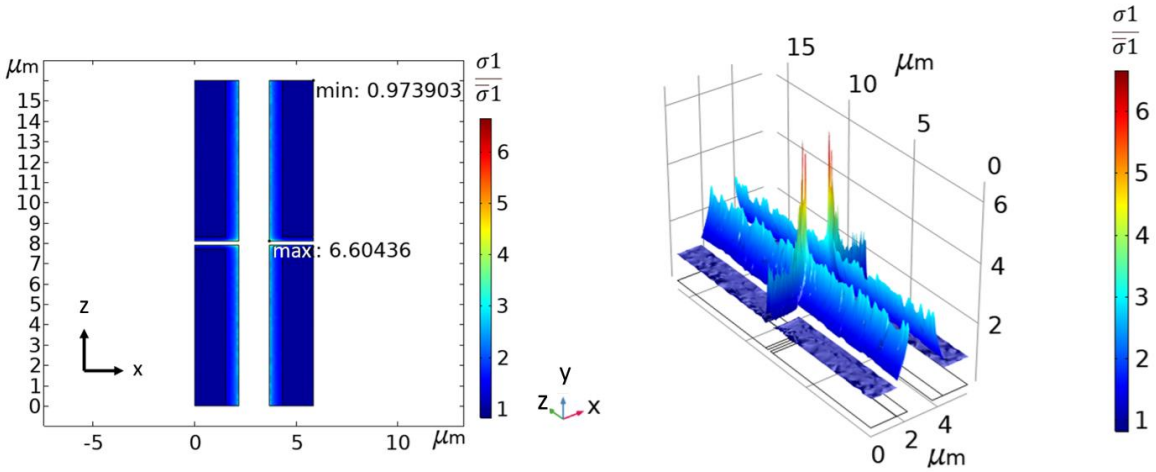

Figure 3-17. Concentration pattern of the first principal stress due to a load perpendicular to the tubules and LBs

However, this high SCF is focused on a very small area. SCF decreases rapidly to values around 4 when moving away from this area. In the real geometry of the microstructure sharp corners probably do not exist. Therefore, the maximum value of SCF is expected to be lower than the estimated one. Nevertheless, the connections between the tubules and the LBs are clearly weak zones where failure may appear due to a higher stress concentration than only a LB or a tubule.

The stress concentration factor distribution due to the load case 3, shown in Figure 3-18.a and Figure 3-18.b indicates that the SCF is lower than in the previous cases as high as the previous load case.

a) b)

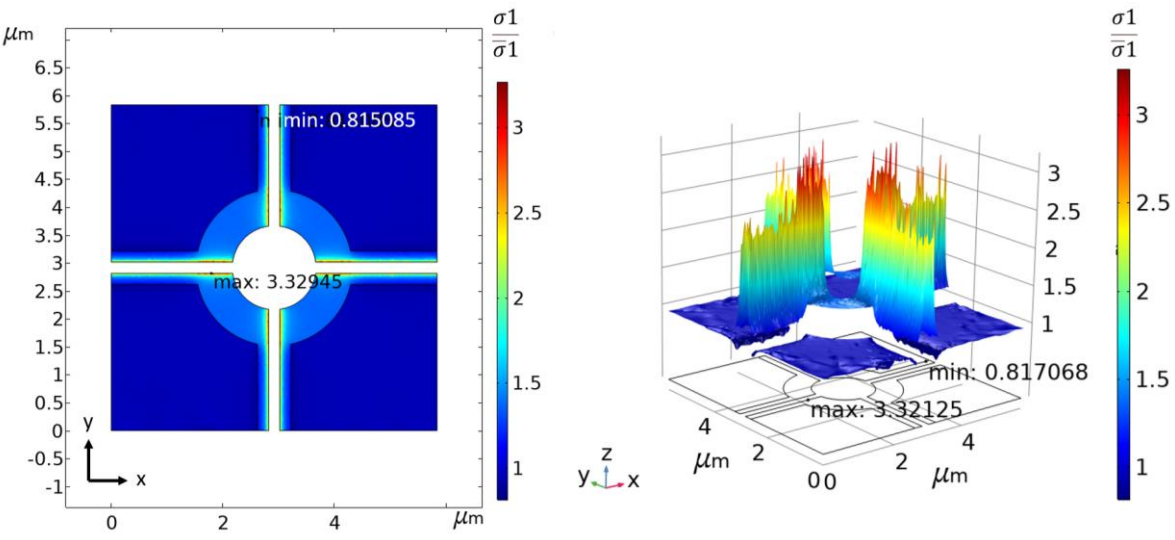

Figure 3-18. Concentration pattern of the first principal stress due to a load perpendicular to the LBs and parallel with the tubule

The maximum SCF in the load case shown in Figure 3-17, which agrees with the results of Vennat et al. (2021) [92], can be understood by the following analysis. In the load case 1, the

encircled point is the location where the load is perpendicular to two connected cylindrical holes. Each cylindrical hole causes a SCF of approximately 3 and the interaction of those SCFs is inducing a very high SCF when the LBs are considered. However, this is not the case for the load case 3, where the load is perpendicular to two cylindrical holes, which are not connected. This is shown in Figure 3-19.b, where the dashed yellow lines, which are drawn on the inner sides of the lumens of tubules and LBs do not intersect.

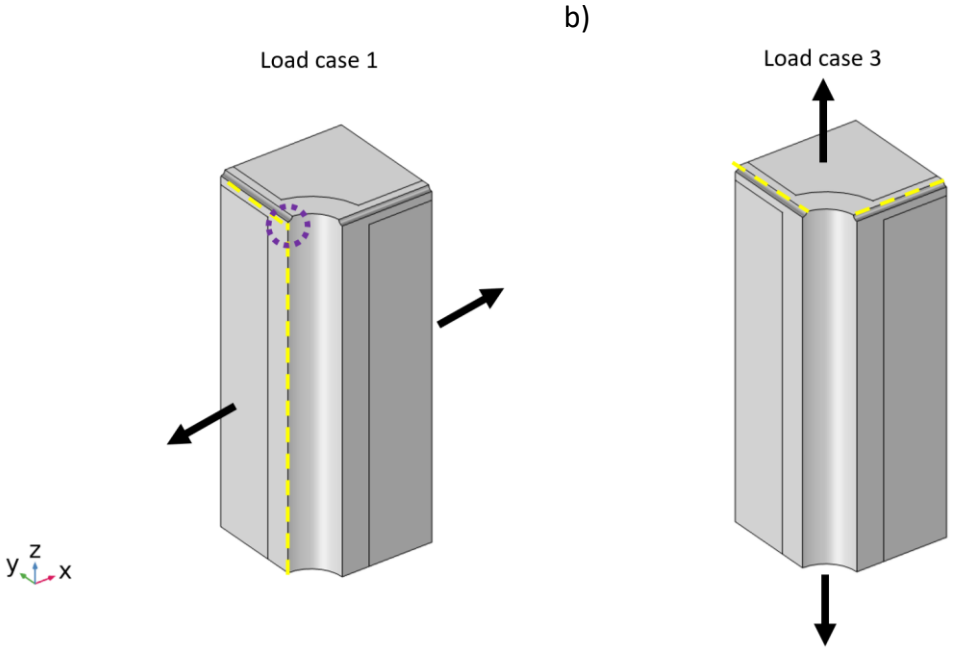

Figure 3-19.a) the point with the highest SCF is encircled. b) a load case with a less critical stress concentration

Continuous production of PTD: a way of repairing dentin?

The previous results confirm that the inner surfaces of peritubular cuffs and lateral branch collars and above all their intersections are candidates for microcrack initiation. But a natural restoration mechanism may limit the risk of microcrack propagation during the numerous masticatory cycles of daily life as the space between the crack lips are probably refilled with the continuously depositing PTD [11].

This hypothesis should be validated by an experimental study of the hypermineralized cuffs. An idea could be to try to see a refilled crack which is probably recognizable by the orientation of its HAP crystals. For this Transmission Electron Microscopy (TEM) observations could be led to analyze the nanostructure of dentin, as discussed in a preliminary study presented in appendix A.

As mentioned, in some cases the PTD finally fills the tubules and makes the dentin sclerotic. The stress concentration was calculated for a sclerotic RUC, which led to a modest maximum SCF of approximately 1.2. This highlights the effect of the porous phase, i.e., lumens of tubules and LBs in causing stress concentration. The lower stress concentrations for the

sclerotic dentin means a higher resistance of dentin. However, this comes with the price of lowering the toughness of dentin [17].

3.5 Conclusion

In this chapter, a micromechanical model was used to characterize the behavior of dentin at the microscale. This scale was chosen to study the effect of the microstructure features, namely the tubules and lateral branches. The main findings on the elastic behavior of dentin follow:

- The LBs do not significantly affect the elastic properties of dentin.
- The elastic anisotropy of dentin due to the tubular structure increases by moving from the enamel to the pulp.
- The anisotropy of ITD, due to the orientation of collagen fibrils, partially cancels out the anisotropy due to the tubules.

The FE simulations allow computing the stress distribution inside the repeated unit cell and reveal the importance of the connection between the tubules and lateral branches, notably in terms of stress concentration. When dentin is loaded in the orientation parallel with the LBs, the stress concentrations due to the tubule and the LB interact, which leads to a drastic rise of the SCF. Crack is very likely to initiate at those intersections, but as mineral apposition continues during life, the crack is perhaps “repaired” naturally.

In this model, the microscale constituents of dentin have been considered: PTD, ITD, and tubule lumens and the collars and lumens of lateral branches. The next step of modeling the dentin can be modeling the nanoscale. A first attempt to model the nanoscale was made by introducing the anisotropy of ITD. However, considering the collagen fibrils and the HAP nanocrystals will need further data on the orientation of the collagen fibrils and their connection with the HAP nanocrystals, which can be obtained by experimental means such as Transmission Electron Microscopy.

In the next chapter, a tensile test on dentin will be performed at the microscale (that is to say, at the same relevant scale as the proposed model). The specimen size will be small enough to avoid the local variations in the density or orientation of tubules or in their diameter. This test will clarify the role of tubules and LBs in the failure of dentin.

4 An in-situ micro-tensile test on dentin

4.1 Introduction and motivation

In the past, compression tests, tensile tests, shear tests, and flexural tests have been done to characterize the mechanical behavior of dentin. Examples of studies including such types of tests are, respectively, reported in the papers by Huang et al. (1992) [106], Sano et al. (1994) [82], Watanabe et al. (1996) [107], and Arola & Reprogel (2006) [108]. The results of some compression and tensile tests are reviewed in Chapter 2. One advantage of the 'ideal' compression and tensile tests over shear and flexural tests is that in these tests, the stress is uniaxial and uniform in the testing zone if the microstructure in this zone is homogeneous.

The compression tests seem to be more relevant to the natural loading of teeth, which are primarily under compression during mastication. However, the compressive loads are not the main concern for dentin because its compressive strength ranging from 160-350 MPa [24] is significantly higher than its tensile strength, which ranges from 30-130 MPa [24].

In the previous studies reviewed in this work, tensile tests have been performed to characterize the elastic properties and the tensile strength. The latter is a more decisive property for brittle materials like dentin. Small size dentin samples have been machined with cross-section areas in the range of 0.25 to 1.5 mm². Small cross-section areas help to minimize the microstructure variation in the sample, which affects the results.

Another advantage of the micro-tensile tests is their ability to investigate the mechanical properties in different orientations, which nanoindentation tests cannot. LaVan & Sharpe (1999) [109] stated that indentation techniques could not identify directional variations in the mechanical properties. However, micro-tensile tests reveal the orientation-dependence of the measured mechanical properties.

In this research, a micro-sized sample by FIB-SEM technique was prepared, which is a great technological challenge. After several attempts, it was possible to shape a sample with a 30x12x13 μm^3 gauge zone, including a few tubules. To the author's knowledge, this is the smallest tensile sample ever tested. Microscopic samples allow characterizing the tensile mechanical behavior of dentin independently from the variation in the distribution and morphology of tubules.

First, some of the previous studies on the mechanical tensile experiments on dentin and their practical aspects are reviewed. Then the design of the micro-tensile test developed in this research is described. Finally, preliminary results obtained from the test are presented.

4.2 Tensile tests on dentin: a review

4.2.1 The design of the tensile samples

One specific challenge in designing the shape of the samples for tensile tests is that they need to be gripped at both ends. Therefore, usually, the samples have shapes like an hourglass, dumbbell, or dogbone. Typical shapes and geometric characteristics of dentin tensile samples are presented in Table 4-1. However, machining such complex shapes on a very small sample made of a brittle material is more difficult than making a simple bar,

which is usual for compression and flexural tests. Hence, compression experiments on dentin were the first mechanical tests done in 1895 by Black [110]. In his study, 2 mm-sized cubic samples were used. Nevertheless, due to the complexity of making small tensile specimens, it was only in 1962 that Bowen & Rodriguez reported the first tensile tests on dentin, finding a tensile strength of roughly 41 MPa [111]. These studies usually used burrs to machine the sample, a method with which samples have cross-sections in the order of 1 mm². Therefore, these samples were not small enough to probe the mechanical properties of dentin *independently from the variation in its tubular microstructure*. Lehman (1967) [84] was aware of this when he published similar values to those of Bowen & Rodriguez for tensile strength of hollow cylindrical samples with cross-sectional areas of approximately 5.1 mm².

Sano et al. (1994) [82] reduced the cross-section area of the micro-sample of dentin to 0.25 mm², which is to our knowledge the smallest cross-section area in this literature review. The authors reported a size effect in the Ultimate Tensile Strength (UTS) results with a higher UTS for smaller samples. The same size effect was also observed by Inoue et al. (2003) [112]. Sano et al. (1994) [82] argued that this size effect is because smaller samples have fewer defects. This result agrees with those found for many other brittle materials, for example, the study by Fischer et al. (2002) [113] on brittle non-metallic materials.

The shapes of the samples in Sano et al. (1994) [82] study are shown in Figure 4-1.a. They tested both hourglass and dumbbell-shaped samples to investigate the possible effects of stress concentration in the latter kind of sample. Surprisingly, they did not observe a significant difference between the results of samples of the two shapes.

Another point to consider is the mode by which the sample is fixed in the testing device, shown in Table 4-1. Sano et al. (1994) [82] used glue to stick the sample to the testing device, but they mentioned that the force is only borne by the ridges (Figure 4-1.b). The fixation technique is mentioned in Table 4-1, because it depends on the scale of the test. The microscale tests that are discussed in this chapter have a different fixation method.

a) sample size	b) Grips used to apply the load on the dumbbell-shaped samples
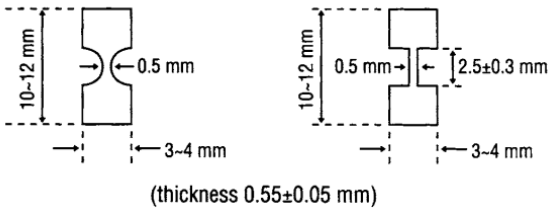	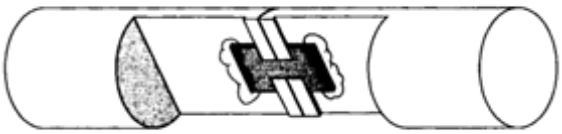

Figure 4-1.a) The samples, b) The set-up developed by Sano et al. (1994) [82]

By assuming an average tubular density of 30000 tubules/mm² in the middle dentin, about 7500 tubules exist in the cross-section of 0.25 mm² if perpendicular to the tubules axes. Even though this was not the case, this value estimates the number of tubules contained in the gauge zone of the sample volume. The estimated number of tubules is more than enough to

make the sample representative of the mechanical properties of dentin. According to Jeanneret et al. (2017) [114] a representative volume element of dentin for the elastic properties includes at least about 60 tubules. Therefore, even the cross-section area of 0.25 mm², the minimum among the reviewed studies, is too big to estimate the UTS independently from the microstructure variation.

There are other phenomena, which are involved in the scattering of experimental results on uniaxial tensile or compression tests. Small misalignment can cause additional and parasitic bending strains in the sample. It is even more important that the sample is small because the sample is more difficult to handle. Second, in tensile tests, the friction between the grips and the specimen affects the stress distribution. The friction impacts the results of tensile strength more significantly in small-sized specimen than in specimens of conventional size.

Table 4-1. Cross-section area, gauge length, and shapes of the dentin samples

Author	Cross-section	Gauge length	Shape of the sample	Attachment
Giannini et al. (2004) [115]	0.5 mm²	-	Hourglass-shaped	Glue
Miguez et al. (2004) [116]	0.25 mm²	-	Hourglass-shaped	?
Inoue et al. (2003) [117]	0.25 mm²	-	Hourglass-shaped	Glue
Inoue et al. (2002) [118]	1 mm²	1.5 mm	Dumbbell-shaped	?
Liu et al. (2002) [119]	1.5 mm²	1.8 mm	Dumbbell-shaped	?
Staninec et al. (2002) [120]	Not mentioned		Hourglass-shaped	Glue
Lertchirakarn et al. (2001) [12]	1.13 mm²	-	Hourglass-shaped	?
Carvalho et al. (2001) [121]	0.5 mm²	-	Hourglass-shaped	Glue
Sano et al. (1994) [82]	0.25 mm²	2.5 mm	Hourglass-shaped and dumbbell-shaped	?

4.2.2 A review of some aspects of the studies of tensile behavior on dentin

Stress-strain curve

Sano et al. (1994) [82] and Staninec et al. (2002) [120] presented typical stress-strain curves of tensile tests on dentin.

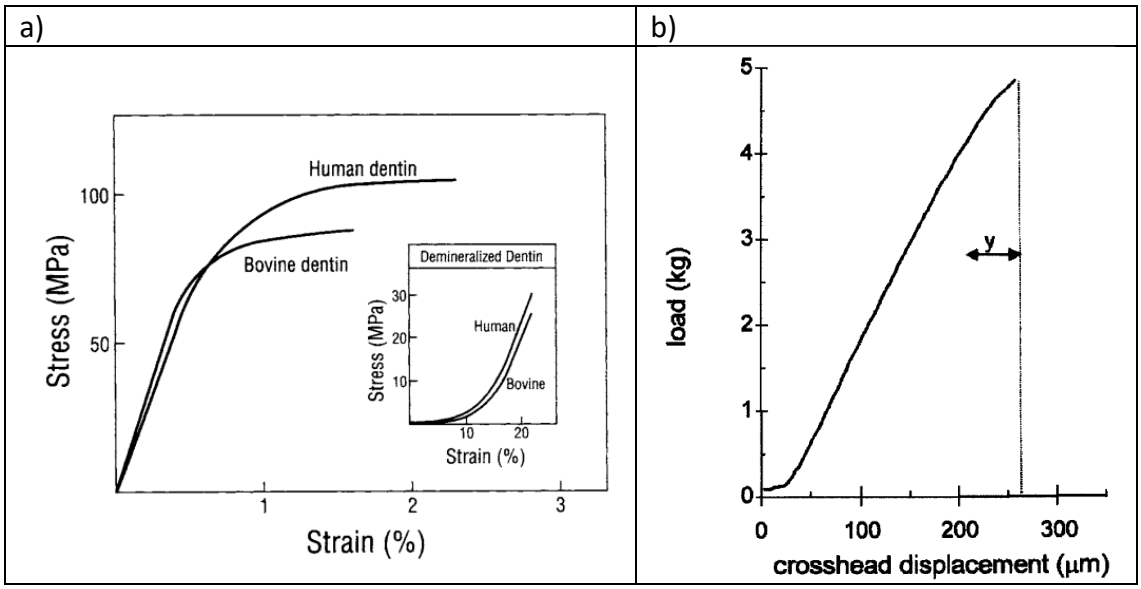

Figure 4-2.a) Tensile stress-strain curves of normal and demineralized dentin, obtained by Sano and al. (1994) on human and bovine dentins, b) Tensile stress-strain curve by Staninec et al. (2002).

In these stress-strain curves shown in Figure 4-2, it can be remarked:

1) In the curve given by Sano et al. (1994) [82], the yield strength (with a 0.2% offset) is estimated to be 89 MPa for human dentin. Noticeably, some post-yield nonlinear deformation is observed in both curves, even though less in the study by Staninec et al. (2002) [120]. They attributed the post-yield behavior to the growth of damage.
2) In the study by Sano et al. (1994) [82], a maximum strain of 2% is observed for dentin. This maximum strain means a maximum displacement of 50 μm for the gauge length of the samples in this study, which is 2.5 mm. However, the maximum displacement in the study by Staninec et al. (2002) [120] is bigger, and as visible in Figure 4-2.b is about 250 μm, which is about five times the displacement by Sano et al. (1994) [82]. Generally, bigger displacements are less prone to errors.
3) The imprecisions of the measurement system will introduce artifacts to these small displacements. It is more visible by the high nonlinearity observed at the curve's beginning (Table 4-2). The lack of nonlinearity in the beginning of the stress-strain curve given by Sano et al. (1994) [82] means that the researchers have succeeded in eliminating the tow region in the stress-strain curve, which is due to the imperfect connection of grips and the sample in the beginning of the experiment. This reveals the challenges of measuring the displacement and consequently Young's modulus for a small sample, which is the cause why only one of the reviewed studies has measured Young's modulus of dentin.

4) Staninec et al. (2002) [120] measured the crosshead displacement, which means a relatively high possibility of error in measurements. However, Sano et al. (1994) [82] used displacement sensors of the type Linear Variable Differential Transformer (LVDT), which have a better resolution.

Anisotropy of the Ultimate Tensile Strength

In previous studies, specimens were also tested in the longitudinal and transverse direction to the tubules to characterize how the orientation of tubules affects the tensile strength of dentin. In the following, the ultimate tensile strength (UTS) measured in both orientations are respectively called UTS_L and UTS_T.

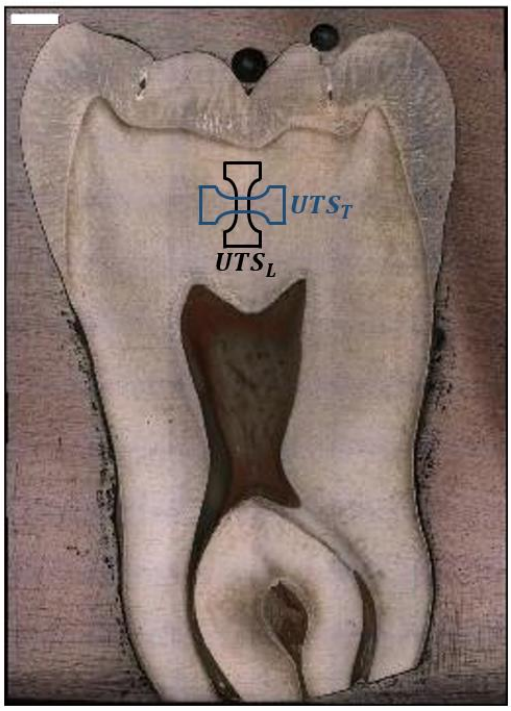

Figure 4-3. Sketch of a tooth with transverse and longitudinal tensile specimens (scale bar: 0.5 mm).

The influence of orientation of the tubules on the UTS studied in the literature is summarized in Table 4-2. Most studies have given the same orientation of anisotropy, namely $UTS_t > UTS_l$, except the results of Inoue et al. (2002) [118], who in both coronal and radicular dentin reported the other orientation ($UTS_t < UTS_l$). However, a later paper by some of the same researchers (Inoue et al. (2003) [122]) resulted in the usual anisotropy orientation (Table 4-2).

Lertchirakarn et al. (2001) [12] explained this anisotropy of UTS by mentioning that unlike a fracture perpendicular to tubules, which happens parallel with the planes of collagen fibrils and separates them, a fracture plane parallel with the tubules necessitates the disruption of the network of collagen fibrils, and this increases the measured strength.

Table 4-2. The orientation-dependence of the tensile strength of dentin (the study with the unusual anisotropy orientation is colored in gray)

Study	Location in dentin	Young's modulus	UTS_l Longitudinal tensile strength (SD)	UTS_t Transverse tensile strength (SD)	Oblique tensile strength
Giannini et al. (2004) [115]	Superficial	-	61.6 (16.2) MPa	-	-
	Middle		48.7 (16.6) MPa	-	-
	Deep		33.9 (7.9) MPa	-	-
Miguez et al. (2004) [116]	Coronal	-	73.1 (21.2) MPa	140.4 (48.6) MPa	-
	Radicular		63.2 (22.6) MPa	95.9 (26.1) MPa	-
Inoue et al. (2003) [117]	Superficial coronal	-	77.6 (24.7) MPa	99.8 (27.9) MPa	-
	Middle coronal		65.2 (21.2) MPa	94.5 (30.7) MPa	-
	Deep coronal		50.9 (15.4) MPa	65 (32.5) MPa	-
Inoue et al. (2002) [118]	Coronal	-	76.7 – 79.6 MPa	34.9 – 44.5 MPa	-
	Radicular		56.3 – 90.1 MPa	43.3 MPa	-
Liu et al. (2002) [119]	Radicular	-	32.64 (4.69) MPa	38.93 (5.28) MPa	95.18 (23.8) MPa (α<90°)
Lertchirakarn et al. (2001) [12]	Radicular	-	41.1 (2.1) MPa	59.6 (5.2) MPa	45.9 (6.5) MPa (α=45°) 50.1 (4.9) MPa (α=67.5°) Diametral
Carvalho et al. (2001) [121]	Coronal	-	58 (11) MPa	80 (13) MPa	-
Sano et al. (1994) [82]	Midcoronal	13.7 (3.4) GPa	-	93.8 (11.1) to 105.5 (16.4) MPa	-

Location-dependence of the UTS

The location-dependence of the tensile strength in dentin, as reported in some studies, is summarized in Table 4-3. The location inside dentin is defined based on the relative closeness to the pulp or to the enamel (or cementum for radicular dentin). The locations closer to the enamel are called outer dentin, and the locations closer to the pulp are called inner dentin. Lertchirakarn et al. (2001) [12] compared the ultimate tensile strength of root and crown dentin and did not observe a significant difference between them.

Table 4-3. Dependence of the results of UTS measurement on the location inside dentin

	Dependence on the location in dentin
Giannini et al. (2004) [115]	$UTS_{outer} > UTS_{inner}$
Inoue et al. (2003) [117]	$UTS_{outer} > UTS_{inner}$
Staninec et al. (2002) [120]	$UTS_{outer} > UTS_{inner}$
Inoue et al. (2002) [118]	$UTS_{Radicular} > UTS_{Coronal}$ The location inside coronal dentin does not matter
Lertchirakarn et al. (2001) [12]	No significant difference between $UTS_{Radicular}$ and $UTS_{Coronal}$

Inoue et al. (2002) [118] have shown that the location inside the coronal dentin did not have a significant effect on the value of UTS. Still, the root dentin was significantly stronger than the coronal dentin. The authors mentioned the higher amount of collagen fibrils in the root dentin as a probable reason for this difference.

Inoue et al. (2003) [117] found that superficial dentin has a significantly higher UTS than the middle and deep dentin. Deep dentin is known to have a higher tubular density than superficial dentin, but no significant correlation could be found between the tubular density and the UTS.

Giannini et al. (2004) [115] too reported the highest UTS in the superficial dentin. Instead of tubular density (investigated by Inoue et al. (2003) [117]), they focused on the solid area of dentin. They recognized the lower porosity and the bigger solid area fraction as a cause for the higher UTS in the superficial dentin.

Strain based failure criterion

Among the mentioned studies, Staninec et al. (2002) [120] discussed the failure criterion of dentin. They suggested a formerly used criterion for bone i.e., the critical strain to failure based on the maximum principal strain, also known as the St. Venant criterion.

Other failure criteria proposed in the literature for brittle and porous materials (ceramic for example) can be used to characterize the failure of dentin based on stresses (e.g., Dormieux et al. (2006) [123]).

Crack initiation

Another subject of interest for this work and other studies on dentin is the role of tubules on the fracture behavior of dentin. Their role can be understood by the stress concentrations around the lumens, which was also discussed in Chapter 3. This is supported by the visualization of the microcracking pattern in a study by Eltit et al. (2013) [124]. As shown in Figure 4-4, the microcracks seem to have been initiated at the sides of tubules where the first principal stress is concentrated. This will also be shown in a 2D FE simulation of the tensile test, detailed in section 4.3.9.

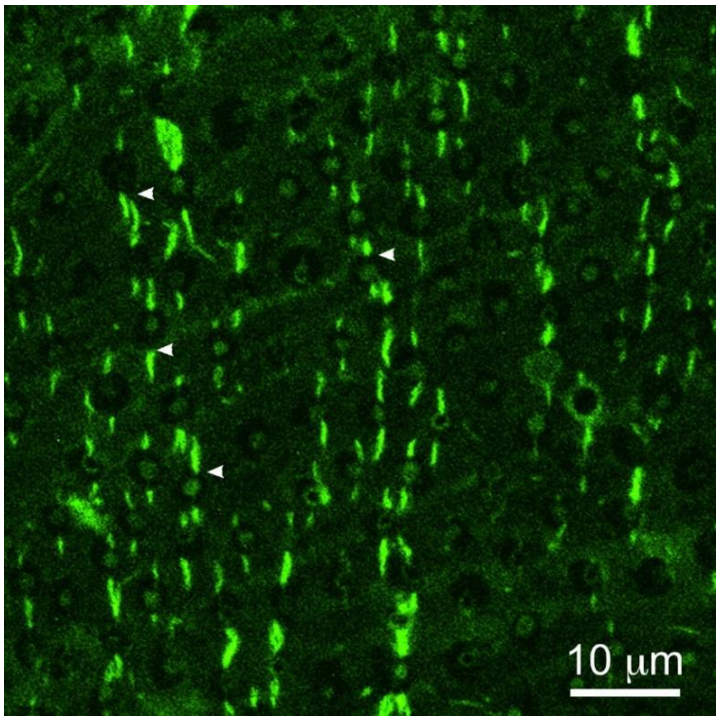

Figure 4-4. The microcracks in coronal dentin under horizontal tension, visualized by CLSM [124]

4.2.3 Conclusion of the literature review

Despite the large number of tests performed on dentin, to our knowledge, not many tensile tests have been performed at a scale small enough to limit the effect of the morphological variation in the microstructure. It is also noticed that the impact of LBs was neither observed nor discussed.

The proposed experiment in this chapter aims to bridge this gap by designing an in-situ test at the microscale that has become possible thanks to recent FIB-SEM technology. In the following section, the design of the test and a first experiment carried out on a dentin micro-sample are presented.

4.3 Designing and performing the experiment

4.3.1 Making a micro-sample of dentin

A third molar of a young adult patient was chosen for this experiment. The process of sample preparation was divided into three steps:

1) Cutting a submillimetric sample: From the dentin sample, a disk with a thickness of 0.6 mm (Figure 4-5) was cut in the coronal zone with a rotating diamond saw.
2) Treatment: The disk was then dehydrated with alcohol bathes, with the dehydration protocol described in Chapter 1, section 1.2.1. Dehydration is necessary for working with the sample in vacuum in the SEM. Then, the sample was stuck on an aluminium stub with silver paint. Finally, it was sputter-coated with gold to become conductive. Being conductive prevents the accumulation of charge on the sample surface, which will consequently lead to a deflection of the ion or electron beam emitted from the electron microscope. The result of these two steps is shown in Figure 4-5.

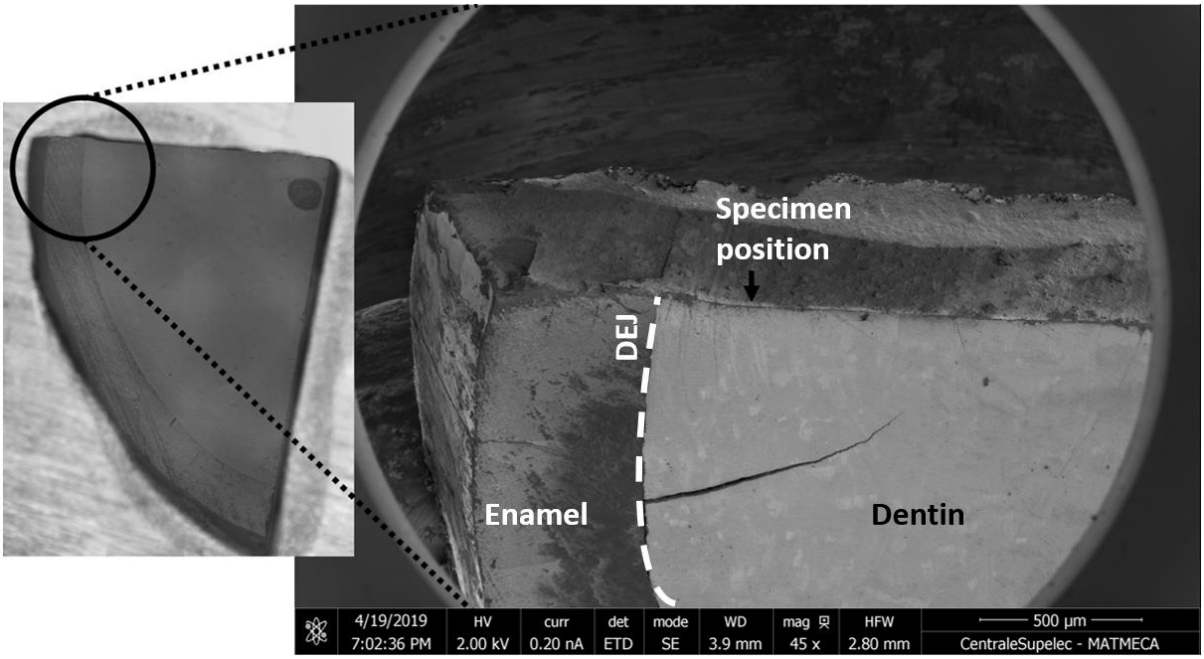

Figure 4-5. The quarter disk and the chosen location of the sample for milling the micro-tensile specimen (marked by an arrow)

3) Machining of the specimen inside the SEM: The location of the tensile specimen in the dentin sample is chosen based on the distribution of the lateral branches in the dentin and with the goal of avoiding the complicated shapes of major branches in the specimen. The distribution of lateral branches near the DEJ was shown in Chapter 1, Figure 1-3. Therefore, the chosen location for milling the micro-specimen is in the middle dentin and 270 µm away from the DEJ (shown by an arrow in Figure 4-5).

4.3.2 Designing the shape of the specimen

The shape of a tensile specimen must be appropriate for being fixed inside the grips that will pull on the sample. A few proper shapes are dogbone, hourglass, and dumbbell-shaped specimens. A dogbone shape was chosen, which has a gauge section with a constant width and a gauge length long enough to measure the strain and consequently estimate the Young's modulus.

The locations (zones) where the test piece is attached to the grips are indeed known to be affected by additional stress concentration. Therefore, in a brittle material like dehydrated dentin, the fracture might happen there and not in the gauge zone. If it happens, the tensile strength cannot be well estimated. An effective parameter in this matter is the fillet radius of the specimen. Therefore, the effect of the fillet radius on the stress concentration was studied by finite element simulations in the following subsection.

Finite element simulations to study the effect of the size of the fillet radius

Three tensile test 2D FE simulations of a quarter of the sample (Figure 4-6) with a length $l = 20\ \mu m$ and a width $W = 10\ \mu m$ (in the grip) of sample were performed with various fillet radii 'r' to limit the stress concentration near the heads of the sample (Figure 4-6). The ratio '$r/(W/2)$' is defined to characterize the size of the fillet radius: The parameters of this ratio, 'r' and 'W' are visualized in Figure 4-6.a.

The loading and boundary conditions applied on the quarter of the elastic sample modeled in these simulations (Figure 4-6.a) were as follows: a total load of $0.5\,mN$ uniformly distributed over the contact surface pushes the left side of the specimen to the left. The boundary of the load application is highlighted in blue in Figure 4-6.a. To take account of the horizontal symmetry, the lower side of the geometry had roller boundary conditions (vertical displacement of the nodes fixed). To take account of the vertical symmetry, the right side of the specimen is bound to move horizontally (horizontal rollers). A homogenized elastic modulus of 20 MPa was attributed to the material. Because dentin is known to be brittle, the concentration of the first principal stress was studied in these various geometries to give an idea of the locations with the highest tensile stresses. The stress concentration factor for the first principal stress was defined by $\frac{\sigma_I}{\bar{\sigma}_I}$, where σ_I is the first principal stress and $\bar{\sigma}_I$ is the surface average of the first principal stress (Figure 4-6.b to Figure 4-6.d). In addition, the maximum and minimum of the first principal stress are indicated as well.

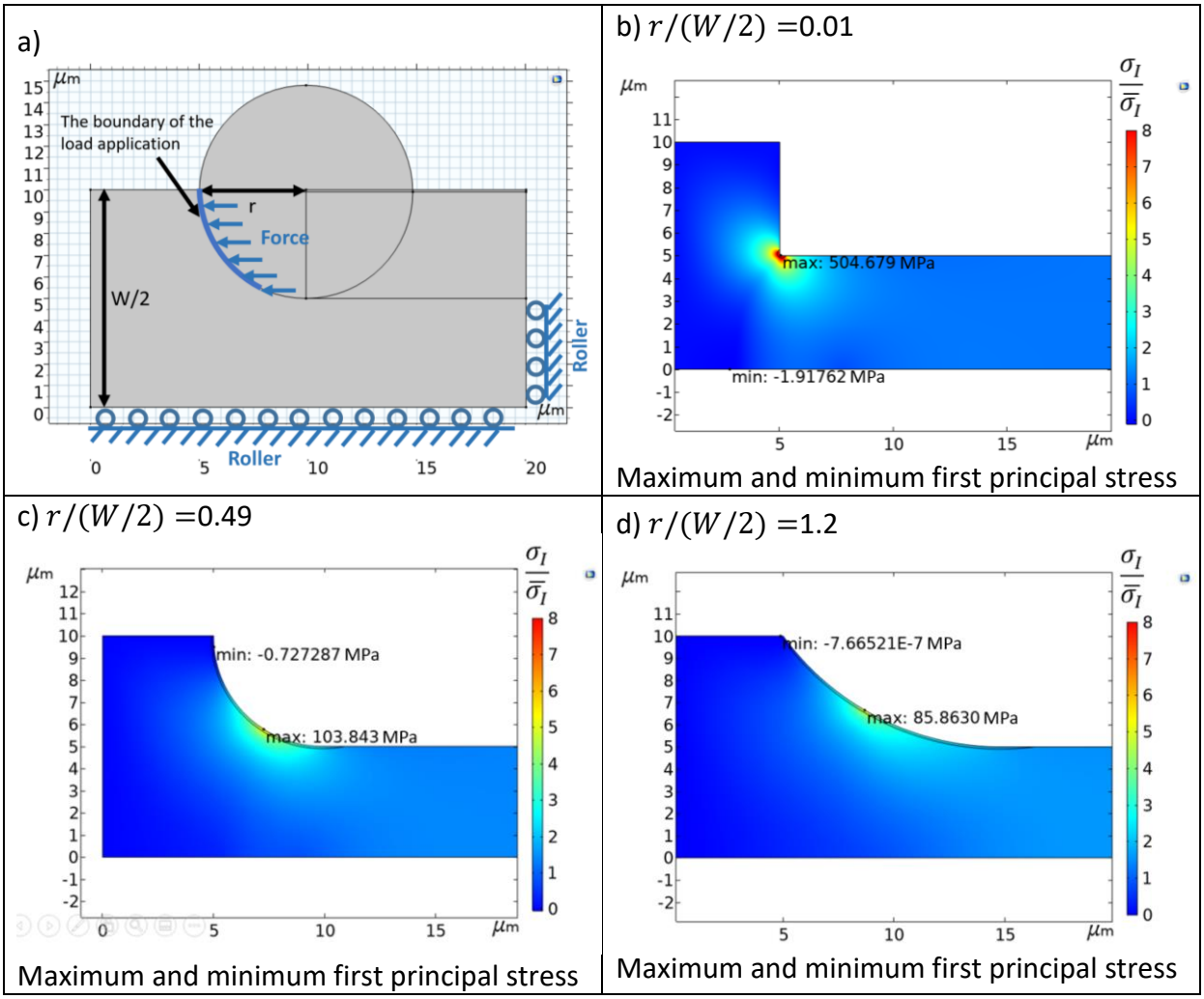

Figure 4-6. a) The geometry for the simulation of the tensile specimen, a quarter of the sample is considered, The following three figures are the maps of the concentration factor of the first principal stress for three geometries: b) The simulation with a ratio "r/(W/2)" equal to 0.01, c) The simulation with a ratio "r/(W/2)" equal to 0.49, d) The simulation with a ratio "r/(W/2)" equal to 1.2

As it can be seen in Table 4-4, it is not possible to completely avoid stress concentration. Therefore, it is predictable that some tests will fail due to stress concentration and therefore will not be usable.

As shown in Figure 4-6.b-d and as expected, the lowest stress concentration in the model is obtained with the biggest fillet radius. This supports the assumption that a tensile specimen should have a relatively big fillet radius (as shown in Table 4-4). Therefore, the ratio '$r/(W/2)$' equal to 1.2 was chosen for the specimen geometry in the experiment for this thesis.

Table 4-4. The effect of the fillet size on the maximum concentration of the first principal stress

Ratio of the fillet radius to the half-width of the sample ($r/(\frac{W}{2})$)	Average horizontal stress in the gauge zone (total force divided by the cross-section area of the gauge zone)	Maximum stress by applying a load of $0.5\ mN$	Maximum stress concentration factor ($\frac{\sigma_I}{\bar{\sigma}_I}$) for the first principal stress
0.01	20 MPa	504.7 MPa	28.8
0.49	20 MPa	103.8 MPa	7.1
1.2	20 MPa	85.9 MPa	6.8

4.3.3 Machining a microscopic specimen

The machining process was done inside the scanning electron microscope Nanolab 660, equipped with a focused ion beam (FIB).

The sample was set at the eucentric point where the ion and electron beams coincide. There, it was possible to both visualize the sample by the electron beam and mill it by the FIB [125]. The FIB with its high energy can remove layers of material in the targeted area.

The first step of milling on the sample was done to free a block of dentin, which was the basis for making the tensile specimen. For this, a non-precise milling was done by applying high current of 21 nA. However, because it requires removing lots of material, this step takes tens of hours.

4.3.4 Handling the microscopic tensile sample

Handling a micro-tensile sample is challenging because such a small specimen can break by the mildest impact. Therefore, it should be handled by the nanomanipulator integrated with the SEM (Gianola & Eberl (2009) [126]). Nanomanipulator controls and moves a needle. The needle is welded to the sample by a gas injector which injects Platinum at the welding location. This welding process is called Platinum IBID (ion beam induced deposition). Then the specimen can be moved and controlled by moving the nanomanipulator needle (Figure 4-8.b).

One important and practical point about welding by this method is performing a “purge”. This process makes the resting gas from previous usage exit the needle-sized nozzle. Because it was not done in our first try, the sample was blown away from the needle and was lost.

4.3.5 The testing device

An in-situ test device, designed at MSSMat (Ben Salem et al. (2020) [127]) and shown in Figure 4-7 was used for the micro-tensile experiment. This device was put inside the SEM Helios Nanolab 660.

In this set-up for the experiment, the positioning (Y and Z) of the specimen is done by two piezo-electromechanical actuators with a precision of 1 nm. A rotation motor fixed on a third piezo-stage pulls the specimen by a Tungsten needle in the X-direction.

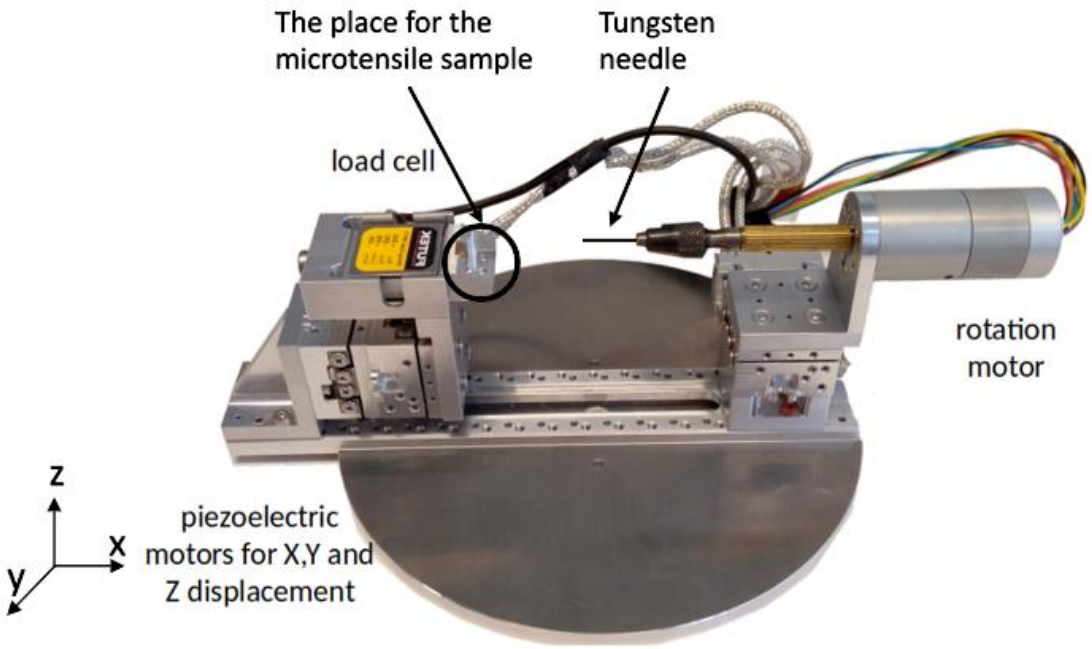

Figure 4-7. The in-situ test device developed at MSSMat laboratory for micro-tensile test (University Paris-Saclay, CentraleSupélec, CNRS)

A load cell is used to record the load. It is made by FUTEK with a maximum load capacity of 500 mN and a 0.5 mN resolution. It records the load with a frequency of 10 Hz. The piezo stage for the X displacement is equipped with an encoder to control the displacement precisely. However, deformation computed from the stage displacement does not represent the deformation of the specimen because part of it is due to the compliance and movement of the test devices.

4.3.6 The traditional set-up of the tensile test

In the traditional design of in-situ micro-tensile tests [127], by carving four sides around a selected zone, a block is freed for making the tensile specimen (Figure 4-8.a). This big milling is done by a high current of 21 nA and a voltage of 30 kV. This process is time-consuming and takes about 47 hours. Then, using the gas injector, this block is welded by Platinum IBID (Ion Beam Induced Deposition) to the nanomanipulator ‘Easylift’. Once it is welded, it can be separated from the rest of the sample by focused ion beam (Figure 4-8.b). The block with the

approximate dimensions 14x110x50 μm^3 is then moved to the Tungsten needle, which is connected to the rotation motor and is welded on its tip (Figure 4-8.c). The dog-bone shape is milled on the block while it is welded on the needle. Then, the tensile specimen is moved to a grip that is made inside a Molybdenum plate (Figure 4-8.d). Once the specimen is welded inside the Molybdenum grip, the specimen can be separated from the Tungsten needle. Then it is fitted inside the grip on the same needle and is pulled.

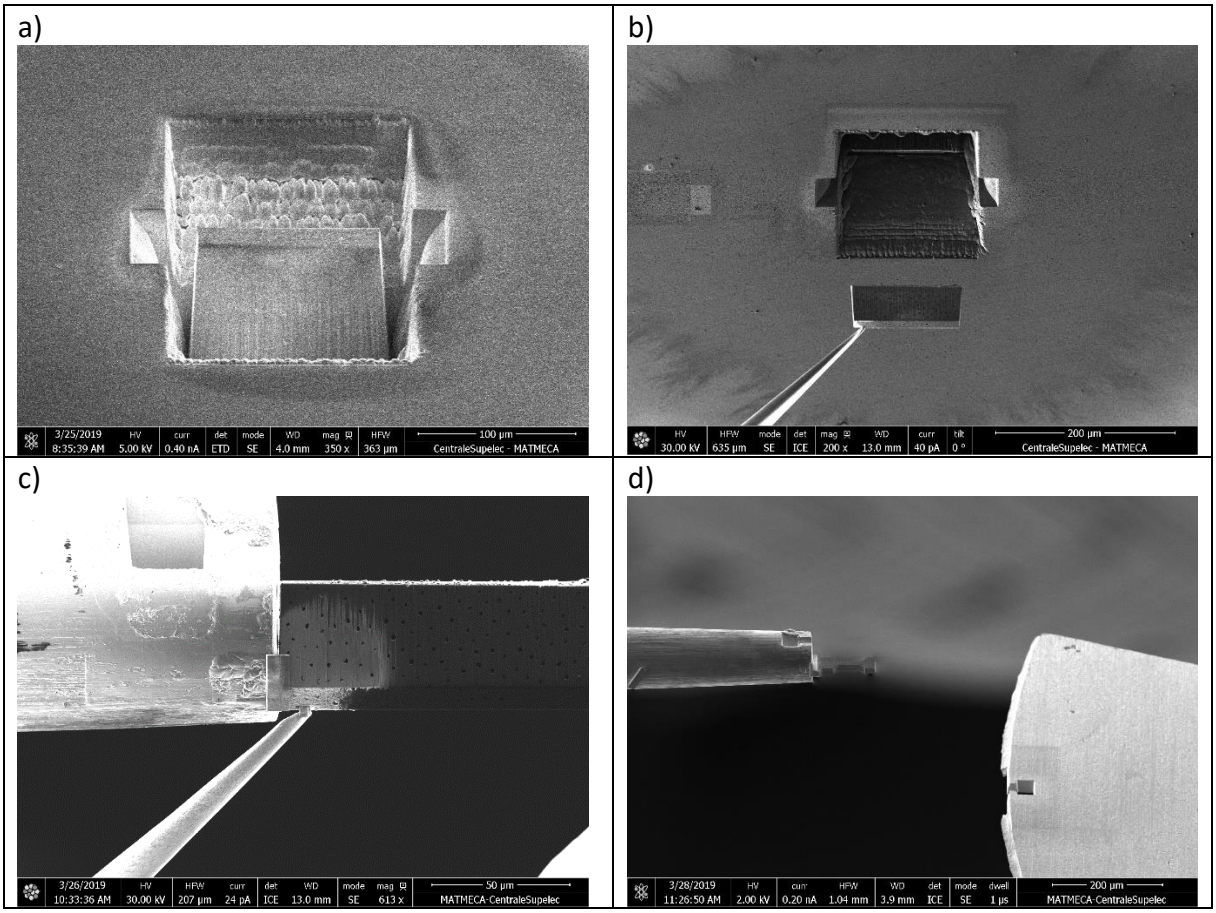

Figure 4-8. a) a block of dentin, the four sides of which are carved out by FIB, b) the block of dentin is welded to the nanomanipulator and is separated from the dentin quarter disk, c) the block of dentin is welded to the Tungsten needle, d) the dentin block is milled to a dog-bone shape and is moved toward the grip inside a Molybdenum plate.

The experiment shown in Figure 4-8 was not completed because the purge was not done and the sample was lost.

4.3.7 A new design of the tensile specimen

The design of the next specimen is a newer version of the in-situ tensile experiment introduced in the paper by Arnaud et al. (2021) [128]. The specimen was prepared at the edge and on the sample's surface and was not separated from the rest of the sample (Figure 4-9). Therefore, less milling and manipulation was needed.

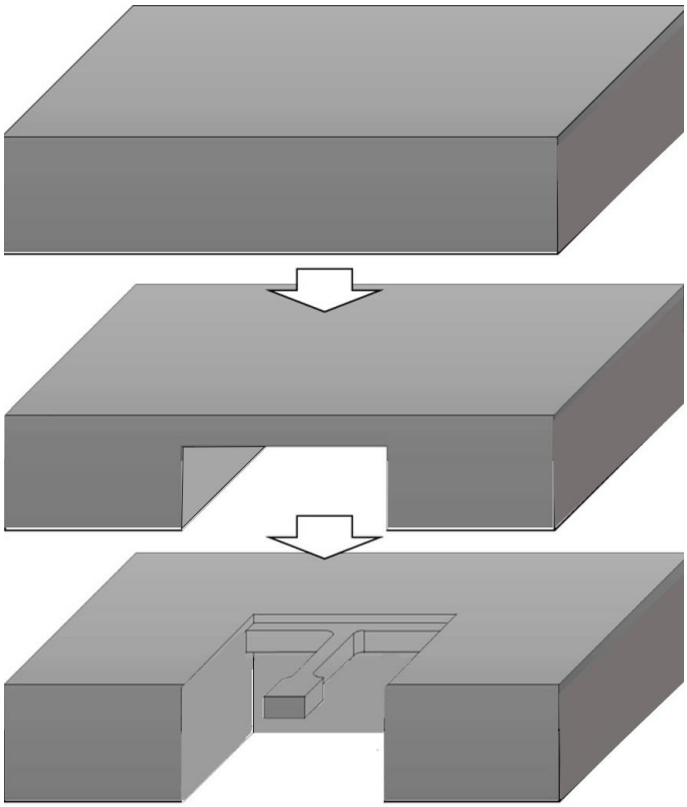

Figure 4-9. Schematic view of the steps of preparing the micro-tensile specimen (Adapted from Arnaud et al. (2021) [128]*)*

Using FIB with a high current of 21 nA, first a big excavation was done below the sample's surface, which took three days. The excavated zone was big enough for the Tungsten needle with a diameter of ~80-100µm to fit inside it (Figure 4-10.a). By the completion of the big milling, a slab of dentin with an approximate thickness of 23 µm was available for manufacturing the specimen. Then, FIB was with a voltage of 21 nA was used to mill the dog-bone shape of the specimen (Figure 4-10.b). Thin layers of material are removed from the upper and lower surfaces of the specimen by FIB to achieve the desired thickness of the tensile specimen, which is approximately 13 µm (Figure 4-10.c and Figure 4-10.d).

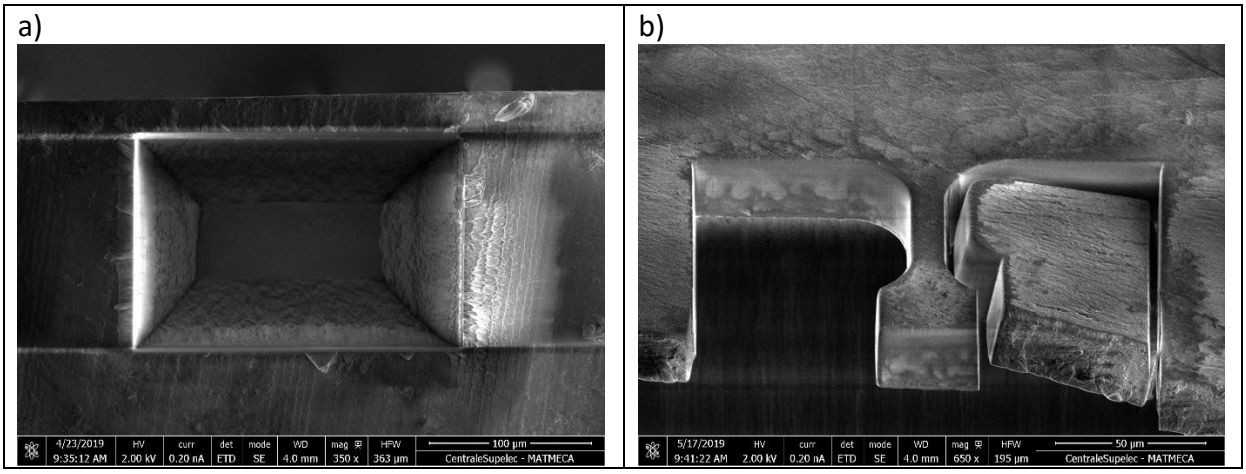

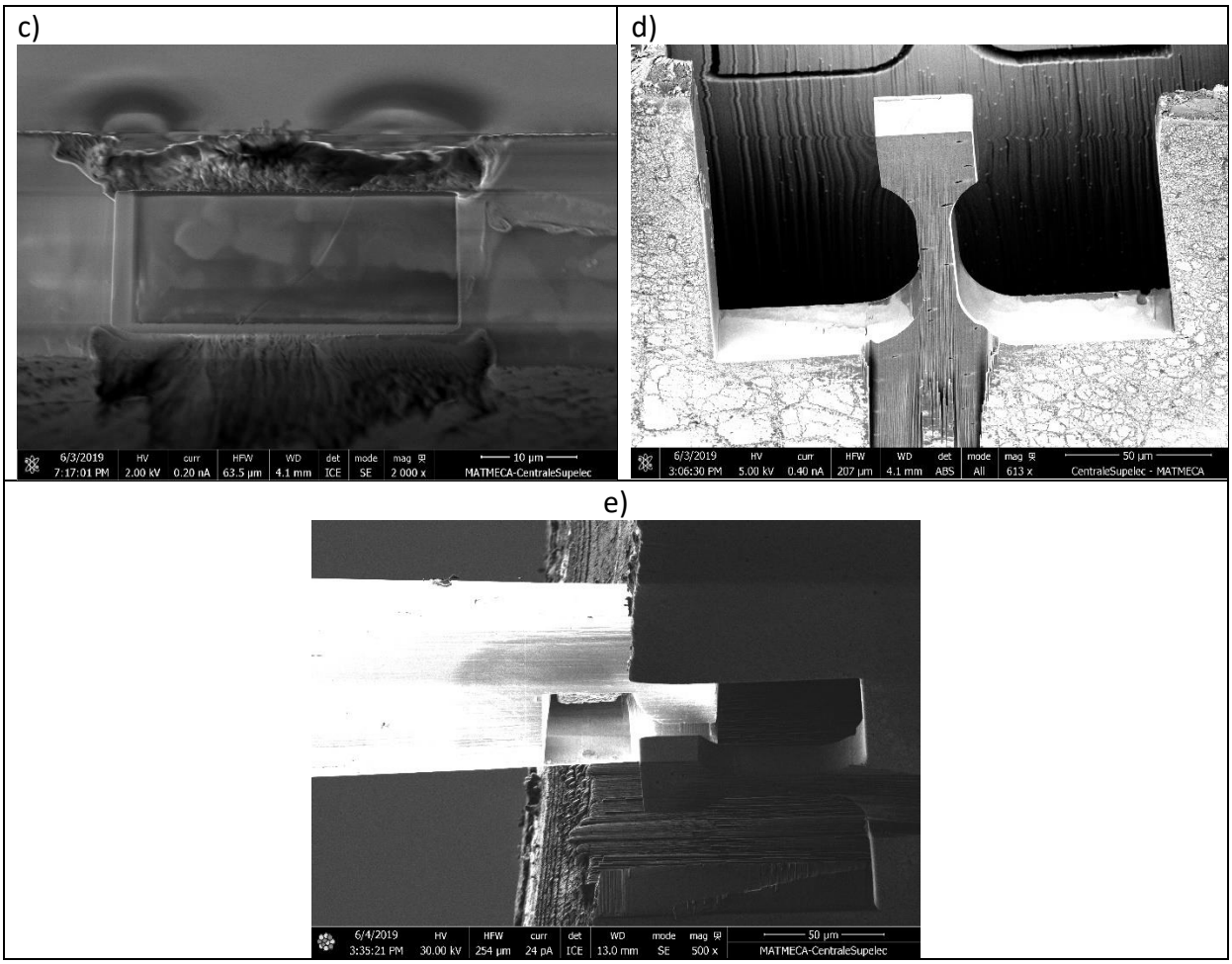

Figure 4-10. Steps of manufacturing the new micro-tensile specimen, a) Milling a space under the location for the specimen, where the Tungsten needle with a grip on it will enter, b) The dog-bone shape milled on the freed slab of dentin, c and d) the upper and lower surfaces of the specimen are polished to achieve the desired thickness, e) the Tungsten needle with a milled grip enters into the space below the micro-tensile specimen.

An unwanted consequence of these milling processes is the curtaining effect (i.e., the increasing surface roughness in the direction of the milling depth), as visible in Figure 4-10.d. A lower current of the ion beam (9.95 nA) was used for final polishing to minimize this effect.

Exertion of the force

Then, the needle with the grip milled on it was moved into the excavated zone. The next delicate step was to move the needle to set the grip exactly beneath the sample using the piezo-electromechanical actuator and then to move it toward the specimen to fit the specimen inside the grip (Figure 4-10.e). Any misfitting in this step would break the specimen.

SEM imaging

To capture the deformation of the specimen, it was imaged during the tensile test. SEM images (1536 pixels width and 1113 pixels height) were acquired with a BSE detector. The horizontal field width (HFW) is 85 µm. The type of the images is 8-bit, which means 256 grey levels from black to white.

The BSE detector was at a working distance of 5 mm, and a 5 kV acceleration voltage for the electron beam. The current s 0.80 nA. A higher current of scanning electron, which could

give a better contrast, was not used because of the significant charging effect on the nonconductive dentin specimen. The conductive gold layer on the specimen was milled away in the manufacturing process.

Regarding the time needed for acquiring the images, the data are the following: Dwell time, meaning the time for the acquisition of one pixel is 0.3 µs and the frame time, meaning the time for acquiring one image is 0.52 s.

Advantages and disadvantages of the new test design

The advantages of the new design for the micro-tensile specimen are summarized as follows:

- The specimen does not need to be separated from the rest of the dentin sample and moved toward the grip. Therefore, the nanomanipulator 'Easylift' is not needed.
- No welding of the specimen is needed. The specimen is already held by the rest of the dentin sample.
- Usually, the contact points between the grip and specimen are locations with stress concentrations. Fortunately, the new design with only one grip has only two points of contact between the specimen and the grip.
- There is no need to have the micromachine inside the SEM for milling the specimen.

However, this new design has its drawbacks as well:

- More curtaining effect happens on the surface of the specimen, because it is milled along its length. The milling direction is observable by the curtaining effect visible in Figure 4-10.d.
- In the previous design, the specimen was put in its location with the same needle that was used to pull the specimen. But in the new design, the orientation of the specimen is defined by the position of the whole dentin sample. Therefore, a misalignment between the specimen and the needle is more probable, which causes an additional flexural solicitation.

4.3.8 Measuring the extension of the sample by DIC

For DIC measurements, the texture of the dentin specimen was not enough. Therefore, Platinum speckles were drawn on the micro-sample (Figure 4-11) using the same gas injector, which was used for welding.

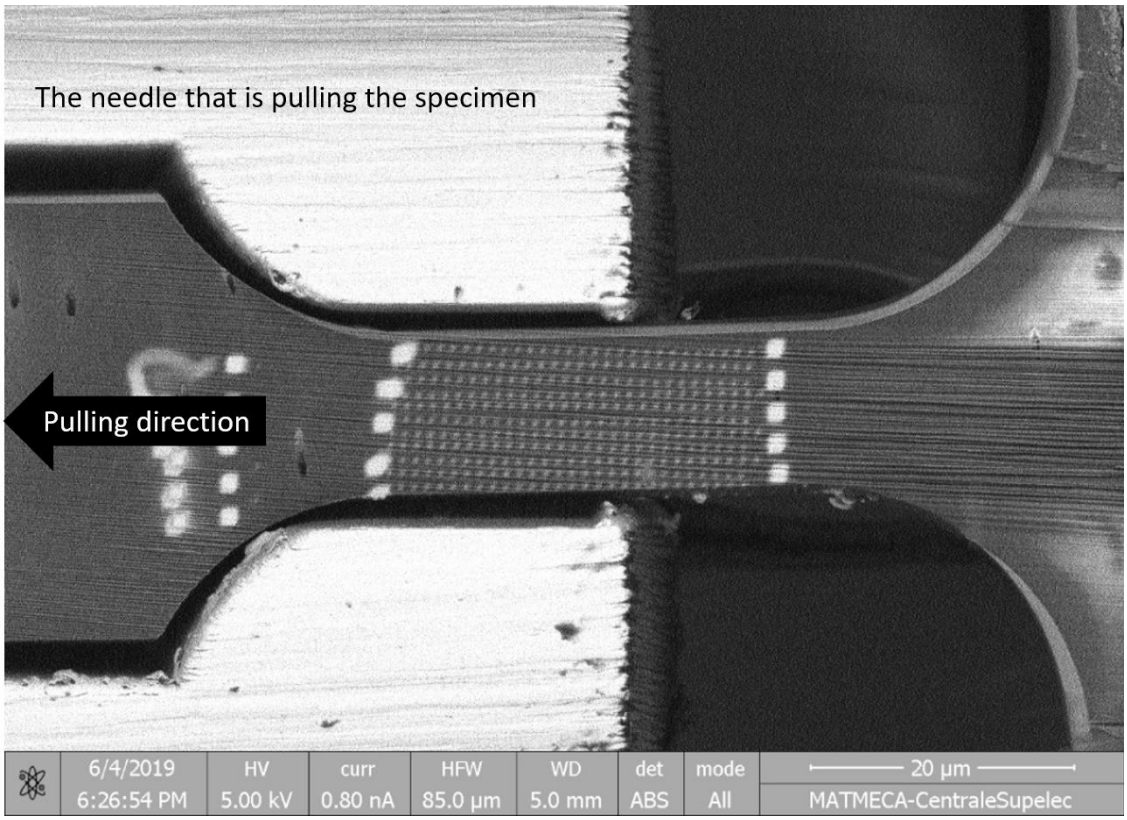

Figure 4-11. The machined microspecimen, settled in the grip inside the Tungsten needle.

Digital Image Correlation

In this section, Digital Image Correlation (DIC) is briefly explained. The DIC measurements were based on a code, which uses the MATLAB code "Correli" [129].

Global "DIC" method is developed in the works of Hild and Roux. The paper by Hild & Roux (2012) [130] is the basis reference for this section. By assuming $f(\boldsymbol{x})$ to describe the grey levels of the image of the undeformed configuration, the "texture conservation" hypothesis is stated:

$$f(\boldsymbol{x}) = g\big(\boldsymbol{x} + \boldsymbol{u}(\boldsymbol{x})\big) \tag{4.1}$$

where $g(\boldsymbol{x})$ is the deformed configuration and $\boldsymbol{u}(\boldsymbol{x})$ is the displacement, which can be determined by minimizing the squared of the residual $\phi(\boldsymbol{x}) = f(\boldsymbol{x}) - g(\boldsymbol{x} + \boldsymbol{u}(\boldsymbol{x}))$:

$$\tau(\boldsymbol{u}) = \int_{\Omega} \phi^{2(x)} d\boldsymbol{x} \tag{4.2}$$

In the global DIC method, the sought displacement field is assumed to be continuous and is therefore decomposed on a suitable basis.

$$\boldsymbol{u}(\boldsymbol{x}) = \int_{\Omega} \sum u_n \boldsymbol{\Psi}_n(\boldsymbol{x})\, d\boldsymbol{x} \tag{4.3}$$

where $\boldsymbol{\Psi}_n$ are the finite element shape functions and u_n are the associated degrees of freedom, which for a 2D DIC problem are displacements in x and y direction.

An iterative procedure is followed for the minimization of τ. Then, if $\boldsymbol{u^i}$ denotes the displacement at iteration i, by assuming small increments ($d\boldsymbol{u} = \boldsymbol{u^{i+1}} - \boldsymbol{u^i}$), a Taylor expansion linearizes the term $g(\boldsymbol{x} + \boldsymbol{u}(\boldsymbol{x}))$.

$$g\big(\boldsymbol{x} + \boldsymbol{u}(\boldsymbol{x})\big) \approx g(\boldsymbol{x}) + \boldsymbol{u}(\boldsymbol{x}).\nabla g(\boldsymbol{x}) \approx g(\boldsymbol{x}) + \boldsymbol{u}(\boldsymbol{x}).\nabla f(\boldsymbol{x}) \tag{4.4}$$

This equation assumes that $\nabla f(\boldsymbol{x})$ and $\nabla g(\boldsymbol{x})$ are almost equal, because the difference between the configurations f and g is small. This equation can be used to rewrite $\frac{\partial \tau}{\partial \{\boldsymbol{u}\}^i}$ in a matrix-vector product, which will be minimized in an iterative procedure:

$$\frac{\partial \tau}{\partial \{\boldsymbol{u}\}^i} = [M]\{d\boldsymbol{u}\} - \{\boldsymbol{b}\}^i = \{\boldsymbol{0}\} \tag{4.5}$$

M and $\{\boldsymbol{b}\}$ are studied as the following:

$$\boldsymbol{M}_{mn} = \int_\Omega [\nabla f(\boldsymbol{x}).\boldsymbol{\psi}_m(\boldsymbol{x})][\nabla f(\boldsymbol{x}).\boldsymbol{\psi}_n(\boldsymbol{x})]d\boldsymbol{x} \tag{4.6}$$

$$\boldsymbol{b}_m^{\boldsymbol{i}} = \int_\Omega \big[f(\boldsymbol{x}) - \tilde{g}^i(\boldsymbol{x})\big][\nabla f(\boldsymbol{x}).\boldsymbol{\psi}_m(\boldsymbol{x})]d\boldsymbol{x} \tag{4.7}$$

And

$$\tilde{g}^i(\boldsymbol{x}) = g\left(\boldsymbol{x} + \boldsymbol{u^i}(\boldsymbol{x})\right) \tag{4.8}$$

Mechanical regularization

In this case, a mechanical regularization is done to improve the convergence. This is done by adding an additional term to τ:

$$\tau(\boldsymbol{u}) = \int_\Omega \phi^{2(\boldsymbol{x})}d\boldsymbol{x} + \int_\Omega (\boldsymbol{u} - \boldsymbol{u}_{FE})^2 d\boldsymbol{x} \tag{4.9}$$

where $\boldsymbol{u}_{FE}$ is the displacement calculated by finite element method. Minimizing the difference with the finite element solution $\boldsymbol{u}_{FE}$ guarantees that the $\boldsymbol{u}$ resulting from minimization is mechanically acceptable. The finite element solution is done by attributing a plane stress stiffness matrix to the specimen.

Testing the MATLAB code

To verify the DIC code, it was tested on images of the sample that were deformed with specific scales. Using the software imageJ, the original image was expanded with a factor of 1.01 in the x-direction, which means a strain of 0.01 in that direction. The DIC results from comparing this, and the reference image are presented in Figure 4-12.

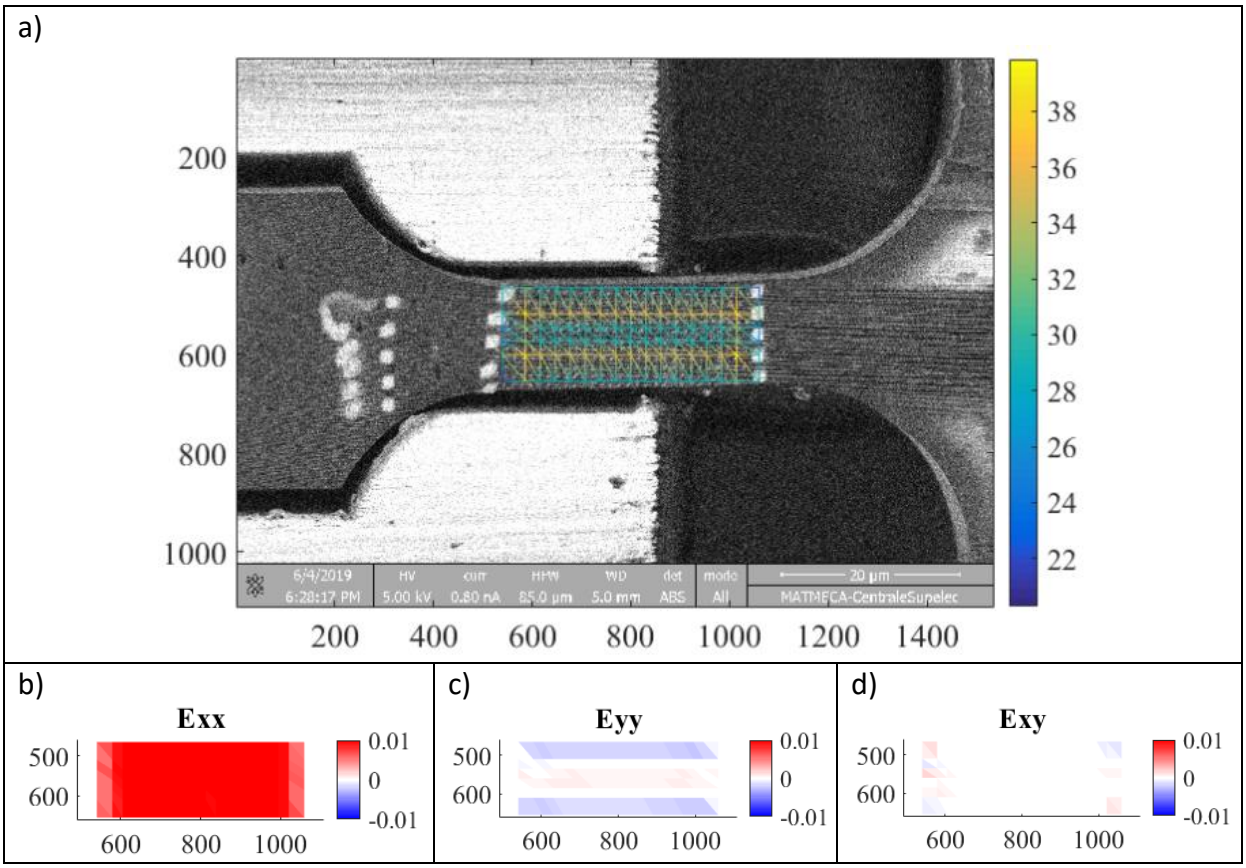

Figure 4-12.a) The meshed SEM image of the original configuration of the specimen. The next three figures are the measured strains for a manually induced strain with a magnitude of 0.01 in the x-direction from left to right, b) normal strains in the x-direction, c) normal strains in the y-direction, and d) shear strains in the xy-plane, (mesh size: 25 pixels)

The measured strains in the *x*-direction (E_{xx}) agree well with the expected strain due to the manually induced deformation. The errors in the elements on the boundary were compared with the measured strains.

The mesh size

The mesh size used for the results shown in Figure 4-12 is 25 pixels. Various sizes of mesh were tested to show the effect of the mesh size. The mesh sizes and the computed strains are shown in Table 4-5 below:

Table 4-5. Resulting strains for various mesh sizes

Mesh size (pixels)	The average computed strain in x-direction (The expected value: 0.01)
25	0.0095
35	0.0098
75	0.0098
100	0.0098
150	0.0092

These results agree well with the expected 0.01 strain in the x-direction. Therefore, the code has proven to measure the displacements correctly. In all the tests with various mesh sizes, the magnitude of the strain in the *y*-direction was lower than 0.001.

4.3.9 A 2D simulation of the experiment

In order to better understand and interpret the tensile test, it was simulated using the Finite Element Method (COMSOL).

The model

Figure 4-13 shows the modelled geometry corresponding to the theoretical designed geometry of the micro-sample.

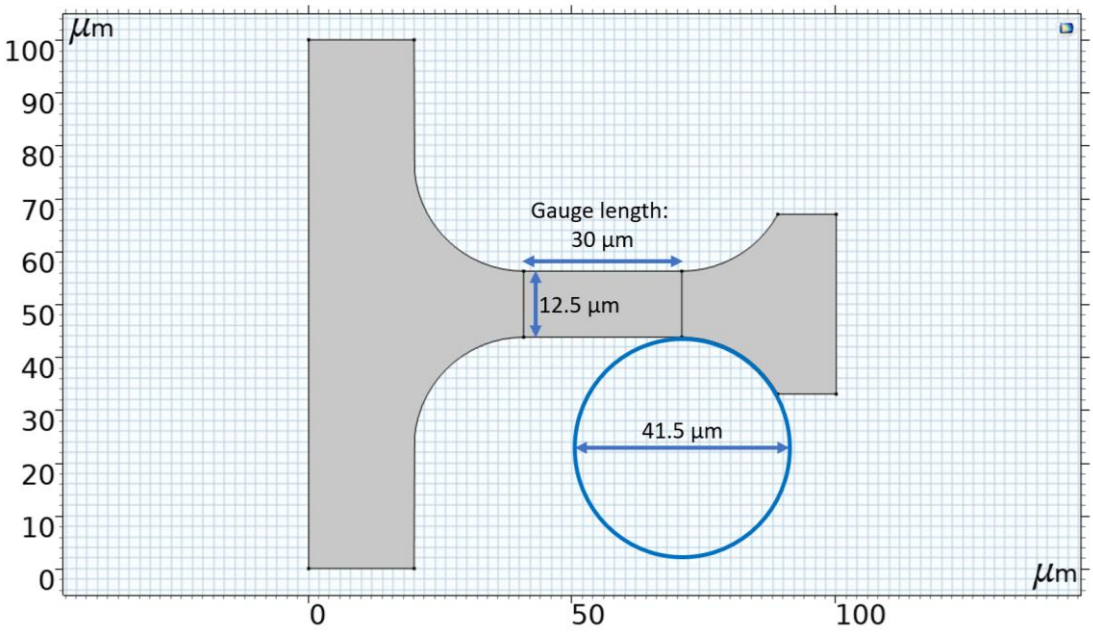

Figure 4-13. 2D geometry of the test piece created in COMSOL

Because the tubules on the micro-sample were unfortunately not visible, a segmented SEM image of the dentin approximately at the location of the experiment was used for making a vectorized image in the dxf format (Figure 4-14). The vectorization was done with the software Inkscape.

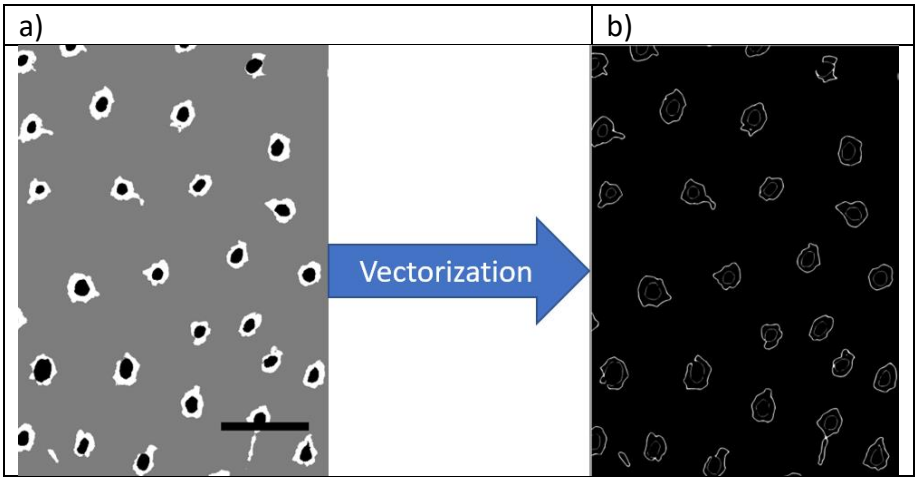

Figure 4-14.a) The segmented image of dentin microstructure, b) the vectorized version by the software Inkscape.

The resulting dxf file was intersected with the shape of the micro-tensile specimen in COMSOL Multiphysics 5.4 to build the simplified geometry of the specimen (Figure 4-15).

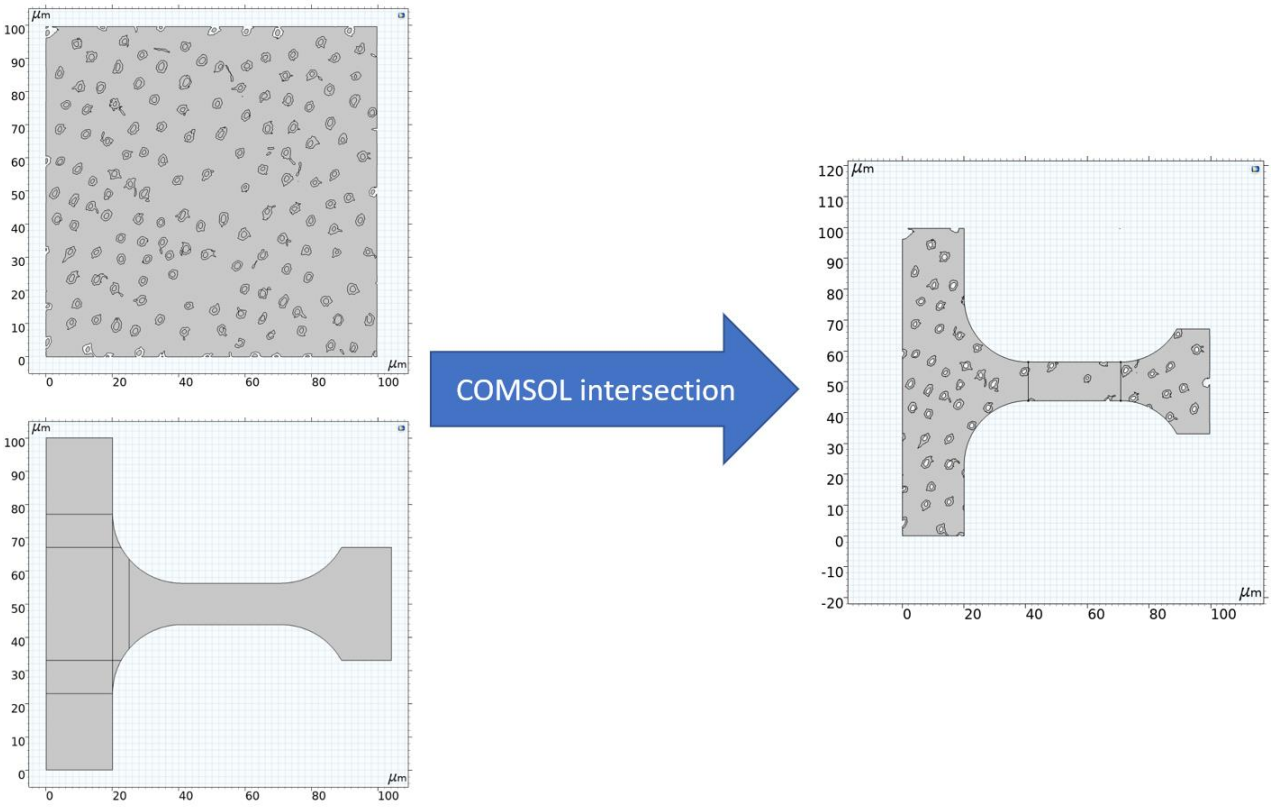

Figure 4-15. Intersection of the geometry of the micro-tensile specimen with the vectorised image of the dentin surface produces a 2D geometry of a specimen that includes tubules.

The right image in Figure 4-15 shows that the microstructure cannot be neglected considering the small scale of the micro-sample. Consequently, the tubules were meshed. The meshing was done with free triangular mesh elements of quadratic serendipity type (260962 elements).

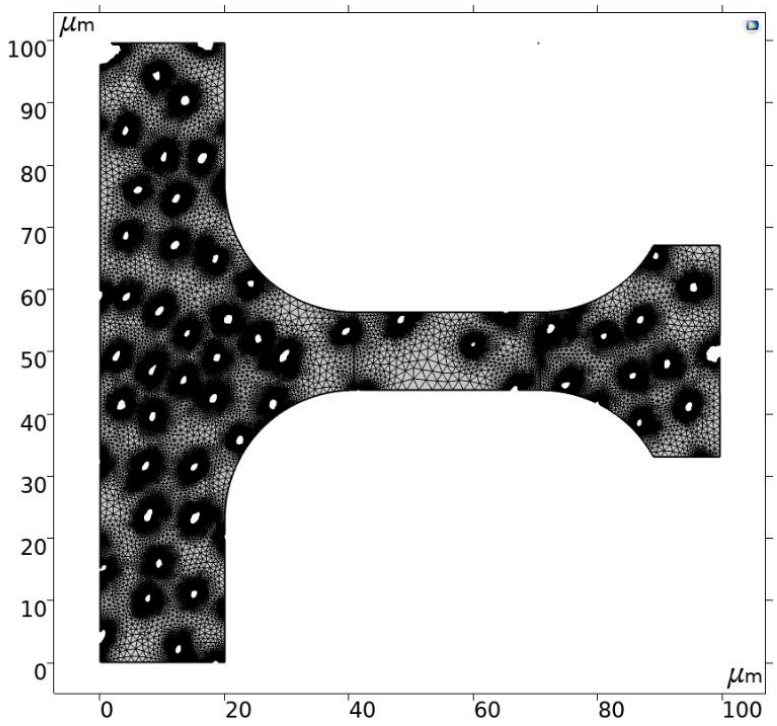

Figure 4-16. Meshing the 2D geometry of the test piece by 261098 free triangular elements

The left boundary of the specimen (highlighted in blue in Figure 4-17.a) is fixed, and the edges of the grip that are in contact with the needle (highlighted in blue in Figure 4-17.b) are pulled 0.15 µm rightward.

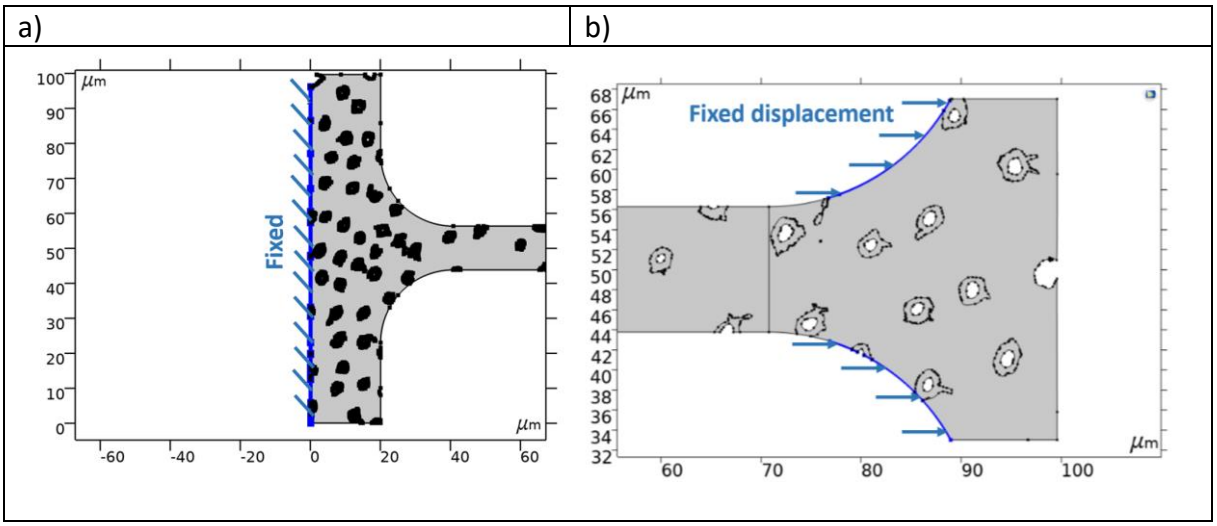

Figure 4-17. Boundary conditions of the 2D simulation of the micro-tensile test. The fixed boundary condition on the left image and the prescribed displacement in the positive x-direction on the right one

The materials of the simulation were assumed to be isotropic and linear elastic, and their moduli (Table 4-6) were taken from the results of Chapter 2. The post-yield nonlinear behavior of the materials was not modelled. This is relatively acceptable for dried dentin, which is brittle and behaves linearly elastic up to fracture.

Table 4-6. Elastic propertiesi of dentin constituents from the Chapter 2

	Young's modulus (GPa)	Poisson's ratio
PTD	44	0.3
ITD	30	0.3

Results of the simulation

By assuming that dentin as a brittle material is most vulnerable to tensile load, the first principal stress, describing the tensile stress is plotted in Figure 4-18.

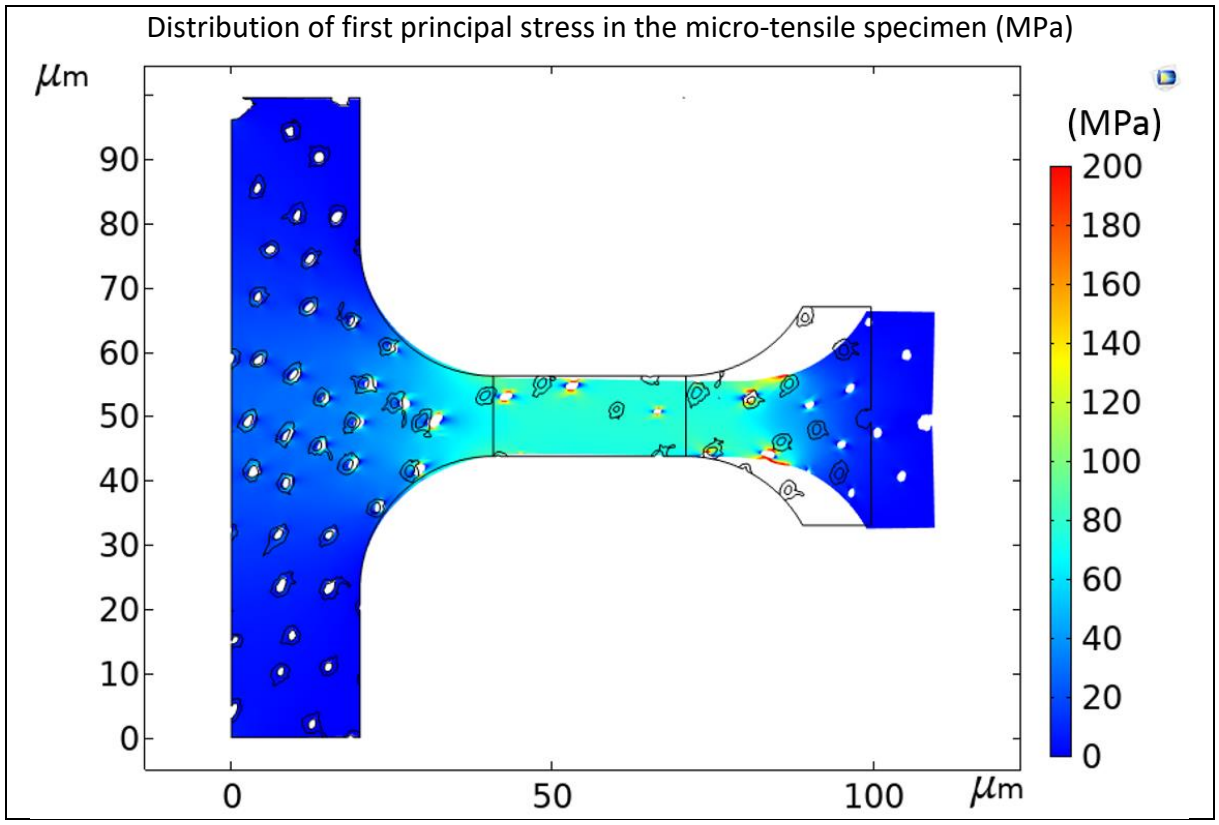

Figure 4-18. The distribution of the first principal stress, visualized on the sketch of the specimen with deformations multiplied by 100.

By revealing the magnitude of displacement that can cause a particular value for the first principal stress, such a simulation can be used to estimate the ultimate extension (and strain) in a displacement-controlled experiment.

The simulation here by applying a displacement of 0.15 µm lead to an average first principal stress of around 90 MPa in a large portion of the gauge zone, which is in the range of the UTS reported in the literature. Therefore, the maximum extension of 0.15 µm of the gauge length and an average axial strain of 0.005 are 'first estimations' for the applied displacement and strain in the micro-tensile experiment.

Figure 4-18 can also be used to study the possible location of crack initiation if a SEM image can be obtained on the tested sample. High stress concentrations on the needle side, especially at tubule location, suggest a risk of initiating cracks.

Another point in Figure 4-18 is the slight anisotropy in the deformation of the specimen. It is slightly bent downwards, which is because of the heterogeneity of the material.

4.4 Micro-tensile Test Results and Discussion

During the in-situ experiment, the load was applied in five steps, and during each step multiple quick SEM images were taken (with a frame time of 0.5 s, and a resolution of 1536x1024). At the end of each step, a slow image was taken (a frame time of 6.6 s, and a resolution of 3072x2048). The SEM images were used for a "Digital Image Correlation" study using Correli software, which is explained in the subsection 4.4.2. The application of the load continued until the sample failed.

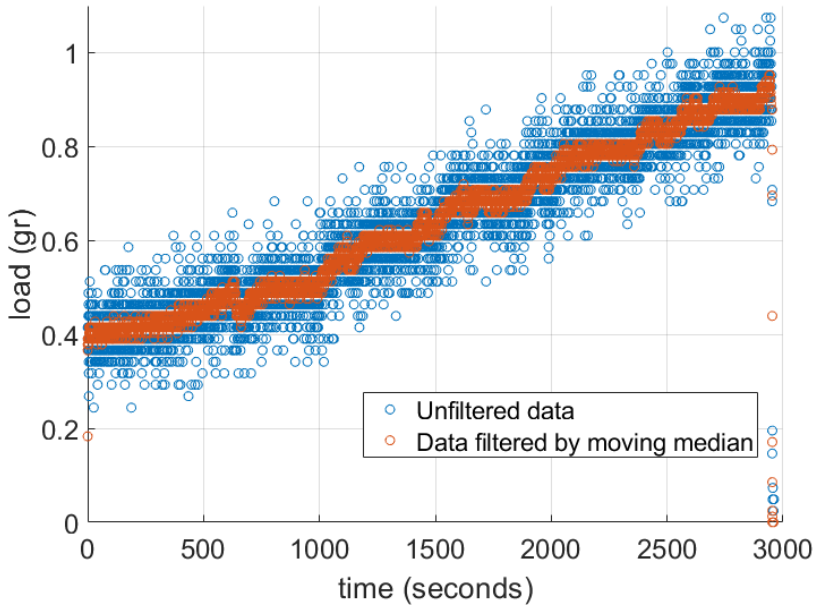

Figure 4-19. The signal of the load applied on the specimen (blue empty dots), and the load data filtered by a moving-median filter (orange dots).

The filter 'moving median' was used with groups of 10 values in each median. It was preferred over a 'mean' filter because it excludes the irrelevant data and keeps the sharpness of the jumps in the signal (e.g., the fracture moment). In the experiment, a very sudden decrease was observed, which means a sudden fracture (Figure 4-19), which means that the dried dentin, especially in its dried state under vacuum in the SEM, was brittle.

4.4.1 Tensile Strength

The highest recorded load is 9.5 mN and the cross-sectional area of the test piece is about 12x13 µm² (Figure 4-20). Therefore, the UTS was estimated to be 61 MPa. As it will be shown in section 4.4.3 on fractography, the sample is nearly perpendicular to the tubule orientation. Therefore, the measured strength is categorized as UTS_t. This is in the range from the literature review given in Table 4-2, which is from 35 to 140 MPa.

We are aware that the strength of a material should be repeatedly measured to give results with statistical meaning. However, due to time constraints, only one measurement was done

in this thesis work. We tried to do more micro-tensile tests, but the samples were lost during the sample preparation or in the process of loading.

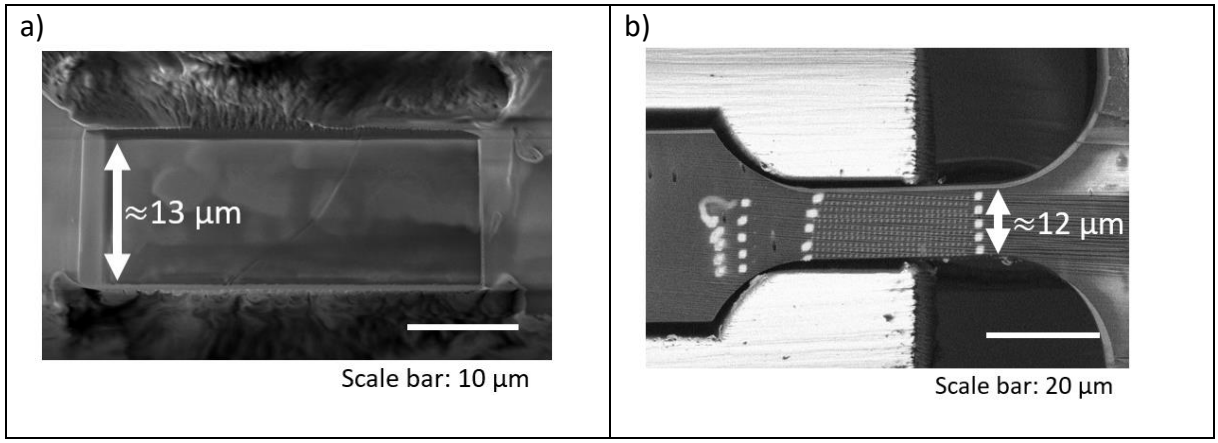

Figure 4-20. The measurement of the specimen dimensions for estimating the cross section of the specimen. a) the head of the specimen before being positioned inside the grip from the longitudinal view, b) the specimen viewed from the perpendicular view

4.4.2 Strain measurement (DIC)

For the estimation of Young's modulus, both the axial strain and axial stress of the specimen should be measured. DIC was used to estimate the displacement fields and consequently the strains. A mesh size of 25 pixels (Figure 4-21) gave acceptable results, and worked well for analysing the images of the experiment.

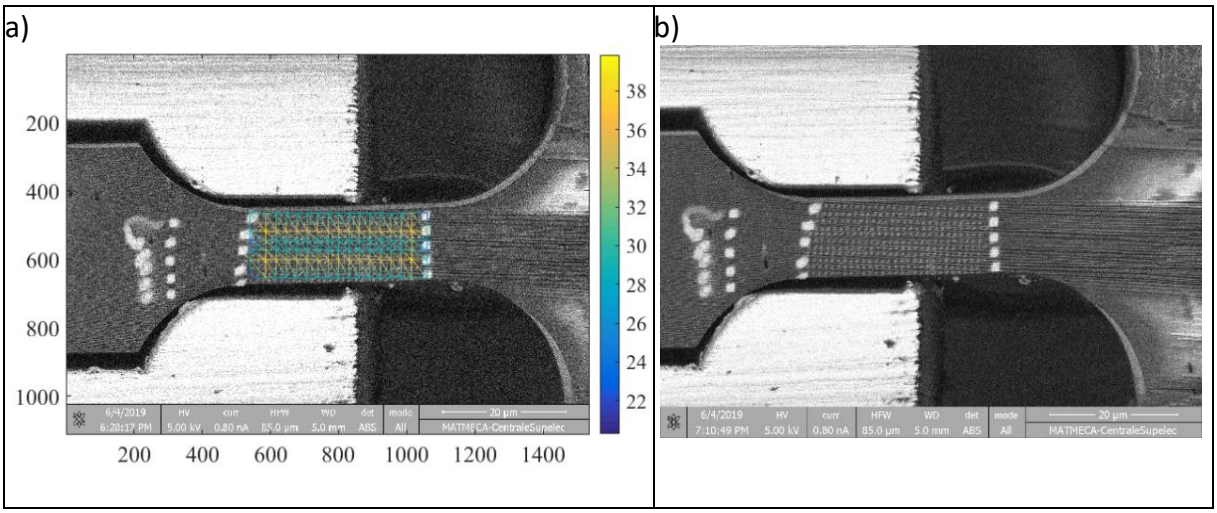

*Figure 4-21.*a) the specimen in the beginning, the triangular mesh used is visualized, b) the specimen later in the experiment.

The strains resulting from the DIC analysis are shown in Figure 4-22.

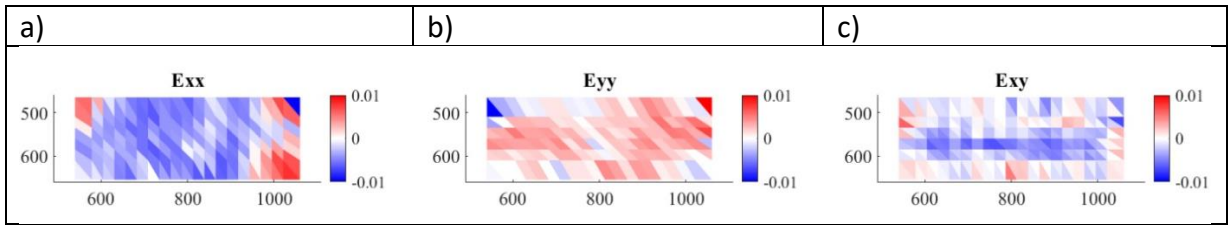

Figure 4-22. The measured strains by DIC for the maximum load before fracture (about 9 mN). From left: a) normal strain in the loading orientation, b) normal strain in the orientation perpendicular, c) shear strain

The unexpected result is that the average strain in the loading orientation (x-axis) is negative.

$$mean(\epsilon_{xx}) = -0.0026\ (SD = -0.0032) \tag{4.10}$$

It should be pointed out that the average strain above is approximate because it is the average of the strain in all elements in the gauge region. But this means that the nodes on the border have a smaller share in the average because they take part in fewer elements than the nodes in the middle.

However, this error might be neglected in comparison with the main artifacts that caused the negative strain measured in the *x*-direction.

One explanation for the negative ϵ_{xx} is that the specimen has had an important out-of-plane movement. For example, it might have rotated around the *y*-axis. In this case, the specimen would seem to shorten due to perspective effects, even it is in fact becoming slightly longer due to the tensile load.

It can be shown that the artificial strain due to the rotation with an angle of α and in the orientation perpendicular to the rotation axis ($\epsilon_{rot|-}$) is equal to:

$$\epsilon_{rot|-} = 1 - \cos\alpha \tag{4.11}$$

This is by assuming that the specimen is horizontal in the beginning. If in the beginning of the experiment the specimen is tilted by an angle α_0, the equation takes the following form:

$$\epsilon_{rot|-} = \cos\alpha_0 - \cos\alpha \tag{4.12}$$

Therefore, if rotation of the sample is assumed to be the reason for artificial strains, then the observed expansion in the y-direction can only be when the specimen is tilted around an axis parallel with the *x*-axis in the beginning and becomes more horizontal during the experiment.

Further work is needed to make a conclusion on this matter.

4.4.3 Fractography

The fracture of the sample occurred in the gauge zone at 13° from the direction perpendicular to the sample length (Figure 4-23). Investigating the fracture surface in other images (Figure 4-24 and Figure 4-25) reveals that the fracture plane was determined by the path of a tubule.

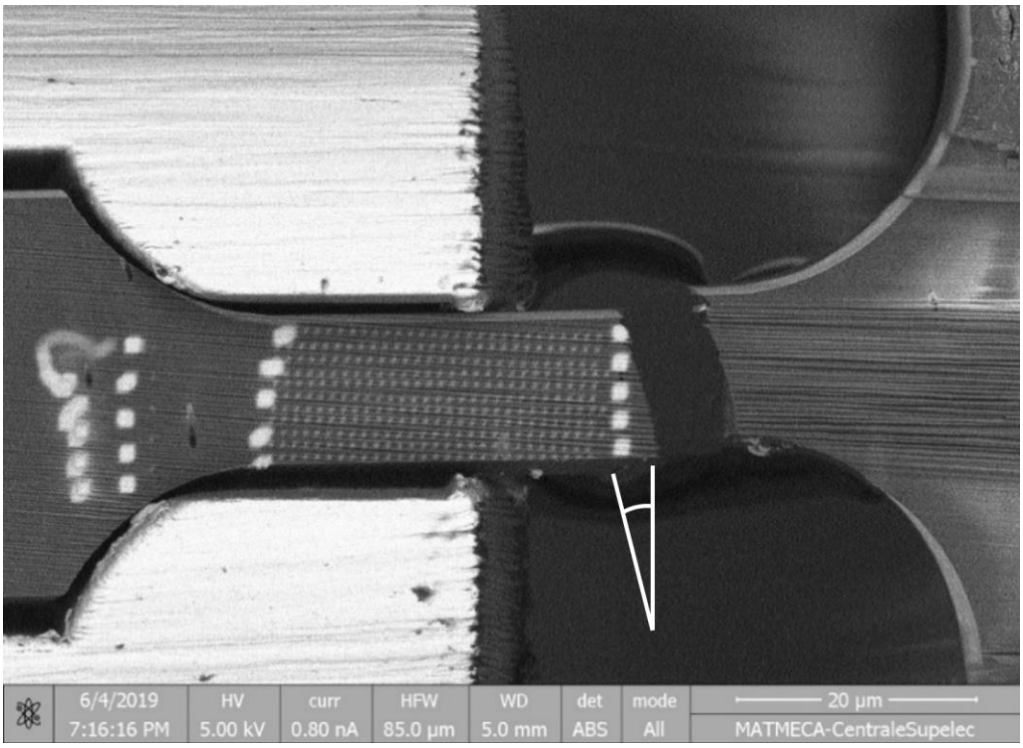

Figure 4-23. The fractured specimen. The angle of the fracture plane with the vertical line is 13°.

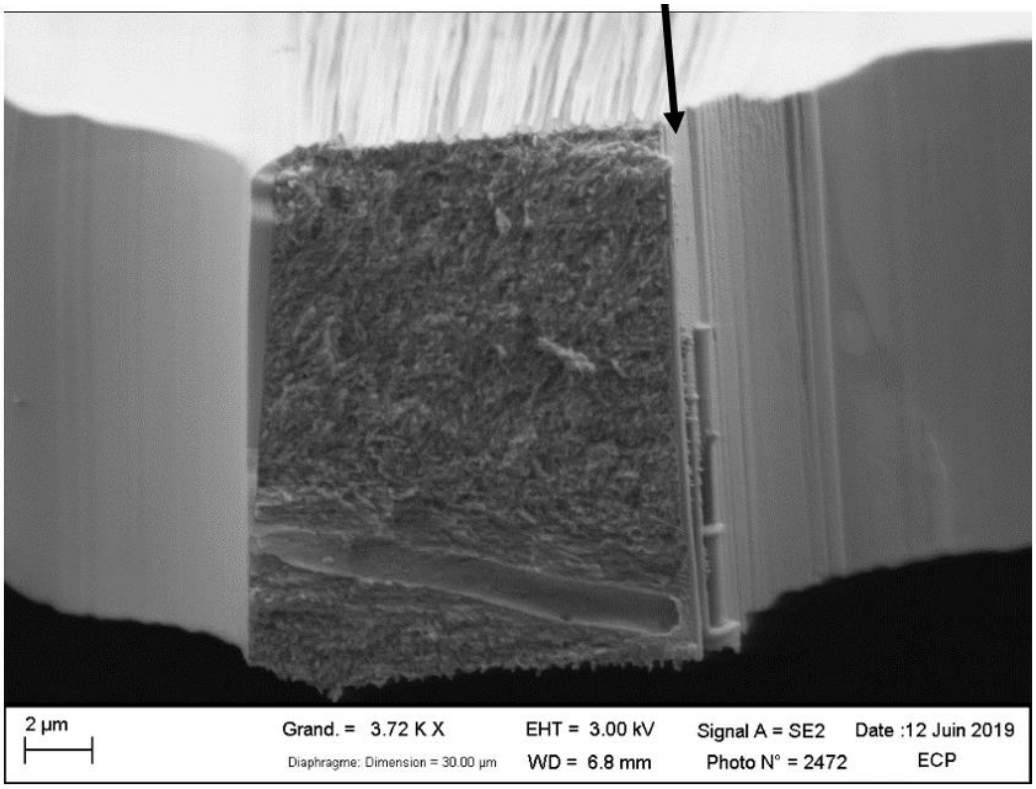

Figure 4-24. The fracture surface (the curtaining effect is visible on the side of the fracture plane, shown by an arrow)

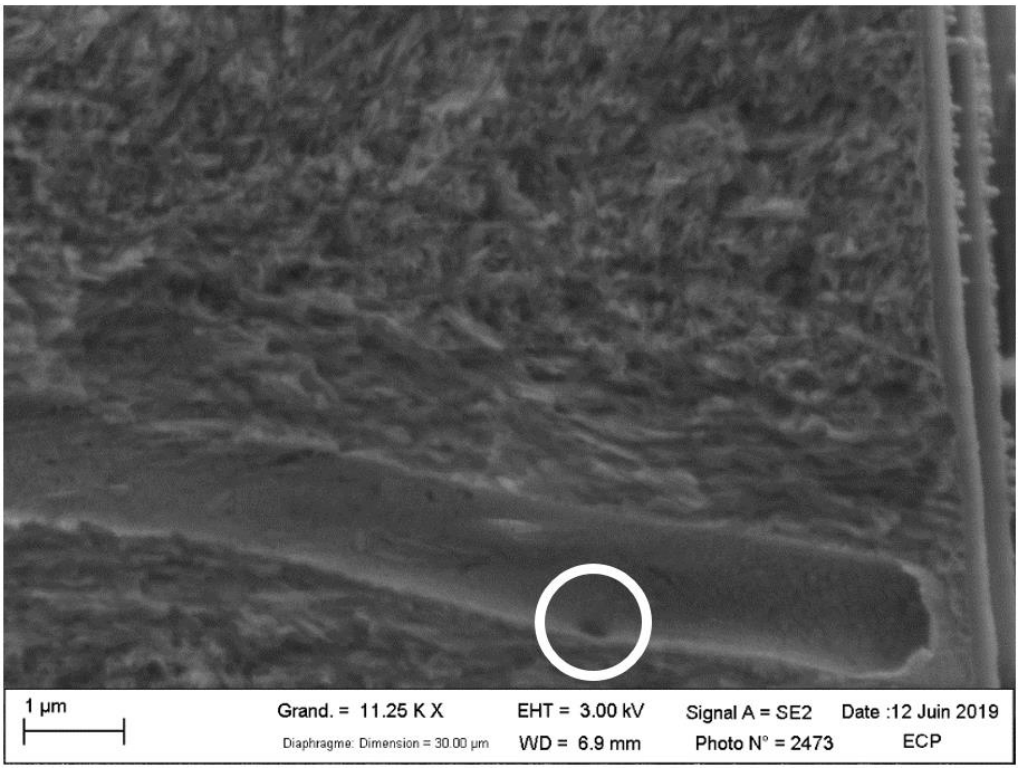

Figure 4-25. Detail of the fracture surface (a small pore is encircled inside the tubule lumen, which seems to be the lumen of a lateral branch)

Beside the fracture plane, lines are visible that seem to be artifacts of the milling process (Figure 4-24). This means that the milling process also played a role in defining the fracture plane.

Another surprising point is that the specimen was broken on the side opposite to the grip while the simulation (Figure 4-18) shows a lower concentration of the stress on this side. One reason for this might be that the stress concentrations due to tubules and LBs (which do not exist in the 2D simulation) have been bigger than those due to the grip.

For comparison between the results from the experiment and the simulation, an important point is that a 2D simulation cannot include the connections between tubules and lateral branches. However, as shown in Chapter 3 section 3.4.2, such locations in dentin have the maximum stress concentrations. One of these connection points is visible in Figure 4-25, which we think might have initiated the crack that has caused the failure of the sample.

4.5 Conclusion and perspective

A tensile test was done on a bone-shape micro-sample of dentin with a gauge length of 30 µm and a cross-section area of approximately 12x13 µm². The fabrication of such a micro-sample is a complex, time-consuming process (preparing a sample takes about three days). It is demonstrated that it is possible to shape such a sample with an appropriate FIB-SEM in a highly heterogeneous material like dentin. Trial and error learning helped to refine the parameters of the process. It is demonstrated that with an appropriate FIB-SEM, it is possible to shape such a sample in a highly heterogeneous material like dentin. However,

because this experiment is very sensitive, it is highly possible that relevant estimations of the mechanical properties cannot be achieved.

DIC technique is a suitable approach to estimate the strain distribution in the micro-sample and consequently to perform local measurements. However, due to the smallness of the sample and significant out-of-plane movement during loading, some future developments of the DIC technique have to be done to leverage the SEM images. Because the strains were not measured properly, the estimation of Young's modulus was not possible.

SEM images of the broken specimen allowed a fractography study on the sample. The fractography showed that the fracture had followed the path of a tubule, which was nearly perpendicular to the loading axis. The existence of a LB near the fracture surface supported the suggestion put forward in Chapter 3: high stress concentrations at the connections between tubules and LBs probably play a role in the initiation of cracks.

Further work has to be done to improve the protocol and to optimize the test and the analysis of the results.

5 Conclusion and perspective

This thesis aimed to characterize and model dentin reliably. The bibliographical review highlighted a large discrepancy in the measured properties of dentin, justifying the main objectives of this research, namely increasing the available knowledge on the microstructure of dentin and the distribution of its mechanical properties related to morphological parameters.

We chose to focus the experimental investigation on a young and healthy permanent tooth. So, the results are representative of a specific and standard type of dentin. This way, it is exempt from the variations due to age and pathologies. Based on the literature, a protocol of sample preparation and storage has been designed to minimize the errors in the experiment results.

An important challenge of this thesis was to characterize the local variations of the mechanical properties due to the graded microstructure of dentin. Therefore, an investigation of the dentin microstructure was done, both in its morphological and mechanical aspects. The resulting knowledge on the microstructure was used for a micromechanical model of dentin.

First, the morphology of dentin was comprehensively studied by SEM. A protocol was developed for acquiring, treating, and analyzing SEM images of dentin in BSE mode. Using the developed protocol, a coronal sample of dentin was imaged thoroughly in its thickness, i.e., from the enamel to the pulp. The tubular microstructure of dentin showed a gradient, which was morphologically quantified by image analysis. By studying the gradients of the dentin microstructure, we gave new insights into the division of dentin into various types and zones (primary and secondary dentin, mantle dentin, etc.). We estimated a 30 µm thickness for mantle dentin and 280 µm thickness for secondary dentin. The main novelty of the image analysis was the refined analysis of the lateral branches of tubules. This analysis was done at three locations in the sample: both the density and dimensions of lateral branches were measured near the enamel, in the middle, and near the pulp.

A numerical tool named "Virtual Nanoindentation" was developed in this thesis. It helped planning and analyzing nanoindentation experiments to characterize dentin both in heterogeneous and homogenized ways: shallow nanoindentations characterized the micro-constituents of dentin. Deep nanoindentations characterized the dentin as a homogenized composite. Three locations in dentin have been specially investigated: near the enamel, in the middle, and near the pulp. The differences between the results of real and virtual nanoindentation tests are explained by variations inside each phase, which can be natural or due to damage. Because such variations are not taken into account in the "Virtual Nanoindentation" tool.

A micromechanical model of a heterogeneous material was used to estimate the dentin's average elastic and fracture properties. It is based on micromechanics of a periodic medium. The distribution of tubules in the microstructure of the dentin agrees with such type of medium. A repeated unit cell (RUC) was built based on the results of the morphological

analysis taken before. The RUC contains one principal tubular lumen surrounded by intertubular dentin (ITD). Both materials are considered homogeneous. The lateral branches (LB) detected by SEM and characterized are also taken into the building of the RUC. To our knowledge, this is the first micromechanical model including lateral branches and is, in this aspect, more complete than previous models in the literature. The mechanical properties of the constituents introduced in the model were taken from the nanoindentation tests. Simulating the model at three locations on the dentin sample led to interesting results. The homogenized anisotropic elastic properties of dentin were calculated: It was observed that the LBs had a neglectable effect on the elastic stiffness of dentin. The numerical simulations also explained the locally various degrees of elastic anisotropy throughout the dentin. The analysis of the stress distributions in the RUC for different mechanical solicitations revealed significant stress concentrations around the tubules and lateral branches, especially close to the junction of both. These locations of stress concentration factor reaching values more than four might be starting points for cracks.

The combination of numerical approach and experimental investigation (images + nanoindentation) needs to be validated by another test. Thus, an in-situ micro-tensile test was designed, and a first test was done. FIB-SEM machined the sample for this experiment. The FIB machining was a time-consuming process and took about three days. The specimen prepared this way is the smallest one ever shaped on dentin for a tensile test. The specimen is small enough (with a gauge zone with dimensions 30x12x13 μm^3) so that its results do not depend on the variations in the tubular microstructure of dentin. This first preliminary test showed the feasibility of such a test and gave a first estimate for the tensile strength of dentin (about 60 MPa). The author is aware that for giving an estimate of the strength, more tests are needed. Other tests can also be done at various locations and orientations in dentin to capture the gradedness and anisotropy of the tensile strength.

Because the tensile solicitations caused the fracture of the sample, the fracture surfaces of the specimen were separated and could be studied. The fracture surface followed the path of a tubule and revealed a lateral branch. Therefore, it supported the idea that the stress concentrations around the connections between the tubules and the lateral branches initiate the cracks.

Estimating a value for Young's modulus from an in-situ micro-tensile test was challenging and not done for this specimen. However, further investigations and improvements in the testing procedure might allow the estimation of Young's modulus in future experiments.

Based on the multi-scale characterization of dentin, a micromechanical model has been built. All the protocols used for this characterization and modeling can be used to study more healthy dentin samples to have a better statistical view of the results.

The same protocols can be used on altered or pathological dentin samples to understand the mechanical consequences of the pathologies better and to have new clues to probe the link between structure and properties.

Further in-situ micro-tensile tests may be done at various locations and orientations in dentin. Such tests will allow studying the local variation in the UTS and its anisotropy and consequently will enrich the knowledge of the deformation mechanisms occurring in this biomaterial. From our point of view, such tests are essential to provide a solid foundation (or base) for models developed in the literature. Another interest is to test different kinds of teeth to investigate the effect of aging and pathologies on dentin.

Also, in the future, it seems interesting to improve the dialog between the experimental results and the FE simulations of the test that are taken in parallel. A 3D simulation of the test is possible if the pieces of the tested micro-specimens are preserved. Then, the pieces can be imaged in 3D by the FIB-SEM technique. Then, the resulting 3D images can be meshed and used for simulation.

The next level for characterizing dentin is to include the nanostructure in the model and thus making it a multi-scale model. If the nanostructure's morphology is achieved, the micromechanical model could also include the collagen fibrils and the mineral lamellae. For this goal, TEM has been used to image a healthy dentin sample. Using the TEM results, the future models of dentin might include the nanostructure and therefore be more comprehensive.

6 References

[1] L.H. He, M. V. Swain, Nanoindentation of tooth tissues, in: Handb. Nanoindentation with Biol. Appl., 2010. doi:10.4032/9789814267601.

[2] A.L. Yettram, K.W.J. Wright, H.M. Pickard, Finite Element Stress Analysis of the Crowns of Normal and Restored Teeth, J. Dent. Res. 55 (1976). doi:10.1177/00220345760550060201.

[3] A. Nanci, En Cate: Oral Histology : Development, Structure and Function, Nanci A, Ten Cate A. Ten Cate Oral Histol. Dev. Struct. Funct. Missouri Mosby; 2013. (2013). doi:10.1038/sj.bdj.2012.772.

[4] J.P. Van Nieuwenhuysen, W. D'Hoore, J. Carvalho, V. Qvist, Long-term evaluation of extensive restorations in permanent teeth, J. Dent. 31 (2003) 395–405. doi:10.1016/S0300-5712(03)00084-8.

[5] T.R. Raphaële Adjerad, Alex Amiotte-Suchet, Bénédicte Boisguerin, Khadija Jabri, Julie Latourelle, Edouard Maugendre, Myriam Mikou, Salimeh Monirijavid, Mickaël Portela, Les dépenses de santé en 2020, 2020.

[6] D. Ericson, E. Kidd, D. McComb, I. Mjör, M.J. Noack, Minimally Invasive Dentistry--concepts and techniques in cariology., Oral Health Prev. Dent. 1 (2003). doi:10.3290/j.ohpd.a8222.

[7] E. Vennat, W. Wang, R. Genthial, B. David, E. Dursun, A. Gourrier, Mesoscale porosity at the dentin-enamel junction could affect the biomechanical properties of teeth, Acta Biomater. 51 (2017). doi:10.1016/j.actbio.2017.01.052.

[8] A. Misra, P. Spencer, O. Marangos, Y. Wang, J.L. Katz, Parametric study of the effect of phase anisotropy on the micromechanical behaviour of dentin-adhesive interfaces, J. R. Soc. Interface. 2 (2005) 145–157.

[9] I.A. Mjör, I. Nordahl, The density and branching of dentinal tubules in human teeth, Arch. Oral Biol. (1996). doi:10.1016/0003-9969(96)00008-8.

[10] J.H. Kinney, S.J. Marshall, G.W. Marshall, The mechanical properties of human dentin: A critical review and re-evaluation of the dental literature, Crit. Rev. Oral Biol. Med. 14 (2003) 13–29. doi:10.1177/154411130301400103.

[11] A. Nanci, Ten Cate ' s Oral Histology Development , Structure , and Function ANTONIO NANCI , PhD (McGill), PhD Honoris causa (University of Messina), E. (2017).

[12] V. Lertchirakarn, J.E.A. Palamara, H.H. Messer, Anisotropy of tensile strength of root dentin, J. Dent. Res. 80 (2001) 453–456. doi:10.1177/00220345010800021001.

[13] M. T, R. M, Grotthuss mechanisms: from proton transport in proton wires to bioprotonic devices, J. Phys. Condens. Matter. 28 (2016). doi:10.1088/0953-8984/28/2/023001.

[14] H.G. Fromme, H. Riedel, Messungen über die Weite der Dentinkanälchen an nichtentmineralisierten bleibenden Zähnen und Milchzähnen., Dtsch. Zahnarztl. Z. 25 (1970).

[15] A. Linde, M. Goldberg, Dentinogenesis, Crit. Rev. Oral Biol. Med. (1994). doi:10.1177/10454411930040050301.

[16] R.K. Nalla, A.E. Porter, C. Daraio, A.M. Minor, V. Radmilovic, E.A. Stach, A.P. Tomsia, R.O. Ritchie, Ultrastructural examination of dentin using focused ion-beam cross-sectioning and transmission electron microscopy, Micron. 36 (2005). doi:10.1016/j.micron.2005.05.011.

[17] A. Nazari, D. Bajaj, D. Zhang, E. Romberg, D. Arola, Aging and the reduction in fracture toughness of human dentin, J. Mech. Behav. Biomed. Mater. 2 (2009). doi:10.1016/j.jmbbm.2009.01.008.

[18] N.F. Bissada, Symptomatology and clinical features of hypersensitive teeth, Arch. Oral Biol. 39 (1994). doi:10.1016/0003-9969(94)90185-6.

[19] G. Fosse, P.K. Saele, R. Eide, Numerical density and distributional pattern of dentin tubules, Acta Odontol. Scand. 50 (1992). doi:10.3109/00016359209012764.

[20] J.H. Kinney, J. Oliveira, D.L. Haupt, G.W. Marshall, S.J. Marshall, The spatial arrangement of tubules in human dentin, J. Mater. Sci. Mater. Med. 12 (2001). doi:10.1023/A:1011232912734.

[21] L. Tjäderhane, M.R. Carrilho, L. Breschi, F.R. Tay, D.H. Pashley, Dentin basic structure and composition-an overview, Endod. Top. 20 (2009). doi:10.1111/j.1601-1546.2012.00269.x.

[22] M. Goldberg, D. Septier, K. Bourd, R. Hall, J.C. Jeanny, L. Jonet, S. Colin, F. Tager, C. Chaussain-Miller, M. Garabédian, A. George, H. Goldberg, S. Menashi, The dentino-enamel junction revisited, Connect. Tissue Res. (2002). doi:10.1080/03008200290000817.

[23] R.Z. Wang, S. Weiner, Strain-structure relations in human teeth using Moire fringes, J. Biomech. 31 (1997) 135–141. doi:10.1016/S0021-9290(97)00131-0.

[24] W. Wang, Multi-scale mechanical characterization of dentin, (2014).

[25] E. Vennat, C. Bogicevic, J.M. Fleureau, M. Degrange, Demineralized dentin 3D porosity and pore size distribution using mercury porosimetry, Dent. Mater. 25 (2009). doi:10.1016/j.dental.2008.12.002.

[26] R. Garberoglio, M. Brännström, Scanning electron microscopic investigation of human dentinal tubules, Arch. Oral Biol. 21 (1976) 355–362. doi:10.1016/S0003-9969(76)80003-9.

[27] M.B. Lopes, M.A.C. Sinhoreti, A. Gonini Júnior, S. Consani, J.F. McCabe, Comparative study of tubular diameter and quantity for human and bovine dentin at different depths, Braz. Dent. J. 20 (2009). doi:10.1590/s0103-64402009000400003.

[28] T.L. Lenzi, C.D.A.B. Guglielmi, V.E. Arana-Chavez, D.P. Raggio, Tubule density and diameter in coronal dentin from primary and permanent human teeth, Microsc. Microanal. 19 (2013). doi:10.1017/S1431927613012725.

[29] I. Zanette, B. Enders, M. Dierolf, P. Thibault, R. Gradl, A. Diaz, M. Guizar-Sicairos, A. Menzel, F. Pfeiffer, P. Zaslansky, Ptychographic X-ray nanotomography quantifies

mineral distributions in human dentine, Sci. Rep. (2015). doi:10.1038/srep09210.

[30] W. Ketterl, The dentin in permanent human teeth, Stoma (Heidelb). 14 (1961) 79–96.

[31] L. TRONSTAD, Ultrastructural observations on human coronal dentin, Eur. J. Oral Sci. 81 (1973). doi:10.1111/j.1600-0722.1973.tb01500.x.

[32] N. Nakabayashi, D. Pashley, Hybridization of Dental Hard Tissues, Chicago Quintessence. (1998).

[33] J.S. Earl, R.K. Leary, J.S. Perrin, R. Brydson, J.P. Harrington, K. Markowitz, S.J. Milne, Characterization of dentine structure in three dimensions using FIB-SEM, J. Microsc. 240 (2010). doi:10.1111/j.1365-2818.2010.03396.x.

[34] D.H. Pashley, Dynamics of the pulpo-dentin complex, Crit. Rev. Oral Biol. Med. 7 (1996). doi:10.1177/10454411960070020101.

[35] P. Roschger, H. Plenk, K. Klaushofer, J. Eschberger, M.D. Grynpas, A. Boyde, T.M. Boyce, J.G. Skedros, A new scanning electron microscopy approach to the quantification of bone mineral distribution: Backscattered electron image grey-levels correlated to calcium Kα-line intensities, Scanning Microsc. 9 (1995).

[36] A. Distante, C. Distante, Handbook of image processing and computer vision: Volume 2: From image to pattern, 2020. doi:10.1007/978-3-030-42374-2.

[37] I. Arganda-Carreras, V. Kaynig, C. Rueden, K.W. Eliceiri, J. Schindelin, A. Cardona, H.S. Seung, Trainable Weka Segmentation: A machine learning tool for microscopy pixel classification, Bioinformatics. 33 (2017). doi:10.1093/bioinformatics/btx180.

[38] J. Schindelin, I. Arganda-Carreras, E. Frise, V. Kaynig, M. Longair, T. Pietzsch, S. Preibisch, C. Rueden, S. Saalfeld, B. Schmid, J.Y. Tinevez, D.J. White, V. Hartenstein, K. Eliceiri, P. Tomancak, A. Cardona, Fiji: An open-source platform for biological-image analysis, Nat. Methods. 9 (2012). doi:10.1038/nmeth.2019.

[39] M.-L. CA, Stereological tools in biomedical research, An. Acad. Bras. Cienc. 75 (2003) 469–486. doi:10.1590/S0001-37652003000400006.

[40] C. Arson, Y. Yasothan, R. Jeanneret, A. Benoit, N. Roubier, E. Vennat, AN ALTERNATIVE to PERIODIC HOMOGENIZATION for DENTIN ELASTIC STIFFNESS, J. Mech. Med. Biol. 20 (2020). doi:10.1142/S0219519419500817.

[41] E. Couve, Changes in the Predentin Thickness and Mineralization Front Configuration in Developing Human Premolars, Cells Tissues Organs. 130 (1987) 324–328. doi:10.1159/000146464.

[42] P. Gupta, H. Kaur, M.S. G.S., M.K. Jawanda, N. Sahi, Human Age Estimation from Tooth Cementum and Dentin, J. Clin. Diagn. Res. 8 (2014) ZC07. doi:10.7860/JCDR/2014/7275.4221.

[43] G. Constantinides, K.S. Ravi Chandran, F.J. Ulm, K.J. Van Vliet, Grid indentation analysis of composite microstructure and mechanics: Principles and validation, Mater. Sci. Eng. A. (2006). doi:10.1016/j.msea.2006.05.125.

[44] M. Khelifa, V. Fierro, J. Macutkevič, A. Celzard, Nanoindentation of flexible graphite:

yxperimental versus simulation studies, Adv. Mater. Sci. 3 (2018) 1–11. doi:10.15761/AMS.1000142.

[45] Y. Kadin, M. Mazaheri, V. Zolotarevskiy, C. Vieillard, M. Hadfield, Finite elements based approaches for the modelling of radial crack formation upon Vickers indentation in silicon nitride ceramics, J. Eur. Ceram. Soc. 39 (2019) 4011–4022. doi:10.1016/J.JEURCERAMSOC.2019.05.058.

[46] A.C. Fischer-Cripps, Nanoindentation, 1st ed., Springer, 2002.

[47] Y.J. Park, G.M. Pharr, Nanoindentation with spherical indenters: finite element studies of deformation in the elastic–plastic transition regime, Thin Solid Films. 447–448 (2004) 246–250. doi:10.1016/S0040-6090(03)01102-7.

[48] ISO - ISO 14577-1:2015 - Metallic materials — Instrumented indentation test for hardness and materials parameters — Part 1: Test method, (n.d.). https://www.iso.org/standard/56626.html (accessed October 7, 2021).

[49] B. van Meerbeek, G. Willems, P. Lambrechts, G. Vanherle, J.P. Celis, J.R. Roos, M. Braem, Assessment by Nano-indentation of the Hardness and Elasticity of the Resin-Dentin Bonding Area, J. Dent. Res. 72 (1993) 1434–1442. doi:10.1177/00220345930720101401.

[50] E. Broitman, Indentation Hardness Measurements at Macro-, Micro-, and Nanoscale: A Critical Overview, Tribol. Lett. 2016 651. 65 (2016) 1–18. doi:10.1007/S11249-016-0805-5.

[51] R. Wimmer, B.N. Lucas, T.Y. Tsui, W.C. Oliver, Longitudinal hardness and Young's modulus of spruce tracheid secondary walls using nanoindentation technique, Wood Sci. Technol. (1997). doi:10.1007/s002260050022.

[52] W.C. Oliver, G.M. Pharr, Measurement of hardness and elastic modulus by instrumented indentation: Advances in understanding and refinements to methodology, J. Mater. Res. 19 (2004) 3–20. doi:10.1557/jmr.2004.19.1.3.

[53] X. Li, B. Bhushan, A review of nanoindentation continuous stiffness measurement technique and its applications, Mater. Charact. 48 (2002) 11–36. doi:10.1016/S1044-5803(02)00192-4.

[54] M.F. Doerner, W.D. Nix, A method for interpreting the data from depth-sensing indentation instruments, J. Mater. Res. 1 (1986) 601–609. doi:10.1557/JMR.1986.0601.

[55] R.H. Atkinson, Hardness Tests for Rock Characterization, Compr. Rock Eng. Vol. 3. (1993) 105–117. doi:10.1016/B978-0-08-042066-0.50012-4.

[56] J. Boussinesq, Application des potentiels à l'étude de l'équilibre et du mouvement des ..., 1882. https://books.google.fr/books?hl=fr&lr=&id=7vZYAAAAYAAJ&oi=fnd&pg=PA15&dq=%22j+boussinesq%22+%221882%22&ots=sZphbhatwW&sig=DFnNnOP7tJDNrkpLwABeUzS8ztc&redir_esc=y#v=onepage&q=%22j boussinesq%22 %221882%22&f=false (accessed October 7, 2021).

[57] I.N. Sneddon, The relation between load and penetration in the axisymmetric boussinesq problem for a punch of arbitrary profile, Int. J. Eng. Sci. 3 (1965) 47–57. doi:10.1016/0020-7225(65)90019-4.

[58] A.C.C. Fischer-Cripps, Mechanical Engineering Series: Introduction to Contact Mechanics, 2006.

[59] J.E. Jakes, D.S. Stone, The edge effect in nanoindentation, Philos. Mag. (2011). doi:10.1080/14786435.2010.495360.

[60] G. Guidoni, M. Swain, I. Jäger, Nanoindentation of wet and dry compact bone: Influence of environment and indenter tip geometry on the indentation modulus, Philos. Mag. (2010). doi:10.1080/14786430903201853.

[61] D. Mercier, TriDiMap Documentation, (2016).

[62] P. Sudharshan Phani, W.C. Oliver, A critical assessment of the effect of indentation spacing on the measurement of hardness and modulus using instrumented indentation testing, Mater. Des. (2019). doi:10.1016/j.matdes.2018.107563.

[63] J.H. Kinney, M. Balooch, S.J. Marshall, G.W. Marshall, T.P. Weihs, Atomic force microscope measurements of the hardness and elasticity of peritubular and intertubular human dentin, J. Biomech. Eng. (1996). doi:10.1115/1.2795939.

[64] J.H. Kinney, M. Balooch, S.J. Marshall, G.W. Marshall, T.P. Weihs, Hardness and young's modulus of human peritubular and intertubular dentine, Arch. Oral Biol. 41 (1996) 9–13. doi:10.1016/0003-9969(95)00109-3.

[65] S. Habelitz, G.W. Marshall, M. Balooch, S.J. Marshall, Nanoindentation and storage of teeth, J. Biomech. 35 (2002) 995–998. doi:10.1016/S0021-9290(02)00039-8.

[66] D. Ziskind, M. Hasday, S.R. Cohen, H.D. Wagner, Young's modulus of peritubular and intertubular human dentin by nano-indentation tests, J. Struct. Biol. 174 (2011) 23–30. doi:10.1016/j.jsb.2010.09.010.

[67] J.H. Kinney, M. Balooch, G.W. Marshall, S.J. Marshall, A micromechanics model of the elastic properties of human dentine, Arch. Oral Biol. 44 (1999) 813–822. doi:10.1016/S0003-9969(99)00080-1.

[68] S.R. Cohen, N. Apter, S. Jesse, S. Kalinin, D. Barlam, A.I. Peretz, D. Ziskind, H.D. Wagner, AFM Investigation of Mechanical Properties of Dentin, Isr. J. Chem. (2008). doi:10.1560/ijc.48.2.65.

[69] H. Ryou, E. Romberg, D.H. Pashley, F.R. Tay, D. Arola, Nanoscopic dynamic mechanical properties of intertubular and peritubular dentin, J. Mech. Behav. Biomed. Mater. 7 (2012) 3–16. doi:10.1016/j.jmbbm.2011.08.010.

[70] G. Balooch, G.W. Marshall, S.J. Marshall, O.L. Warren, S.A.S. Asif, M. Balooch, Evaluation of a new modulus mapping technique to investigate microstructural features of human teeth, J. Biomech. 37 (2004) 1223–1232. doi:10.1016/j.jbiomech.2003.12.012.

[71] N. Meredith, M. Sherriff, D.J. Setchell, S.A.V. Swanson, Measurement of the microhardness and young's modulus of human enamel and dentine using an

indentation technique, Arch. Oral Biol. (1996). doi:10.1016/0003-9969(96)00020-9.

[72] R. Wang, S. Weiner, Human root dentin: Structural anisotropy and Vickers microhardness isotropy, Connect. Tissue Res. 39 (1998) 269–279. doi:10.3109/03008209809021502.

[73] G.W. Marshall, M. Balooch, R.R. Gallagher, S.A. Gansky, S.J. Marshall, Mechanical properties of the dentinoenamel junction: AFM studies of nanohardness, elastic modulus, and fracture, J. Biomed. Mater. Res. 54 (n.d.) 87–95.

[74] H. Fong, M. Sarikaya, S.N. White, M.L. Snead, Nano-mechanical properties profiles across dentin-enamel junction of human incisor teeth, Mater. Sci. Eng. C. 7 (1999) 119–128. doi:10.1016/s0928-4931(99)00133-2.

[75] L. Angker, M. V. Swain, N. Kilpatrick, Micro-mechanical characterisation of the properties of primary tooth dentine, J. Dent. (2003). doi:10.1016/S0300-5712(03)00045-9.

[76] Z. Wang, K. Wang, W. Xu, X. Gong, F. Zhang, Mapping the mechanical gradient of human dentin-enamel-junction at different intratooth locations, Dent. Mater. (2018). doi:10.1016/j.dental.2017.11.001.

[77] H.H.K. Xu, D.T. Smith, S. Jahanmir, E. Romberg, J.R. Kelly, V.P. Thompson, E.D. Rekow, Indentation damage and mechanical properties of human enamel and dentin, J. Dent. Res. 77 (1998) 472–480. doi:10.1177/00220345980770030601.

[78] J.H. Kinney, R.K. Nalla, J.A. Pople, T.M. Breunig, R.O. Ritchie, Age-related transparent root dentin: mineral concentration, crystallite size, and mechanical properties, Biomaterials. 26 (2005) 3363–3376. doi:10.1016/J.BIOMATERIALS.2004.09.004.

[79] J.H. Kinney, J.R. Gladden, G.W. Marshall, S.J. Marshall, J.H. So, J.D. Maynard, Resonant ultrasound spectroscopy measurements of the elastic constants of human dentin, J. Biomech. 37 (2004) 437–441. doi:10.1016/J.JBIOMECH.2003.09.028.

[80] J. Jantarat, J.E.A. Palamara, C. Lindner, H.H. Messer, Time-dependent properties of human root dentin, Dent. Mater. 18 (2002) 486–493. doi:10.1016/S0109-5641(01)00074-4.

[81] P. JE, W. PR, T. CD, M. HH, A new imaging technique for measuring the surface strains applied to dentine, J. Dent. 28 (2000) 141–146. doi:10.1016/S0300-5712(99)00054-8.

[82] H. Sano, B. Ciucchi, W.G. Matthews, Tensile Properties of Mineralized and Demineralized Human and Bovine Dentin, J. Dent. Res. 73 (1994) 1205–1211. doi:10.1177/00220345940730061201.

[83] J.D. Currey, K. Brear, Hardness, Young's modulus and yield stress in mammalian mineralized tissues, J. Mater. Sci. Mater. Med. 1 (1990). doi:10.1007/BF00705348.

[84] M.L. Lehman, Tensile Strength of Human Dentin, J. Dent. Res. 46 (1967) 197–201. doi:10.1177/00220345670460011001.

[85] A.H. Burstein, J.D. Currey, V.H. Frankel, D.T. Reilly, The ultimate properties of bone tissue: The effects of yielding, J. Biomech. (1972). doi:10.1016/0021-9290(72)90017-6.

[86] X. Chen, J.J. Vlassak, Numerical study on the measurement of thin film mechanical properties by means of nanoindentation, J. Mater. Res. 16 (2001) 2974–2982. doi:10.1557/JMR.2001.0408.

[87] M. Hardiman, T.J. Vaughan, C.T. McCarthy, The effects of pile-up, viscoelasticity and hydrostatic stress on polymer matrix nanoindentation, Polym. Test. (2016). doi:10.1016/j.polymertesting.2016.04.003.

[88] I. Furin, M.I. Pastrama, H. Kariem, K.W. Luczynski, O. Lahayne, C. Hellmich, A New Nanoindentation Protocol for Identifying the Elasticity of Undamaged Extracellular Bone Tissue, in: MRS Adv., 2016. doi:10.1557/adv.2016.130.

[89] K. Tai, F.J. Ulm, C. Ortiz, Nanogranular origins of the strength of bone, Nano Lett. (2006). doi:10.1021/nl061877k.

[90] B. An, Y. Xu, D. Zhang, Crack initiation and propagation in composite microstructure of dentin, Int. J. Solids Struct. (2017). doi:10.1016/j.ijsolstr.2017.02.005.

[91] Y.T. Cheng, C.M. Cheng, Scaling, dimensional analysis, and indentation measurements, Mater. Sci. Eng. R Reports. (2004). doi:10.1016/j.mser.2004.05.001.

[92] E. Vennat, A. Hemmati, N. Schmitt, D. Aubry, The role of lateral branches on effective stiffness and local overstresses in dentin, J. Mech. Behav. Biomed. Mater. 116 (2021) 104329. doi:10.1016/J.JMBBM.2021.104329.

[93] S. Nemat-Nasser; M. Hori, Micromechanics, Volume 37 st Edition Overall Properties of Heterogeneous Materials, (n.d.).

[94] Z. Hashin, S. Shtrikman, A variational approach to the theory of the elastic behaviour of multiphase materials, J. Mech. Phys. Solids. 11 (1963) 127–140. doi:10.1016/0022-5096(63)90060-7.

[95] Z. Hashin, B.W. Rosen, The Elastic Moduli of Fiber-Reinforced Materials, J. Appl. Mech. 31 (1964) 223–232. doi:10.1115/1.3629590.

[96] Q.H. Qin, M. V. Swain, A micro-mechanics model of dentin mechanical properties, Biomaterials. 25 (2004). doi:10.1016/j.biomaterials.2003.12.042.

[97] B. Bar-On, H. Daniel Wagner, Elastic modulus of hard tissues, J. Biomech. 45 (2012). doi:10.1016/j.jbiomech.2011.12.003.

[98] Y.J. Yoon, Estimation of the elastic constants of dentin, Int. J. Precis. Eng. Manuf. 14 (2013). doi:10.1007/s12541-013-0043-9.

[99] E.S.-P.-L. notes in physics, undefined 1980, Non-homogeneous media and vibration theory, Ci.Nii.Ac.Jp. (n.d.). https://ci.nii.ac.jp/naid/10003192133/ (accessed October 13, 2021).

[100] D. (Doïna) Cioranescu, P. Donato, An introduction to homogenization, (1999) 262.

[101] S. Seyedkavoosi, I. Sevostianov, Multiscale micromechanical modeling of the elastic properties of dentin, J. Mech. Behav. Biomed. Mater. 100 (2019) 103397. doi:10.1016/J.JMBBM.2019.103397.

[102] J. (Jean) Lemaître, J.-L. Chaboche, Mechanics of solid materials, (1990) 556.

[103] D. Arola, R.K. Reprogel, Effects of aging on the mechanical behavior of human dentin, Biomaterials. 26 (2005) 4051–4061. doi:10.1016/J.BIOMATERIALS.2004.10.029.

[104] H.C. Wu, B. Mu, On stress concentrations for isotropic/orthotropic plates and cylinders with a circular hole, Compos. Part B Eng. 34 (2003) 127–134. doi:10.1016/S1359-8368(02)00097-5.

[105] A.F. Liu, Mechanics and mechanisms of fracture : an introduction, (2005) 458.

[106] T.J.G. Huang, H. Schilder, D. Nathanson, Effects of moisture content and endodontic treatment on some mechanical properties of human dentin, J. Endod. 18 (1992) 209–215. doi:10.1016/S0099-2399(06)81262-8.

[107] L.G. Watanabe, G.W. Marshall, S.J. Marshall, Dentin shear strength: Effects of tubule orientation and intratooth location, Dent. Mater. 12 (1996) 109–115. doi:10.1016/S0109-5641(96)80077-7.

[108] D.D. Arola, R.K. Reprogel, Tubule orientation and the fatigue strength of human dentin, Biomaterials. 27 (2006). doi:10.1016/j.biomaterials.2005.10.005.

[109] D.A. LaVan, W.N. Sharpe, Tensile testing of microsamples, Exp. Mech. 39 (1999). doi:10.1007/BF02323554.

[110] G. V. BLACK, An investigation of the physical characters of the human teeth in relation to their diseases, and to practical dental operations, together with the physical characters of filling-materials., Dent. Cosm. 36 (1895) 469–484.

[111] R.L. BOWEN, M.S. RODRIGUEZ, Tensile strength and modulus of elasticity of tooth structure and several restorative materials, J. Am. Dent. Assoc. 64 (1962) 378–387. doi:10.14219/JADA.ARCHIVE.1962.0090.

[112] T. INOUE, H. TAKAHASHI, F. NISHIMURA, Anisotropy of Tensile Strengths of Bovine Dentin Regarding Dentinal Tubule Orientation and Location., Dent. Mater. J. 21 (2011) 32–43. doi:10.4012/dmj.21.32.

[113] H. Fischer, W. Rentzsch, R. Marx, A modified size effect model for brittle nonmetallic materials, Eng. Fract. Mech. 69 (2002) 781–791. doi:10.1016/S0013-7944(01)00126-6.

[114] R. Jeanneret, C. Arson, E. Vennat, Homogenization of Dentin Elastic Properties Based on Microstructure Characterization, Statistical Back-Analysis, and FEM Simulation, Poromechanics 2017 - Proc. 6th Biot Conf. Poromechanics. (2017) 1339–1346. doi:10.1061/9780784480779.166.

[115] G. M, S. CJ, de C. RM, Ultimate tensile strength of tooth structures, Dent. Mater. 20 (2004) 322–329. doi:10.1016/S0109-5641(03)00110-6.

[116] P.A. Miguez, P.N.R. Pereira, P. Atsawasuwan, M. Yamauchi, Collagen Cross-linking and Ultimate Tensile Strength in Dentin:, Http://Dx.Doi.Org/10.1177/154405910408301014. 83 (2016) 807–810. doi:10.1177/154405910408301014.

[117] S. Inoue, P. Pereira, … C.K.-D. materials, undefined 2003, Effect of depth and tubule direction on ultimate tensile strength of human coronal dentin, Jstage.Jst.Go.Jp. 22 (2003) 39–47. https://www.jstage.jst.go.jp/article/dmj1982/22/1/22_1_39/_article/-

char/ja/ (accessed October 5, 2021).

[118] T. INOUE, H. TAKAHASHI, F. NISHIMURA, Anisotropy of Tensile Strengths of Bovine Dentin Regarding Dentinal Tubule Orientation and Location, Dent. Mater. J. 21 (2002) 32–43. doi:10.4012/DMJ.21.32.

[119] J. LIU, M. HATTORI, K. HASEGAWA, M. YOSHINARI, E. KAWADA, Y. ODA, Effect of Tubule Orientation and Dentin Location on the Microtensile Strength of Bovine Root Dentin, Dent. Mater. J. 21 (2002) 73–82. doi:10.4012/DMJ.21.73.

[120] M. Staninec, G.W. Marshall, J.F. Hilton, D.H. Pashley, S.A. Gansky, S.J. Marshall, J.H. Kinney, Ultimate tensile strength of dentin: Evidence for a damage mechanics approach to dentin failure, J. Biomed. Mater. Res. 63 (2002) 342–345. doi:10.1002/JBM.10230.

[121] R. Carvalho, … C.F.-J. of A., undefined 2001, Tensile strength of human dentin as a function of tubule orientation and density., Researchgate.Net. (2001). https://www.researchgate.net/profile/Carlos-Augusto-Fernandes/publication/11470457_Tensile_strength_of_human_dentin_as_a_function_of_tubule_orientation_and_density/links/02e7e538655016c3ab000000/Tensile-strength-of-human-dentin-as-a-function-of-tubule-orientation-and-density.pdf (accessed October 5, 2021).

[122] S. Inoue, P.N.R. PEREIRA, C. Kawamoto, M. Nakajima, K. KOSHIRO, J. TAGAMI, R.M. CARVALHO, D.H. PASHLEY, H. SANO, Effect of Depth and Tubule Direction on Ultimate Tensile Strength of Human Coronal Dentin., Dent. Mater. J. 22 (2011) 39–47. doi:10.4012/dmj.22.39.

[123] L. Dormieux, D. Kondo, F.-J. (Franz-J. Ulm, Microporomechanics, (2006) 328.

[124] F. Eltit, V. Ebacher, R. Wang, Inelastic deformation and microcracking process in human dentin, J. Struct. Biol. 183 (2013) 141–148. doi:10.1016/j.jsb.2013.04.002.

[125] C.A. Volkert, A.M. Minor, Focused Ion Beam Microscopy and Micromachining, MRS Bull. 32 (2007) 389–399. doi:10.1557/MRS2007.62.

[126] D.S. Gianola, C. Eberl, Micro- and nanoscale tensile testing of materials, JOM. 61 (2009) 24–35. doi:10.1007/S11837-009-0037-3.

[127] G. Ben Salem, E. Héripré, P. Bompard, S. Chapuliot, A. Blouin, C. Jacquemoud, Mechanical Behavior Characterization of a Stainless Steel Dissimilar Metal Weld Interface : In-situ Micro-Tensile Testing on Carburized Martensite and Austenite, Exp. Mech. 2020 608. 60 (2020) 1037–1053. doi:10.1007/S11340-020-00633-1.

[128] P. Arnaud, E. Heripre, F. Douit, V. Aubin, S. Fouvry, R. Guiheux, V. Branger, G. Michel, Micromechanical tensile test investigation to identify elastic and toughness properties of thin nitride compound layers, Surf. Coatings Technol. 421 (2021) 127303. doi:10.1016/J.SURFCOAT.2021.127303.

[129] S. Leclerc, H; Neggers, J; Mathieu, F; Hild, F; Roux, Correli 3.0, 2015. https://scholar.google.com/scholar_lookup?title=Correli 3.0%2C IDDN.FR.001.520008.000.S.P.2015.000.31500&publication_year=2015&author=H. Leclerc&author=J. Neggers&author=F. Matthieu&author=F. Hild&author=S. Roux

(accessed October 11, 2021).

[130] F. Hild, S. Roux, Comparison of Local and Global Approaches to Digital Image Correlation, Exp. Mech. 52 (2012) 1503–1519. doi:10.1007/S11340-012-9603-7.

[131] M. LECLERCQ, Étude de la nanostructure de la dent, 2021.

[132] P. Das, Optical Properties of Low Dimensional Structures Using Cathodoluminescence in a High Resolution Scanning Electron Microscope, University of Calcutta, 2014. https://www.researchgate.net/publication/316548571_Optical_Properties_of_Low_Dimensional_Structures_Using_Cathodoluminescence_in_a_High_Resolution_Scanning_Electron_Microscope (accessed October 11, 2021).

[133] M. Karlík, Úvod do transmisní elektronové mikroskopie, (2011).

[134] K. Grandfield, V. Vuong, H.P. Schwarcz, Ultrastructure of Bone: Hierarchical Features from Nanometer to Micrometer Scale Revealed in Focused Ion Beam Sections in the TEM, Calcif. Tissue Int. 2018 1036. 103 (2018) 606–616. doi:10.1007/S00223-018-0454-9.

[135] R. Rezakhaniha, A. Agianniotis, J.T.C. Schrauwen, A. Griffa, D. Sage, C.V.C. Bouten, F.N. van de Vosse, M. Unser, N. Stergiopulos, Experimental investigation of collagen waviness and orientation in the arterial adventitia using confocal laser scanning microscopy, Biomech. Model. Mechanobiol. 2011 113. 11 (2011) 461–473. doi:10.1007/S10237-011-0325-Z.

7 Appendix A: A TEM study on the nanostructure of dentin

7.1 Introduction

This appendix presents some preliminary results of 'Transmission Electron Microscope' (TEM) imaging of the dentinal tissue. In this thesis, I mainly focused on the microstructure of dentin. However, as seen in section 3.4.1 in the part about the anisotropy of ITD, the role of nanostructure is also interesting to investigate. So, within my thesis work I investigated for the first time at MSSMat laboratory the dentin nanostructure by TEM. I proved the possibility of such study and paved the way for further deeper studies (not in the scope of this thesis). So in this appendix, the method I used to prepare the sample and my preliminary results are highlighted.

7.2 Materials and methods

7.2.1 Sample preparation

The dentin sample was taken from a deciduous incisor of a 6-year old person. The sample was embedded in resin. Then it was cut to reveal a section, which showed an interface between dentin and both enamel and pulp. The sample was polished up to 5 µm. After dehydration with the same protocols as in Chapter 1, the sample was coated with carbon.

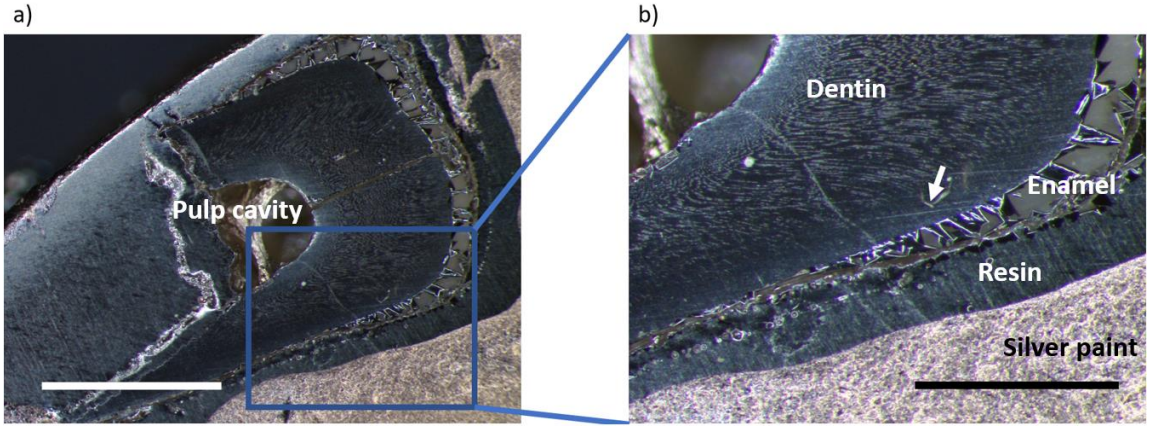

Figure 7-1.a) The tooth sample from which the TEM lamella is prepared (Scale bar: 2 mm). b) Detail of the same sample. The location of the sample is shown by an arrow (Scale bar: 1 mm).

A TEM lamella with the dimensions 11x6.5x0.1 µm is prepared at 0.07 mm from DEJ, where a tubule is connected to a lateral branch (Figure 7-2).

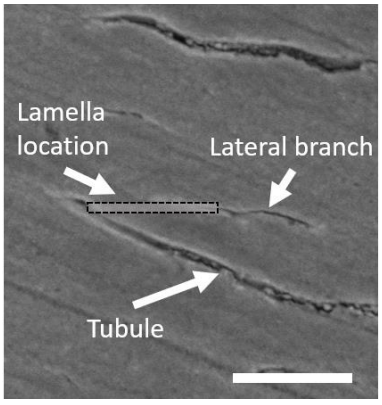

Figure 7-2. The location chosen for milling the TEM lamella (Scale bar: 10 µm).

The steps of sample preparation are shown in Figure 7-3.a to Figure 7-3.h.

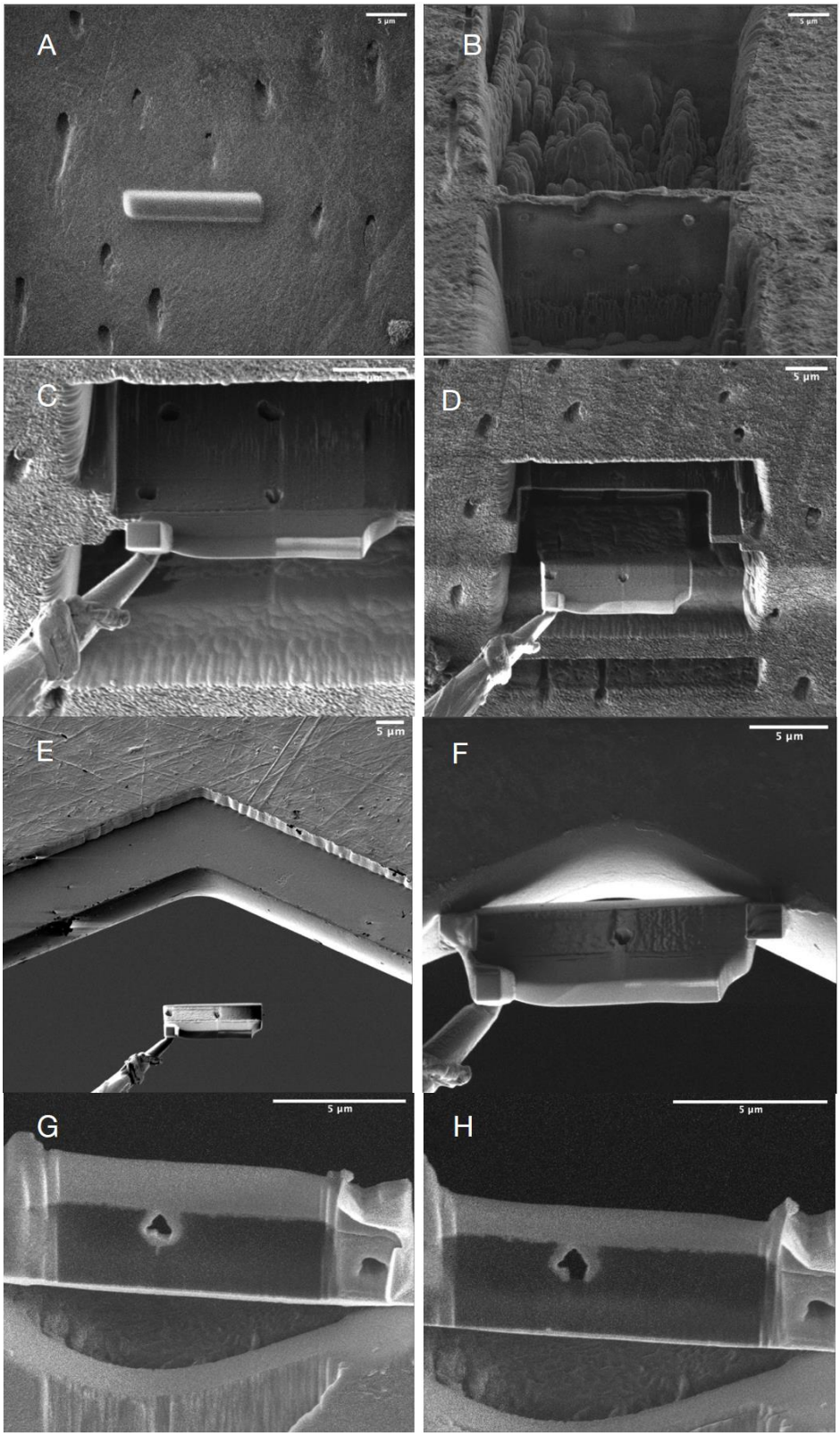

Figure 7-3. Steps of TEM lamella preparation on a dentin sample (not the sample discussed in this thesis), a) The zone of interest with a protective layer of Platinum, b) Revelation of the lamella by abrading the material above and below the lamella with Ga+ ions, c) Fixation of the micromanipulator at the section by Platinum, d) Cutting the section with a U-shape and in-situ extraction, e) Transporting the lamella to the TEM grid, f) Fixation of the TEM grid with Platinum for the thinning step of the lamella, g) Thinning of lamella, h) Lamella of 100 nm thickness, [131]

A protective layer of Platinum is deposited on the zone of interest. Platinum is injected in gas state and is adsorbed by the surface of the specimen. It will protect the zone of interest from the gallium ions that the FIB uses to mill around the specimen.

First, a preliminary block with a bigger thickness than the planned thickness is freed from four sides by milling. The milling is a long process, which takes half to one day. Then, a delicate procedure begins with the goal of manipulating and refining the lamella: The micromanipulator of the electron microscope is approached to the section and is welded to it. Then the lamella can be detached from the dentin sample by the focused ion beam. By retracting the micromanipulator, the lamella is taken away from the dentin sample. This step is sensitive, and the dentin lamella might be lost if the welding of the lamella is not solid enough.

The next step is to insert the copper grid and to weld the lamella to it. After welding the lamella to the copper grid, it is possible to detach the lamella from the micromanipulator using the Gallium ion beam.

Then the lamella is thinned by the focused ion beam to make the specimen transparent for electrons, which happens when it has a thickness of about 100 nm. The thinning is done by a lower current to reduce the curtaining effect, which is known to affect the microscopic images.

7.2.2 Observation device and methods

The microscope used for this study was a “Titan G2 60-300”. It was used to observe the sample in both TEM and STEM modes. The schematic views of these modes are given in Figure 7-4.

A schematic view of TEM mode imaging is shown in Figure 7-4.a. In this mode, a beam with a diameter of approximately 1 µm transmits through the sample and makes an image on the image plane. “In this case, the transmitted electron beam is selected and the diffused electrons are blocked. In fact, the zones which absorb or disperse the electrons, e.g. the hydroxyapatite nanocrystals, appear darker while the zones which transmit the electrons, e.g. collagen fibrils, appear lighter.

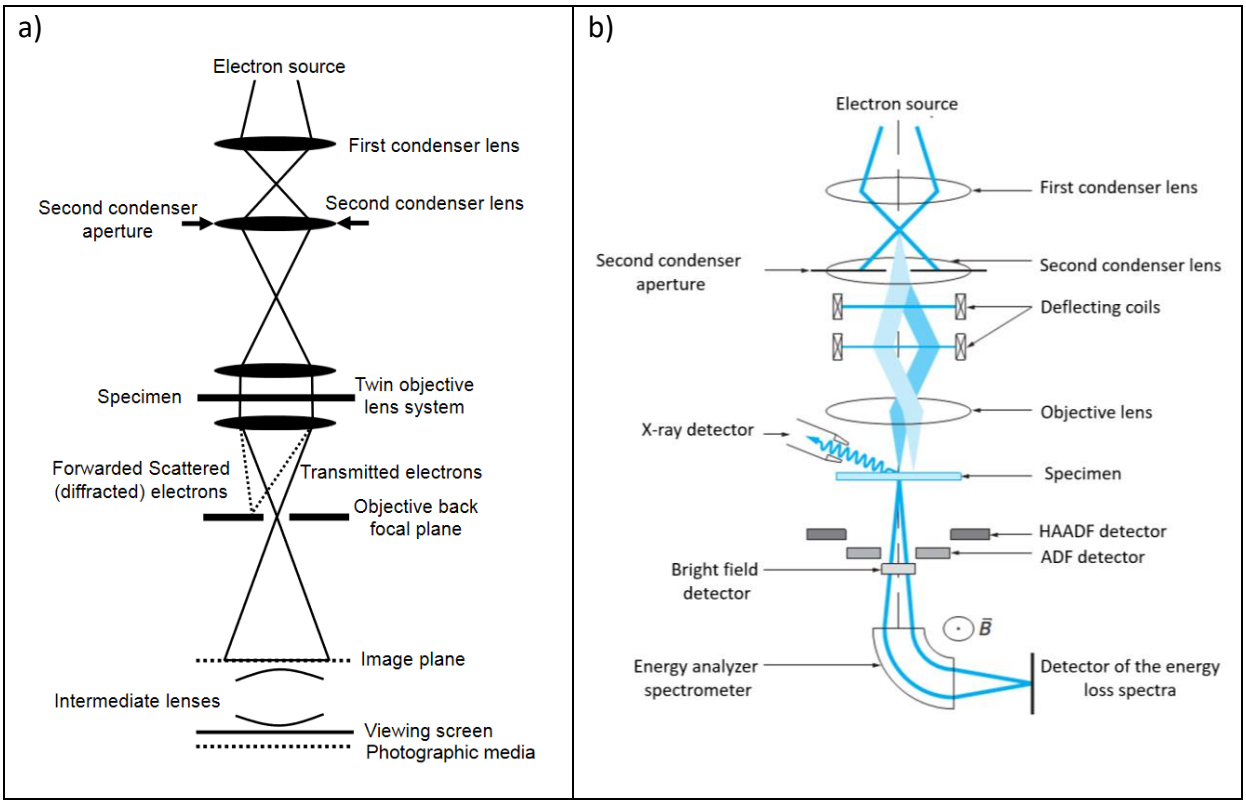

Figure 7-4.a) A schematic diagram of the transmission electron microscope [132]*, b) Schema of Scanning Transmission Electron Microscope* [133].

Figure 7-4.b shows a schema of Scanning Transmission Electron Microscopy mode (STEM). "The TITAN microscope can function in the mode STEM. In this case, the electron beam is focalized by multiple magnetic lenses to a very fine beam with a diameter of 0.05 to 0.2 nm, which scans the thin lamella and is detected by an annular detector. This mode allows a very good spatial resolution by reducing the aberrations because the image is reconstructed point by point. This functioning mode is generally coupled with analytical techniques like the high-angle annular imagery mode in dark field. High-Angle Annular Dark Field imaging is abbreviated as HAADF." In this method the annular detector is situated around the electron beam to gather the diffused electrons and not the transmitted electrons. Therefore, the materials with a higher atomic number like the hydroxyapatite crystals will appear brighter, because they diffuse more electrons. However, the collagen fibrils with their lower atomic numbers appear darker because they transmit more electrons.

7.2.3 Image analysis

ImageJ was used for the measurements of the dimensions of the constituents of dentin at the nanoscale in TEM images. The most visible features in the TEM images are the mineral lamellae (MLs), which are also discussed by Grandfield et al. (2018) [134]. For studying the orientation of these features, a plugin of ImageJ named OrientationJ is used.

7.3 Results and discussion

The location of TEM lamella in the sample, the lamella on the sample holder and its TEM images are shown in Figure 7-5. The existence of the porous phase (lumen) in the chosen location, caused a disruption in the TEM lamella, which is visible in Figure 7-5. Therefore, the remaining part of the lamella was studied.

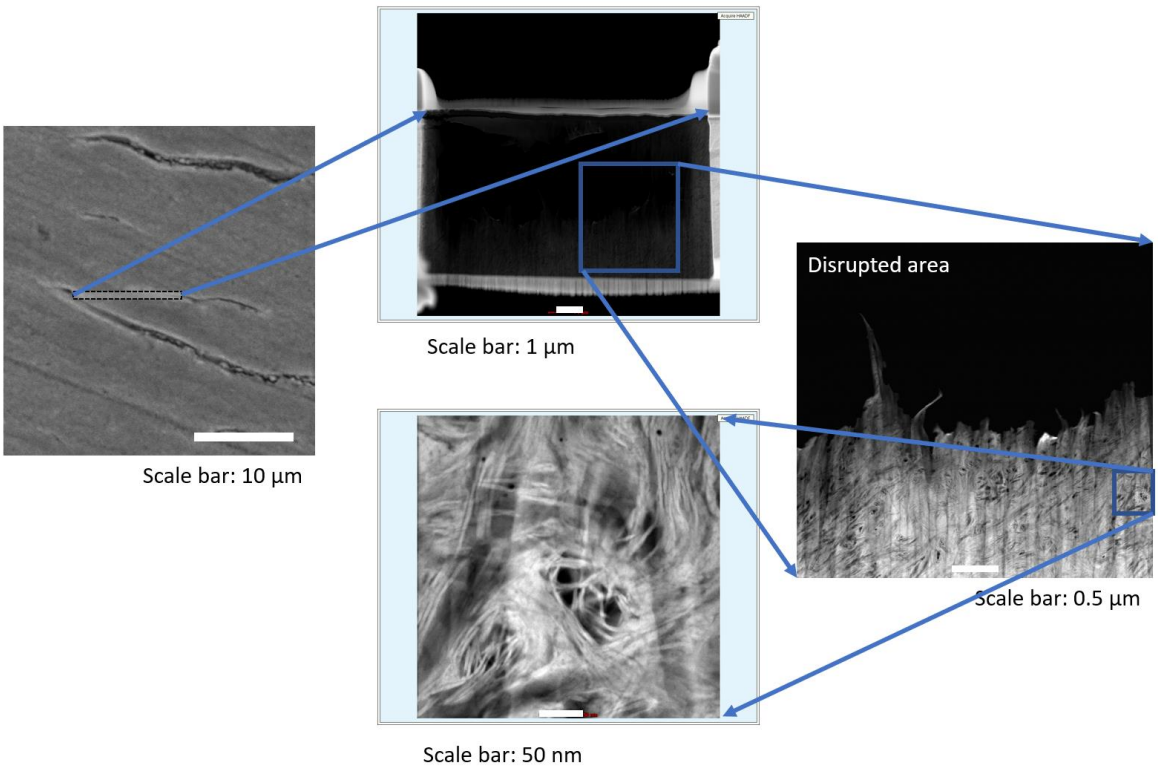

Figure 7-5. The location in the deciduous tooth, and the TEM images that were taken.

An example of a STEM image from the dentin sample is shown in Figure 7-6.

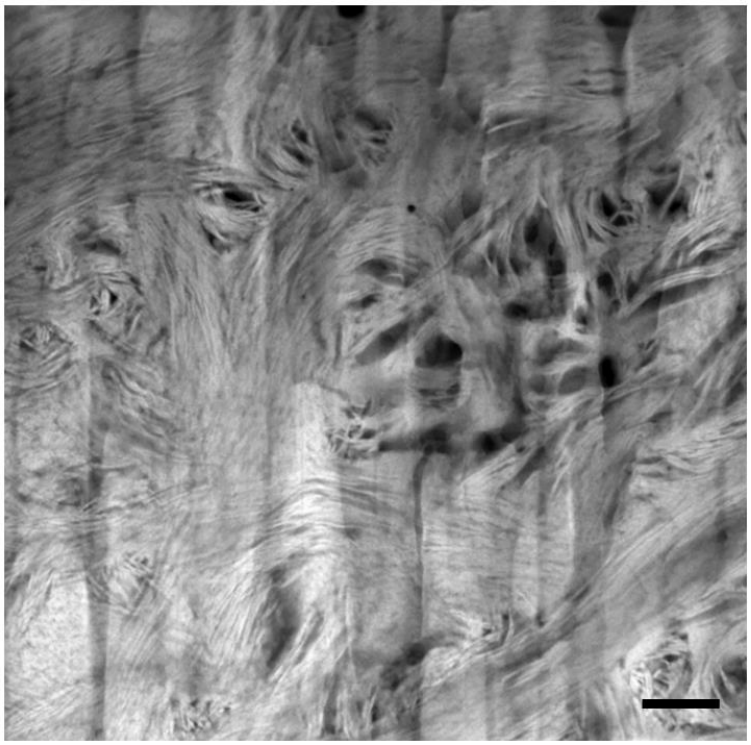

Figure 7-6. STEM image of dentin nanostructure (Scale bar: 100 nm)

7.3.1 Measured dimensions

In this subsection, the TEM images are used for measuring the dimensions of the nanostructure features

Thickness of the minerals

Average thickness of the extrafibrillar minerals was measured for 16 examples, which resulted in an average thickness of 5.27 nm (SD=1.36). This value is close to the value given by Kinney et al. (2001), which was approximately 5 nm. As reported by Grandfield et al. (2008) [134], a variation is visible in the thickness of individual MLs, which they attributed to a torsion of the minerals.

Diameter of the collagen fibrils

As shown in Figure 7-7, the resolution of a TEM image is enough to recognize the D-banding pattern of the collagen fibrils. The diameter of the detected collagen fibril in this image is about 60 nm.

However, in Figure 7-7 elliptical spaces are seen between the mineral lamellae, which have an average minor diameter of 15 nm. This diameter is smaller than the known collagen diameter, which is approximately 50-100 nm [10]. One explanation suggested by Grandfield et al. (2018) [134] could be that such ellipses represent a part of a collagen fibril, through which mineral lamellae pass.

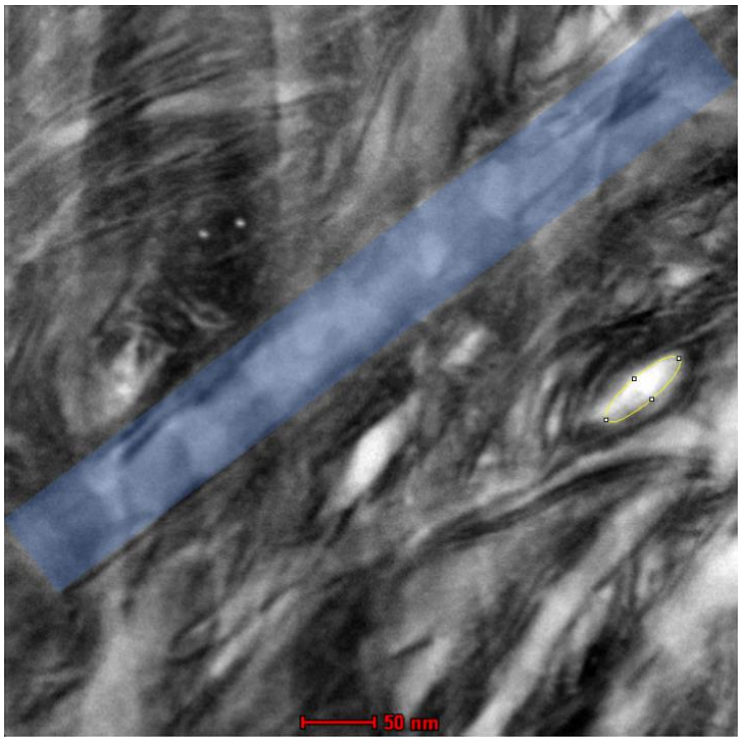

Figure 7-7. A collagen fibril (with the intrafibrillar pattern) is highlighted with blue (bright field STEM)

7.3.2 Orientation of the mineral lamellae

A previous study around the collagen fibrils stated that the MLs are parallel with them [134]. This seems to be the case in this study as well (Figure 7-7). To study the orientation of the MLs more generally, the plugin OrientationJ is used. For the theory of this plugin, the reader is referred to Rezakhaniha et al. (2012) [135].

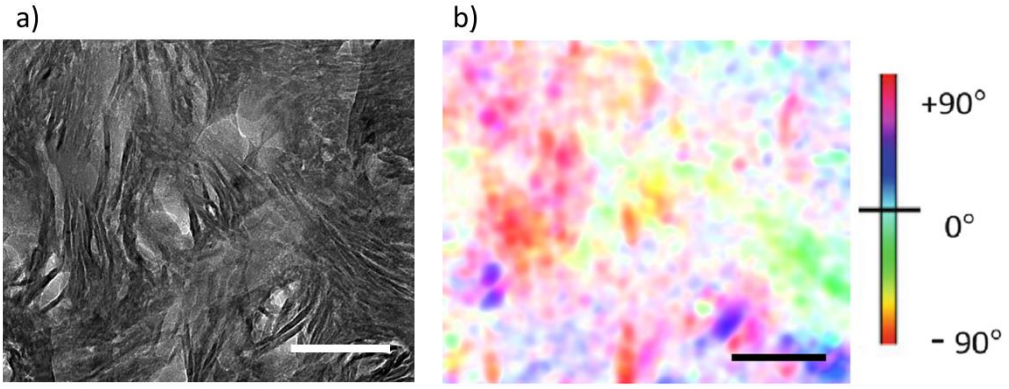

Figure 7-8.a) The STEM image, which is studied by the OrientationJ plugin,

b) The analysis by OrientationJ (Scale bars: 100 nm)

For studying the orientation of a feature, OrientationJ gets a window size, which affects the results. If the window size is too small, then lots of random orientations will be identified. Therefore, the orientation plot will show noise. However, if the window size is too big, the measured orientation spreads to the nearby locations, where there is not any feature with a specific orientation.

After testing various sizes, a window with a size of 6x6 pixels seemed to be the most proper. 6 pixels on the studied image (Figure 7-8.a) is equal to 2.4 nm and is smaller than the dimensions of MLs. The results of the "orientation analysis" with this window size is shown in Figure 7-8.b together with the original image. The histogram of the orientation is shown in Figure 7-9.a.

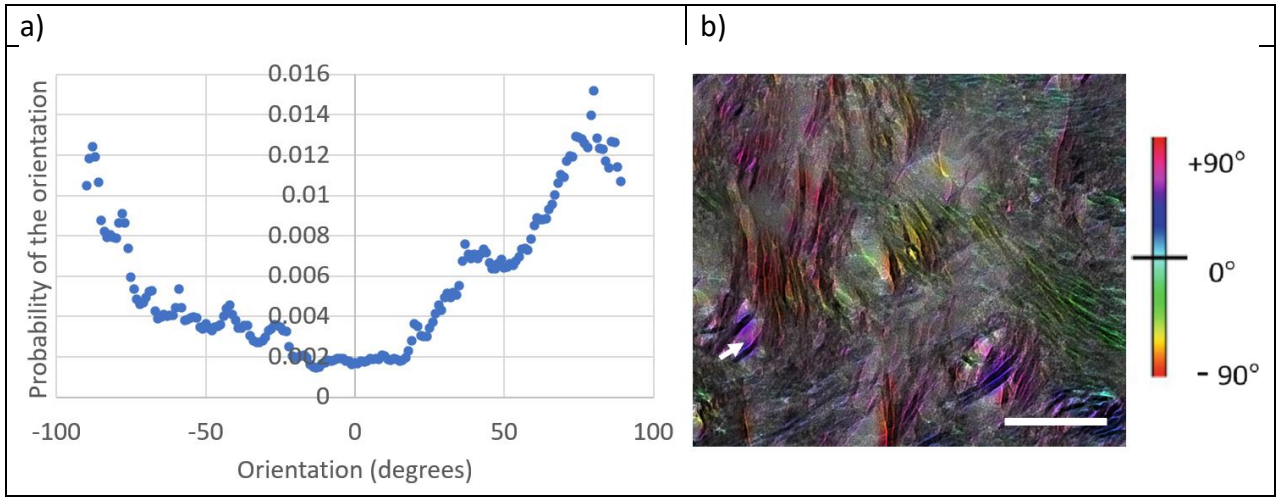

Figure 7-9. The distribution of orientations in the TEM image in a histogram and by color code. (Scale bar: 100 nm)

As seen in the results shown in Figure 7-9.a, the dominant direction is 64°. However, one should not conclude that the MLs are ordered and regularly oriented. As shown by the white arrow in Figure 7-9.b, some of the detected orientations belong to the zones in between the MLs.

7.4 Conclusion

The idea of this study is:

- To define a method to have a TEM lamella
- To show examples of obtained images
- To show what we can get from the images

This study approves the general observation that the orientation of the mineral lamellae around the collagen fibrils is adjusted to surround the collagen fibrils peripherally. Otherwise, not a specific orientation is observed for the collagen fibrils and mineral lamellae. Finding such organizations and orientations will need further studies with TEM lamellae at different positions and orientations [131].

8 Appendix B: Synthèse

Pour améliorer les restaurations dentaires, le tissu dentinaire, une structure multi- échelle doit être encore mieux caractérisé. A l'échelle microscopique, la dentine présente des tubules enrobés de dentine intertubulaire (abrégé ITD). Les tubules sont constitués d'une lumière tubulaire et d'un collier péritubulaire (abrégé PTD) hautement minéralisé. À l'échelle nanoscopique, l'ITD est constituée de fibrilles de collagène et de cristaux d'hydroxyapatite. Jusqu'à ce jour, il n'y a toujours pas d'accord sur la façon dont la structure multi-échelle de la dentine affecte ses propriétés mécaniques (niveau et orientation de l'anisotropie, gradient spatiaux).

Cette thèse apporte des éléments nouveaux clarifiant le rôle de la microstructure dentinaire sur ses propriétés mécaniques. Deux pistes ont été suivies, celle de la simulation numérique et celle de l'expérimentation à une échelle où la microstructure varie peu. À fin d'alimenter et analyser l'expérimentation et la simulation, des propriétés morphologiques et mécaniques de la microstructure ont été obtenues par imagerie MEB et nanoindentation.

Les propriétés morphologiques de la dentine ont été mesurées. Les paramètres classiques ont été mesurés (dimensions, fractions surfaciques des constituants, densité des tubules, …). Une analyse originale a été menée sur le réseau poreux secondaire de la dentine constituée de branchements latéraux (dits « Lateral Branches » en anglais, abrégé comme LBs) ; des données inédites ont été obtenues.

Des essais de nanoindentation ont été planifiés et réalisés pour caractériser les entités de taille microscopique. Selon la profondeur de l'indentation, les propriétés mécaniques des constituants de la dentine à l'échelle microscopique (ITD et PTD séparément) ou le composite homogénéisé (le tissu dentinaire fait de vides, d'ITD et de PTD) ont été mesurées.

Pour simuler les résultats « expérimentaux » obtenus à une certaine profondeur d'indentation à partir d'une micrographie, un outil a été développé (Virtual Nanoindentation), adapté pour l'étude des gradients de propriétés de la dentine dont la microstructure varie en fonction de la localisation. Il a ainsi été possible de porter un regard critique sur les modules locaux des constituants mesurés par les essais.

Ces résultats nous ont permis de développer une modélisation micromécanique de la dentine à différentes localisations (près de l'émail, au milieu du tissu, près de la cavité pulpaire). En considérant une microstructure périodique et en exploitant les données morphologiques, une cellule représentative périodique a été définie et les propriétés des constituants sont issues des résultats expérimentaux. Les simulations numériques ont permis notamment de calculer la matrice de rigidité élastique homogénéisée et locale de la dentine. Ces simulations numériques ont permis de comparer la matrice de rigidité élastique des microstructures avec ou sans LB. Aucun effet significatif des LBs sur la rigidité élastique de la dentine n'a été observé, mais une plus forte concentration de contraintes a été constatée dans les zones où les LB se connectent aux tubules.

Finalement, un test de micro-traction in situ (sous MEB) de dentine a été développé pour caractériser le comportement mécanique du tissu dentaire « homogénéisée » et étudier les

gradients spatiaux de propriétés liés aux gradients de microstructure dans la dentine. Effectué sur une « micro éprouvette » (30 µm de longueur utile, 13 µm d'épaisseur), il est encore en cours d'amélioration, mais sa faisabilité a été prouvée dans ce travail. Cet essai complémentaire à la nanoindentation apportera un éclairage supplémentaire sur le lien entre la microstructure et le comportement mécanique du tissu dentinaire.

université PARIS-SACLAY

ÉCOLE DOCTORALE
Sciences mécaniques et énergétiques, matériaux et géosciences (SMEMAG)

Titre : Étude morphologique et mécanique multi-échelle de la dentine : vers une meilleure compréhension des relations microstructures-propriétés

Mots clés : Biomécanique ; Dentine ; Caractérisation morphologique ; Nanoindentation ; Homogénéisation numérique ; Essai de micro-traction in-situ ;

Résumé : Pour améliorer les restaurations dentaires, le tissu dentinaire, une structure multi-échelle doit être mieux caractérisé. A l'échelle microscopique, la dentine présente des tubules enrobés de dentine intertubulaire (ITD). Les tubules sont constitués d'une lumière tubulaire et d'un collier péritubulaire (PTD) hautement minéralisé. À l'échelle nanoscopique, l'ITD est constituée de fibrilles de collagène et de cristaux d'hydroxyapatite. À ce jour, il n'y a toujours pas d'accord sur la façon dont la structure multi-échelle de la dentine affecte ses propriétés mécaniques (niveau et orientation de l'anisotropie, gradient spatiaux).

Cette thèse apporte des éléments nouveaux clarifiant le rôle de la microstructure dentinaire sur ses propriétés mécaniques. Deux pistes ont été suivies, celle de la simulation numérique et celle de l'expérimentation à une échelle où la microstructure varie peu. Pour alimenter et analyser l'expérimentation et la simulation, des propriétés morphologiques et mécaniques de la microstructure ont été obtenues par imagerie MEB et nanoindentation.

Les propriétés morphologiques de la dentine ont été mesurées. Les paramètres classiques ont été mesurés (dimensions, fractions surfaciques des constituants, densité des tubules, ...). Une analyse originale a été menée sur le réseau poreux secondaire de la dentine constituée de branchements latéraux (LB) ; des données inédites ont été obtenues.

Des essais de nanoindentation ont été réalisés pour caractériser les entités de taille microscopique. Selon la profondeur de l'indentation, les propriétés mécaniques des constituants de la dentine à l'échelle microscopique (ITD et PTD séparément) ou le composite homogénéisé (le tissu dentinaire fait de vides, d'ITD et de PTD) ont été mesurées. Pour simuler les résultats « expérimentaux » obtenus à une certaine profondeur d'indentation à partir d'une micrographie, un outil a été développé (Virtual Nanoindentation), adapté pour l'étude des gradients de propriétés de la dentine dont la microstructure varie en fonction de la localisation. Il a ainsi été possible de porter un regard critique sur les modules locaux des constituants mesurés par les essais.

Ces résultats nous ont permis de développer une modélisation micromécanique de la dentine à différentes localisations (près de l'émail, au milieu du tissu, près de la cavité pulpaire). En considérant une microstructure périodique et en exploitant les données morphologiques, une cellule représentative périodique a été définie et les propriétés des constituants sont issues des résultats expérimentaux. Les simulations numériques ont permis notamment de calculer la matrice de rigidité élastique homogénéisée et locale de la dentine. Ces simulations numériques ont permis de comparer la matrice de rigidité élastique des microstructures avec ou sans LB. Aucun effet significatif des LB sur la rigidité élastique de la dentine n'a été observé, mais une plus forte concentration de contraintes a été constatée dans les zones où les LB se connectent aux tubules.

Enfin, un test de micro-traction in situ (sous MEB) de dentine a été développé pour caractériser le comportement mécanique du tissu dentaire « homogénéisée » et étudier les gradients spatiaux de propriétés liés aux gradients de microstructure dans la dentine. Effectué sur une « micro éprouvette » (30 µm de longueur utile, 13 µm d'épaisseur), il est encore en cours d'amélioration, mais sa faisabilité a été prouvée dans ce travail. Cet essai complémentaire à la nanoindentation apportera un éclairage supplémentaire sur le lien entre la microstructure et le comportement mécanique du tissu.

université PARIS-SACLAY

ÉCOLE DOCTORALE
Sciences mécaniques et énergétiques, matériaux et géosciences (SMEMAG)

Title : Multiscale morphological and mechanical study of dentin : towards a better understanding of structure-properties relationship

Keywords : Biomechanics ; Dentin ; Morphological characterization ; Nanoindentation ; Numerical homogenization ; Micro-tensile test ;

Abstract : Researchers aim to improve dental restorations. This goal requires a better characterization of dentinal tissue, a multiscale structure. At the microscopic scale, dentin has tubules surrounded by intertubular dentin (ITD). The tubules consist of a tubular lumen and a highly mineralized peritubular collar (PTD). At the nanoscale, ITD consists of collagen fibrils and hydroxyapatite crystals. To date, there is still no agreement on how the multiscale structure of dentin affects its mechanical properties (degree and orientation of anisotropy, spatial gradient).

This thesis brings experimental and numerical elements clarifying the role of the dentin microstructure on its mechanical properties. Two tracks were followed : numerical simulation and experimentation at a scale where the microstructure varies little. To feed and analyze the experimentation and simulation, morphological and mechanical properties of the microstructure were obtained by SEM imaging and nanoindentation.

The morphological properties of dentin were measured. In addition to measuring the classical parameters (dimensions, area fractions of the constituents, the density of the tubules), an original analysis was conducted on the secondary porous network of dentin consisting of lateral branches (LB) ; new data were obtained.

Nanoindentation tests were performed to characterize the entities of the microscopic size. Depending on the indentation depth, the mechanical properties of the microscale dentin constituents (ITD and PTD separately) or the homogenized composite (the dentinal tissue made of voids, ITD, and PTD) were measured.

In order to simulate the "experimental" results obtained at a certain indentation depth from a micrograph, a tool was developed (Virtual Nanoindentation), adapted for studying the gradients of dentin properties, whose microstructure varies by location. It was thus possible to take a critical look at the local moduli of the constituents measured by the tests.

These results allowed us to develop a micromechanical model of dentin at different locations (near the enamel, in the middle of the tissue, near the pulp cavity). By considering a periodic microstructure and exploiting the morphological data, a periodic representative cell was defined, and the properties of the constituents were derived from the experimental results. Numerical simulations have been used to calculate the homogenized and localized elastic stiffness matrix of the dentin. These numerical simulations allowed comparing the elastic stiffness matrix of the microstructures with and without LBs. No significant effect of LBs on the elastic stiffness of dentin was observed, but a higher stress concentration was found in areas where LBs connect to tubules.

Finally, an in-situ micro-strain test (under SEM) of dentin was developed to characterize the mechanical behavior of the "homogenized" dental tissue and to study the spatial gradients of properties related to the microstructure gradients in dentin. The test, carried out on a "micro-specimen" (30 µm useful length, 13 µm thickness), is still being improved, but its feasibility has been proven in this work. This test, complementary to nanoindentation, will shed additional light on the link between the microstructure and the mechanical behavior of the tissue.

Maison du doctorat de Université Paris-Saclay
2e étage, aile ouest, École normale supérieure Paris-Saclay
4 avenue des Sciencs
91190 Gif-sur-Yvette, France